



THE UNIVERSITY OF  
**WAIKATO**  
*Te Whare Wānanga o Waikato*

Research Commons

<http://researchcommons.waikato.ac.nz/>

## Research Commons at the University of Waikato

### Copyright Statement:

The digital copy of this thesis is protected by the Copyright Act 1994 (New Zealand).

The thesis may be consulted by you, provided you comply with the provisions of the Act and the following conditions of use:

- Any use you make of these documents or images must be for research or private study purposes only, and you may not make them available to any other person.
- Authors control the copyright of their thesis. You will recognise the author's right to be identified as the author of the thesis, and due acknowledgement will be made to the author where appropriate.
- You will obtain the author's permission before publishing any material from the thesis.

# Heat Integrated Milk Powder Production

A thesis

submitted in fulfilment

of the requirements for the degree

of

**Doctorate of Philosophy in Engineering**

at

**The University of Waikato**

by

**TIMOTHY G. WALMSLEY**



THE UNIVERSITY OF  
**WAIKATO**  
*Te Whare Wānanga o Waikato*

2014



“The glory of God is intelligence,  
or, in other words, light and truth.”

Doctrine and Covenants 93:36



# Abstract

---

Dairy processing is critical to New Zealand's (NZ) economy producing NZ\$13 billion in exports for 2012 while consuming 32 PJ of fossil fuels for process heat. Three quarters of NZ dairy exports are milk powders. This thesis presents methods to reduce process heat use in Milk Powder Plants (MPP) through improved heat integration and addresses key technical challenges preventing industrial implementation. My original contributions to literature include: (1) a novel design method called the Cost Derivate Method (CDM) that cost optimally allocates area in direct heat exchange networks, (2) a new design methodology for integration of semi-continuous process clusters using a Heat Recovery Loop (HRL) with a Variable Temperature Storage (VTS) system for improved heat recovery, (3) an experimentally validated deposition model for predicting critical air conditions that cause milk powder fouling, and (4) a thermo-economic assessment tool for the optimisation of industrial spray dryer exhaust heat recovery projects via a Liquid Coupled Loop Heat Exchanger (LCHE) system.

By applying Pinch Analysis to an industrial MMP, this work confirms that heat must be recovered from the milk spray dryer exhaust air (~75 °C) to achieve maximum heat integration in MPPs. For stand-alone MPPs exhaust heat is best used to indirectly preheat the inlet dryer air reducing steam use by 12.7 % for a 55 °C exhaust outlet. Additional economic heat recovery from condensate and vapour flows decreased steam use by a further 6.9 %. Application of the CDM to the liquid and vapour sections of new MMP maximum energy recovery networks reduced total cost by 5.8 %. For multi-plant dairy factories, a second industrial case study showed the exhaust heat may be integrated with neighbouring plants via a HRL with VTS to increase site heat recovery by 10.8 MW including 5.1 MW of exhaust heat recovery, compared to 7.9 MW using a conventional HRL design method with constant temperature storage.

A key barrier preventing exhaust heat recovery implementation in NZ MPPs is the possibility of milk powder fouling. Dryer exhaust air contains a low concentration of powder that when exposed to low temperatures at high humidity becomes sticky. For a heat exchanger face air velocity of 4 m/s, experimental data from milk powder fouling tests of flat plates, tubes and fins indicates particulate fouling becomes severe when the exhaust air temperature reaches 55 °C. Higher face velocities are shown to lower this critical exhaust temperature for avoiding severe fouling, which gives potential for increased heat recovery but for increased pressure drop. Lower face velocities show the opposite effect. Designing exhaust heat recovery systems entail an acute trade-off between heat transfer, pressure drop and fouling. Two important design parameters are the number of tube rows in the exhaust heat exchanger and the face velocity. The outputs of a thermo-economic spreadsheet tool suggest LCHE systems for a dryer producing 23.5 t/h is economic. With a face velocity of 4 m/s and 14 rows of finned round tube, the project had an estimated payback of 1.6 years, a net present value of NZ\$3 million and internal rate of return of 71 %. This tool will empower industry with greater confidence to uptake exhaust heat recovery technology as a vital method for improving the heat integration of MPPs in NZ.

# Acknowledgements

---

At the close of this chapter of life it is most appropriate to reflect and recognise those individuals who have got me to where I am today and express my heartfelt gratitude. This thesis, although written and authored by myself, would not have been possible without the support of my wife Puti Walmsley and my son David Ihaia, my chief supervisor Prof Michael Walmsley (who is also my uncle), and my other supervisors Dr Martin Atkins and Dr James Neale. There have been many stimulating discussions over the past three years, which have generated some of the key pillars and chapters of this thesis. I have relished the opportunity to be part of the Energy Research Group led by Prof Peter Kamp and the School of Engineering at the University of Waikato. I would also like to thank Andrew Morrison for his timely input to my work while at Conference PRES 2012, and Chloe Sellers, Dayne Addenbrooke, Rene Engelbrecht, and Thomas White, all of whose fourth year engineering research projects aligned with my thesis topic.

I would like to recognise the tremendous financial support granted by the Todd Foundation and the University of Waikato through their respective scholarships. Without which support there would have much less food on the table at home, and perhaps no table to speak of in the first place. Also to the Claude McCarthy trust for their support to attend the 2013 Conference PRES in Rhodes, Greece.



# Contributing Publications

---

The bulk of the results contained in this thesis have been published in respectable international engineering journals. The greater parts of Chapter 3 along with Chapter 4 are published in Applied Thermal Engineering [3,7]. Chapter 5 is published in Energy [4], and related work is included in the Handbook of Process Integration [1]. Chapter 6 is published in the Journal of Food Engineering [5]. Half of the results in Chapter 7 is published in the Proceedings of the Heat Exchanger Fouling and Cleaning Conference [14] and is under review for publication in Applied Thermal Engineering [2], while the other half of Chapter 7 is published in Advanced Powder Technology [9]. Chapter 8 is accepted for publication in Chemical Engineering Transactions [6]. Early versions of various chapters are found in Chemical Engineering Transactions [8,10,12,13] and the proceedings of various local and international conferences [14-20].

Research comprising this thesis has been presented at several international and local conferences. Most notably the work in Chapter 3 was awarded best student poster at Conference PRES 2012 and Chapter 4 was selected for a keynote lecture at Conference PRES 2013.

## Book Chapter

- [1] M. R. W. Walmsley, M. J. Atkins, **T. G. Walmsley**, 2013. Application of Heat Recovery Loops to Semi-continuous Processes for Process Integration (Chapter 20), in: Handbook of Process Integration (PI). Woodhouse Publishing Co., Cambridge, UK.

## Journal Articles

- [2] **T. G. Walmsley**, M. R. W. Walmsley, M. J. Atkins, J. R. Neale, 2014. Analysis of skim milk powder deposition on stainless steel tubes in cross-flow. Applied Thermal Engineering, in review.
- [3] **T. G. Walmsley**, M. R. W. Walmsley, M. J. Atkins, J. R. Neale, 2014. A derivative based method for cost optimal area allocation in heat exchanger networks. Applied Thermal Engineering, accepted article.
- [4] **T. G. Walmsley**, M. R. W. Walmsley, M. J. Atkins, J. R. Neale, 2014. Integration of industrial solar and gaseous waste heat into heat recovery

- loops using constant and variable temperature storage. Energy, accepted article.
- [5] **T. G. Walmsley**, M. R. W. Walmsley, M. J. Atkins, J. R. Neale, C. M. Sellers, 2014. An experimentally validated criterion for skim milk powder deposition on stainless steel surfaces. Journal of Food Engineering 127, 111-119.
  - [6] **T. G. Walmsley**, M. R. W. Walmsley, M. J. Atkins, J. R. Neale, 2014. Thermo-economic Assessment Tool for Industrial Milk Spray Dryer Exhaust Heat Recovery Systems with Particulate Fouling. Chemical Engineering Transactions 39, accepted article.
  - [7] **T. G. Walmsley**, M. R. W. Walmsley, M. J. Atkins, J. R. Neale, 2013. Improving energy recovery in milk powder production through soft data optimisation. Applied Thermal Engineering 61, 80-87.
  - [8] **T. G. Walmsley**, M. R. W. Walmsley, M. J. Atkins, J. R. Neale, 2013. A derivative method for minimising total cost in heat exchanger networks through optimal area allocation. Chemical Engineering Transactions 35, 1171-1176.
  - [9] **T. G. Walmsley**, M. R. W. Walmsley, M. J. Atkins, J. R. Neale, 2013. Fouling and pressure drop analysis of milk powder deposition on the front of parallel fins. Advanced Powder Technology 24, 780-785.
  - [10] M. R. W. Walmsley, **T. G. Walmsley**, M. J. Atkins, J. R. Neale, 2013). Integration of solar heating into heat recovery loops using constant and variable temperature storage. Chemical Engineering Transactions 35, 1183-1188.
  - [11] M. R. W. Walmsley, **T. G. Walmsley**, M. J. Atkins, J. R. Neale, 2013. Methods for improving heat exchanger area distribution and storage temperature selection in heat recovery loops. Energy 55, 15-22.
  - [12] **T. G. Walmsley**, M. R. W. Walmsley, M. J. Atkins, J. R. Neale, 2012. Optimal stream discharge temperatures for a dryer operation using a thermo-economic assessment. Chemical Engineering Transactions 29, 403-408.
  - [13] M. R. W. Walmsley, **T. G. Walmsley**, M. J. Atkins, J. R. Neale, 2012. Area targeting and storage temperature selection for heat recovery loops. Chemical Engineering Transactions 29, 1219-1224.

## Conference Papers

- [14] **T. G. Walmsley**, M. R. W. Walmsley, M. J. Atkins, J. R. Neale, D. M. Addenbrooke, 2013. Critical flow aspects for mitigating deposition of skim milk powder on tubes in cross-flow. Proceedings of the International Conference on Heat Exchanger Fouling and Cleaning – 2013, Budapest, Hungary, 272-278.

- [15] **T. G. Walmsley**, M. R. W. Walmsley, M. J. Atkins, J. R. Neale, 2013. Increasing Plate Heat Exchanger Thermal Duty: An Industrial Case Study. Proceedings of the NZ Conference of Chemical and Materials Engineering, Auckland, New Zealand.
- [16] R. Engelbrecht, **T. G. Walmsley**, M. R. W. Walmsley, 2013. Milk Powder Deposition in Cross-Flow Heat Exchangers. Proceedings of the NZ Conference of Chemical and Materials Engineering, Auckland, New Zealand.
- [17] **T. G. Walmsley**, M. R. W. Walmsley, M. J. Atkins, J. R. Neale, 2012. An investigation of milk powder deposition on parallel fins. Chemeca Conference Lecture S02-1, Wellington, New Zealand.
- [18] **T. G. Walmsley**, M. R. W. Walmsley, M. J. Atkins, J. Hoffmann-Vocke, J. R. Neale, 2012. Numerical performance comparison of different tube cross-sections for heat recovery from particle-laden exhaust gas streams. Procedia Engineering 42, 1476-1490.
- [19] M. R. W. Walmsley, **T. G. Walmsley**, M. J. Atkins, J. R. Neale, 2012. Design and operation methods for better performing heat recovery loops. Chemeca Conference Lecture S14-2, Wellington, New Zealand.
- [20] **T. G. Walmsley**, M. R. W. Walmsley, M. J. Atkins, J. R. Neale, J. Hoffmann-Vocke, 2011. Tube shape selection for heat recovery from particle-laden exhaust gas streams. SCENZ/ICHEME New Zealand Conference, Hamilton, New Zealand (no proceedings).



# Table of contents

---

<b>Abstract</b> .....	<b>I</b>
<b>Acknowledgements</b> .....	<b>III</b>
<b>Contributing Publications</b> .....	<b>V</b>
<b>Table of contents</b> .....	<b>IX</b>
<b>Nomenclature</b> .....	<b>XIII</b>
<b>Chapter 1 Introduction</b> .....	<b>1</b>
1.1. Background .....	1
1.2. Thesis aim.....	6
1.3. Thesis outline .....	7
<b>Chapter 2 Literature review</b> .....	<b>9</b>
2.1. Introduction.....	9
2.2. A brief introduction to milk drying.....	10
2.3. Advances in the process heat integration of milk powder factories ....	13
2.4. Performance and fouling of gaseous heat recovery exchangers .....	33
2.5. Conclusion .....	57
<b>Chapter 3 Improving heat recovery in stand-alone milk powder plants</b> .....	<b>59</b>
3.1. Introduction.....	59
3.2. Industrial milk powder production process .....	60
3.3. Methodology .....	62
3.4. Stream analysis and energy targeting .....	65
3.5. Heat exchanger networks.....	71
3.6. Conclusion .....	77
<b>Chapter 4 Cost optimal area allocation in milk powder plant HENs</b> .....	<b>79</b>
4.1. Introduction.....	79
4.2. Derivation of the Cost Derivative Method for cost optimal area allocation.....	80
4.3. Application of the Cost Derivative Method.....	98
4.4. Milk powder plant case study .....	100
4.5. Simple distillation case study (non-dairy).....	105
4.6. Method limitations and future developments.....	107
4.7. Conclusion .....	109

<b>Chapter 5 Increasing total site heat integration in large multi-plant dairy factories.....</b>	<b>111</b>
5.1. Introduction .....	111
5.2. Targeting, design and modelling methodologies for HRLs.....	113
5.3. Data collection and characterisation.....	124
5.4. Steady state HRL targets and design .....	127
5.5. Transient modelling of HRL performance.....	138
5.6. Conclusion .....	147
<b>Chapter 6 A criterion for skim milk powder deposition on stainless steel surfaces .....</b>	<b>149</b>
6.1. Introduction .....	149
6.2. Theory of particle-wall contact mechanics.....	150
6.3. Experimental methods.....	154
6.4. Experimental deposition results.....	161
6.5. Validation of deposition criterion .....	164
6.6. Conclusion .....	166
<b>Chapter 7 Thermal and hydraulic performance analysis of fins and tubes.....</b>	<b>167</b>
7.1. Introduction .....	167
7.2. Methods .....	168
7.3. Experimental results for single tubes in cross-flow .....	172
7.4. Experimental results for parallel plates.....	183
7.5. Application of experimental results .....	188
7.6. Conclusion .....	189
<b>Chapter 8 Thermo-economic assessment tool for industrial milk spray dryer exhaust to inlet air heat recovery systems .....</b>	<b>191</b>
8.1. Introduction .....	191
8.2. Method for modelling indirect exhaust heat recovery system.....	192
8.3. Exhaust heat recovery industrial case study.....	204
8.4. Importance of site selection for dryer exhaust heat recovery .....	208
8.5. Conclusion .....	210
<b>Chapter 9 Conclusions and recommendations for future work.....</b>	<b>211</b>
9.1. Conclusions .....	211
9.2. Recommendations for future work.....	212
<b>References.....</b>	<b>215</b>
<b>Appendix A Lists of figures and tables .....</b>	<b>229</b>

List of figures .....	229
List of tables .....	237
<b>Appendix B Common <math>\epsilon</math>-NTU relationships and their derivatives .....</b>	<b>239</b>
<b>Appendix C Cost Derivative Method: Derivations, proofs and examples</b> .....	<b>243</b>
<b>Appendix D Exhaust-inlet liquid coupled loop heat exchanger system</b> .....	<b>265</b>



# Nomenclature

---

## Roman

<p><math>A</math> area (<math>m^2</math>)</p> <p><math>a</math> solar loss coefficient</p> <p><math>a_w</math> water activity</p> <p><math>B</math> proportionality constant</p> <p><math>b</math> capital cost coefficient (<math>\\$/m^2</math>)</p> <p><math>C</math> heat capacity flow rate (<math>kW/^\circ C</math>)</p> <p><math>\hat{C}</math> specific heat capacity flow rate (<math>MJ/^\circ C \cdot t</math>)</p> <p><math>C^*</math> ratio of minimum to maximum heat capacity flow rates for <math>\epsilon</math>-NTU method</p> <p><math>CC</math> annualised capital cost (<math>\\$/y</math>)</p> <p><math>c_p</math> heat capacity at constant pressure (<math>kJ/kg \cdot ^\circ C</math>)</p> <p><math>c_b</math> particulate concentration in air flow (<math>kg/kg</math>)</p> <p><math>D</math> groups of variables/constants (varies)</p> <p><math>D_1</math> dimensionless constant</p> <p><math>D_2</math> temperature constant (<math>^\circ C</math>)</p> <p><math>d</math> diffusivity (<math>m/s</math>)</p> <p><math>d</math> diameter (<math>m</math>)</p> <p><math>E</math> energy (<math>kJ</math>)</p> <p><math>E^*</math> power per heat transfer area (<math>kW/m^2</math>)</p> <p><math>F</math> force (<math>N</math>)</p>	<p><math>F</math> heat exchanger correction factor</p> <p><math>FC</math> annualised fixed cost (<math>\\$/y</math>)</p> <p><math>f</math> friction factor</p> <p><math>G</math> heat duty flow-on function</p> <p><math>G</math> shear modulus (<math>Pa</math>)</p> <p><math>H</math> enthalpy (<math>kW</math>)</p> <p><math>h</math> heat transfer film coefficient (<math>kW/^\circ C \cdot m^2</math>)</p> <p><math>I</math> cost index</p> <p><math>I</math> solar irradiance (<math>kW/m^2</math>)</p> <p><math>j</math> Colburn j factor</p> <p><math>K</math> mass transfer coefficient (<math>kg/s \cdot m^2</math>)</p> <p><math>k</math> constant (varies)</p> <p><math>L</math> groups of variables/constants</p> <p><math>NTU</math> number of transfer units</p> <p><math>m</math> mass (<math>kg</math>)</p> <p><math>\dot{m}</math> mass flow rate (<math>kg/s</math>)</p> <p><math>n</math> variously defined</p> <p><math>P</math> pressure (<math>Pa</math>)</p> <p><math>P</math> temperature effectiveness</p> <p><math>Pr</math> Prandtl number</p> <p><math>\rho</math> utility price (<math>\\$/kWh</math>)</p> <p><math>\hat{p}</math> annual utility price (<math>\\$/kW \cdot y</math>)</p> <p><math>Q</math> heat duty (<math>kW</math>)</p> <p><math>q</math> specific heat duty (<math>kJ/kg</math>)</p>
--	--

$R$	heat transfer resistance ( $^{\circ}\text{C} \cdot \text{m}^2/\text{kW}$ )	$t$	time (s)
$R$	ratio of fluid heat capacity flow rates for P-NTU method	$t^+$	particle relaxation time
$Re$	Reynolds number	$U$	overall heat transfer coefficient ( $\text{kW}/^{\circ}\text{C} \cdot \text{m}^2$ )
$RH$	relative humidity (%)	$UC$	utility cost ( $\$/\text{y}$ )
$RM$	rolling moment	$u_{\infty}$	average (heat exchanger face) gas velocity (m/s)
$r$	particle radius ( $\mu\text{m}$ )	$W$	work (J)
$S$	annual savings ( $\$/\text{y}$ )	$X$	mass fraction of water on a dry basis (kg/kg)
$S$	spacing (m)	$x$	thickness (m)
$St$	Stanton number	$Y$	Young's modulus (Pa)
$s$	probability of sticking	$Y^*$	modified Young's modulus (Pa)
$T$	temperature ( $^{\circ}\text{C}$ )		
$TC$	total annual cost ( $\$/\text{y}$ )		

### Greek

$\alpha$	ratio of heat exchanger area to volume ( $\text{m}^2/\text{m}^3$ )	$\lambda$	calculated variable
$\beta$	stream split fraction	$\mu$	viscosity ( $\text{Pa} \cdot \text{s}$ )
$\gamma$	adhesion bond strength ( $\text{J}/\text{m}^2$ )	$\nu$	Poisson's ratio
$\Delta$	positive difference between two states	$\xi$	deposit bond strength factor
$\delta$	penetration depth (m)	$\xi$	coefficient of restitution
$\varepsilon$	heat exchanger effectiveness	$\rho$	density ( $\text{kg}/\text{m}^3$ )
$\eta$	degree of integration	$\sigma$	ratio of finned area to total area ( $\text{m}^2/\text{m}^2$ )
$\Theta$	impact angle ( $^{\circ}$ )	$\tau_t$	time constant (s)
$\theta$	heat duty flow-on factor	$\tau_w$	wall shear stress (Pa)
		$\varphi$	frontal open area ( $\text{m}^2/\text{m}^2$ )

### Subscripts/superscripts

*	shifted	$\infty$	bulk or average
1	inlet	a	adhesion
2	outlet	add	additional

amb	ambient	lc	cold storage
ave	average	lh	hot storage
b	buoyancy	loop	loop stream
CR	condenser loop return	max	maximum
c	cold stream	min	minimum
co	cold stream outlet	n	normal
cont	contribution	O	optical
cap	capillary or capital	o	outside
crit	critical	out	outlet
d	drag	p	particle
dew	dew point	pd	plastic deformation
ele	electrostatic	pro	process
f	final	r	recovery
f	fouling	rot	rotational
g	gravity	s	sticking, supply or solar
h	hot stream	sp	set point
ho	hot stream outlet	t	tangential or target
i	inside	tot	total
in	inlet	ut	utility
L	lift	w	water
l	lactose, limiting or loop		

### **Abbreviations**

$\Delta T_{LM}$	log-mean temperature difference method	CTS	constant temperature storage
$\epsilon$ -NTU	effectiveness-number of transfer units method	FB	fluidised bed
CDM	cost derivative method	HE	heat exchanger
CFD	computational fluid dynamics	HEN	heat exchanger network
CIP	clean-in-place	HRL	heat recovery loop
COP	coefficient of performance	IRR	internal rate of return
COW	water removed from milk	LCHE	liquid-coupled loop heat exchanger

MER	maximum energy recovery network	RE	heat recovery exchanger
MVR	mechanical vapour recompression	SEC	specific energy consumption
NPV	net present value	SMP	skim milk powder
P-NTU	temperature effectiveness-number of transfer units method	TE	terminal heat recovery exchanger
PA	pinch analysis	TSA	total site analysis
PDM	pinch design method	TSM	time slice model
PI	process integration	TVR	thermal vapour recompression
		UE	utility exchanger
		VTS	variable temperature storage

# Chapter 1

## Introduction

### 1.1. Background

An estimated 30 % of manufacturing energy use in New Zealand derived from coal, natural gas and wood, or 32.1 PJ, was consumed by dairy processing for process heat in 2012. Other significant energy users include petroleum and chemical manufacturing, pulp and paper and wood processing as shown in Figure 1-1. The heat demand of dairy processing arises primarily from milk powder production. In 2012 the New Zealand dairy industry processed roughly 18 billion litres of milk to generate nearly a quarter of national exports, i.e. NZ\$13 billion (Statistics NZ, 2013). Recent conversions from sheep and beef farming to dairying, together with the construction of new processing plants, has fuelled the exponential growth of dairy processing over the last decade. As a result the total heat demand of dairy processing is growing whereas demand in other industrial sectors, such as pulp and paper and wood processing, is contracting.

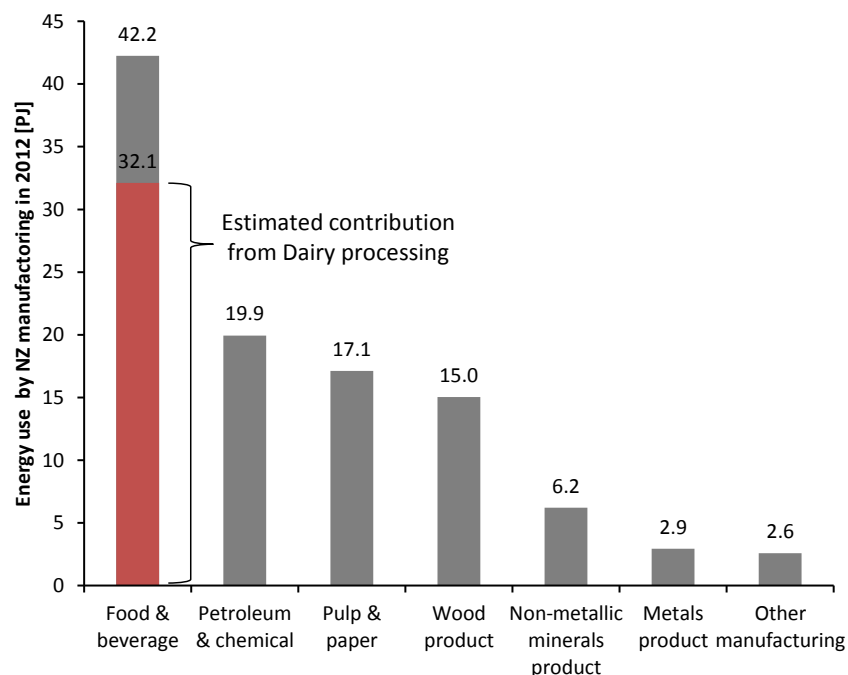


**Figure 1-1: Process heat use for manufacturing derived from coal, natural gas and wood in 2012 (“New Zealand Energy Use: Industrial and trade sector 2012,” 2013).**

Conversion of raw milk into powdered milk is energy intensive due to the high energy content associated with the vapour-liquid phase change of water as it is traditionally removed by evaporation. The milk powder process involves two dewatering operations as illustrated in Figure 1-2. The first dewatering unit operation is a multi-effect evaporator train. In the New Zealand dairy industry, modern evaporator trains are integrated with mechanical and thermal vapour recompression units for improved heat efficiency. Milk enters the evaporators at about 10 % solids and leaves the evaporators at approximately 52 % solids. This solids level represents the present practical and operational ceiling due to the rheology of the concentrate. The concentrated milk is atomised and dried to form micron-sized milk powder particles at approximately 96 % solids in the spray dryer and fluidised bed operations. From these dewatering operations three heat source streams are generated each with a different phase from which heat can be recovered. Maximising heat recovery in the milk powder process is chiefly about the best utilization of these heat sources.

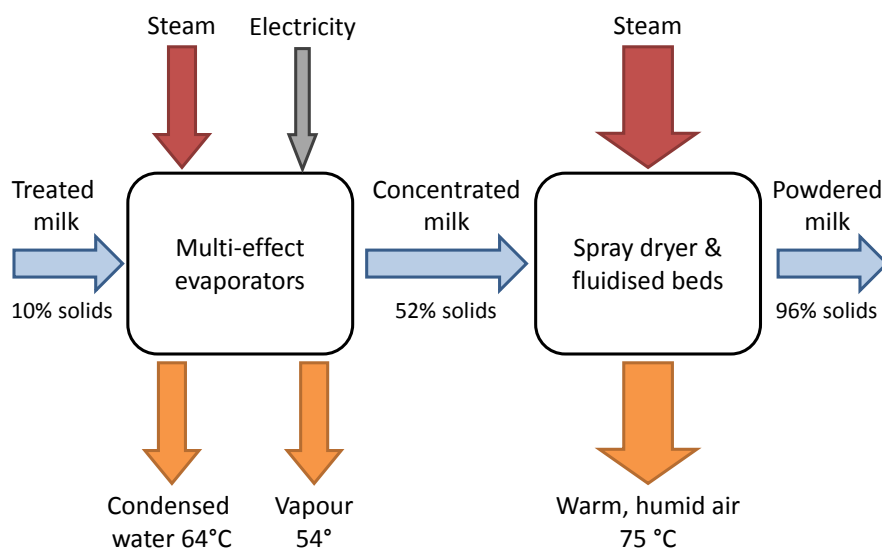


**Figure 1-2: The conversion of liquid milk into powdered milk using spray drying.**

Industrial process heat consumption in large-scale milk powder plants is considerably reduced by heat recovery. However a recent study has suggested that heat recovery from warm dryer exhaust air flows could decrease steam use by a further 10 – 20 % (Atkins et al., 2011), which equates to a savings potential of 2.4 – 4.8 PJ/y for all milk powder production in New Zealand. In the past recovery

of low-grade heat from dryer exhaust air flows has been overlooked as an economic priority possibly due to energy costs in dairy processing representing only a small proportion of the total production cost (Klemeš et al., 2008), in addition to several technical challenges.

Increasing global concerns over rising energy prices, future energy security and pollution are, however, forcing industries to look further into the future and become more energy efficient. Figure 1-3 shows the costs of coal and natural gas in New Zealand have been increasing faster than the cost of capital. Energy projects that had a four year payback in 2002 will now have a payback of 2 – 3 years. Low priority heat recovery projects from previously ignored streams are now being reconsidered and the associated technical challenges need solutions.

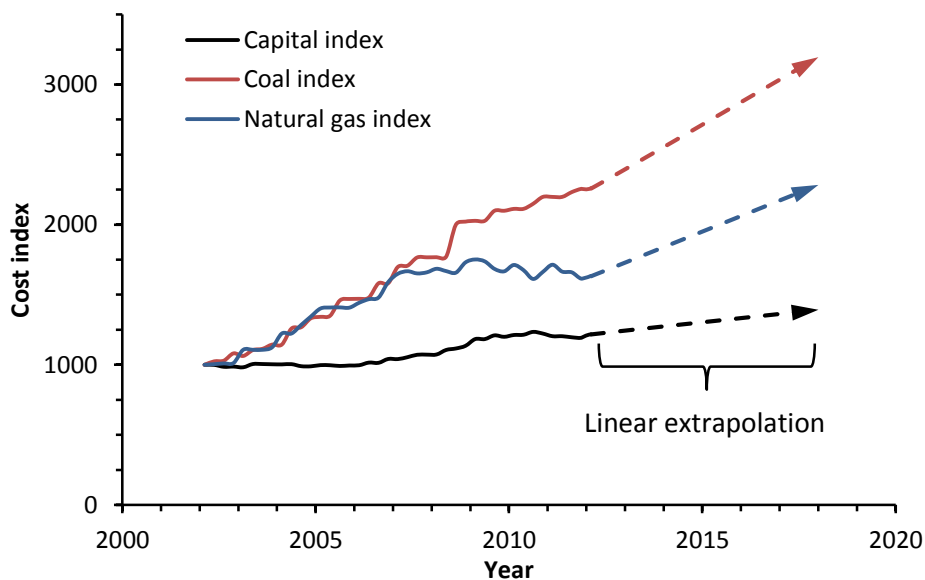


**Figure 1-3: Comparison of food processing capital to energy costs in New Zealand showing a linear extrapolation (Statistics NZ, 2013).**

The New Zealand dairy industry has been cautious to uptake spray dryer exhaust heat recovery. In the mid-1980's, the Plains Co-Op Dairy Ltd factory installed a glass tube air-to-air exhaust heat recovery system. Energy surveys of its performance showed heat recovery decreased by 40 % after 13 h of operation (Neale, 2014). In 2008, the Edendale dairy factory built a new state-of-the-art dryer (ED4), which was also the world's largest milk dryer at the time, and had plans to install a liquid coupled loop exhaust heat recovery system. The exhaust heat exchanger was built but never installed due to concerns over milk powder

fouling causing disruptions to plant production. Since that time an additional twelve milk powder spray dryers have been built in New Zealand all without exhaust heat recovery, which is evidence that exhaust heat recovery is not standard industry practice in New Zealand.

Economic heat recovery from dryer exhaust air flows is non-trivial and faces several technical challenges that are both general and site specific in nature. Key engineering research questions include: Where is the best place to use dryer exhaust heat? How does dryer exhaust heat recovery affect current industrial heat integration strategies? Will milk powder fouling significantly degrade the performance of a dryer exhaust heat exchanger? How does heat recovery impact on the initiation and rate of fouling? These engineering research questions represent gaps in the knowledge as well as hurdles to wide-spread industrial uptake of dryer exhaust heat recovery.

The first two questions are related to the integration of the milk powder process. The idea of Process Integration (PI) is to take a holistic approach to process design and optimisation that looks at how a collection of processes or systems are best integrated. PI techniques, such as Pinch Analysis (PA), have been applied to determine the minimum heating and cooling requirements of numerous processes (Linnhoff and Flower, 1978), including the milk powder process (Lovell-Smith and Baldwin, 1988; Robertson and Baldwin, 1993), and to design practical strategies to achieve the minimum energy target (Linnhoff and Hindmarsh, 1983). PA involves the application of fundamental thermodynamic principles to provide understanding where heat recovery in a process is constrained as indicated by so called Pinch temperatures, from which realistic targets for increased energy recovery and cost savings may be calculated (Kemp, 2005). Using Pinch temperatures as a starting point, non-obvious heat exchanger network designs may be developed to significantly improve the overall profitability of heat recovery systems.

PI techniques have been successfully applied to semi-continuous dairy processes where plants run for a matter of hours or days before cleaning is required to

guarantee product quality (Klemeš, 2013). Total site methodologies have extended the practical application of PA to improve the heat integration of large multi-plant/process sites (Klemeš et al., 1997). In particular, indirect integration of low temperature processes, such as dairy processes, using a Heat Recovery Loop (HRL) system has also been investigated (Atkins et al., 2012a). However lacking in the dairy space is a thermo-economic assessment and optimisation of the economic profitability of increasing heat recovery in dairy processing, and more particularly milk powder processing. Such established techniques in conjunction with thermo-economic assessment may be applied to explain how dryer exhaust heat may be integrated on dairy processing sites. However this does not address the questions relating to heat exchanger fouling.

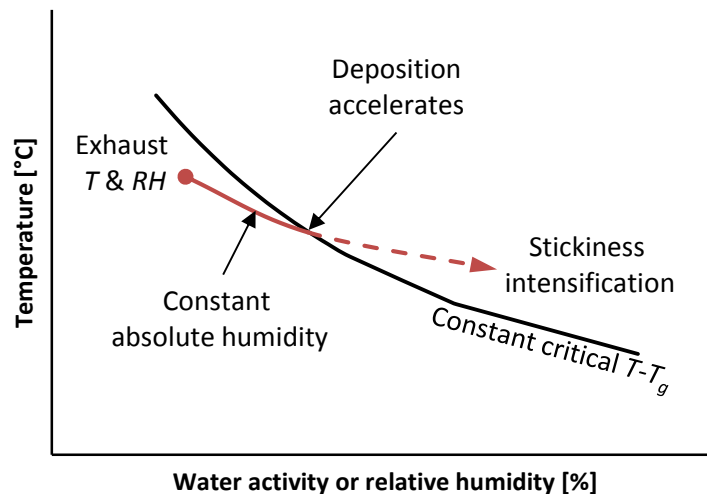


**Figure 1-4: Intensification of milk powder stickiness as exhaust heat is recovered.**

Particulate fouling of dryer exhaust heat exchanger systems is probable and, in the most severe cases, may lead to plant downtime reducing powder production and leading to significant profit loss. Although very little research has focused on air-side milk powder fouling of heat exchangers, there have been several studies that have addressed the problem of milk powder stickiness and deposition in the context of the spray dryer, fluidised bed, cyclone and baghouse (filters) unit operations. The surface stickiness of milk powder, which is an amorphous material, is intrinsically related to the concepts of glass transition temperature and viscosity (Downton et al., 1982). As a result the stickiness of powder particles can intensify as heat from the dryer exhaust air is recovered and the air temperature

is decreased as illustrated in Figure 1-4. The deposition of milk powder particulate on wall surfaces is also dependent on the particle impact velocity (Murthi et al., 2010), particle size (Zhao, 2009), and the wall geometry, temperature and material (Woo et al., 2009). At present the literature lacks a validated model that describes the primary variables that influence the attachment of sticky milk powder particles. Gaining a fundamental understanding of milk powder stickiness and its deposition on heat exchanger surfaces is essential to help determine methods to mitigate fouling and identify upper boundaries for heat recovery that are advantageous to stay within.

## **1.2. Thesis aim**

The aim of the research is to investigate how to maximise economic heat recovery in milk powder production. The scope of the research includes stand-alone milk powder plants and milk powder plants co-located with other dairy processes on a single large site. Focus in the research is targeted for New Zealand milk powder plants and dairy factories, and economics are based on the best available local data. Analysis of stand-alone milk powder plants include the evaporator and spray dryer sections of the plant, which always operate simultaneously, but excludes milk treatment because it operates on a separate schedule and is often an already highly integrated process with little opportunity for increased heat recovery. Large multi-plant dairy sites have several independent processes such as milk powder, milk treatment, butter, cheese, casein, whey, utilities, etc. Integration between the process and utility systems is not considered in this thesis. For hot utility, a single price is assumed since combined heat and power generation at NZ dairy factories is rare. When utility savings are identified, it is assumed there is an equal reduction in utility generation and utility cost.

To achieve the overall aim, the thermodynamic constraints of heat recovery within milk powder plants are investigated and strategies for improving heat recovery are designed. Novel methodologies for the optimisation of direct heat exchange networks and the design of HRLs with a variable temperature storage system for site integration is developed. The role of dryer exhaust air in increasing heat recovery is determined and the level of milk powder fouling on heat transfer

surfaces is experimentally tested. A key output from this thesis is a spreadsheet tool that can model the performance and economic viability of a dryer exhaust heat recovery system.

### **1.3. Thesis outline**

Chapter 2 thoroughly reviews the key literature and advances in the areas of PI and heat exchangers that are most relevant to the thesis aim. It examines the current state of the art for heat integration of the milk powder process. It highlights that heat recovery from the dryer exhaust air is critical to achieving a step change in milk powder plant energy efficiency. Even though there appears to be no established scheme for how this heat is best utilised for the milk powder plant case. Key methodology for analysing how heat recovery from the exhaust is best integrated into the milk powder process and/or other on-site processes is presented. The second half of Chapter 2 focuses on the challenge posed by milk powder fouling in an exhaust heat exchanger and its adverse effects on thermal and hydraulic heat exchanger performance. To round out the chapter, the fundamentals of milk powder stickiness and deposition is critically reviewed.

The subsequent six chapters represent the bulk of the numerical and experimental results. Chapter 3 applies conventional PI techniques to investigate how heat integration in stand-alone milk powder plants can be improved. It highlights the importance of correctly selecting the discharge temperature of streams leaving the process and the impact these temperatures have on heat recovery targets set by PA. A keystone to increasing integration within the milk powder plant is heat recovery from the dryer exhaust air. Practical heat exchanger network structures are established and compared to current industry practice. Two of these network structures from Chapter 3 are further optimised in Chapter 4 where a novel mathematical method of cost optimal area allocation in heat exchanger networks is derived from fundamental heat exchanger cost and design equations. This new method has wider appeal than just the dairy industry: the method is generally applicable.

Chapter 5 places the milk powder plant in the context of a large dairy factory containing multiple other dairy processes and investigates the potential for improved heat integration at the total site level. Inter-plant heat recovery targets are set for indirect heat recovery systems operated with constant and variable temperature heat storage. Using historical plant data, the indirect heat recovery systems are modelled and performance forecasts are established, underlining the improved effectiveness of the new variable temperature approach in unlocking much greater inter-plant heat recovery potential. Heat from the dryer exhaust of the milk powder plants proves to be a highly valuable source for heating other low-temperature on-site dairy processes.

After establishing how dryer exhaust heat recovery is best integrated in stand-alone milk powder plants and large dairy factories, the next two chapters focus on understanding how milk powder entrained in the exhaust air will interact with and foul heat exchanger surfaces. Chapter 6 identifies the underlying mechanisms driving milk powder fouling by experimentally quantifying the conditions controlling airborne particle deposition on flat plates. A fundamental contact mechanics model describing the collision and attachment of adhesive, elastic particles forms the basis for engineering a semi-empirical model that adequately expresses the experimental results. Chapter 7 increases the scale of the experimental work to look at deposition on the face of fins and the front of tubes. The semi-empirical model developed in Chapter 6 is compared to results obtained in Chapter 7. Particular focus is given to understanding how fast the pressure drop increases as fouling occurs in the heat exchanger like geometries.

The final piece of the thesis is Chapter 8, which demonstrates a spreadsheet tool that has been developed to quickly assess the performance and economy of the application of exhaust heat recovery to a new or existing industrial milk powder plant. Incorporated in the tool is knowledge gained in Chapters 6 and 7 to make predictions for the rate of fouling and its associated impact on dryer exhaust heat recovery and air flow resistance. Chapter 9 summarises the major findings of the research and provides recommendations for areas of future work.

# Chapter 2

## Literature review

---

### 2.1. Introduction

The literature relevant to the thesis aim broadly falls into the closely related categories of Process Integration (PI) and heat exchanger performance and design as shown in Figure 2-1. These two research fields are enormous and, as a result, the scope of this literature review chapter is limited to those areas of research that are considered to be the most relevant to the aim. In the first section, important studies that have looked at heat integration of the milk powder process, either at the individual plant level or total site level, are critically analysed. The next section highlights the most significant advances in the field of PI with particular focus on how these methodologies apply to low temperature processes involving intra- and inter-plant heat integration. The latter half of the review focuses on gaseous heat recovery systems, and its acute design trade-off between heat transfer and hydraulic resistance, and the impact of particulate fouling on overall performance. The review is concluded by drawing attention to gaps in the knowledge that need addressing and the key methodologies relevant to achieving the thesis aim.

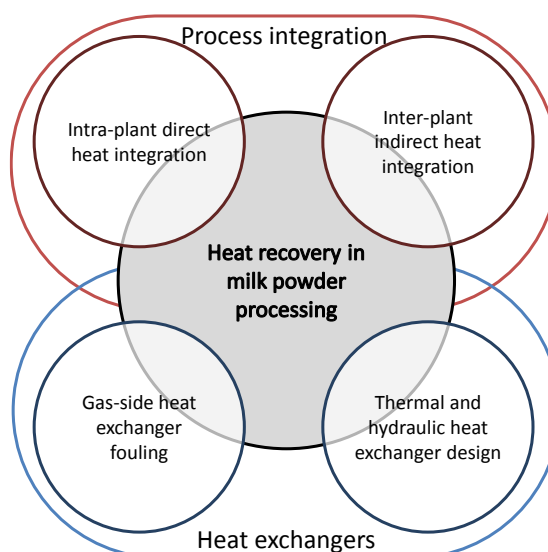


Figure 2-1: Key areas relating to maximising heat recovery in milk powder processing.

## 2.2. A brief introduction to milk drying

A schematic of a typical industrial milk powder plant is illustrated in Figure 2-2 with two distinct dewatering processes: multi-effect evaporators and spray dryer with fluidised beds. Prior to milk being concentrated in the evaporator units, milk from the farm is processed in milk treatment. In milk treatment, raw milk is separated into skim milk and cream, and its composition standardised. Cream is pasteurised at about 85 °C and standardised milk is stored below 8 °C until it is required in the drying operations. Milk treatment is a highly self-integrated heating and cooling process that operates independent of the dewatering processes and therefore is not considered for direct integration. At large milk powder plants and dairy factories, milk treatment typically has multiple processing trains that run in parallel to each other.

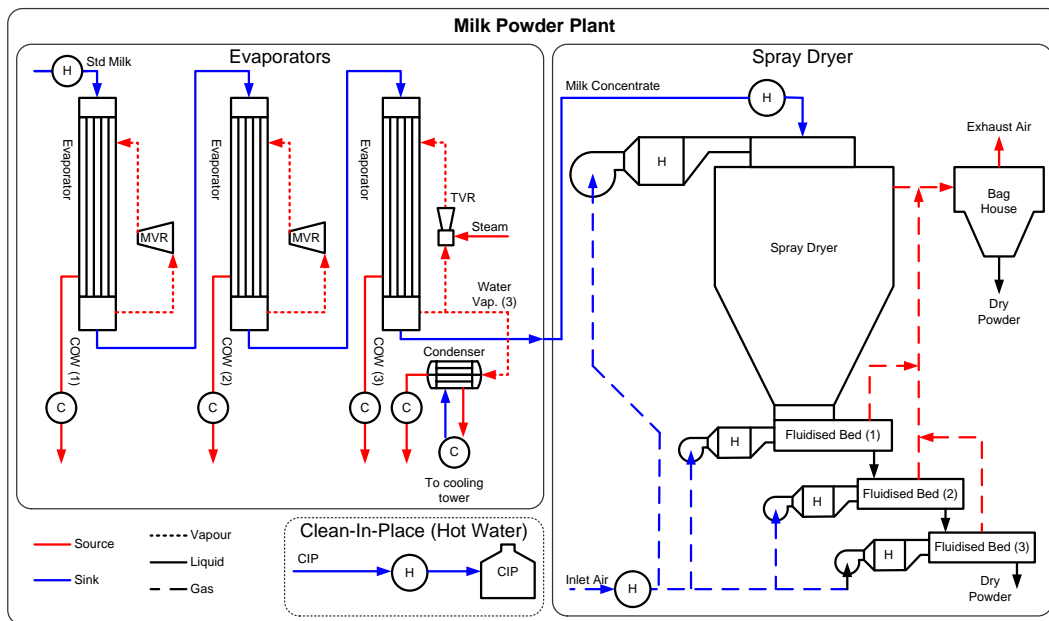


Figure 2-2: Milk powder plant schematic.

The first dewatering stage occurs in multi-effect evaporators. In this stage standardised milk at 9 – 10% solids by weight is concentrated to between 50 – 52% solids. A common method for integrating the evaporator units is using Mechanical Vapour Recompression (MVR) and Thermal Vapour Recompression (TVR) as shown in Figure 2-2. Low pressure vapour is normally bled from the evaporators to provide additional preheating of the standardised milk and direct steam injection is commonly applied before milk enters the evaporators to minimise

microbial growth. Typically evaporator unit operations are washed every 10 – 16 hours whereas the spray dryer is washed every two to four weeks depending on the product. As a result plants tend to also have multiple trains of multi-effect evaporators allowing for continuous operation of the spray dryer.

The next stage of the process is spray drying. In spray drying, milk concentrate is atomized and sprayed in a large conical shaped chamber. Co-current to the milk droplets, hot air at about 200 °C enters the chamber and, in a few seconds, the outer shells of the milk particles are dried. The majority of the product falls to the bottom of the chamber while warm humid air exits on the side of the main chamber anywhere between 70 – 85 °C depending on the operation of the dryer and the product. Connected to the base of the spray dryer is a fluidised bed train, through which powder is conveyed providing the necessary residence time for removal of moisture still at the particle's core and for cooling down of the powder. Dry powder leaves at 4 – 6% moisture by weight. The dryer air exhausts through cyclones and/or baghouses to remove most of the entrained powder before being emitted to atmosphere. The concentration of powder in the exhaust air ranges from 2 to 20 mg/m<sup>3</sup> (Zillwood, 2010).

Demand for process heat at New Zealand dairy factories is typically met by on-site generation of ~40 bar steam using boilers. Most North Island factories use natural gas as the fuel to the boiler whereas the South Island factories and the remainder of North Island factories use coal. Electricity needs are satisfied by the national grid. The requirement for 40 bar steam exists to allow heating of the inlet dryer air to 200 °C. The TVR unit operation uses medium pressure (~10 bar) steam, while other processes such as the separation of milk and cream are more heat sensitive and may need hot water. Lower temperature hot utility requirements are normally generated by downgrading 40 bar steam to 10 bar steam at a let-down station (without a back pressure steam turbine) and by using a steam-powered hot water loop. As a result hot utility at New Zealand dairy factories is priced at the same rate in terms of \$/MWh for 40 bar steam, 10 bar steam and hot water.

The specific energy consumption (SEC) of milk powder plants has been reported in literature on a few occasions as listed in Table 2-1. Xu and Flapper (2011) provide the most comprehensive collection of SEC data for milk powder production in terms of thermal and electrical energy use. Lovell-Smith and Baldwin (1988) conducted an energy use survey of New Zealand plants whereas Robertson and Baldwin (1993) studied a typical milk powder plant and published what they calculated as achievable SEC levels. It is important to note that the specific details of the milk powder product, plant configuration, the quality of the measurements, and the number of plants involved surrounding each of the numbers in Table 2-1 are not given in the original papers making it difficult to explain the cause of such large SEC ranges. The SEC of milk drying is also strongly influenced by the amount of heat recovery, the concentration of the milk exiting the evaporators, and the temperature efficiency of the spray dryer.

**Table 2-1: Specific energy consumption for industrial milk powder production in various countries. Sources: <sup>a</sup> Xu and Flapper (2011), <sup>b</sup> Lovell-Smith and Baldwin (1988), <sup>c</sup> Robertson and Baldwin (1993).**

	SEC Thermal [GJ/t <sub>p</sub> ]	SEC Electrical [GJ/t <sub>p</sub> ]
Australia <sup>a</sup>	10.2 – 20.6	1.4
Europe <sup>a</sup>	28.5 – 190	0.6 – 31.4
Great Britain <sup>a</sup>	20.7 <sup>a</sup>	-
Kenya <sup>a</sup>	11.8	0.9
Netherlands <sup>a</sup>	8.7 – 16.4 <sup>a</sup>	-
Scandinavia <sup>a</sup>	12.6	1.6
USA <sup>a</sup>	9.2	1.9
NZ (1984/85) <sup>b</sup>	12.3 – 37.8	-
NZ (early 1990's) <sup>c</sup>	7.5 – 9.1	-

## **2.3. Advances in the process heat integration of milk powder factories**

### **2.3.1. Stand-alone milk powder plant heat integration**

Reducing the energy requirement of evaporator unit operations has been the focus of numerous studies and included in several chemical engineering books, e.g. Minton (1986). The majority of literature and industry documentation on the heat integration of milk evaporators have focused on the set-up and operational aspects of the evaporator train (Westergaard, 2010).

Figure 2-3 is a schematic illustrating the two general principles used in the dairy industry to design and integrate the evaporator unit operation. Method A reduces steam use by reusing vapour from one effect in the next effect, which requires a vacuum to be pulled on the product side that must increase from effect to effect to provide a temperature driving force for heat transfer. Method B uses vapour recompression technology such as TVR and MVR to compress the vapour from one effect and reuse it in the same effect (or an upstream effect). The compression increases the pressure and temperature of the vapour and, in some situations, a small indirect steam heater (not shown in Figure 2-3b) is installed to provide additional temperature lift after the MVR. In the New Zealand dairy industry, method A is often found in older plants, whereas method B is found in newer plants.

At the 2005 World Dairy Summit, Hanneman and Robertson (2005) presented an overview of heat recovery and integration examples in the dairy industry. Their report covered the utility system, the milk treatment process, the cream treatment process, the cheese process, the clean-in-place system, and the milk powder process. For the evaporator section of the milk powder process, Hanneman and Robertson compared a five effect evaporator train integrated with a TVR to a single evaporator effect integrated with an MVR. Based on an efficiency of 40 % for electricity generation from natural gas, their analysis showed the MVR scheme required 55 % less natural gas consumption. However the analysis failed to utilise the additional low pressure vapour generated in the TVR units that can

be integrated as a heat source in the surrounding (or background) process heating requirements.

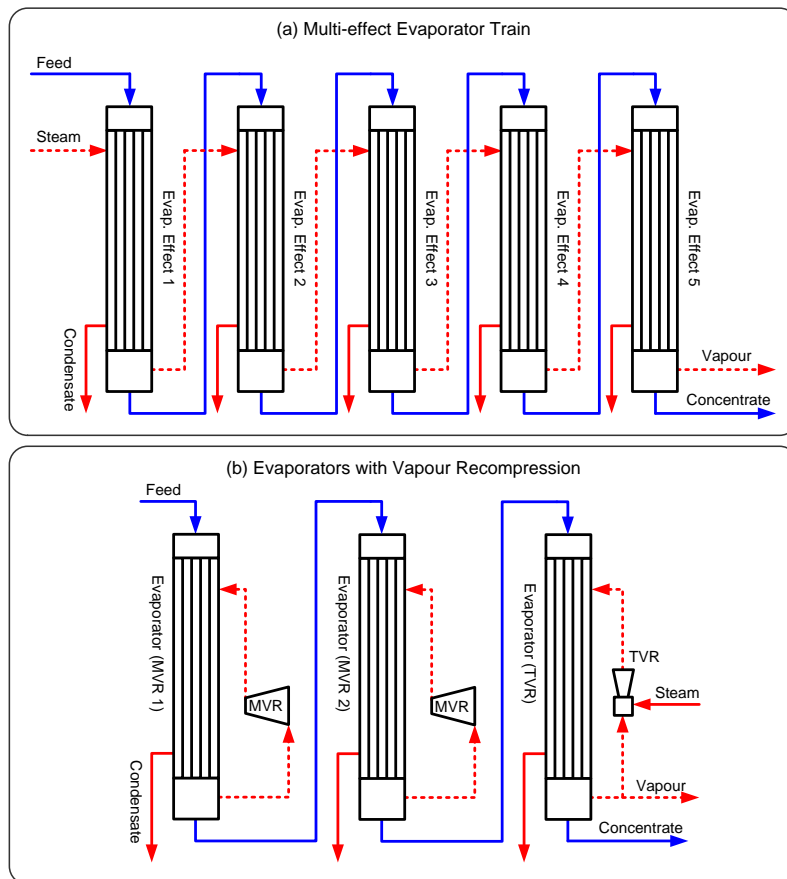


**Figure 2-3: Common falling film evaporator integration methods in the dairy industry.**

Figure 2-4 compares on a temperature versus enthalpy graph the differences between an evaporator integrated with: (a) no vapour recompression and single effect, (b) MVR and (c) TVR (Westphalen and Wolf Maciel, 2000). In Figure 2-3a, the entire evaporation and condensation loads must be done using other process streams and/or utility. The efficiency of this system can be vastly improved by considering multiple evaporator effects where the condensing load from one effect is used as the evaporation heat input requirement in another effect. In the MVR case, no heating or cooling loads are needed or generated. Electric motors generate mechanical work to drive the compressor, which causes a pressure and temperature lift in the vapour. In the TVR case, about two thirds of the vapour from evaporation is combined with medium or high pressure utility steam, which results in a vapour mixture with a higher pressure and temperature than the evaporation load. The additional third of vapour not upgraded must be condensed

using process heating needs or utility to pull a vacuum in the evaporator. When evaporators are integrated using vapour recompression units compared to a traditional multi-effect evaporator train, fewer effects are needed to achieve the same level of energy efficiency.

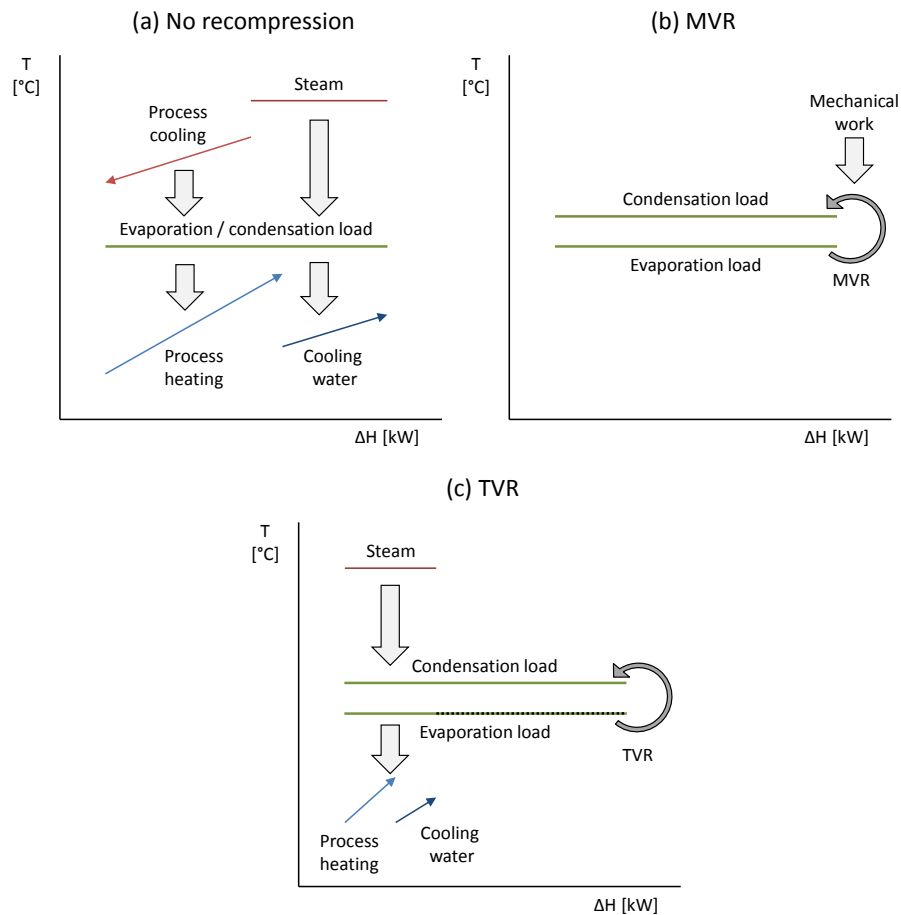


**Figure 2-4: Heat integration of evaporator systems with the background process heating and cooling requirements.**

Substantial gains in energy efficiency has been realised in other industries when evaporator systems are purposefully designed to effectively integrate with the background process (Smith and Jones, 1990). Operating temperatures, vapour bleed rates and the flash condensate systems are modelled in terms of temperature and enthalpy and compared to the heating and cooling demands of the background process (Westphalen and Wolf Maciel, 2000). Using PI techniques, such as Pinch Analysis (PA), researchers have demonstrated that such a systems design approach can lead to further reducing utility use in the order of 30 % depending on the application. For example Axelsson et al. (2008) looked at the

integration of evaporators in hardwood and softwood mills and identified an economic steam savings of 36 %, and Westphalen and Wolf Maciel (2000) found a steam savings of 23 % for a three-effect evaporator system at a crystal glucose plant. For this systems design approach, focus is given to understanding how process heating and cooling needs can help supply heat to or utilise waste heat from the evaporator system (Figure 2-4). However the design procedure of evaporators must also give consideration to the product and, in particular, how operating temperatures affect its quality.

The temperature operating window of milk evaporator trains is tightly constrained to between 45 – 68 °C due to milk being a heat-sensitive material (Westergaard, 2010). Above 68 °C denaturation of milk proteins occurs degrading the quality of the final product whereas 45 °C is the practical lower limit for the operating temperature of the final evaporator effect. Besides the increased technical difficulty of pulling larger vacuums, lactose (a majority component of skim milk solids) may crystallize at temperatures below 45 °C.

Robertson and Baldwin (1993) applied PA to look at the integration of milk evaporators with the spray dryer and milk treatment plants. Their results based on a composite curve energy targeting approach showed a potential specific steam savings of 0.48 GJ/t<sub>p</sub> (based on one tonne of product), which was equivalent to a 6 % steam utility savings. However Robertson and Baldwin did not report the development of HENs to achieve the potential savings. In an earlier work, Lovell-Smith and Baldwin (1988) applied PA based on minimum temperature differences contributions to obtain a potential savings of 24 % for milk powder plants. The study recommends to the dairy industry a number of possible energy savings projects. However, like Robertson and Baldwin, the work of Lovell-Smith and Baldwin does not clearly present the entire HEN. In both studies the pinch temperature of the milk powder process is reported to be around 50 °C, however the stream data used to calculate this pinch temperature is not obvious in either Lovell-Smith and Baldwin (1988) or Robertson and Baldwin (1993). Recently Olsen and Wellig (2011) applied the PinCH Engineering software package to perform a thermo-economic assessment of heat recovery in a milk powder plant case study.

In particular Olsen and Wellig demonstrated using composite curves the importance of integrating the milk evaporators with MVR units to upgrade the temperature of large sections of the hot composite curve enabling heat recovery to significantly increase.

Spray dryers are typically poorly integrated due to the low temperature of waste heat contained in the exhaust air. However several case studies on spray dryer heat integration for a range of industries from the 1980's subsidised by the UK's energy efficiency demonstration scheme showed 2 - 4 years as a typical payback and a steam savings of 10 % (Mercer, 1986; Reay, 1982). In the United States, many milk powder plants have installed exhaust heat recovery systems for pre-heating the inlet air. Besides heat recovery, another benefit for this practice is to minimise inlet dryer air humidity. For these plants, hot air for drying is generated using direct fired natural gas combustion, which combustion reaction increases the air's moisture content. Inlet air pre-heating reduces the fuel consumption, which reduces moisture in the air, which maximises the drying capacity of the air. New Zealand plants, however, favour indirect heating methods of the dryer air using steam or indirect gas fired air heaters. The additional benefit of lower inlet air humidity is not present in the New Zealand case.

Three methods of exhaust heat recovery are illustrated in Figure 2-5. Option A is a direct heat recovery of the exhaust air to a process stream. A barrier to this method is the distance between the exhaust air stream and the potential heat sink. Spray dryer exhausts are normally located above the main drying chamber whereas all sink streams are located several floors below. In the case of the inlet air, it may seem reasonable to provide a direct air to air preheat at the top of the chamber shortly before the air enters the dryer. Such options are often less economic for existing plants due to space constraints caused by the substantial cost of the building that houses the dryer. Option B is, therefore, the most practical option for using exhaust heat recovery to preheat the inlet air as was rightly recognised by Atkins et al. (2011).

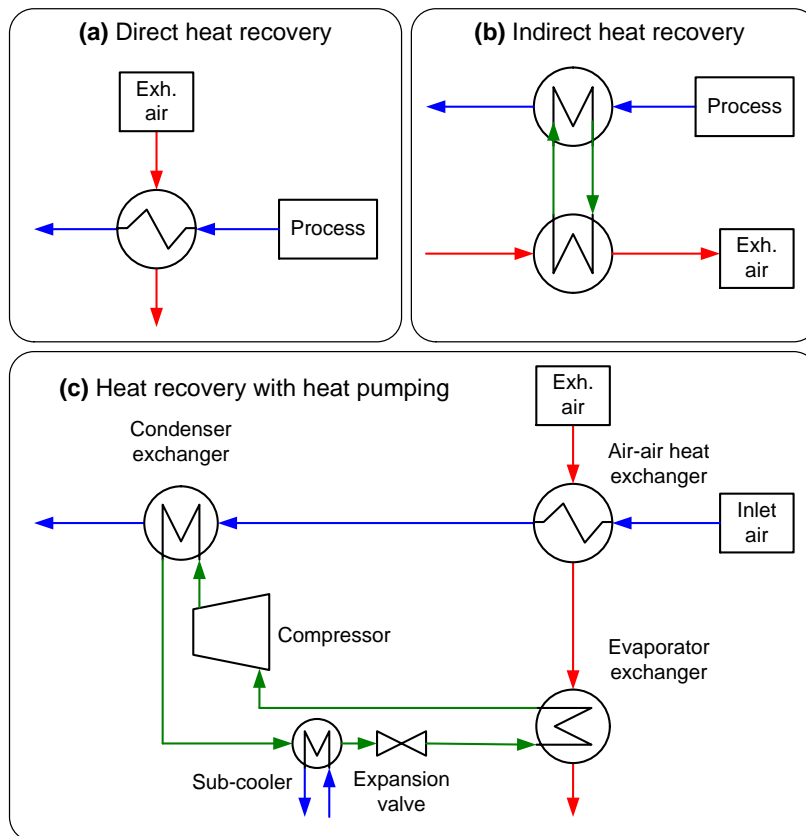


**Figure 2-5: Options of spray dryer exhaust heat recovery.**

Atkins et al. (2011) focused on the benefit of spray dryer exhaust heat recovery using a liquid coupled loop heat exchanger system (also often called a run-around coil), i.e. option B, to overall heat recovery in the milk powder process. The inlet air to the dryer (25 °C), site hot water (15 °C) and raw milk (10 °C) were considered as possible heat sinks for the recovered exhaust heat and their results are summarised in Table 2-2. Atkins et al. concluded that splitting the exhaust air to heat the inlet air and SHW achieves highest level of heat recovery with limited complexity.

Wang and Cleland (2011) investigated option C in Figure 2-5. Their results showed the conventional air-air heat exchanger has potential to recover 15 % of the inlet air heating requirement and the heat pump system added an additional 25 % of heat recovery. However the electrical running cost of the compressor reduced the overall cost savings to 20 %, which implies a net heat pump savings of about 5 %. Wang and Cleland (2011) recommended the use of R-134 as the working fluid and the heat pump's coefficient of performance (COP) for R-134 was between 3 and 4. The COP is greatest for small temperature lifts. As the temperature lift is increased

implying greater steam substitution, the COP falls significantly. The cost savings for heat pumps is sensitive to the margin between the COP and the ratio of thermal to electrical power prices, which is traditionally about 3. When the margin is small, the additional saving struggles to justify the significant capital expenditure and risk for implementing an industrial scale heat pump system. In addition particulate fouling of an exhaust heat exchanger intensifies with lower exhaust outlet temperatures resulting from increased heat recovery (T. G. Walmsley et al., 2013a). With significantly greater capital cost for the heat pump system compared to conventional heat recovery techniques, the heat pump option at present has longer payback times than conventional heat recovery techniques. Therefore focus is directed towards conventional heat recovery, and heat pump options for spray dryer integration are deemed out of scope for this thesis.

**Table 2-2: Summary of hot utility savings for the several heat recovery schemes (Atkins et al., 2011).**

Sink for exhaust heat	Heating requirement [kW]	Additional heat recovery [kW]	Exhaust air $T_{out}$ [°C]	Condensate water $T_{out}$ [°C]
N/A (Base case)	32693	-	75	20
Inlet air	28524	4169	51	20
Site hot water (SHW)	27677	5016	46	20
Split exhaust to inlet air and SHW	25893	6800	38	20
Raw milk (with mass integration)	25733	6960	38	26

Previous studies on the heat integration of the milk powder plant contain a few weaknesses. Besides the work of Atkins et al. (2011), the studies failed to clearly report a HEN for an integrated milk powder plant. Thermo-economic assessments were based purely on utility and capital cost targets calculated from the composite curve, not on HEN designs. The heat recovery schemes of Atkins et al. (2011) were a step forward; but since the study solely focused on how heat from the spray dryer exhaust air can be integrated with the rest of the process, it missed additional heat recovery opportunities from liquid condensate water from the

evaporators, which may be more economic. Atkins et al. (2011) correctly noted that milk powder fouling of an exhaust heat recovery system is likely to be an issue since the outlet temperature of the exhaust air for some of the heat recovery schemes were close to the exhaust air's dew point of 39 °C.

Another limitation of the previous studies on the integration of the milk powder plant is no consideration was given to optimising the soft process stream data. In the milk powder process, some of the stream data is "soft", meaning that some flow or temperature values can vary without impacting the product quality, the process, and its safety. Variations to present stream data may be achieved in several ways, such as by applying new control set-points to the existing process. Designers can use this flexibility to their advantage by varying soft data within a defined range to obtain a minimum energy use target. This principle is called the plus-minus principle (Linnhoff and Hindmarsh, 1983). Soft data selection can significantly impact the energy targets and the development of heat exchanger network structures. A classic example in the milk powder process of a stream with a soft target temperature is the exhaust air from the spray dryer. Selection of this temperature significantly affects the energy target and the location of the so-called pinch temperature (Walmsley et al., 2012a). It is important, therefore, to apply a systematic approach to selecting soft data to ensure the best solution is found for the milk powder process.

The milk powder process, like many other processes, contains liquid, condensing vapour and gaseous process streams, which have very different heat transfer resistances and film coefficients. When analysing the milk powder plant, it is therefore important to account for these differences in heat transfer film coefficients to ensure the energy targets are meaningful and the solution minimises total cost.

Even with all the analysis of milk powder plants, Atkins et al. (2012b) suitably observed that the heat integration scheme of the milk powder plant varies from plant to plant and that there appears to be no standard, i.e. best practice, integration scheme found in industry or literature. There appears also to be value

in understanding how the selection of a waste stream's discharge temperature affects the energy targets and the development of a HEN. Development of a standard (best practice) integration scheme for the milk powder plant is, therefore, of significant engineering research value to industry for new and existing plants.

### **2.3.2. Total site heat integration for dairy factories**

Significant improvement in total site heat recovery can be achieved through total site heat integration (Klemeš et al., 1997). Effectively applying traditional total site integration techniques to semi-continuous dairy processes is a significant challenge due to the time dependency of the process streams (Klemeš et al., 2008). Lovell-Smith and Baldwin (1988) looked at the site integration between a milk powder plant, butter plant, casein plant and utility service plant. After generating the heat recovery options, Lovell-Smith and Baldwin recognised that plants may have different operating hours rendering direct integration ineffective at times.

Atkins et al. (2010b) addressed the challenge of integrating non-continuous processes where the milk powder plant formed part of an illustrative example that also included butter and cream plants. The challenge of integrating non-continuous processes arises from the facts that a process will shut for cleaning while others are still running, and milk supply in New Zealand varies throughout the year. As a result the heat demand and supply of dairy processes significantly vary with time making direct integration at the total site level, i.e. inter-plant, uneconomic. Atkins et al. proposes that indirect heat recovery through the application of an indirect heat recovery system, i.e. Heat Recovery Loop (HRL), as illustrated in Figure 2-6 is most practical under such circumstances. A HRL can be integrated with the hot water utility system or run as an independent system. Thermal storage relaxes the limitation of heat interchange between time dependent streams and provides operating flexibility to the system. High heat capacity liquids like water are the most suitable heat transfer medium for low temperature processes (<100 °C).

There are several aspects to the design of a HRL that need to be considered. The major design decisions are (in no particular order): (1) selection of streams to include on the HRL, (2) variability and availability of the streams, (3) selection of the hot and cold storage temperatures, (4) capacity of the thermal storage, (5) areas of the heat exchangers, and (6) control and operation of the HRL. Some of these aspects have been investigated in previous studies. Atkins et al. (2010b) applied a graphical pinch based technique to a dairy case study to demonstrate how the selection of HRL storage temperatures may be varied through-out a production year to maximise the heat recovery return. Based on a similar case study Atkins et al. (2012a) analysed the thermal storage requirement of the HRL, which is needed to facilitate HRL operation and to improve heat recovery in the face of plant disruptions and stream variability. M. R. W. Walmsley et al. (2013b) looked at the effect of sizing HRL heat exchangers based on various characterisations of a process stream’s flow rate. Their study concluded that basing the heat exchanger area on the time average flow rate gave the highest heat recovery for a range of total heat exchanger areas in the HRL.

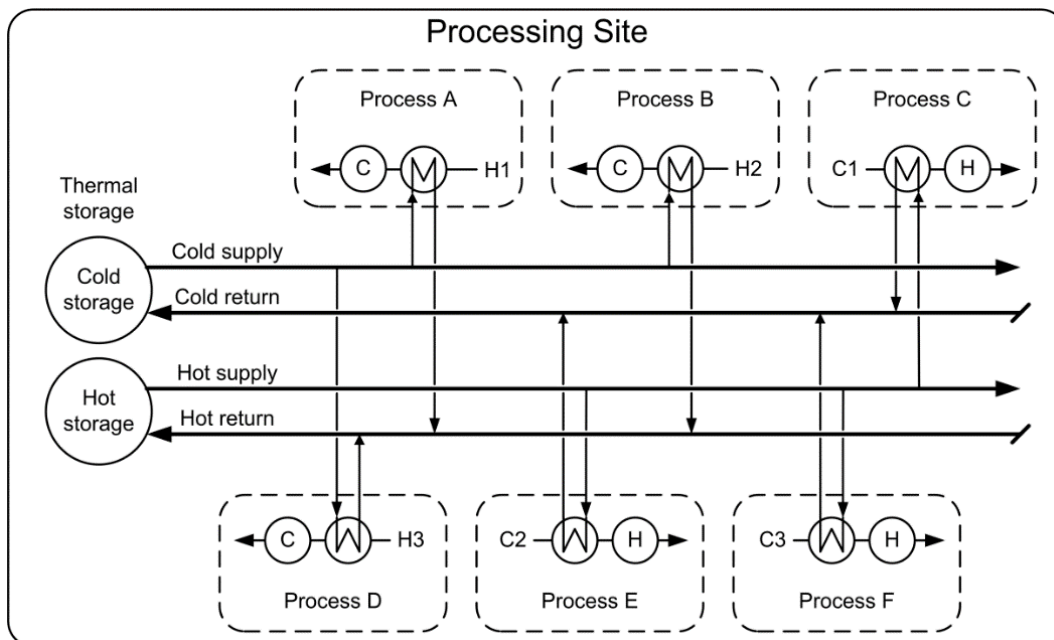


**Figure 2-6: Indirect HRL integration system with storage.**

For rigorously scheduled batch processes Chen and Ciou (2009) looked at the concept of a HRL with variable temperature – variable mass storage. Mixed Integer Non-Linear programming formed the basis of the novel design generated by

Chen and Ciou. Their results showed a variable temperature storage system is able to recover more heat for the same total heat exchanger area than the conventional constant temperature storage operation.

The concept of a HRL with variable temperature storage has not been applied to a dairy factory or semi-continuous processes. Developing a graphical method based on PA for designing a HRL with variable temperature storage is viewed as a step forward. HRLs also contain much of the pumping, piping and storage infrastructure needed for industrial solar. Harvesting renewable solar energy is one method for replacing steam derived from fossil fuels, which effectively increases the process heat efficiency of the milk powder plant and site.

Total site heat integration may be further improved by more efficient utility production. At most New Zealand dairy factories low pressure steam is generated by letting down high pressure steam. Efficient electricity production from a back pressure steam turbine is feasible, but the decision for installing a turbine is controlled by economics. Boiler efficiency could be improved by considering a condensing economiser as opposed to the standard non-condensing economiser, but again this is largely an economic question.

There are logical reasons for restricting closer integration between the process and utility systems. The two systems are physically separated and isolated because the cleanliness requirement for food production is paramount. Transferring waste heat from dairy process streams such as the milk dryer exhaust air to the utility system is less effective than improving the intra-plant integration of the utility system. For example, since the boiler exhaust air (~180 °C) exits at a much higher temperature than the dryer exhaust air (75 °C), it would be more economical to preheat the boiler air using a condensing economiser instead of directly or indirectly using heat from the dryer exhaust. As a result this thesis takes the approach of minimising process heat demand by improving intra- and inter-process heat integration as the primary method for increasing energy efficiency.

### **2.3.3. Process Integration techniques**

PI is a systems approach to process design and optimisation encompassing systematic methods and techniques to analyse and determine how to minimise specific process demand for heating, cooling, electricity, water, and other utilities. PI studies are normally comprised of three general steps: (1) utility targeting, (2) network design, and (3) process and network optimisation.

The most significant contribution in this field over the past four decades has been the development of PA (Linnhoff and Hindmarsh, 1983). The pinch concept was originally applied to heat integration problems as a graphical approach to heat exchanger network synthesis. Now, three decades later, it has a proven track record for achieving energy savings in a range of industries and applications (Klemeš et al., 2010). Besides heat integration PA has been successfully applied to mass integration problems to minimise the consumption of utilities such as water (Wang and Smith, 1994) and hydrogen (Towler et al., 1996). Both heat and mass integration have received considerable attention from researchers and industry, and have been included in many textbooks (El-Halwagi, 2006; Klemeš, 2013). PA has also been extended to problems in general that can be represented by supply and demand profiles that contain both a quality and quantity such as supply chains (Singhvi and Shenoy, 2002), carbon emissions (Tan and Foo, 2007), and national energy sectors (Walmsley et al., 2014).

Extensions to the original method, such as targeting total area, batch processes (Linnhoff et al., 1988), heat exchanger shells (Ahmad and Smith, 1989), pressure drop (Polley et al., 1990), and utility systems (Dhole and Linnhoff, 1993), have been developed to improve its industrial relevance and profitability. The literature also contains numerous computer programming based network synthesis techniques (Zamora and Grossmann, 1998). Using algorithms such as the transshipment model, computer programs have been created to cycle through hundreds of possible network combinations to decide on the best network structure given the process data and constraints.

For a critical review and further information regarding the development of HEN synthesis up to 2002 refer to Linnhoff (1993), Smith (2000) and Furman and Sahinidis (2002). PI together with PA and its application have been comprehensively covered in references documents and books by Linnhoff (1982), Shenoy (1995), Biegler et al. (1997), Gundersen (2000), Smith (2005), El-Halwagi (2006), Kemp (2007), Seider et al. (2009). For up-to-date methodology development refer to the recently published Handbook of Process Integration (Klemeš, 2013).

### **2.3.3.1. Pinch Analysis**

PA is a graphical approach to PI and may be applied to a wide variety of heat, energy and mass integration problems. Its cornerstones are the construction of the composite curve (Figure 2-7a), shifted composite curve (b) and grand composite curve (c), together with the identification of pinch points. For heat integration problems these curves express the heat supply and demand of a process in terms of temperature and enthalpy. In this approach the hot and cold stream composite curves are shifted by  $\Delta T_{min}/2$ , where  $\Delta T_{min}$  is the minimum approach temperature. A key element of PA of heat integration problems is the identification of pinch temperatures, which indicate where heat recovery is most constrained. Designers can use this system decomposition to successfully design heat exchanger networks that reach heat recovery and utility use targets expressed by the composite curves.

In Figure 2-7a, the gap between the hot and cold composite curves indicate the temperature driving force available for heat recovery. The composite curves are shifted by  $\Delta T_{min}/2$  on the temperature axis and overlapped on the enthalpy axis such that the two curves touch without crossing over each other. Where the hot and cold shifted composite curves touch in Figure 2-7b is call a pinch temperature. A process can have multiple pinch temperatures and near pinch temperatures that constrain options for heat recovery around those temperatures. The horizontal distance between the hot and cold composite curves indicates the amount of excess heating or cooling available at individual temperatures. These differences are expressed using the grand composite curve in Figure 2-7c. The red lines on

Figure 2-7c imply excess heat is available and the blue lines imply excess cooling is present.

Targeting and Heat Exchanger Network (HEN) design based on the selection of  $\Delta T_{min}$  is an established part of the PA method. HENs generated using pinch methodology effectively compensate for pinch temperature regions where heat recovery is most constrained. As a result non-obvious HEN structures are often developed that are naturally efficient for heat recovery. For further information regarding the “how to” of the Pinch Design Method (PDM) refer to the Handbook of Process Integration (Klemeš, 2013).

One of the important enhancements of the original PA method is the application of a contribution minimum temperature difference,  $\Delta T_{cont}$ , as a replacement for the global minimum temperature difference,  $\Delta T_{min}$ , concept to produce more meaningful utility targets and process insights (Smith, 2005). Where streams have low heat transfer resistance, i.e. condensing vapour, a small  $\Delta T_{cont}$  is selected. On the other hand gaseous streams are much more resistant to heat transfer and therefore have a higher  $\Delta T_{cont}$ . The summation of the  $\Delta T_{cont}$ 's of matched streams is equivalent to  $\Delta T_{min}$ . Such a modification is critical when analysing the milk powder plant, which contains liquid, vapour and gaseous streams.

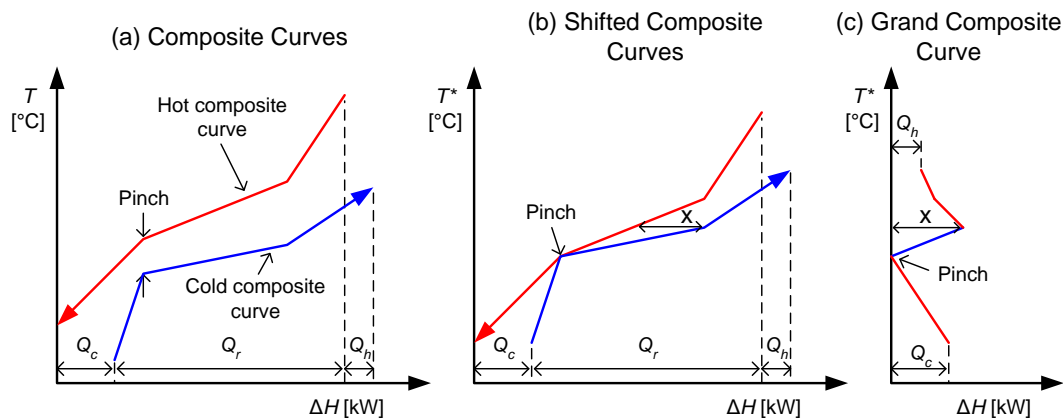


**Figure 2-7: Relationship between the composite curve, shifted composite curve and grand composite curve.**

However the  $\Delta T_{cont}$  (or  $\Delta T_{min}$ ) constraint does not ensure cost optimal HEN area allocation within a HEN structure generated using PA and PDM. This is partially due to differences in utility prices, stream heat transfer film coefficients, heat

exchanger types and flow arrangements, heat exchanger capital costs, and heat exchanger approach temperatures. Simple methods for  $\Delta T_{min}$  relaxation through dual minimum approach temperatures, where one  $\Delta T_{min}$  is selected for heat recovery targeting and the other  $\Delta T_{min}$  is applied to individual exchangers, have been proposed to provide flexibility at the heat exchanger area sizing stage (Shenoy, 1995). However such a method vastly multiplies the degrees of freedom of a cost optimisation.

Relatively few studies have focused on optimising the distribution of heat exchanger area in a HEN with a fixed structure (i.e. stream matches). Ait-Ali and Wade (1980) mathematically derived conditions to determine the optimal heat recovery area allocation in multi stage heat exchanger systems with any number of exchangers in series. The derivation was based on the log-mean temperature difference ( $\Delta T_{LM}$ ) heat exchanger design method. Key limitations of the method are that it only applies to multi-stage heat exchanger systems (not HENs in general), assumes counter flow heat transfer and does not account for cost. Focus is directed towards achieving maximum heat recovery for a given total area, which does not necessarily equate to minimum total cost. Besides the method of Ait-Ali and Wade (1980), the literature contains a few studies that have applied computer programs to find optimal solutions by brute force and/or smart heuristics and algorithms, which are reviewed later in this chapter in section 2.3.3.4.

### **2.3.3.2. Batch integration**

Batch processes operate with discrete units of material being processed stage by stage over a specified cycle time and materials do not continually leave and enter the process (Douglas, 1988). Instead there are numerous start-ups and shut-downs and stream variables regularly change in a prescribed manner. Integration of batch processes is therefore more cumbersome than integration of continuous processes (Obeng and Ashton, 1988) and normally requires an indirect heat integration approach with storage for successfully inter-process integration. Methods for designing indirect heat recovery systems for batch systems have been proposed by numerous authors. Although these methods are tailored for batch processes, but the principles also apply for semi-continuous processes such as

diary processes especially when integrating across multiple plants on the same site (Morrison et al., 2007).

Linnhoff and co-workers (Linnhoff et al., 1988; Obeng and Ashton, 1988) applied the conventional PA method (Linnhoff and Hindmarsh, 1983) to energy targeting of a simple batch process using a Time Slice Model (TSM) but presented no HEN synthesis. At a similar time Kemp and MacDonald (1988, 1987) and later Kemp and Deakin (1989) extended the TSM approach to heat integration of batch processes including development of a HEN. In this method the integration of individual production time slices are considered before being amalgamated into a single HEN that successfully meets the heat recovery targets for each time slice. Various programming techniques such as Mixed Integer Linear Programming (MILP) have also been applied to improve the integration of batch processes by attempting to optimize the scheduling and HEN design (Jung et al., 1994; Lee and Reklaitis, 1995; Papageorgiou et al., 1994; Vaselenak et al., 1986). The basis for integrating batch processes is that the process is operated in a cyclic fashion and the scheduling of the operations are interdependent and constrained. Rescheduling of the operations may be permitted depending on the constraints of the process and final product.

Stoltze et al. (1993) presented a simple method to target the number of heat storage tanks and their temperatures to maximise heat recovery savings. Later Stoltze et al. (1995) proposed a combinatorial approach called the permutation method where a search is performed among a set of feasible operating temperatures of heat storage tanks and a sub-set of process streams to be integrated, to find the most cost-effective configuration of process stream – tank matches. The storage tanks are assumed to be fixed temperature - variable mass systems and the feasible operating temperatures of the tanks were based on the supply and target temperatures of process streams. The heuristic rules restricted the solution domain to enable an exhaustive search. The method was further developed by Mikkelsen (1998) using a post-optimisation stage for fine tuning the system variables but the method has been difficult to apply in practice. Variable temperature and variable mass storage for indirect heat recovery has been

investigated by Chen and Ciou (2009) for batch systems. The constraint of fixed temperature heat storage was shown to reduce heat recovery for the same size storage tanks. MILP was used to find the optimal storage volumes for minimal external utility and total annual cost for the overall heat recovery system.

Pourali et al. (2006) extended the idea of a problem table decomposition to batch processes. By carefully considering process specific operational and economic constraints, they applied a TSM approach with the extension of including energy storage to a batch process case study to yield an integration solution with improved energy recovery and productivity.

A graphical Pinch based methodology for indirect heat recovery using constant temperature – variable mass heat storage has been articulated by Krummenacher and Favrat (2001). This method used the Time Average Model and composite curve to identify storage temperatures and hot and cold utility targets. Figure 2-8 is taken from Krummenacher and Favrat (2001) showing how the method is able to design a HRL with four storage temperature levels. From the composite curve plot, the storage temperatures are obtained, the heat flow between the storage tanks is known and the total heat recovery may be determined. Previous studies on total site integration for dairy factories have applied the method of Krummenacher and Favrat to design a suitable HRL. Further examples of the practical application of this method is presented by M. R. W. Walmsley et al. (2013a). At present the graphical technique for designing HRLs with constant temperature storage has not been extended to look at HRLs with variable temperature storage.

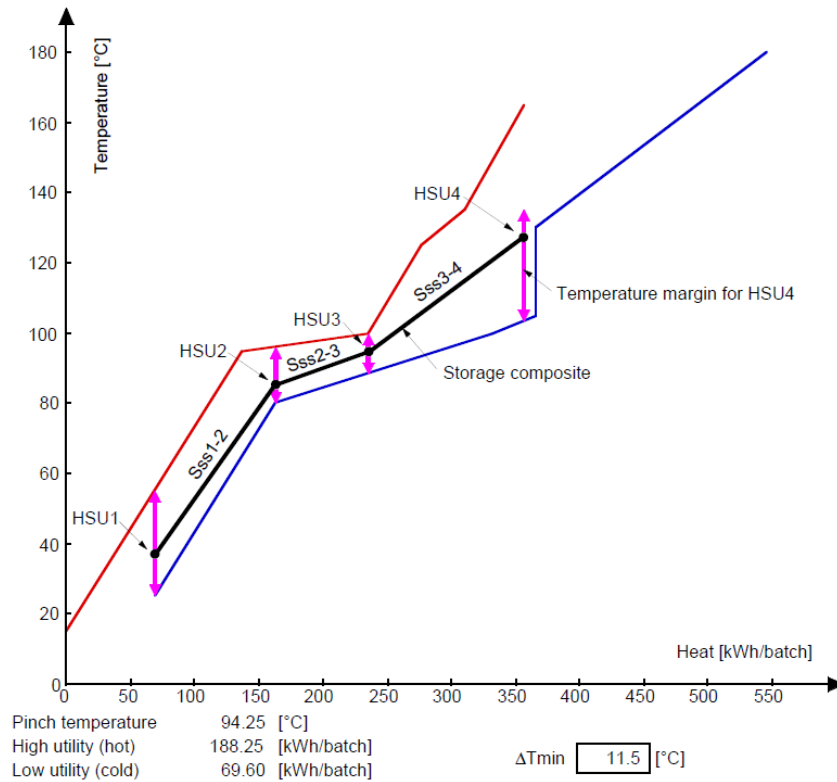


**Figure 2-8: Indirect heat integration using multiple Heat Storage Units (HSU) (Krummenacher and Favrat, 2001).**

### 2.3.3.3. Total Site Analysis

Total Site Analysis was also developed to integrate entire processing sites or groups of sites that are serviced by a centralised utility system for increased overall heat recovery and reductions in utility use and carbon emissions (Dhole and Linnhoff, 1993; Linnhoff and Dhole, 1993). The TSA concept is to use the site-wide utility system as an indirect heat recovery system between different plants and factories. Total Site source and sink profiles combine the GCCs (minus the internal heat recovery portions, or heat pockets) from individual plants to calculate Total Site targets for heat recovery, and utility use and temperature (Klemeš et al., 1997). By using the utility system as a means to indirectly transfer heat from one plant to another plant, the method overcame the impracticalities of integrating streams that separator by some distance and prevented the development of large spaghetti HENs for an entire site.

Insight based techniques (Ahmad and Hui, 1991; Fodor et al., 2012; Goršek et al., 2006; Klemeš et al., 1997) and mathematical programming based techniques (Bagajewicz and Rodera, 2002, 2000; Kralj et al., 2005, 2002; Rodera and

Bagajewicz, 1999) have been developed and applied to the problem of Total Site Integration. Both approaches have their relative merits and weaknesses and can be employed iteratively or simultaneously (Sieniutycz and Jeżowski, 2009). Methods have also been developed to apply and extend traditional pinch analysis to batch (Kemp, 2007; Klemeš et al., 2008) and semi-continuous types of plants (Atkins et al., 2012b, 2010b; Becker et al., 2011). Varbanov and Klemeš (2011) investigated how renewable energy sources may be integrated into TSA as a way to further reduce fossil fuel use. Integration of renewables via the utility system is sensible as a way to counteract the variability of the renewable energy source. A modified pinch analysis similar to TSA (Klemeš et al., 1997) and the batch integration method of Kruppenacher and Favrat (2001) has been applied to heat recovery targeting of a large multi-plant dairy processing site with a HRL for different operating states throughout the year (Atkins *et al.*, 2010).

#### **2.3.3.4. Computer programming techniques**

Computer programming has been applied to designing optimal heat exchanger networks. Escobar and Trierweiler (2013) provide a succinct history of the application of computer programming to PI. One of the most significant contributions to this field was made by Yee et al. (Yee and Grossmann, 1990; Yee et al., 1990a, 1990b) in a three part paper series. Yee et al. developed a superstructure approach to HEN synthesis as shown in Figure 2-9 and applied a Mixed Integer Nonlinear Programming (MINLP) model to find the “optimal” HEN design. The network superstructure was organised into stages, and streams entering a stage were split so that almost any combination of matches was possible. As a result the superstructure effectively contains nearly all possible process stream matches. In the model, necessary constraints for a feasible solution were imposed so that the heat exchanger loads were balanced, the heat exchanger temperatures were thermodynamically feasible, and the target temperature of all streams were met using heat recovery and/or utility. Additional constraints, such as restricted matches and no stream splitting, were easily included in the computer program. After inputting the required data the MINLP model attempts to find the solution that minimises total cost.

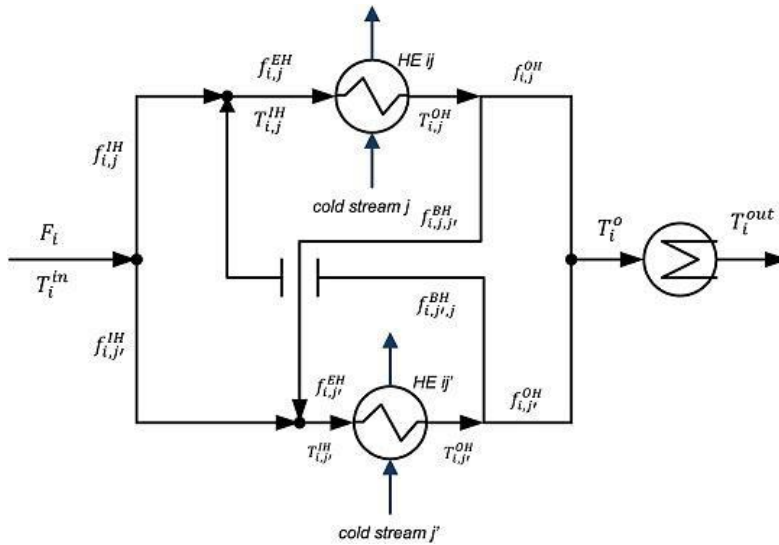


Figure 2-9: Example of a network superstructure for stream  $i$  (Escobar and Trierweiler, 2013).

Extensions and variations of the Yee et al. superstructure approach and other computer programming approaches are numerous. However the programming approaches have failed to gain significant use in industry due to the significant scale issue (Sieniutycz and Jeżowski, 2009). As the scale of the problem increases, the required computational time grows exponentially. As a result, recent efforts have focused on applying meta-heuristic optimisation methods to help solve this well-known issue (Furman and Sahinidis, 2001). Another solution has been to decompose the integration problem into independent sub-sets so that less computationally demanding linear programming techniques can apply (Pettersson, 2005).

To an extent, PA also has difficulty scaling to large problems; especially for heat exchange matches away from the pinch temperatures. Using a hybrid computer programming and heuristics approach to synthesis and HEN design is, therefore, one method to achieve the best of both approaches to HEN synthesis (Gorji-Bandpy et al., 2011). Heuristics can be derived from insight based methods such as the PDM.

## 2.4. Performance and fouling of gaseous heat recovery exchangers

Two significant problems are encountered in gaseous heat recovery: (1) high heat transfer resistance of gases and (2) the presence of entrained particulate matter causing fouling and increased resistance to heat transfer on the gas side of the exchanger. As heat transfer resistance increases, heat exchanger duty decreases, for constant area, and heat becomes more expensive to recover. In a boiler recuperator, a particulate foulant layer 2 mm thick can reduce the overall heat transfer coefficient by 5 % (Stehlík, 2011). Foulant layers also increase heat exchanger pressure drop, which increases the energy input requirement of fans and blowers to maintain a constant gas flow rate. To restore heat exchanger performance after fouling, heat exchanger surfaces require cleaning. Depending on the particulate and the foulant bond strength, foulant layers may prove difficult to remove. Where extended surfaces, such as fins need to be rigorously cleaned, deformation of the fins may occur and the long-term performance of the exchanger will be compromised. This section reviews some of the fundamentals of heat exchanger design and performance including the potential for particle fouling in a gaseous flow heat recuperator

### 2.4.1. Heat exchanger fundamentals

#### 2.4.1.1. Heat exchanger sizing and rating

The most commonly used heat exchanger sizing methods are the  $\Delta T_{LM}$  method and the effectiveness-number of transfer units ( $\epsilon$ -NTU) method (Kays and London, 1998). In their complete forms, the two methods are mathematically consistent although the required inputs are different. Eq. 2-1 presents the fundamental equation for the  $\Delta T_{LM}$  method and Eq. 2-2 presents the equation for the  $\epsilon$ -NTU method.

$$Q = F(UA\Delta T_{LM}) \quad (2-1)$$

$$Q = \epsilon C_{\min} \Delta T_{\max}, \quad \text{where } \epsilon = f(NTU, C^*), \quad NTU = \frac{UA}{C_{\min}}, \quad C^* = \frac{C_{\min}}{C_{\max}} \quad (2-2)$$

where  $F$  is a heat exchanger correction factor for the heat exchanger arrangement. The relationship between  $\varepsilon$  and  $NTU$  is also heat exchanger arrangement dependent and common  $\varepsilon$ - $NTU$  relationships are presented in Appendix B. Given  $F$  and  $UA$ , the  $\Delta T_{LM}$  method requires input of the four temperatures in and out of the heat exchanger whereas the  $\varepsilon$ - $NTU$  method requires the input of heat exchanger inlet temperatures and heat capacity flow rates of the two streams. A key advantage of the  $\varepsilon$ - $NTU$  method is its ability to directly calculate unknown outlet temperatures, which is not possible for the  $\Delta T_{LM}$  method (Kays and London, 1998).

Another method similar to the  $\varepsilon$ - $NTU$  method is the temperature effectiveness P- $NTU$  method. When the flow rates of streams vary significantly, it can be difficult to know which stream has the minimum and maximum  $C$  as required by the  $\varepsilon$ - $NTU$  method. In these situations it is advantageous to base effectiveness and  $NTU$  on one of the streams instead of the stream with the minimum  $C$ . This is the basis of the P- $NTU$  method. The relationships between  $P$  and  $NTU$  for various heat exchanger arrangements are the same as the effectiveness- $NTU$  relationships for the  $\varepsilon$ - $NTU$  method (Kakaç and Liu, 2002). Table 2-3 compares the definitions for effectiveness and  $NTU$  in the  $\varepsilon$ - $NTU$  and P- $NTU$  methods.

**Table 2-3: Comparison of definitions for effectiveness and  $NTU$  in the  $\varepsilon$ - $NTU$  and P- $NTU$  methods.**

	Effectiveness		Number of Transfer Units	
	$\varepsilon$ - $NTU$	P- $NTU$	$\varepsilon$ - $NTU$	P- $NTU$
Stream 1	$\varepsilon \equiv \frac{C_1(T_1^{out} - T_1^{in})}{C_{\min} \Delta T_{\max}}$	$P_1 \equiv \frac{T_1^{out} - T_1^{in}}{\Delta T_{\max}}$	$NTU \equiv \frac{UA}{C_{\min}}$	$NTU_1 \equiv \frac{UA}{C_1}$
Stream 2	$\varepsilon \equiv \frac{C_2(T_2^{in} - T_2^{out})}{C_{\min} \Delta T_{\max}}$	$P_2 \equiv \frac{T_2^{in} - T_2^{out}}{\Delta T_{\max}}$	$NTU \equiv \frac{UA}{C_{\min}}$	$NTU_2 \equiv \frac{UA}{C_2}$

A key component of heat exchanger design equations is the overall heat transfer coefficient  $U$ . The inverse of the overall heat transfer coefficient,  $U$ , in Eq. 2-1 and 2 based the sum of heat transfer coefficients and thermal resistances,  $R$ , is

$$\frac{1}{U} = \frac{1}{h_h} + R_{f,h} + R_w + R_{f,c} + \frac{1}{h_c} \quad (2-3)$$

where the subscripts refer to various resistances:  $h$  is the hot side,  $w$  is the wall,  $c$  is the cold side,  $f$  is the fouling layer. Typically the thermal resistance of the wall and fouling are small and in many cases can be ignored (Kays and London, 1998). The definition of  $U$  is the same for all heat exchanger sizing and rating methods.

Correlations relating heat transfer and pressure drop to fluid flow and exchanger surface characteristics have long been established in the literature. Kays and London (1998) provides the most comprehensive presentation of correlations for various compact heat exchanger surfaces obtained by their research team in addition to several found in the literature at the time. Correlations are normally presented in terms of the non-dimensional Colburn  $j$  factor or Nusselt,  $Nu$ , number for heat transfer and the Fanning friction factor,  $f$ , for pressure drop. The  $j/f$  ratio is significant as it is directly proportional to the  $h/E$ , where  $h$  is the heat transfer film coefficient and  $E$  is the pumping power as shown in Eq. 2-8. The  $j/f$  ratio is termed the surface Goodness factor (Kays and London, 1998).

$$\frac{h}{E} \cong \frac{2c_p}{Pr^{2/3}u_\infty^2} \sigma^2 \frac{j}{f} \quad (2-4)$$

The Goodness factor is a measure to compare the efficiency of different heat exchanger surfaces on a per square meter basis of heat transfer area. There are, however, other factors that need consideration when selecting the heat exchanger surface such as the cost per square meter, the heat exchanger compactness and the heat exchanger flow arrangement (e.g. counterflow).

#### **2.4.1.2. Liquid coupled loop heat exchanger systems**

The concept of a liquid-coupled loop heat exchanger system (LCHE) for indirect heat transfer is presented in Figure 2-10. This indirect heat exchange system consists of two heat exchangers coupled using an intermediate loop fluid. The loop fluid transports heat from the source stream to the sink stream. LCHE systems are most applicable to situations where source and sink streams are physically distant.

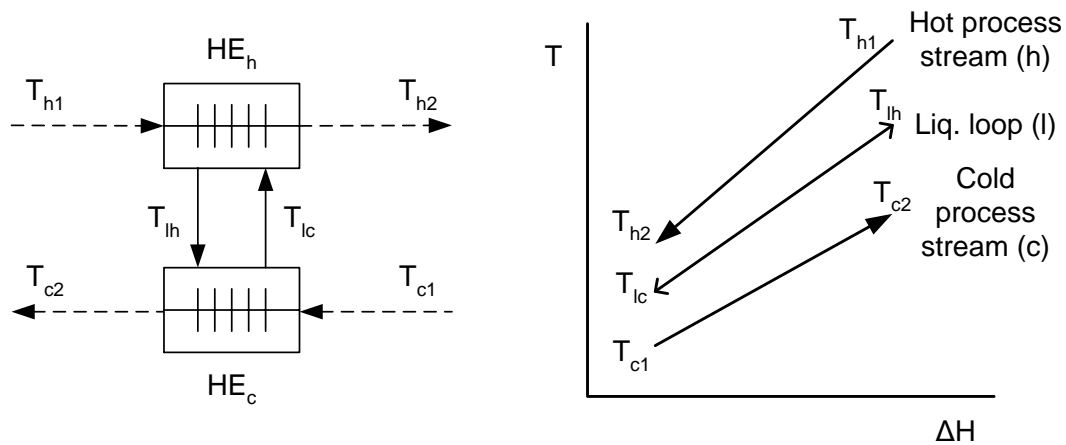


**Figure 2-10: Liquid couple loop heat exchanger system.**

The governing overall effectiveness ( $\varepsilon_o$ ) relationship for the performance of LCHE systems according to Kays and London (1998) is

$$\frac{1}{\varepsilon_o} = \frac{C_{\min,o}/C_{\min,c}}{\varepsilon_c} + \frac{C_{\min,o}/C_{\min,h}}{\varepsilon_h} + \frac{C_{\min,o}}{C_l} \quad (2-5)$$

where  $\varepsilon$  is heat exchanger effectiveness,  $C$  is the heat capacity flow rate and subscripts  $h$  refers to the hot fluid,  $c$  refers to the cold fluid and  $l$  refers to the loop fluid. Holmberg (1975) derived the optimum loop heat capacity flow rate assuming counter-flow heat exchanger arrangement,

$$C_l = \frac{\frac{(UA)_h + (UA)_c}{(UA)_h} + \frac{(UA)_c}{(UA)_c}}{\frac{C_h}{C_h} + \frac{C_c}{C_c}} \quad (2-6)$$

where  $U$  is overall heat transfer coefficient and  $A$  is heat exchanger area.

If it is assumed that  $(UA)_h \gg (UA)_c$ , then  $C_l$  in Eq. 2-6 approaches  $C_h$ . The reverse is also true; if  $(UA)_c \gg (UA)_h$ , then  $C_l$  approaches  $C_c$ . Thus, the optimum  $C_l$  always falls somewhere between  $C_h$  and  $C_c$ . Using a simple spreadsheet, a preliminary investigation into the applicability of Eq. 2-6 to non-counter-flow heat exchanger arrangements has been undertaken. The investigation looked at cases where the LCHE system involved two heat exchangers with the same arrangement and varied the  $UA$  values for the heat exchangers across a wide range. Results showed that Eq. 2-6 is sufficiently accurate to predict the optimum loop flow rate to achieve a

heat transfer within 0.1 % of the maximum possible. The maximum heat transfer was determined using Excel™ Solver.

Holmberg (1975) also derived for counter-flow heat exchangers the optimum ratio of the heat exchanger areas in a LCHE system as

$$\frac{A_{\min}}{A_{\max}} = \sqrt{\frac{U_{\max}}{U_{\min}}} \quad (2-7)$$

For the case where  $U = U_{\min} = U_{\max}$ , the optimum area ratio of the two heat exchangers is unity, i.e.  $A_h = A_c$ . It is important to note that Eq. 2-7 is only cost optimal if the capital cost correlations for the two heat exchangers are the same.

## **2.4.2. Factors affecting heat exchanger particulate fouling**

The five dominant factors affecting a particle's tendency to adhere to rigid surfaces are: (1) particle surface stickiness, (2) air velocity, (3) impact angle, (4) particle size, and (5) wall properties. At present the literature lacks studies on milk powder fouling of gaseous heat recovery systems. There is, however, a significant body of work that focuses on minimising milk powder fouling of spray dryers (Chen et al., 1993; Kota and Langrish, 2006), fluidised bed dryers (Zuo, 2004) and cyclone separation units (Intipunya et al., 2009). Although this body of work stops short of developing a validated model that fully describes the interaction between a single particle and a wall, and the conditions that lead to attachment and fouling.

### **2.4.2.1. Surface stickiness of amorphous powders**

The stickiness of food and dairy powder surfaces is intricately related to the concepts of glass transition temperature and viscosity (Downton et al., 1982). In amorphous materials, such as milk powder, the glass transition temperature,  $T_g$ , identifies the boundary between the material being in a non-sticky glassy state or a sticky rubbery state. The major amorphous component in skim milk powder (SMP) is Lactose, which accounts for about half of SMP by weight. Particle surface viscosity is a measure of the flowability of material at the particle's surface. For air temperatures below  $T_g$ , the surface viscosity is high and molecular movements of

surface lactose are subdued. Above  $T_g$ , molecular mobility rapidly increases while the surface viscosity lowers. Liquid bridges may then readily form between two particles and between particles and solid surfaces. Further temperature increases above  $T_g$  continues to lower viscosity. The amount the air temperature is above  $T_g$ , i.e.  $T - T_g$ , is logarithmically related to viscosity,  $\mu$ , as described by the Williams-Landel-Ferry (1955) equation (or WLF equation), where  $D_1$  is a dimensionless constant and  $D_2$  is a temperature constant for a given amorphous composition. Hence,  $T - T_g$  is a non-linear measure of stickiness through viscosity.

$$\log\left(\frac{\mu}{\mu_g}\right) = \frac{-D_1(T - T_g)}{D_2 + (T - T_g)} \quad (2-8)$$

The glass transition temperature of a material is strongly dependent on the moisture content and water activity at the surface of the particle. For two component substances Gordon & Taylor (1952) suggested a modified rule of mixtures equation to calculate the glass transition temperature of the material, which for SMP may be applied to lactose and water (Hennigs et al., 2001), i.e. the GT model,

$$T_g = \frac{T_{g,l} + k X_{eq} T_{g,w}}{1 + k X_{eq}} \quad (2-9)$$

where  $T_g$  is the glass transition temperature of SMP,  $X_{eq}$  is the equilibrium moisture content on a dry basis,  $T_{g,l}$  and  $T_{g,w}$  are the glass transition temperatures of lactose and  $k$  is a constant. The value of  $k$  may be determined by plotting  $T_g$  versus  $X_{eq}$  (Figure 2-11). Experimental data in Figure 2-11 have been amalgamated from several studies (Haque and Roos, 2004; Hill et al., 1998; Lloyd et al., 1996; Omar and Roos, 2007; Ozmen and Langrish, 2002; Schmitt et al., 1999; Silalai and Roos, 2010; Thomsen et al., 2005) that used a Differential Scanning Calorimeter to determine  $T_g$  for lactose and SMP (where indicated). Johari et al. (1987) found the glass transition temperature of water,  $T_{g,w}$ , to be  $-137^\circ\text{C}$ , whereas for lactose  $T_{g,l}$  is an average of  $103^\circ\text{C}$  from the above list of sources.

Using a least squares method and all data shown in Figure 2-11, constant  $k$  is evaluated as 6.83. A difficulty with measuring  $T_g$  when  $a_w$  is above 0.575 ( $X_{eq} \approx 0.13$  g/g), is lactose experiences thermal instability (Thomsen et al., 2005). A transition in the molecular structure from amorphous to crystalline will also occur at high  $a_w$  (Roos, 2002). As a result there is a noticeable lack of data for equilibrium data greater than 0.13 g/g moisture.

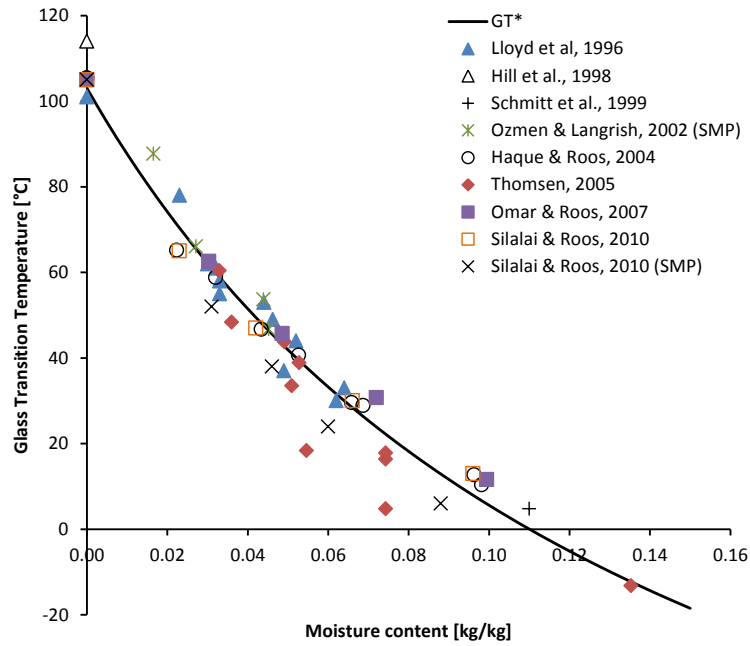


Figure 2-11: Relationship between  $T_g$  and  $X_{eq}$ .

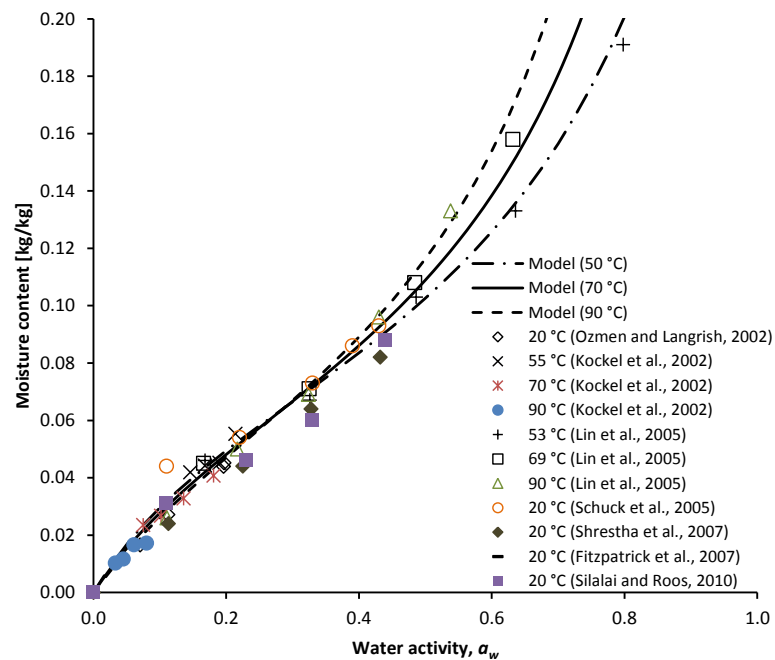


Figure 2-12: Sorption isotherm for skim milk powder.

Isotherm curves relate equilibrium powder moisture content,  $X_{eq}$ , to water activity,  $a_w$ , which assumed to be equal to the air relative humidity (Paterson et al., 2007a). Moisture adsorption and desorption isotherms of SMP has been obtained in many studies over the last decade as shown in Figure 2-12, although only two studies carried out the tests above room temperature, 50 – 90 °C (Kockel et al., 2002; Lin et al., 2005).

SMP has been shown to best follow the Guggenheim–Anderson–de Boer (GAB) (Bell and Labuza, 2000) sorption isotherm model,

$$X_{eq} = X_0 \frac{\alpha \beta a_w}{(1 - \beta a_w)(1 - \beta a_w + \alpha \beta a_w)} \quad (2-10)$$

Where  $X_{eq}$  is the equilibrium moisture content on a dry basis,  $X_0$  is the monolayer moisture content. In the above equation  $\alpha$  and  $\beta$  are exponential functions of temperature,

$$\alpha = \alpha_0 \exp\left(\frac{\Delta H_1}{RT}\right) \quad (2-11a)$$

$$\beta = \beta_0 \exp\left(\frac{\Delta H_2}{RT}\right) \quad (2-15b)$$

where  $\Delta H$  is material specific activation energy on a per mole basis,  $R$  is the universal gas constant and  $T$  is absolute temperature in Kelvin. From the data presented in Figure 2-12, constants  $X_0$  (0.073274 g/g),  $\alpha_0$  (0.16968),  $\Delta H_1$  (9791.9 J/mol),  $\beta_0$  (3.9469) and  $\Delta H_2$  (-4197.0 J/mol) are solved using a least squares technique and Excel™ Solver. Table 2-4 shows that the new GAB constants provide the most accurate  $X_{eq}$  values across a wide range of  $a_w$  compared to three models from literature.

An estimate for  $T_g$  may be calculated from air temperature and humidity using Eq. 2-13 in conjunction with Eq. 2-14. Since  $X_{eq}$  is weakly dependent on temperature, Brooks (2000) successfully developed a polynomial model to relate  $a_w$  (or  $RH$ ) to  $T_g$  with high accuracy,

$$T_g = 530.66 a_w^3 + 652.06 a_w^2 - 366.33 a_w + 99.458, \quad [0 < a_w < 0.575] \quad (2-12)$$

**Table 2-4: Summary of sorption isotherm constants.**

Source	Model	$R^2$ $a_w < 0.40$	$R^2$ $a_w < 0.80$
This work	GAB	0.969	0.972
Lin et al. (2005)	GAB	0.678	0.926
Jouppila et al. (1994)	GAB	0.917	0.557
Papadakis et al. (1993)	SPS	0.930	0.506

However Brooks' equation is limited to the water activity range stated and beyond this range, the model is unreliable. Whereas equations based on the GT model (Eq. 2-13) may be applied to predict  $T_g$  for high values of  $a_w$  with greater confidence because the model is semi-empirical. Paterson et al. (2007a) provide clear evidence that different air temperatures and humidities resulting in the same  $T - T_g$  value have the same surface stickiness (Figure 2-13). Several other researchers agree with this conclusion such as Zhao (2009) and Murti (2006).

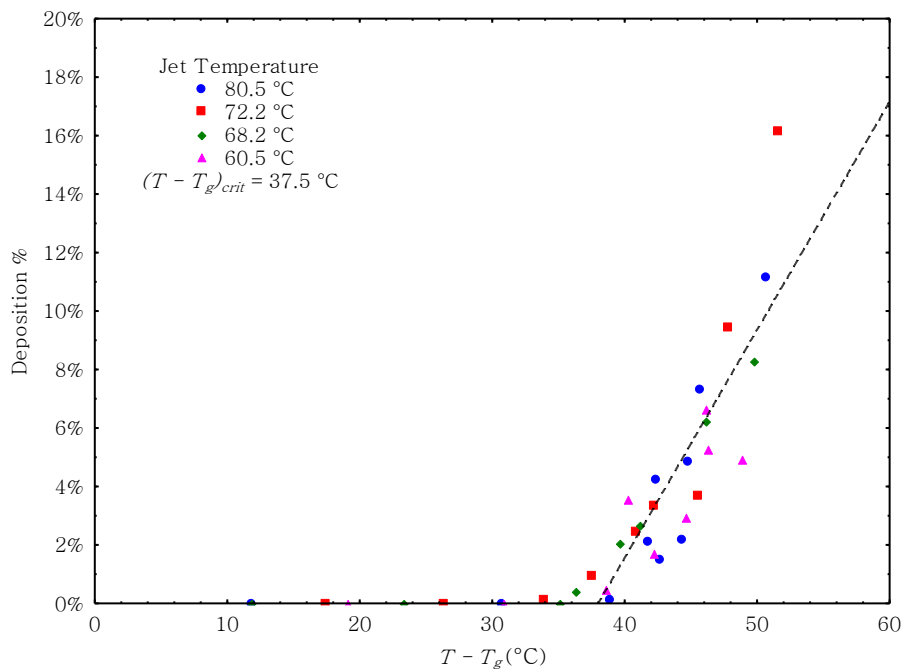


**Figure 2-13: Effect of  $T - T_g$  on percent deposition for whole milk powder (compared the amount of powder tested) obtained using the particle gun test with a reported air velocity of 20 m/s. Data taken from Paterson et al. (2007a).**

### 2.4.2.2. Effect of air velocity and particle impact angle on fouling

The simplest method to reduce particulate fouling is to increase the airside heat exchanger face velocity. Higher velocities result in higher energy particulate-tube impacts reducing fouling (Jegla et al., 2010). Increasing velocity also increases the chance of resuspension of attached particulates into the airflow. Resuspension is the result of random turbulent eddies impacting the surface with greater energy, which dislodges and re-entrains the particulate (Rogers and Reed, 1984).

A recent tool developed to aid the design of heat exchangers subject to particulate fouling is the limiting fouling velocity,  $v_{jf}$  (Abd-Elhady et al., 2004). This tool defines the velocity at which deposited particles begin to roll and become re-entrained into the air flow. Numerical estimates and lab-scale experimental results of  $v_{jf}$  have been found to be in close agreement (Abd-Elhady et al., 2004; Jegla et al., 2010; Zhang et al., 2000). To find  $v_{jf}$ , Jegla et al. (2010) recently defined the rolling moment,  $RM$ , as

$$RM = \frac{F_d \left( 1.399 \frac{d_p}{2} - \delta \right)}{\left( F_a + F_g + F_{el} + F_{cap} - F_b - F_l \right) \frac{d_p}{2}} \quad (2-13)$$

where  $F_d$  is the drag force,  $F_a$  is the force of adhesion,  $F_{el}$  is the electrostatic force,  $F_{cap}$  is the capillary force,  $F_b$  is the buoyancy force,  $F_l$  is the lift force,  $d_p$  is the particle diameter,  $\delta$  is the maximum particle deformation distance, and  $d_c$  is the contact diameter between the particle and wall. The numerator in Eq. 2-21 is related to the hydrodynamic rolling moment and the denominator is related to the adhesion resting moment. The limiting fouling velocity is the air velocity required to make  $RM = 1$ . Additionally, if  $RM > 1$ , then it is assumed fouling is limited because particles will re-entrain into the gas flow. Under these circumstances, the high air velocity acts as a self-cleaning mechanism and results in minimum deposition. In the case of milk powder, no electrostatic force is applicable.

Using the limiting fouling velocity tool for a distribution of particle sizes, Jegla et al. (2010) carried out a numerical technical economic assessment of several heat

exchanger design configurations. The goal of the numerical modelling was to understand how the overall annual cost of the exchanger, which included investment, maintenance and operating components, varied with different designs. The face area and required duty of the exchanger were held constant. Results showed that the benefit gained from increasing the superficial gas velocity, from  $7.6 - 25.6 \text{ ms}^{-1}$ , (i.e. less fouling and lower maintenance costs) outweighed the energy and cost penalties incurred from higher air and water side pressure drops.

Recent studies on milk powder deposition have focused on the effect of impact velocity using the particle gun test (Murti et al., 2010; Zhao, 2009). Research on measuring the effect of velocity is limited because, apart from the particle gun test, milk powder deposition tests lack the ability to control the air velocity over a significant range. Some tests, such as the fluidised bed test, have the ability to vary a superficial velocity, but are limited to a small test range ( $0.2 - 0.5 \text{ ms}^{-1}$ ). As a result, the effect of velocity in such tests has not been a clear focus.

Murti et al. (2010) and Zhao (2009) showed a higher particle velocity would decrease deposition on a flat plate and would require stickier surface conditions to achieve the same level of deposition. Particle gun studies have assumed a particle travels at the same velocity as the encompassing air velocity. Figure 2-14 summarises the stickiness initiation points,  $(T - T_g)_{crit}$ , for a range of velocities. The results of the two studies are significantly different. This difference is the result of changes to the test set-up, which is reviewed in detail later in this review chapter in section 2.4.3.

Murti et al. (2010) also investigated the effect of particle impact angle by changing the jet impingement angle and reported that the angle of impingement had no significant effect on  $(T - T_g)_{crit}$ . However as the angle of impingement moved away from being normal to the plate, the rate of deposition decreased, which has been interpreted as the probability of depositing has decreased.

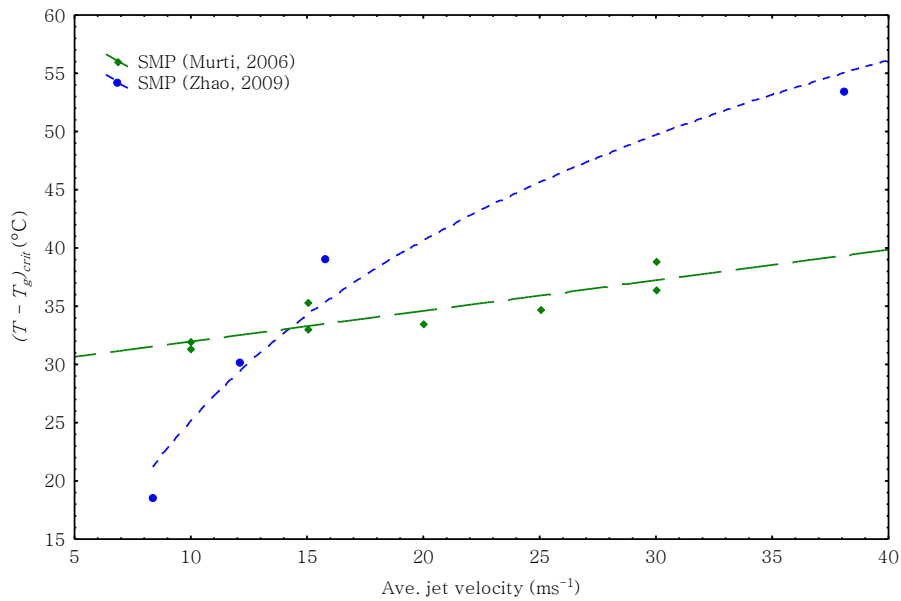
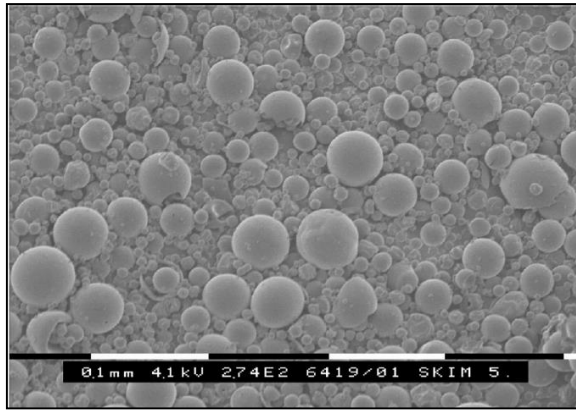


**Figure 2-14: Effect of velocity on  $(T - T_g)_{crit}$  of SMP using the particle gun technique. Median particle size for Zhao (2009) was 61  $\mu\text{m}$  and Murli (2006) did not report a particle size.**

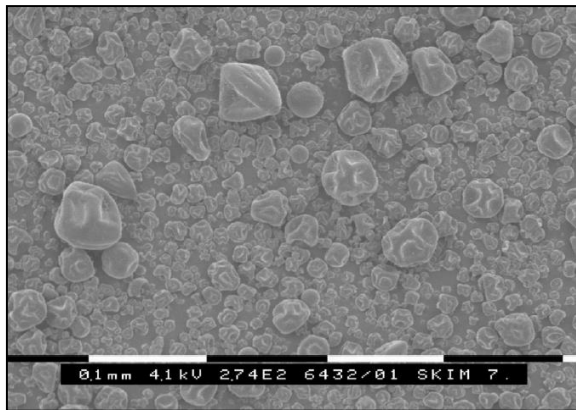
### 2.4.2.3. Effect of particle size distribution on particle deposition

Commercial spray dried powders have a range of size, shape and density particles. Average bulk particle density for powders also varies with fat content (Buma, 1965). Shape and roughness of particles have been found to be influenced by the drying temperature of the inlet air. Nijdam and Langrish (2005) used scanning electron microscope (SEM) to investigate the influence drying temperature has on the shape of milk powder particles. With inlet temperature greater than 200 °C, which is common in industry, the milk powder particles are spherical and smooth as shown in Figure 2-15a. However at lower inlet temperatures, the particles appear shrivelled (Figure 2-15b).

The milk powder particle size distribution entrained in the exhaust air is likely to be smaller than the bulk product. Milk spray dryers have attached to the dryer air outlets cyclones and/or baghouse filters. Both unit operations attempt to separate milk powder from the air flow before being emitted to atmosphere. The particle size distribution also depends on whether a product is agglomerated or non-agglomerated. Measurement of the particle size distribution in the exhaust air is therefore important to consider.



(a) Inlet air temperature - 200°C



(b) Inlet air temperature - 120°C

Figure 2-15: SEM photos of milk powder particles dried using varying inlet air temperatures into a lab scale spray dryer (Nijdam and Langrish, 2005).

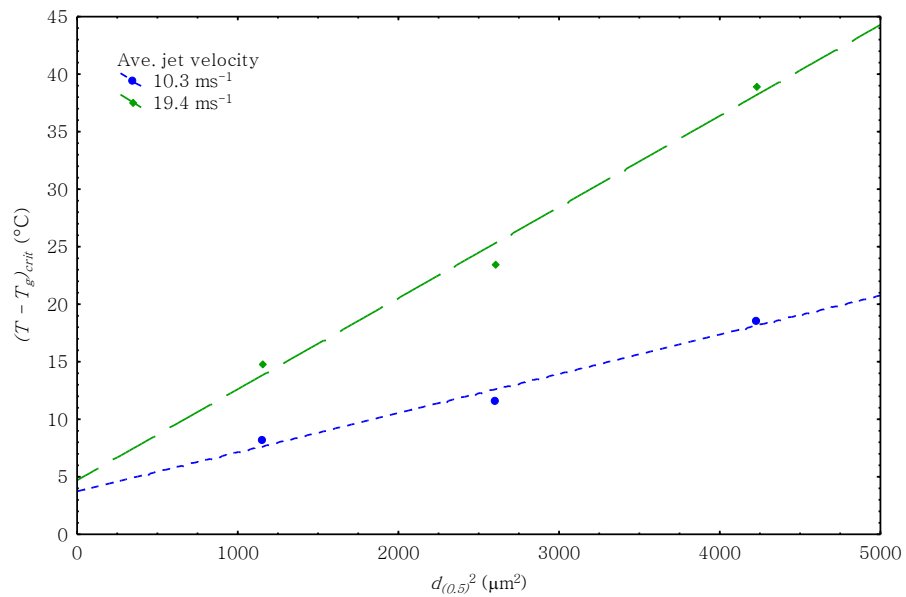


Figure 2-16: Relationship between particle stickiness and a particle surface area factor,  $d_{(0.5)}^2$  for SMP, results from particle gun test (Zhao, 2009).

The recent thesis of Zhao (2009) agreed with the earlier study of Chen et al. (1994) showing that fine particles are more likely to deposit than coarse particles for the same air conditions. Zhao summarised his preliminary results by plotting  $(T - T_g)_{crit}$  against a measure of surface area  $d_{(0.5)}^2$  as shown in Figure 2-16. Besides the work of Zhao (2009), the effect of particle size on particle deposition appears to have been over shadowed by focus on testing different types of products, which may or may not have different particle size distributions.

#### **2.4.2.4. Wall geometry and properties**

Surface properties of the wall influence the strength of the bond between the particle and the wall. Amorphous particles attached to walls by liquid bridging (Downton et al., 1982). The strength of the bridge is related to the degree of wetting that occurs between the particle and the wall. Wetting angle is dependent on the interfacial surface energy of the wall material. When the surface energy of the wall has a significantly lower surface tension than the powder's surface energy, the contact angle is high and wetting is poor, resulting in weak interfacial adhesion bonding. Metals have high surface energy (stainless steel 0.071 N/m). Therefore in theory powder should tend to stick more easily to stainless steel compared to Teflon, which has a surface tension of 0.018 N/m. Coating walls with Teflon were predicted to aid in reducing milk powder deposition (Bhandari and Howes, 2005).

Ozmen and Langrish (2003) studied deposition in a scaled down spray dryer where in different tests the chamber walls were coated with non-stick food grade nylon, powder and bare stainless steel. Their result showed no significant change in amount of wall deposition per unit area for the various wall conditions. A later study at the same University by Kota and Langrish (2006), however, produced results showing surface energy does affect deposition after the chamber was coated with Nylon. Murti et al. (2010) studied several different wall materials and like Ozmen and Langrish reported that the wall material had no effect on the particle deposition. However, in the case of a Teflon surface, it was observed by Murti et al. that particles repelled further to the edge of the target surface (a 75 mm diameter disc) before depositing. If the study had used a small deposition

collection plate, the results may have proven to be different. For milk powder deposition the introduction of low surface energy wall does not appear to significantly affect the deposition of milk powder.

The temperature of the wall may affect milk powder deposition. Chen et al. (1993) insulated a viewing window of a scaled down spray dryer and recorded that deposition in the window area decreased. Chen et al. remarked that the less deposition was a result of no condensation forming on the window. This conclusion appears to overlook that the dew point temperature of the air was likely significantly lower than the temperature of un-insulated viewing window. On the other hand Ozmen and Langrish (2003) showed insulating the spray dryer wall in the conical section had no effect on deposition whereas insulating the straight section of the dryer slightly increased the deposition.

The geometry and design of the heat transfer surface is also a critical factor affecting deposition. Heat transfer enhancement is a popular research area for innovative ways to increase heat transfer and simultaneously reduce fouling (Siddique et al., 2010). Tubes with superior heat transfer, pressure drop and fouling characteristics that standard round tube include: elliptical tubes (Bouris et al., 2001), egg-shaped tubes (Bouris et al., 2005), dimpled tubes (Kukulka et al., 2011), tube bank inserts (Stehlík, 2011), tube bank winglets (Tiwari et al., 2003), etc. Although not present in the process industry, elliptical tube banks with and without fins have found application in aerospace applications where low pressure drops for high heat transfer is seen as critical.

### **2.4.3. Powder stickiness and deposition characterisation techniques**

Initial research on dairy powder stickiness and deposition looked at stickiness development in situations where contact between particles occurred for extended periods of time resulting in powder caking (Hennigs et al., 2001; Wallack and King, 1988). Focus was given to measuring temperature and humidity condition that caused sudden coalescing of particles and agglomeration as shown in Figure 2-17. Stickiness is expressed as  $T - T_g$ , where  $T$  is the air temperature and  $T_g$  is the glass

transition temperature of the powder. Recent trends have widened the research scope and looked at reducing deposit build up in powder plant transport ducts and cyclones where particle impacts on processing chamber and duct walls are more dynamic (Intipunya et al., 2009; Murti et al., 2010, 2009; Zhao, 2009).

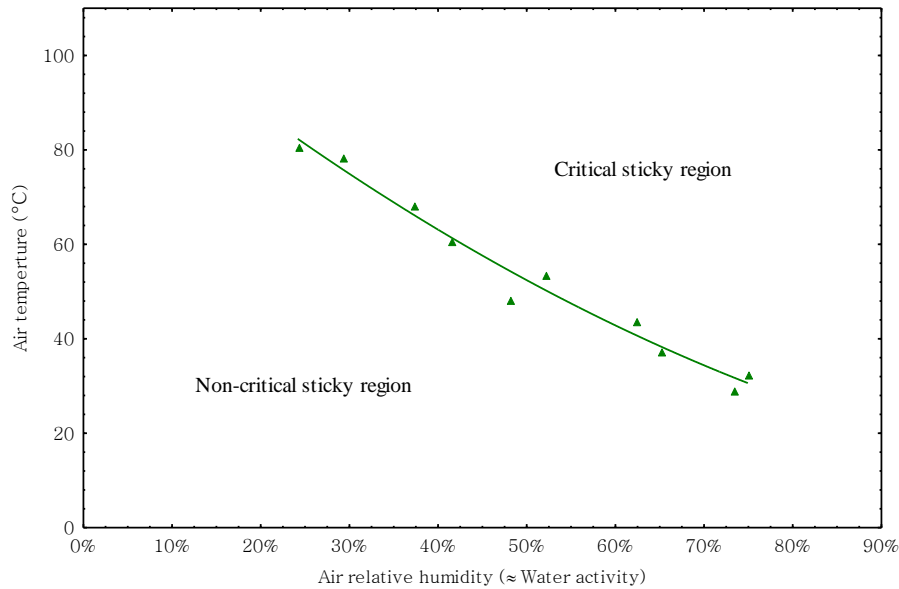


**Figure 2-17: Initiation of stickiness curve for whole milk powder measured using the particle gun test (Zuo, 2004).**

The majority of powder stickiness characterisation tests focus on critical conditions at which particles begin to cohesively stick to each other. Lazar et al. (1956) produced one of the first studies focusing on the agglomeration of tomato powder using a resistance stir test to identify critical air conditions that led to agglomeration. Since then, there have been several developments, improvements and creation of new experimental methods. Recent studies using agglomeration type tests for milk powders have included: mechanical stir test (Hennigs et al., 2001; Kockel et al., 2002; Kudra, 2003), fluidised bed simulation test (Chatterjee, 2004; Chen et al., 2004; Kockel et al., 2002; Verdurmen et al., 2006), viscometer test (Ozkan et al., 2002), unconfined yield strength test (Chen et al., 2004), flowability test (Kim et al., 2005), blow test (Paterson et al., 2005), and centrifugal stickiness test (Goula et al., 2007). Boonyai et al. (2004) gave an excellent review of stickiness measurement techniques and compared several of these methods. They also showed the historical development of some techniques, such as the mechanical stir test.

Caking and agglomeration stickiness characterisation tests are less relevant to this thesis because the majority of particle attachment that occurs on the air-side of heat exchangers is on a much shorter time scale. Key factors such as air velocity cannot be satisfactorily accounted for using caking and agglomeration stickiness characterisation tests.

Particle-wall adhesion is the root cause of deposits found in regions of high air flow. Very few tests in literature focus on understanding particle-wall adhesion with short contact times ( $< 1$  s). In recent years researchers have realised the merits of understanding this more dynamic mode of particle deposition (Bhandari and Howes, 2005). The three main tests that look at particle-wall adhesion is the scaled down spray dryer test (Chen et al., 1993; Kota and Langrish, 2006; Nijdam and Langrish, 2005; Ozmen and Langrish, 2003), the cyclone stickiness test (Boonyai et al., 2006; Intipunya et al., 2009), and the particle gun test (Murti et al., 2010, 2009; Paterson et al., 2007a, 2007b, 2005; M. R. W. Walmsley et al., 2010; T. G. Walmsley et al., 2010; Zhao, 2009; Zuo et al., 2007). Out of these three tests, only the particle gun test has the ability to isolate individual factors that affect deposition. The other two tests are focused more on bulk trends that are specific to a unit operation.

Several recent studies have applied the particle gun test to characterise deposition that occurs in an impingement jet against a flat plate. In the particle gun deposition test, powder is injected into a pre-conditioned airflow that impinges against a target plate giving the powder particles an opportunity to stick or rebound. The quantity of deposition on the collection plate is weighed. Powder particles are assumed to have surface conditions in equilibrium with the conditioned air and impact the plate at the same speed and angle as the impinging jet (Murti et al., 2010). An important advantage of the test is many of the most important factors influencing deposition are controlled and may be isolated; e.g. powder composition, air temperature and relative humidity, particle impact velocity and angle, particle size and shape, and plate material and temperature.

Paterson et al. (2007a) studied how air temperature and humidity affects the initiation and growth of deposition of skim and whole milk powders on a 70 mm diameter circular collection plate. Paterson et al. (2007b) further characterised the deposition propensities of high fat powders. Murti et al. (2009) analysed the robustness of parts of the particle gun test method and later looked at the influence jet velocity, impingement angle and plate material have on deposition (Murti et al., 2010). These original studies by Paterson and co-workers used a vertical jet impingement, a horizontal plate, and an anemometer (unspecified diameter) to measure the air velocity. In reviewing and repeating their work Zhao (2009) observed that at times powder would sit on the collection plate due to gravity, not adhesion, and as a result Zhao changed the orientation of the impingement to be horizontal and the plate to be vertical. There are also questions surrounding the correctness of the airflow measurements reported by Paterson and co. In these works an unspecified size vane anemometer was used to measure the air velocity at the end of the tube. When the vane diameter is larger than the air flow diameter, the accuracy of the velocity reading is reduced.

Zhao (2009) performed experimental and numerical investigations based on the particle gun test and studied the effect of particle size distribution and documented for the first time for the particle gun test the presence of ring shaped deposit morphologies. Through visual observation and Computational Fluid Dynamics modelling, Zhao demonstrated that the ring deposit morphologies were caused by milk particles impacting the plate multiple times before finally attaching. As the stickiness of the particles, i.e.  $T - T_g$ , was increased, Zhao showed the central deposit-free zone shrunk until eventually it disappeared (Figure 2-18). Further increases in  $T - T_g$  concentrated the deposition in the centre of the plate indicating most particles were sticking on first impact, which eliminated the possibility of deposition on the outer area of the plate.

Previous deposition studies based on the particle gun test defined  $(T - T_g)_{crit}$  as the deposition onset point on a deposition % versus  $T - T_g$  graph, e.g. (Zuo et al., 2007). However, Zhao's (2009) results implied that the deposition % is influenced by the size of the collection plate. The air conditions – temperature, humidity and velocity

– that the particles experience away from the jet are also difficult to precisely know and may not be assumed to be the same as the average jet conditions. As a result inclusion of deposits not at the centre of the plate in determining  $(T - T_g)_{crit}$  skews its value to appear lower than its true value for the given jet conditions. For example, one may be led to determine using Figure 2-18 that  $(T - T_g)_{crit}$  is less than 26 °C since deposition is occurring at the periphery of the plate. However, this critical temperature difference is valid to be associated with the stated jet conditions. In view of these issues, a different approach will be needed to determine  $(T - T_g)_{crit}$  that is independent of plate size.

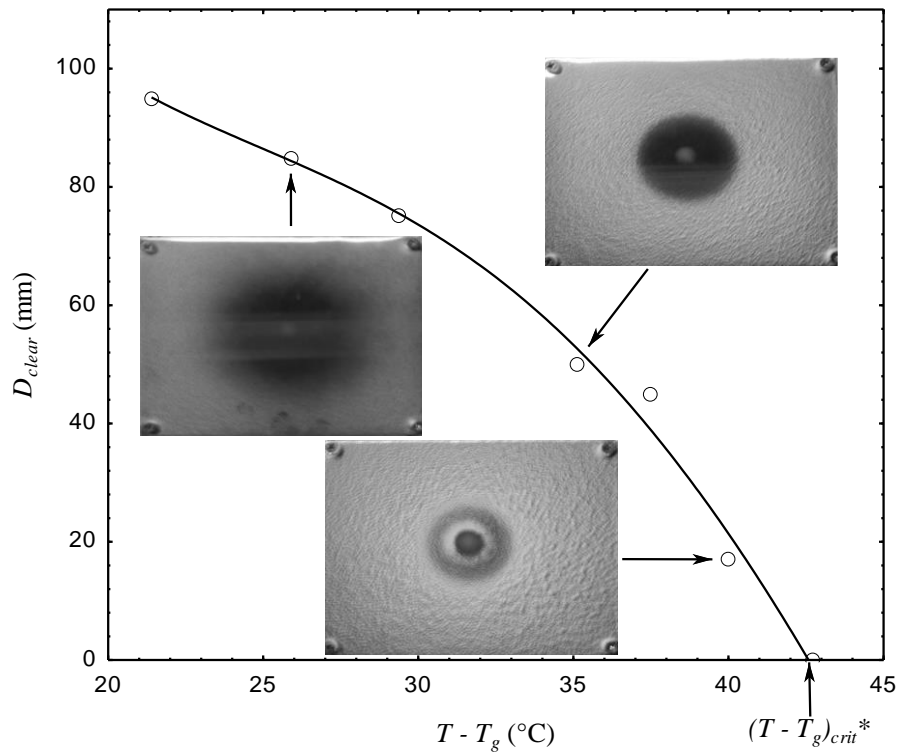


Figure 2-18: Determination of  $(T - T_g)_{crit}^*$  using a clear ring diameter. Test conditions:  $d_{(0.5)}$  61  $\mu\text{m}$ , normal impingement and jet velocity 15.0  $\text{ms}^{-1}$ , data from Zhao (2009).

#### 2.4.4. Approaches to modelling particulate transport and deposition mechanisms

There are two general approaches to modelling the fouling of surfaces. The first approach focuses on bulk effects using mass transfer principles to derive fundamental models that describe the estimated deposit build-up on heat transfer surface with time and its effects on heat transfer and pressure drop. Mass transfer coefficients are calculated from experimental results and are specific to a specific

combination of heat exchanger geometry and particulate. The second approach gives closer attention to the interaction between a single particle and a solid surface. Models are constructed to acutely describe the particle-wall collision that may predict the conditions for when a particle sticks or rebounds. This approach is specific to a particulate type, but can be independent of heat exchanger geometry. This section reviews these two approaches to modelling deposition and the traditional applications of these approaches.

#### 2.4.4.1. Bulk mass transfer approach to modelling fouling

Kakac and Liu (2002) state that the fouling heat transfer resistance,  $R_f$ , for a plain wall is

$$R_f \equiv \frac{x_f}{k_f} \quad (2-14)$$

where  $x_f$  is the deposit thickness and  $k_f$  is the thermal conductivity of the foulant layer. Fouling can be categorised into five types: particulate, crystallisation, corrosion, biofouling, chemical reaction, and solidification. For the application of fouling in spray dryer heat recovery exchangers, the major fouling type is particulate deposition.

According to Webb and Kim (2005), the build-up of deposits is described by

$$\frac{m_f}{A} = \frac{s K c_b}{\tau} \left(1 - \exp\left(-t/\tau\right)\right), \quad \text{where } \tau = \frac{k_0 \xi}{\tau_w} \quad (2-15)$$

In the above equation,  $m_f$  is the mass of fouling,  $s$  is the probability of sticking,  $K$  is the mass transfer coefficient,  $C_b$  is the concentration of the foulant in the bulk air flow and  $A$  is the surface area,  $\tau$  is a time constant,  $\tau_w$  is the wall shear stress and  $k_0$  is a proportionality constant. Eq. 2-15 is rewritten with  $R_f$  as the subject by dividing by the density ( $\rho$ ) and thermal conductivity of the foulant

$$R_f = \frac{s K c_b}{\rho_f k_f \tau} \left(1 - \exp\left(-t/\tau\right)\right) \quad (2-16)$$

Eq. 2-16 suggests that the build-up of deposits and increase in resistance due to fouling is asymptotic, which means the rate of fouling decreases over time until the rate of deposition and removal are similar. Experimental testing can be applied to find the sticking probability, time constant, and mass transfer coefficient in Eq. 2-24. This approach is specific to a heat exchanger design and the sticking probability is related to the powder stickiness. Wall shear stress is assumed to be the controlling mechanism for deposition. The mass transfer approach has limited application to predicting deposition in heat exchanger geometries and designs that have not been experimentally tested.

Deposition of particles may result from a combination of several discrete transport processes and mechanisms (Guha, 2008). These processes are largely dependent on the dimensionless particle relaxation time,  $t^+$ ,

$$t^+ = \frac{\rho_p \rho_f d_p^2 (u^*)^2}{18\mu^2} \quad (2-17)$$

where  $\rho_p$  is the density of the particle,  $\rho_f$  is the density of the fluid,  $d_p$  is the particle diameter,  $u^*$  is the wall friction velocity, and  $\nu$  is the kinematic viscosity of the fluid. The particle relaxation time represents the time scale with which the particles respond to changes in the slip velocity. Typically, three general transport regimes are identified:

1. Turbulent diffusion,  $t^+ < 0.1$
2. Turbulent diffusion-eddy impaction,  $0.1 < t^+ < 10$
3. Particle inertia moderated,  $t^+ > 10$

In the turbulent diffusion regime, deposition is a mass transport problem described by Fick's law. The second regime is a transitional regime whereas particles that fall in the particle inertia regime respond slowly to changes in velocity flow field changes as indicated by the large  $t^+$ . Estimates for the particle relaxation time of milk powder particles bases on a particle density of 1540 kg/m<sup>3</sup> (Hayashi and Handa, 1974), fluid viscosity of 2.03 x 10<sup>-5</sup> Pa·s and particle diameter of 14.8 μm (which approximately corresponds to the 10<sup>th</sup> percentile of particle

diameters by volume in skim milk powder) indicate the dominant transport regime is inertia moderated. This also suggests that wall shear stress may have less influence on the deposition of particles.

#### **2.4.4.2. Contact mechanics approach to modelling deposition**

Contact mechanics has been the subject of several studies over the past century. The elementary study on contact mechanics of spherical bodies was conducted by Hertz (1896, 1881). Extensions to the Hertz theory are very common in the field. The most significant extension is the Johnson-Kendall-Roberts (JKR) theory (Johnson et al., 1971). According to *Scopus*, the JKR theory is cited by over three thousand articles and K.L. Johnson, the lead author, has continued to expand his original treaties in the following years, e.g. (Greenwood and Johnson, 1981; Johnson and Greenwood, 1997; Johnson, 1998, 1996, 1987). More recently, the Thornton and Ning (1998) theory built on the earlier Hertzian and JKR theories to derive a model for predicting the normal restitution behaviour of adhesive elastic-plastic spheres.

Brilliantov et al. (2007, 1996) and Hui et al. (1998) also used results from the Hertzian and JKR theories to derive a normal restitution model of adhesive viscoelastic spheres colliding. In general, food powders are considered as a viscoelastic material (Palzer, 2005). The distinguishing feature of viscoelastic materials is their ability to relax in time, which lowers the stress and gives out heat when placed under a constant strain. However, for short collision contact times where very little stress relaxation has time to occur, the complex solutions of viscoelastic models can be simplified by using elastic-plastic contact models.

In short, the particle-wall collision models require knowledge of several materials properties: surface energy, particle mass (radius and density), force, Young's modulus, Poisson's ratio and yield stress. Surface energy of milk powders is a dynamic quantity because it is heavily influenced by the air temperature and humidity surrounding the particle. Derivations for describing the contact between a particle and rigid wall are normally based on a simplified energy balance of the collision and have mostly focused on normal particle impacts. Ignoring energy lost

to acoustic waves, friction, etc., the energy balance of a particle-surface collision is

$$E_{k,i} = E_{k,f} + W_a + W_{pd} + \Delta E_{rot} \quad (2-18)$$

where  $E_{k,i}$  and  $E_{k,f}$  are the initial and final kinetic energy of a particle colliding with a surface,  $W_a$  is the work of adhesion,  $W_{pd}$  is the energy of plastic deformation, and  $\Delta E_{rot}$  is change in rotational energy (which is often ignored). Expressions essential to finding the work of plastic deformation have been proposed by Davies (1949) based on a limiting elastic velocity beyond which plastic deformation (as opposed to elastic deformation) occurs.

$$v_{pd} = \left( \frac{\pi}{2Y^*} \right)^2 \left( \frac{2}{5\rho} \right)^{1/2} \sigma_e^{5/2} \quad (2-19)$$

where  $\rho$  is the particle density,  $\sigma_e$  is the elastic yield limit and  $Y^*$  is a modified Young's modulus. Likewise expressions for the work of adhesion based on a critical sticking velocity suggested by Professor K. L. Johnson, which is cited in theory of Thornton and Ning (1998).

$$v_{crit} = 1.84 \left( \frac{\gamma^5}{\rho^3 Y^{*2} r^5} \right)^{1/6} \quad (2-20)$$

where  $\gamma$  is the surface adhesion energy and  $r$  is the particle radius. Using these two critical and limiting velocities, Thornton and Ning concluded by deriving an expression of the normal coefficient of restitution of a particle.

$$\xi_n = \sqrt{\frac{6\sqrt{3}}{5} \left( 1 - \frac{1}{6} \left( \frac{v_{pd}}{v_n} \right)^2 \right) \left( \frac{\frac{v_{pd}}{v_n}}{\frac{v_{pd}}{v_n} + 2 \left( \frac{6}{5} - \frac{1}{5} \left( \frac{v_{pd}}{v_n} \right)^2 \right)^{1/2}} \right)^{1/2} - \left( \frac{v_{crit}}{v_n} \right)^2} \quad (2-21)$$

Thornton and Ning (1998) showed the validity of Eq. 2-30 by carrying out a numerical study to solve Newton's laws of motion. The model of

Thornton and Ning is limited to describing normal particle impacts on a rigid surface.

For non-normal impacts Coulomb's law of friction has been successfully applied to approximate the tangential coefficient of restitution of rebounding spheres (Wu et al., 2003). Coulomb's law is a simple relationship between the normal coefficient of restitution,  $\xi_n$ , and the tangential coefficient of restitution,  $\xi_t$ ,

$$\xi_t = 1 - \frac{f(1 + \xi_n)}{\tan \theta} \quad (2-22)$$

where  $f$  is a constant relating to friction (generally around 0.3),  $\xi_n$  is the normal coefficient of restitution and  $\theta$  is the impact angle. Assuming that  $\xi_n$  is known from one of the previously presented normal restitution models,  $\xi_t$  may be approximated provided a good estimate of  $f$  is available. However Coulomb's law of friction has less application to understanding the critical conditions that result in a particle sticking to a surface. Predicting the deposition of particles impacting at oblique angles requires an understanding of how the tangential impact force affects whether a particle attaches or detaches.

Savkoor and Briggs (1977) described mathematically the effect of the tangential force on the size of the contact area between a particle and a surface. Their expressions showed the contact area reduced with increasing oblique impact angles indicating less normal force (i.e. velocity) was needed to break a particle free from the bond. At some critical angle Savkoor and Briggs argued that slip would occur between the particle and surface making attachment impossible. A difficulty with applying the equations of Savkoor and Briggs is to know how the tangential force of a particle is stored and released during a particle's collision. Recent studies such as Konstandopoulos (2006) have proposed the calculation of a critical impact angle beyond which deposition ceased. This provided a simple method to overcome the weaknesses of focusing solely on normal forces when predicting the deposition/rebound of a particle while still somewhat accounting for tangential force contribution. This approach also limited the need to understand how the tangential force varies during a particle's collision.

## **2.5. Conclusion**

Although the literature and industry offer no standard solution for maximising heat recovery in milk powder process, it is clear that heat recovery from the spray dryer exhaust is likely needed to achieve maximum heat recovery. Techno-economic analysis of heat integration options needs to be performed to justify which solution should be the standard, or if there is some new integration scheme that is better. Minimising total cost through optimal area allocation is rarely a feature in heat integration studies and the literature is void of a fundamental method to maximise the benefit of heat exchanger area. When milk powder plants are co-located with other dairy processes on a single site, there is opportunity for inter-plant heat integration to boost overall site heat efficiency. Conventional techniques have been applied to dairy examples to illustrate the potential benefits.

An important technical barrier preventing spray dryer exhaust heat recovery is the potential for heat exchanger fouling. The stickiness of milk powder has been investigated in the context of spray drying and fluidised bed drying but the literature lacks a model that fully describes the critical conditions that result in a particle depositing on a wall and/or another particle. A clear gap in the knowledge is an investigation on the interaction between milk powder particles and heat exchanger surfaces.



# Chapter 3

## Improving heat recovery in stand-alone milk powder plants

---

### 3.1. Introduction

*“Many dairy processes produce waste liquid streams at about 50 °C”*

H. Hanneman and L. J. Robertson  
IDF World Dairy Summit, 2005

Previous studies on an integrated milk powder plant and site have calculated a pinch temperature of about 50 °C (Atkins et al., 2011; Lovell-Smith and Baldwin, 1988; Robertson and Baldwin, 1993), which is strongly affected by the exhaust air stream temperature selection (Walmsley et al., 2012a). Waste heat below this temperature is considered not useful for heat recovery and hence the statement of Hanneman and Robertson (2005) is understandable. With such a high pinch temperature the value of dryer exhaust heat recovery is questionable since its heat is low temperature after heat recovery. As a result heat recovery from the dryer exhaust may be perceived as unnecessary, as it only adds to the already excess waste heat in liquid streams. In this chapter the premise that there is little opportunity for heat recovery in dairy plants, and especially the dryer exhaust, is challenged and heat integration opportunities within a stand-alone milk powder plant are examined.

This chapter investigates how best to integrate stand-alone industrial milk powder plants for maximum heat recovery. Using this analysis it is determined whether or not dryer exhaust heat recovery is technically feasible and economically advantageous. As the basis of the analysis, process and utility stream data from a local dairy plant has been extracted. The stream data for this plant is representative of a typical milk powder plant. Using PA, utility and heat recovery targets are calculated assuming steady stream flow rates and temperatures while

the dryer is in operation. Some stream data for the process are “soft”, meaning that some flow or temperature set points or target values can vary without impacting the process, product quality and safety. As a result soft stream data is varied to analyse the effect on the targets. Designers can use these degrees of freedom to their advantage by varying soft data within defined ranges to obtain a minimum energy use target. After targeting, HENs are developed for the evaporator and spray dryer sections of the milk powder process.

### 3.2. Industrial milk powder production process

The milk powder plant analysed is illustrated in Figure 3-1 with evaporator and spray dryer zones, and a common heat recovery network. Clean-in-place (CIP) water is shown as a third zone. It is important to note that standard industry practice for New Zealand factories is to not recovery heat from the spray dryer exhaust air and to not include CIP water as a heat sink.

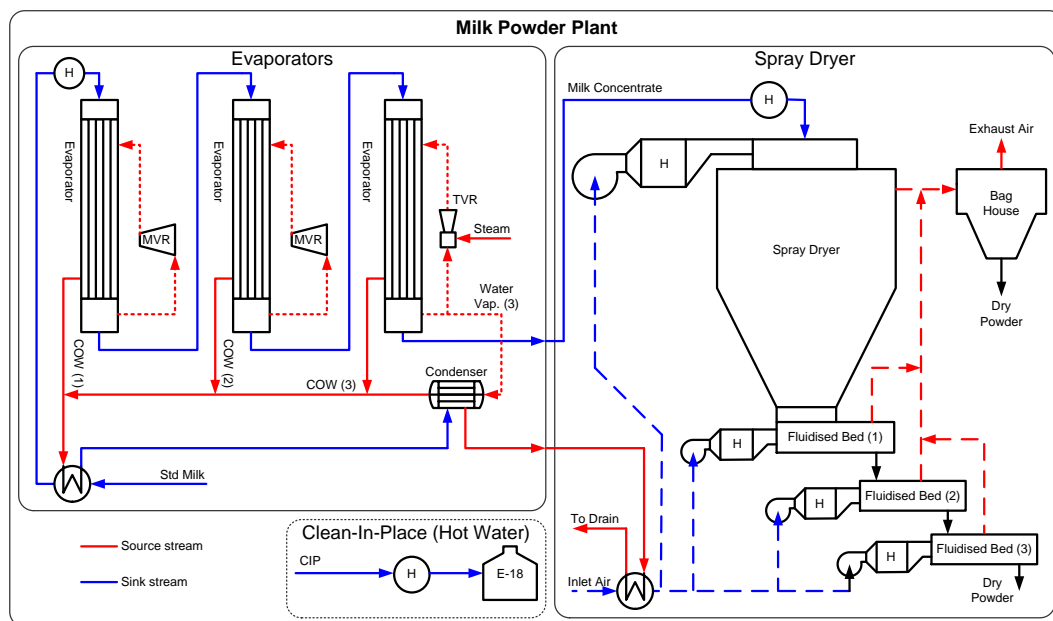


Figure 3-1: Milk powder plant schematic including current HEN.

#### 3.2.1. Extracted heating and cooling process demands

Specific stream data (one tonne of product basis) for a large industrial milk powder plant with a maximum throughput of 23.5 t<sub>p</sub>/h operating for 5000 h/y is presented in Table 3-1. The stream data is presented in specific terms so that it can relate to any plant production rate. The streams include the evaporation and condensing

streams inside the three evaporator effects. The vapour side streams have been upgraded in temperature using mechanical or thermal recompression. The acronym COW is short for condensate of whey and refers to water that is removed from the milk during the evaporation stages. As a process requirement immediately prior to milk being fed into the evaporator, a small amount of steam is directly injected into the milk raising its temperature from 63.4 °C to 69.9 °C. Steam used for direct steam injection is not shown in Table 3-1. The heat demand for the four air streams are shown separately although there is opportunity to: (1) heat all four air streams collectively as the air enters the building, and/or (2) the fluidised bed air streams collectively. The inlet air temperature varies depending on the month and as a result an average temperature has been determined. Soft data are identified using “\*”. Typical industrial utility prices for 2011 are used: steam utility \$45 /MWh, cooling tower water \$0.5 /MWh and chilled water \$35 /MWh.

**Table 3-1: Process stream data extracted for the industrial milk powder plant. Soft temperatures indicated using \*.**

Zone	Stream	Hot/ Cold	State	$T_s$ [°C]	$T_t$ [°C]	$\hat{C}$ [MJ/t <sub>p</sub> ·°C]	$\Delta H$ [MJ/t <sub>p</sub> ]
Evap.	Standardised milk	C	Liq.	8.0	63.4	42.7	-2362
Evap.	Effect 1 after MVR (vapour side)	H	Vap.	75.0	74.9		12321
Evap.	Effect 1 (product side)	C	Vap.	69.9	70.0		-12375
Evap.	COW 1 (from effect 1)	H	Liq.	67.5	13.0*	22.3	1215
Evap.	Effect 2 after MVR (vapour side)	H	Vap.	67.0	66.9		7320
Evap.	Effect 2 (product side)	C	Vap.	61.9	62.0		-7353
Evap.	COW 2 (from effect 2)	H	Liq.	61.0	13.0*	13.1	630
Evap.	Effect 3 after TVR (vapour side)	H	Vap.	59.0	58.9		1495
Evap.	Effect 3 (product side)	C	Vap.	53.9	54.0		-1495
Evap.	Condenser vapour	H	Vap.	54.0	53.9		370
Evap.	Condensate (condenser)	H	Liq.	53.9	13.0*	0.7	27
Evap.	COW 3 (from effect 3)	H	Liq.	54.9	13.0*	2.0	81
CIP	CIP hot water	C	Liq.	15.0	55.0	6.0	-238
Dryer	Milk concentrate	C	Liq.	54.0	65.0	6.0	-65
Dryer	Dryer inlet air	C	Gas	15.0	200.0	18.4	-3411
Dryer	FB inlet air (1)	C	Gas	15.0	49.0	1.6	-53
Dryer	FB inlet air (2)	C	Gas	15.0	45.0	2.3	-69
Dryer	FB inlet air (3)	C	Gas	15.0	32.0	1.7	-29
Dryer	Exhaust air – dew point 39°C	H	Gas	75.0	55.0*	25.7	-513

### 3.3. Methodology

PA has been applied to calculate specific utility and recovery targets for milk powder production. Site utility and heat recovery targets are calculated by shifting individual streams by a  $\Delta T_{cont}$ , which are estimated based on the state of the stream, the best available heat exchanger technology and designer experience. The  $\Delta T_{cont}$  applied are presented in Table 3-2 and the overall heat transfer coefficients together with the  $\epsilon$ -NTU correlation and cost equations are presented in Table 3-3. The minimum approach temperature,  $\Delta T_{min}$ , varies depending on which streams are matched and the respective  $\Delta T_{cont}$ 's of the streams exchanging heat.

**Table 3-2: Initial  $\Delta T_{cont}$  assignment.**

State	$\Delta T_{cont}$ [°C]
Vapour	3.0
Liquid	2.5
Gas	10.0

For large industrial sites, it is normally most economical to maximise heat recovery within individual zones before transferring heat inter-zonally. Intra-zonal targets are found by applying PA to each zone. Inter-zonal targets are derived from an analysis of the entire site, where the source and sink sections of the zonal grand composite curves that require utility are combined to form total site source and sink profiles. These profiles can be pinched to provide the maximum heat recovery target for direct inter-zonal heat exchange. Soft stream data is varied within defined limits to minimise utility targets. Preference is given to heat recovery from liquid streams over gaseous streams (Walmsley et al., 2012a).

HENs are formulated using the PDM (Linnhoff and Hindmarsh, 1983). Exchanger areas are calculated using the  $\epsilon$ -NTU method using the correlations presented in Table 3-3 (Kays and London, 1998; Navarro and Cabezas-Gómez, 2005). Overall heat transfer coefficients,  $U$ , are taken from Kakaç and Liu (2002). Heat exchanger cost equations as a function of area ( $A$ ) have been adapted from Bouman et al. (2005) and multiplied by a Lang factor of 3.5. In retrofit situations a more appropriate Lang factor may be 5.0. Cost equation coefficients in Table 3-3 have

been annualised using a typical discount rate of 10 % and an expected life time of 10 years.

**Table 3-3: Overall heat transfer coefficients (Kakaç and Liu, 2002),  $\epsilon$ -NTU correlations (Kays and London, 1998; Navarro and Cabezas-Gómez, 2005) and cost functions (Bouman et al., 2005) for various types of heat exchangers. Refer to Appendix B for  $\epsilon$ -NTU correlations.**

Type	Purpose	$U$ [W/m <sup>2</sup> .°C]	Explanation of $\epsilon$ -NTU correlations	Cost [\$/y]
Gasket plate heat exchanger	Liq./Liq.	2000	Counterflow exchanger	1800 + 200 A
Finned tube heat exchanger	Gas/Gas	35	Both fluids unmixed crossflow exchanger with two passes	500 A <sup>0.815</sup>
	Gas/Liq.	70	Both fluids unmixed crossflow exchanger with two passes	500 A <sup>0.815</sup>
	Gas/Vap.	80	One fluid condensing exchanger	500 A <sup>0.815</sup>
Shell and tube condenser	Liq./Vap.	1500	One fluid condensing exchanger	1100 A <sup>0.57</sup>

### 3.3.1. Solution constraints

The limits of the soft target temperatures of the COW and exhaust air streams are presented in Table 3-4. The liquid COW stream must discharge below 28 °C to meet environmental regulations. The lower limit discharge temperature is determined by the supply temperature of the coldest process stream and the minimum allowable approach temperature.

**Table 3-4: Soft temperature limits.**

Soft Stream Data	$T_i$ [°C]	
	Lower limit	Upper limit
COW	13	28
Cond. loop return	13	38.5
Exhaust air	55	75
Exhaust loop return	13	42.5

The exhaust air stream is constrained to exit a possible recuperator above 55 °C to limit the potential of excessive fouling (T. G. Walmsley et al., 2013a). Exhaust heat may be recovered using an air-to-air or air-to-liquid heat exchanger system. In existing plants there is often a significant distance between the exhaust and inlet air ducts. Air-to-air heat recovery is economically difficult to justify due to the excessive ducting required to bring the exhaust and inlet air streams together and

the tight space constraints in and around the building enclosing the spray dryer. The exhaust air duct typically exits out the top of the building whereas the inlet air fan and duct is located several levels below the exhaust duct within the building. Air-to-air heat recovery systems may prove economical for Greenfield plants where the building and equipment may be arranged to accommodate such a system.

This work applies an indirect liquid coupled loop integration system for heat recovery from the dryer exhaust air. A liquid couple loop system employs an intermediate fluid such as water to recover heat from the exhaust air, which is then used to heat a cold stream such as the inlet air. Indirect heat recovery systems are more compact than air-to-air heat recovery and are equally applicable to Greenfield and existing plants. Other indirect integration methods, such as heat pipes and heat pumps, are not considered in this work. The supply temperature of this liquid loop is set at 62.5 °C, which is the exhaust air supply temperature, 75 °C, minus the  $\Delta T_{min}$  for heat exchange between gas and liquid streams. The return temperature of the loop is a soft temperature.

Options for direct and indirect heat exchange for matches between the condenser vapour and milk product are investigated. There are concerns in industry that direct heat exchange between the condenser vapour and the standardised milk may result in product contamination if a leak in the heat exchanger were to develop. Such contamination is actually unlikely since the vapour is at low pressure and if a leak were to occur, the flow would be from the milk into the vapour, which apart from a small amount of product loss would not affect the product. Options for indirect matches between the condenser vapour and milk are required to use a liquid coupled loop heat exchanger system. The maximum loop supply temperature is 48.5 °C. The loop return temperature is a soft temperature. If the condenser is matched to any stream in the dryer zone, this heat exchange must also be done indirectly as direct heat exchange is impractical due to the distance between the condenser and the dryer zone air streams.

## 3.4. Stream analysis and energy targeting

### 3.4.1. Site energy analysis

The composite curves for the entire process, including the evaporation, condensing and temperature upgrading that occurs in the evaporators, is presented in Figure 3-2. Soft temperatures have been set at the lower limit values for the respective streams (Table 3-4). The site pinch is 10.5 °C, although this is not representative of the pinch temperatures in individual zones; where the pinch temperature of the evaporator zone is 50.5 °C, and the CIP and the spray dryer zones are both threshold problems.

The multi-effect evaporators can be separated from the background process and plotted on a grand composite curve as shown in Figure 3-3. MVR and TVR units upgrade vapour removed from the milk to a higher temperature and pressure, which allows the vapour to be recycled to the shell side of the evaporators and boil water on the product side. In the TVR, about two thirds of the vapour leaving the third effect is combined with direct steam injection to increase the temperature. The final third of vapour, not upgraded in the TVR, is sent to a condenser.

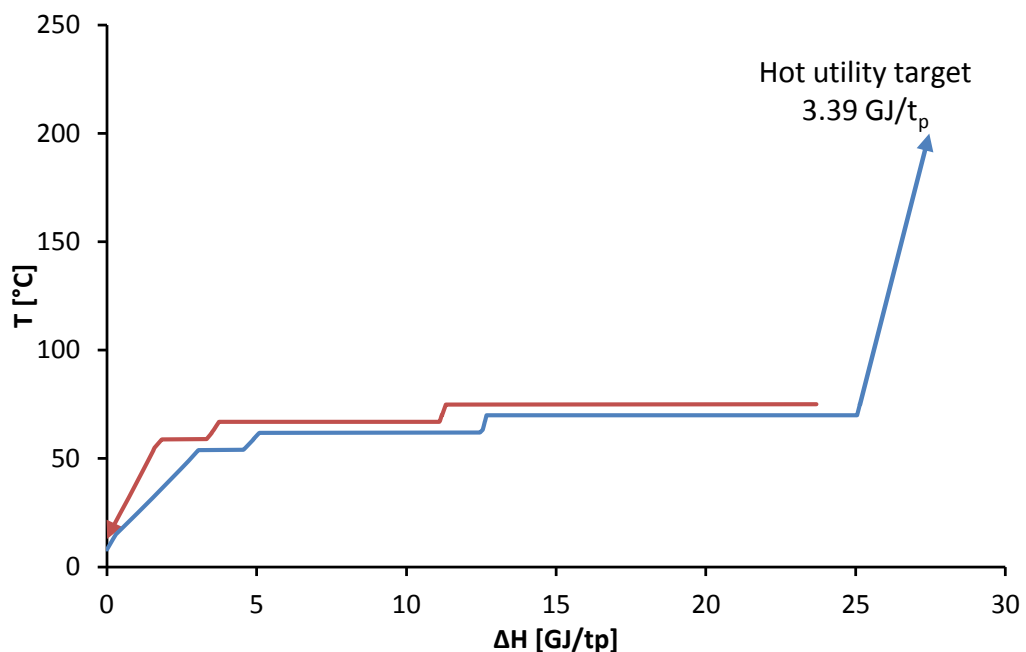


Figure 3-2: Composite curve for entire site including the evaporators including the MVR and TVR units. Soft temperatures: exhaust air  $T_t$  is 55 °C and COW  $T_t$  is 13 °C. Pinch temperature at 10.5 °C.

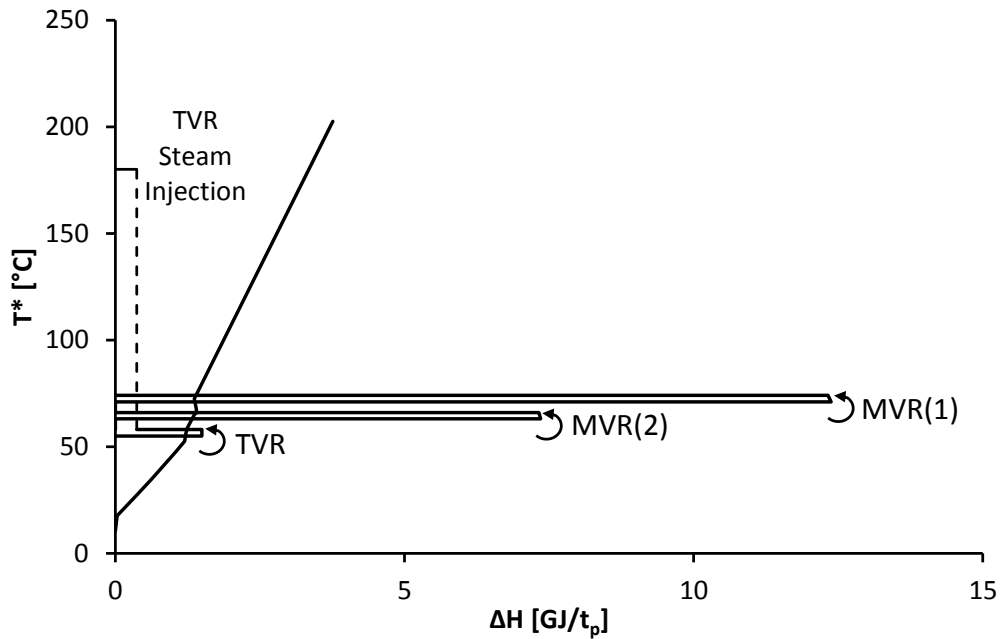
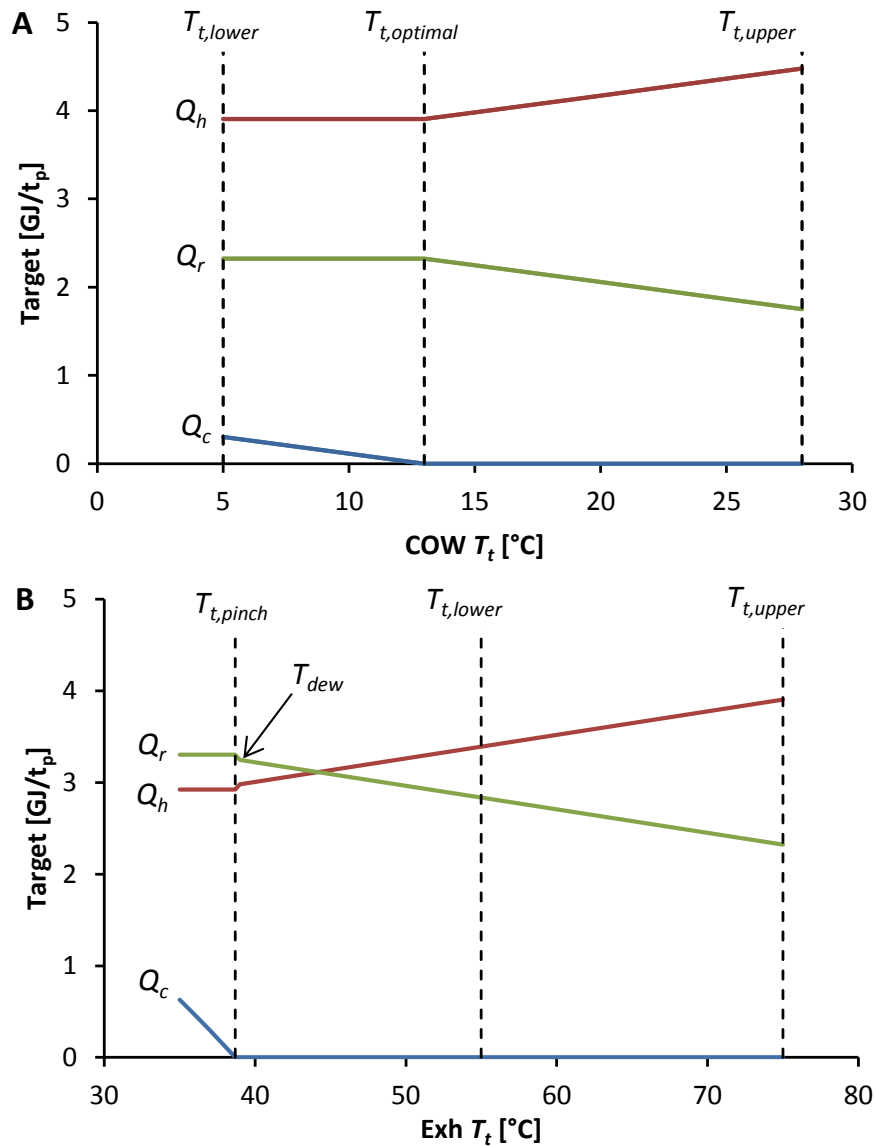


Figure 3-3: Grand composite curve for evaporators and background process. Soft temperatures: exhaust air  $T_t$  is 55 °C and COW  $T_t$  is 13 °C. Pinch temperature at 10.5 °C.

### 3.4.2. Soft temperature selection

Two soft temperatures are  $T_t$  of the exhaust air and COW streams. In Figure 3-4a, the exhaust air  $T_t$  is constant at 75 °C, i.e. no exhaust heat recovery, and the COW  $T_t$  is varied with the  $T_t$  achieving the maximum heat recovery at 13 °C. In Figure 3-4b, the exhaust air  $T_t$  is varied with the COW  $T_t$  set at 13 °C. The optimal exhaust air  $T_t$  is the lower temperature limit of 55 °C. This lower temperature limit was set for the exhaust air to avoid excessive fouling as suggested by T. G. Walmsley et al. (2013a). In reality it may be possible to go below 55 °C to increase heat recovery through low fouling heat exchanger designs and the subject of milk powder fouling in heat exchangers is considered in greater detail in Chapter 7. There is also a thermodynamic limit to exhaust heat recovery for the given minimum approach temperatures. In Figure 3-4b, a dotted line at an exhaust air  $T_t$  of 38.7 °C, which is marginally below the dew point temperature of 39.0 °C, is drawn to indicator the limit of exhaust heat recovery. For this exhaust air  $T_t$ , the analysis shows two pinches: 10.5 °C and 50.5 °C. Recovering heat below 38.7 °C for the exhaust air effectively adds heat below the new pinch temperature, which causes an increase in cold utility and no further reduction in hot utility. It is also important to note that Figure 3-4 is valid for both cases of directly and indirectly integrating the evaporator condenser.



**Figure 3-4:** The effect of the soft target discharge temperatures on heat recovery and utility targets. Graph a – exhaust air  $T_t$  is 75 °C and b – COW  $T_t$  is 13 °C.

The liquid coupled loop between the condenser and sink streams has a supply and return temperature. The supply (hot) temperature of the loop is constrained by the condenser pressure and temperature and is fixed by the selected minimum approach temperature. The cold return temperature from the sink(s) to the condenser, however, is soft since the network is yet to be formulated. Using the pinch targets the effect of the soft condenser loop return temperature ( $T_{CR}$ ) on heat recovery is shown as Figure 3-5a. To maintain the maximum heat recovery target,  $T_{CR}$  must be higher than 18.5 °C (Figure 3-5a). When  $T_{CR}$  is 18.5 °C, a pinch between the shifted total site profiles occurs (Figure 3-6). Setting  $T_{CR}$  to below 18.5 °C requires utility cooling and results in a loss of heat recovery.

In a similar manner heat from the dryer exhaust is recovered using a liquid coupled loop. The supply temperature exiting the exhaust heat exchanger is constrained by the supply temperature of the exhaust air whereas the return temperature to the exhaust heat exchanger is soft. The effect of the exhaust loop return temperature ( $T_{ER}$ ) on heat recovery is shown in Figure 3-5b. When  $T_{ER}$  is 27.5 °C, a pinch in the dryer zone occurs between the  $T_s$  of the inlet air streams and the exhaust loop. If  $T_{ER}$  is set below 27.5 °C, cooling utility would be required to reach the specified  $T_{ER}$  and heat recovery is lost.

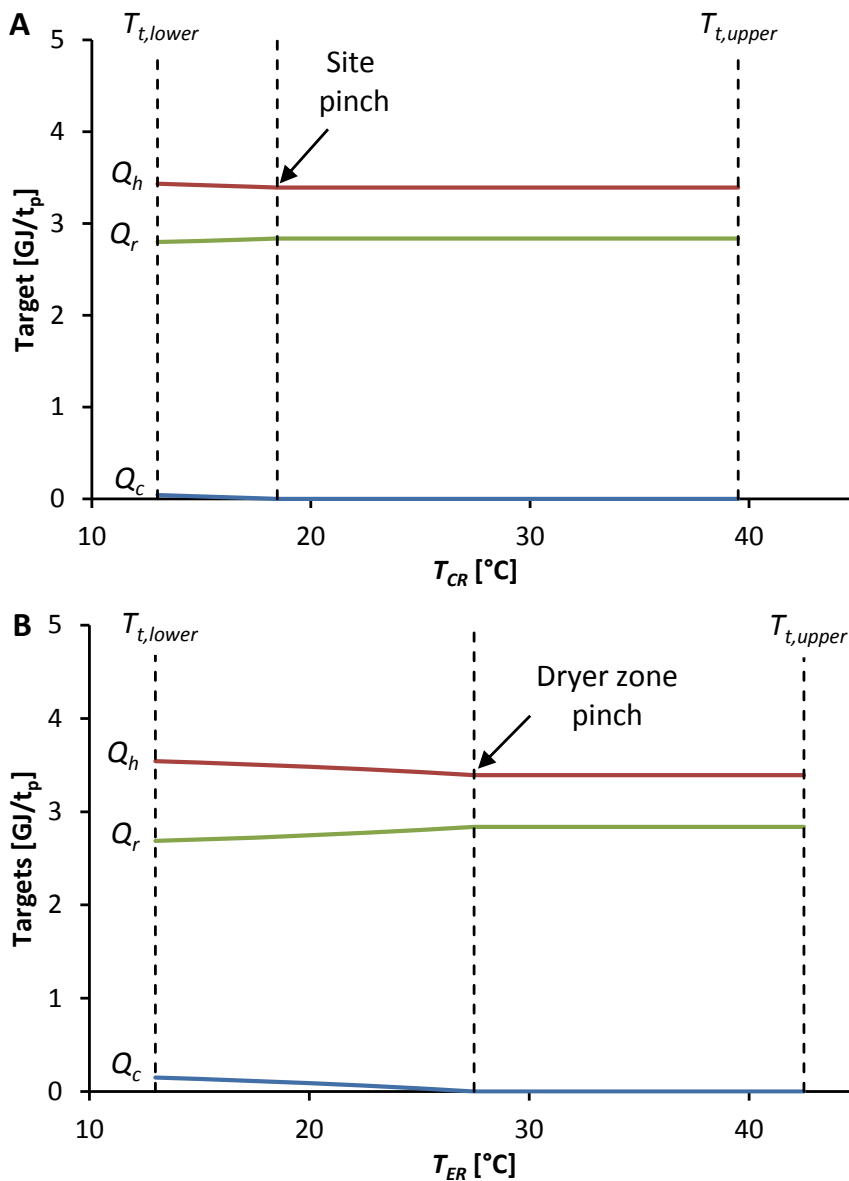


Figure 3-5: The effect of the soft return temperature on heat recovery and utility targets for the condenser loop (a) and the exhaust loop (b). Soft temperatures: exhaust air  $T_t$  is 55 °C and COW  $T_t$  is 13 °C.

The final soft temperature is the inlet air entering the building,  $T_t$ , from which air is drawn into ducts for use in the dryer and fluidised beds. The inlet air temperature to the building varies depending on the month of the year and location of the dairy factory. In this work the inlet air temperature is set at 15 °C, which is representative of an average air temperature for the entire dairy processing season including day/night variations in the North Island of New Zealand.

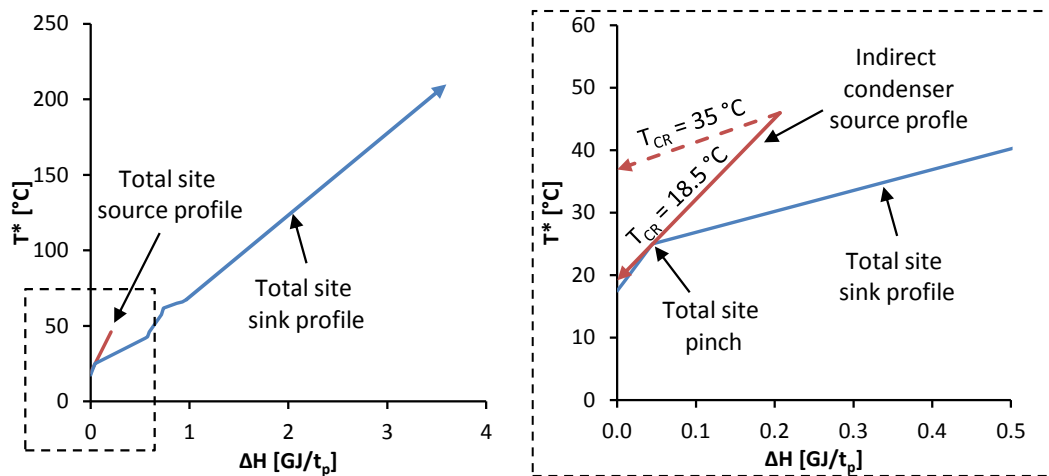


Figure 3-6: Total site profiles. Soft temperatures: exhaust air  $T_t$  is 55 °C, COW  $T_t$  is 13 °C, and condenser loop return  $T_t$  is 18.5 °C.

### 3.4.3. Modified stream data

In summary, the modified stream data of Table 3-1 are presented in Table 3-5. The return temperature of the condenser coupled loop is still a soft temperature that may be optimised later in the analysis. The individual evaporator effects streams have been excluded. The stream data is modified to combine the liquid COW streams into a single stream of a weighted average temperature. Treating the three COW streams as a stream results in a reduction of at least two heat exchangers when the minimum number of heat exchanger units is targeted. Preliminary targeting results further suggest that combining the COW streams has no effect on the energy targets or optimum selection of soft temperatures.

**Table 3-5: Modified process stream data. Soft data indicated using \*.**

Zone	Stream	Hot/ Cold	State	$T_s$ [°C]	$T_t$ [°C]	$\hat{C}$ [MJ/t <sub>p</sub> ·°C]	$\Delta H$ [MJ/t <sub>p</sub> ]
Evap.	Standardised milk	C	Liq.	8.0	63.4	42.7	-2362
Evap.	COW	H	Liq.	64.3	13.0	38.1	1954
Evap.	Condenser vapour (direct) <sup>#</sup>	H	Vap.	54.0	53.9		370
Evap.	Condenser liq. loop (indirect) <sup>#</sup>	H/C	Liq.	48.5 (18.5*)	18.5* (48.5)	12.3*	370
CIP	CIP hot water	C	Liq.	15.0	55.0	6.0	-238
Dryer	Milk concentrate	C	Liq.	54.0	65.0	6.0	-65
Dryer	Dryer inlet air	C	Gas	15.0	200.0	18.4	-3411
Dryer	FB inlet air (1)	C	Gas	15.0	49.0	1.6	-53
Dryer	FB inlet air (2)	C	Gas	15.0	45.0	2.3	-69
Dryer	FB inlet air (3)	C	Gas	15.0	32.0	1.7	-29
Dryer	Liquid loop from Exhaust air	H	Liq.	62.5	27.5*	14.7*	-513

<sup>#</sup>the condenser maybe directly or indirectly integrated into the process.

### 3.4.4. Inter- and Intra-zonal targets

Using the modified stream data of Table 3-5 heat recovery targets for the milk powder plant treated as a single zone or as three separate zones are reported in Table 3-6. Treating the problem as a single zone means heat can be transferred between any streams regardless of location. Whereas the zonal approach divides the plant into zones, in which intra-zonal heat recovery is maximised before inter-zonal heat exporting is considered. In addition, the target for the limiting case of  $\Delta T_{cont}$  (or  $\Delta T_{min}$ ) approaching zero is given.

Results suggest that by treating the powder plant as a single zone it is possible to achieve heat recovery of 2.837 GJ/t<sub>p</sub>, which is 72.3 % of the absolute maximum heat recovery 3.923 GJ/t<sub>p</sub>, which occurs when  $\Delta T_{min} \rightarrow 0$  °C. Without any inter-zonal integration, the total heat recovery targets are 2.653 GJ/t<sub>p</sub> for the case of direct condenser integration, and 2.630 GJ/t<sub>p</sub> for indirect condenser integration. If inter-zonal integration is allowed, after intra-zonal integration, between the evaporator and CIP zones, heat recovery can rise to 2.837 GJ/t<sub>p</sub>, with direct condenser integration, and 2.800 GJ/t<sub>p</sub>, with indirect condenser integration. A further 0.037 GJ/t<sub>p</sub> of heat recovery is possible when heat is exported from the evaporator zone to the dryer zone.

**Table 3-6: Inter- and intra-zonal heat recovery targets.**

Target or Zone	$T_{t,cow}$ [°C]	$T_{t,exh}$ [°C]	Intra-zonal $q_r$ [GJ/t <sub>p</sub> ]	Max. inter-zonal exports		
				To Evap [GJ/t <sub>p</sub> ]	To CIP [GJ/t <sub>p</sub> ]	To Dryer [GJ/t <sub>p</sub> ]
$\Delta T_{min} \rightarrow 0$ °C	8	36	3.923	-	-	-
<i>Totally integrated site</i>	13	55	2.837	-	-	-
Evaporator (condenser directly integrated)	13	-	2.140	-	0.184	0.184 (0.0)
CIP	-	-	0	0	-	0
Dryer	-	55	0.513	0	0	-
<i>Total Zonal 1</i>	13	55	2.653	0	0.184	0
Evaporator (condenser indirectly integrated)	13	-	2.117	-	0.170	0.206 (0.037)
CIP	-	-	0	0	-	0
Dryer	-	55	0.513	0	0	-
<i>Total Zonal 2</i>	13	55	2.630	0	0.170	0.037

## 3.5. Heat exchanger networks

### 3.5.1. Maximum energy recovery networks

Maximum Energy Recovery (MER) networks have been developed using standard pinch network design rules (Linnhoff and Hindmarsh, 1983). Figure 3-7 presents two options for direct condenser integration (MER A and B) and Figure 3-8 presents two options for indirect condenser integration (MER C and D). In developing the networks, priority was given to maximising intra-zonal heat recovery, before allowing inter-zonal integration. Guidance for this approach was provided by the intra- and inter-zonal heat recovery targets (Table 3-6). The options also present two methods for pre-heating the milk stream by using a stream split (MER A and C) or cyclic matching (MER B and D). As suggested in the grid diagram, the FB air streams enter the building together and there is opportunity to provide some heating while together.

The match between the COW and milk streams is critical for achieving the soft target temperature of 13 °C for the COW stream, which was shown during targeting to be essential for maximising heat recovery. Applying a stream split to the milk allowed for heat recovery from the condenser vapour to the milk stream

while still providing sufficient heat capacity flow to the milk/COW match for the COW stream to leave at 13 °C (MER A and C). A well-known alternative strategy for removing a stream split is to introduce a cyclic match (MER B and D).

After maximising heat recovery into the milk, the condenser vapour is matched to the CIP stream. For the indirect condenser integration options, any remaining heat in the condenser stream is matched with the combined fluidised bed air flows. The specific duty of this heat exchanger on the liquid coupled loop is low with only 0.037 GJ/t<sub>p</sub> and is unlikely to be economic in practice. Removing this heat exchanger and using the cold COW stream as a pseudo-cooling utility is one method for relaxing the networks with indirect condenser integration as shown in Figure 3-9. The relaxation incurs a 0.037 GJ/t<sub>p</sub> reduction in heat recovery.

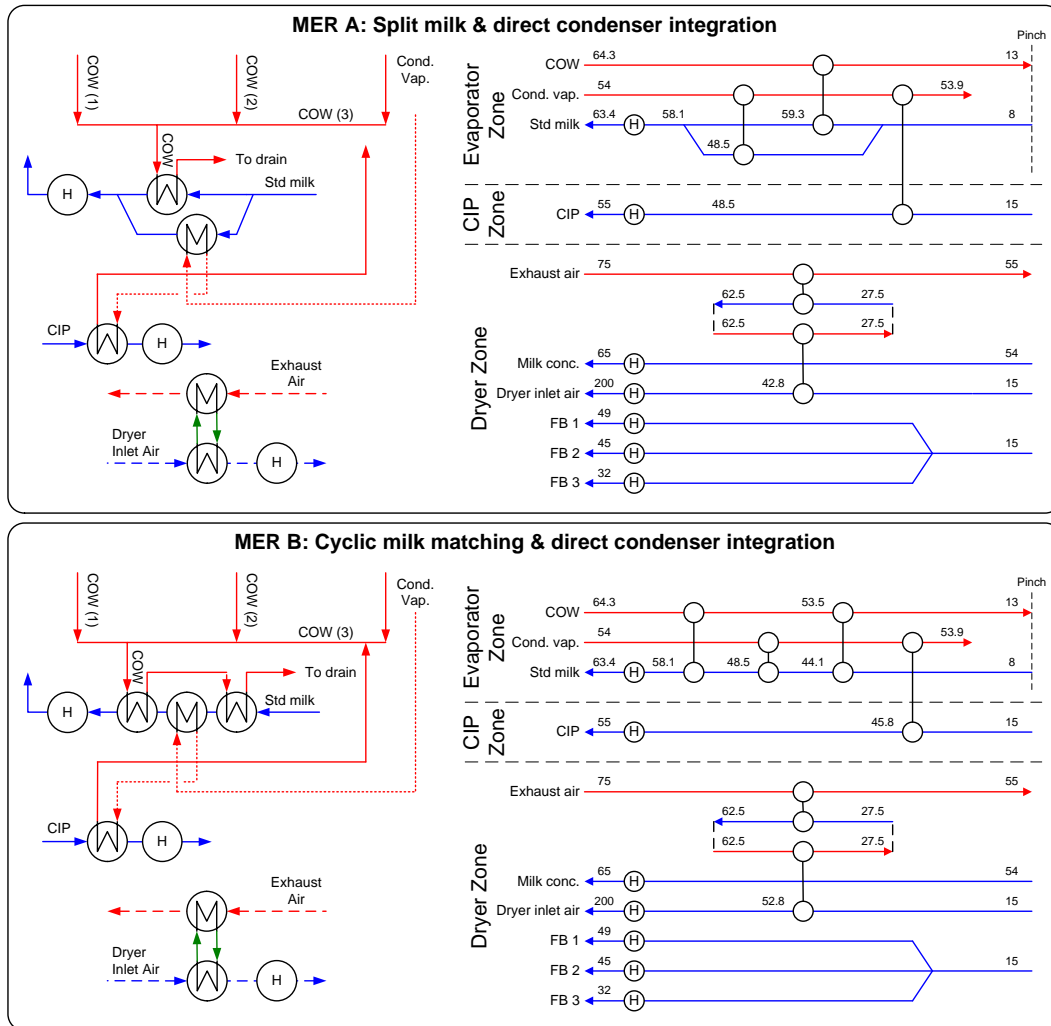


Figure 3-7: Heat exchanger network grid and flow diagrams for the milk powder plant with direct condenser integration.

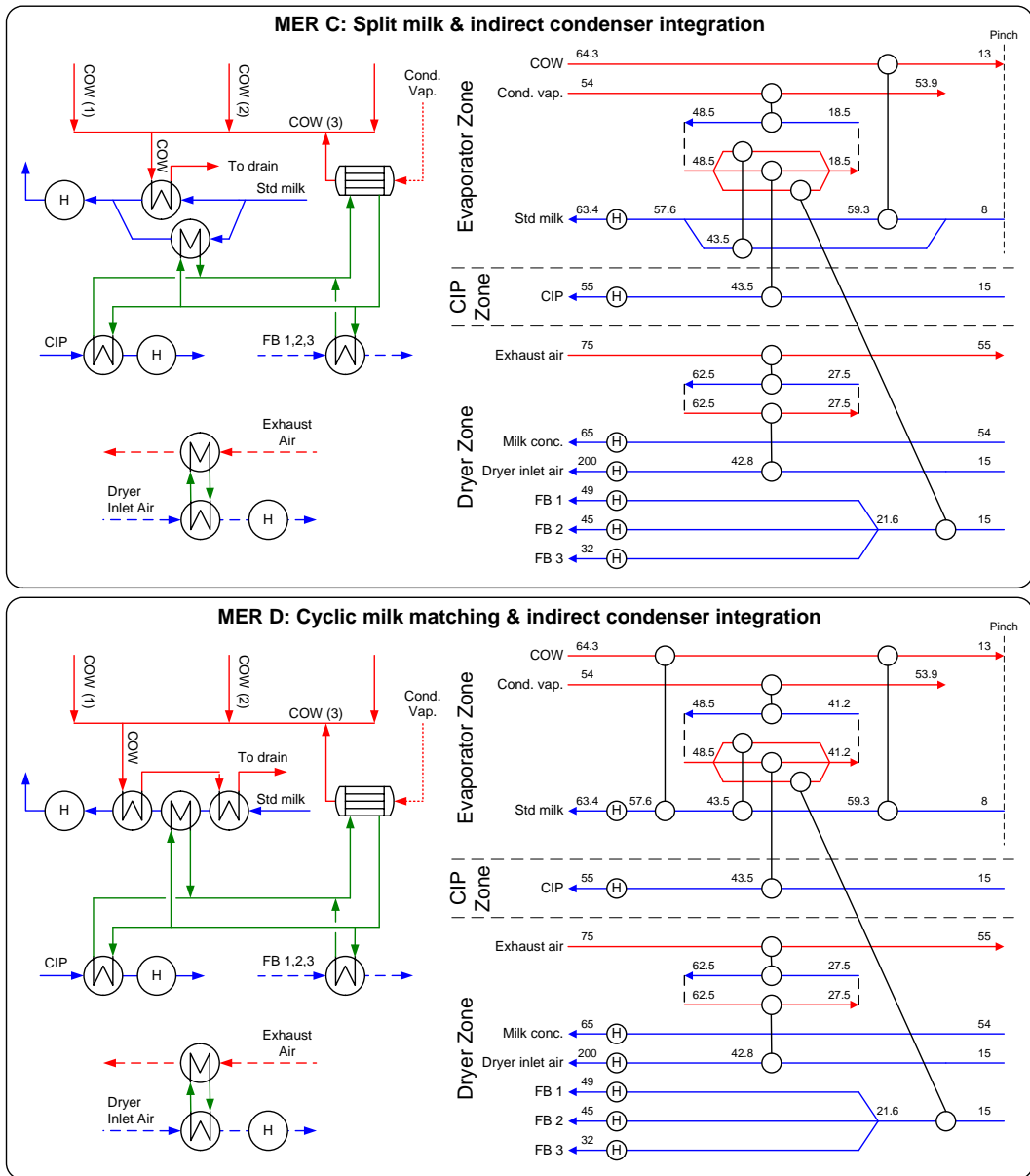
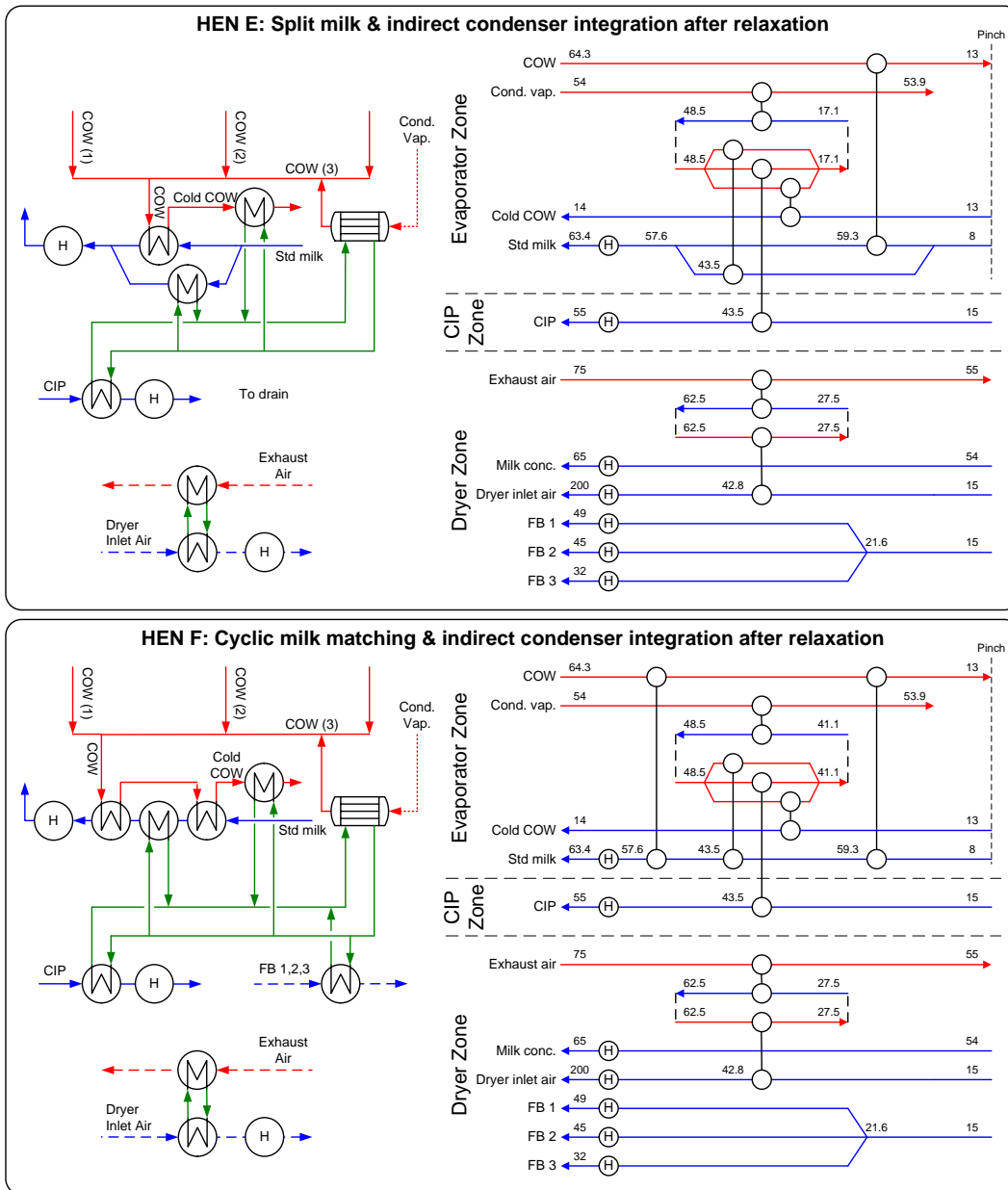


Figure 3-8: Heat exchanger network grid and flow diagrams for the milk powder plant with indirect condenser integration.



**Figure 3-9: Heat exchanger network grid and flow diagrams for the milk powder plant with indirect condenser integration after network relaxation.**

In the MER networks the exhaust air is always matched to the dryer inlet air. Figure 3-10 shows the possible sinks for heat recovery from the exhaust air, after integration of the evaporator and CIP zones (with direct integration of the condenser, and the exhaust air heat source). The best heat sink choice is naturally the dryer inlet air. A second option is to split the exhaust air heat to the dryer and FB air inlet streams, which option would maximise the temperature driving force, but is also capital intensive due to the additional heat exchanger unit(s) and additional ducting and the like.

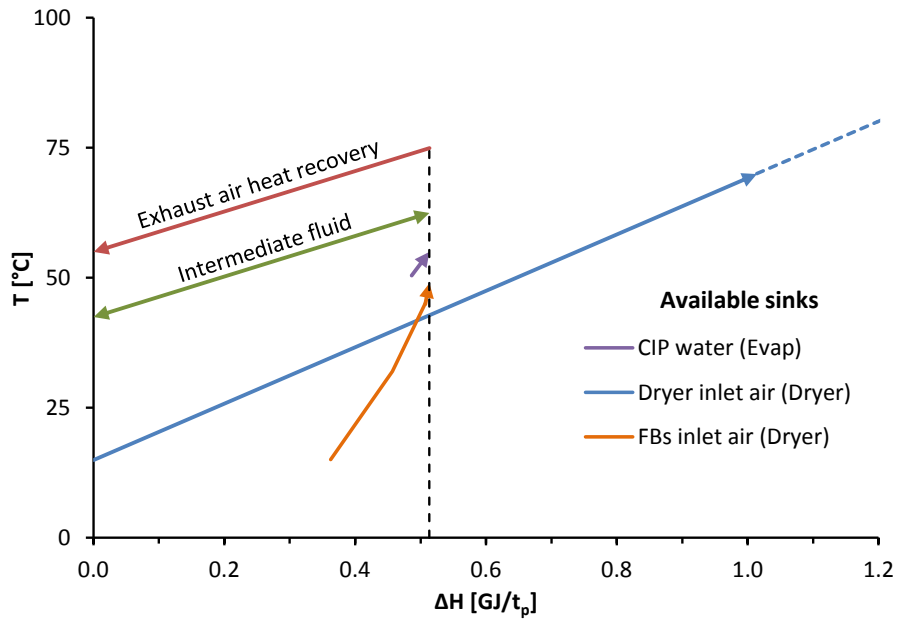


Figure 3-10: Heat sink options for indirect exhaust air heat recovery.

### 3.5.2. Costing and comparison to current industry practice

In the dairy industry there are two common methods for integrating the evaporator and spray dryer sections of the milk powder process (Figure 3-11). Older plants tend to employ Industry method A, whereas newer plants favour Industry method B due to its increased heat recovery. At face value Industry B may appear highly beneficial. However by preheating the inlet air, the temperature driving force for potential exhaust air heat recovery, which would give another step change in energy efficiency, is dramatically reduced and becomes less cost effective.

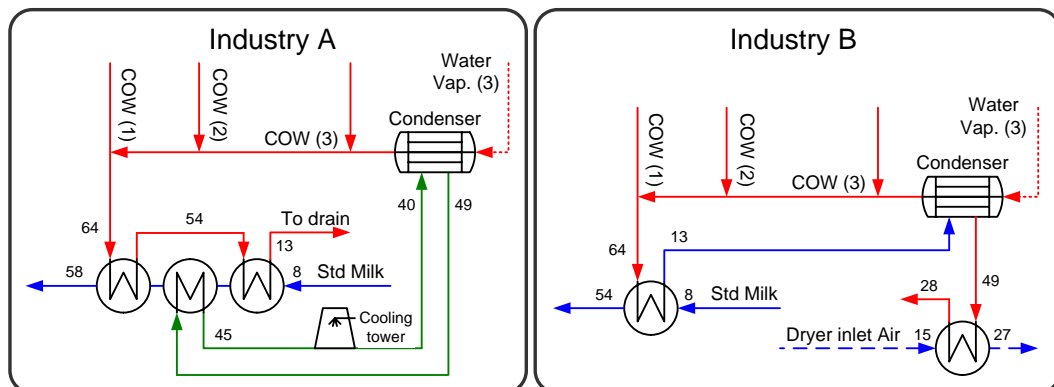


Figure 3-11: Schemes for evaporator zone integration including CIP water.

By applying the same minimum approach temperature difference, the overall heat recovery potential of industry practice is calculated and are compared in Table 3-7

to the MER networks that were developed. In addition, Table 3-7 includes calculation of the degree of heat integration, which is defined as

$$\eta_{HR} = \frac{Q_{r(act)}}{Q_r(\Delta T_{min} \rightarrow 0)} \quad (3-1)$$

where  $Q_{r(act)}$  is the actual heat recovery and  $Q_r(\Delta T_{min} \rightarrow 0)$  is the maximum possible heat recovery for a process (value given in Table 3-6). The degree of heat integration describes how close the heat recovery is to the thermodynamic limit. Using the cost data in Table 3-3 and the current utility prices, estimates for the annual utility, capital and total costs may be calculated and compared.

**Table 3-7: Comparison of proposed MER networks to current industry practice networks based on a dryer producing 23.5 t<sub>p</sub>/h.**

HEN Scheme	Heat exchanger units	Heat recovery [GJ/t <sub>p</sub> ]	Degree of integration $\eta_{HR}$	Total area [m <sup>2</sup> ]	Utility cost [\$ /t <sub>p</sub> ]	Capital cost [\$ /t <sub>p</sub> ]	Total cost [\$ /t <sub>p</sub> ]
MER A	12	2.837	72.3 %	8,692	42.37	9.92	52.29
MER B	13	2.837	72.3 %	8,224	42.37	9.28	51.65
MER C	14	2.837	72.3 %	9,071	42.37	10.53	52.90
MER D	15	2.837	72.3 %	8,883	42.37	10.06	52.43
HEN E	14	2.800	71.3 %	8,936	42.83	10.32	53.15
HEN F	15	2.800	71.3 %	8,750	42.83	9.86	52.69
Industry A	12	2.116	53.9 %	3,968	51.40	4.96	56.36
Industry B	10	2.171	55.3 %	4,600	50.67	5.66	56.33

In terms of heat recovery, implementing any one of the MER networks would increase specific heat recovery by 34 % over Industry A and 30 % over Industry B. Subsequently utility cost decrease, although at the expense of a rise in annual capital cost and an increase in the number of heat exchanger units. MER B, which is direct integration of the condenser and cyclic milk matching, achieves the lowest total cost, which is 9.1 % less than Industry A and 9.0 % less than Industry B. Removing the indirect match between the condenser and fluidised bed air streams in MER C and D reduced total cost, even though utility costs is slightly greater for the relaxed networks.

The degree of heat integration suggests there is significantly more heat recovery that can be gained from the process. An extra 0.190 GJ/t<sub>p</sub> of heat recovery can be

gained from applying a  $\Delta T_{min}$  of zero to the milk/COW match whereas the remaining heat recovery opportunity is tied up with the exhaust air stream, from which an additional 0.896 GJ/t<sub>p</sub> of heat recovery is possible with a  $\Delta T_{min}$  of zero. In this work, a limit of 55 °C on the outlet temperature of the exhaust air was imposed, which means only 0.513 GJ/t<sub>p</sub> of heat is recovered. It may be possible that the 55 °C limit may be lowered through a low fouling heat exchanger design to increase heat recovery.

### **3.5.3. Impact of proposed HENs on product quality**

It is well understood from the literature that liquid milk process streams have accelerated thermophile and microbial growth in the temperature range of 45 – 60 °C (Rademacher et al., 1995). A short residence time in this temperature range is therefore desirable for maintaining product quality over long operating cycles. Factors that increase microbial growth will lead to decreased product quality and/or require shorter run lengths, which is undesirable. The increased cleaning costs which can result from slightly increased microbial growth is very difficult to estimate. Microbial growth is often viewed as a barrier to increasing heat recovery for milk pre-heating or cooling. The integration scheme Industry method A uses heat recovery to pre-heat milk to 58 °C, which is not too dissimilar to the maximum temperature reached in the MER networks (59 °C). Further investigation into the effect of using increased heat recovery for pre-heating milk entering the evaporators on product quality is needed, although out of scope of this thesis.

## **3.6. Conclusion**

The milk powder process has a low pinch temperature (10.5 °C) and therefore any waste heat above 10.5 °C has available a sink stream for the heat to be placed. Heat exchanger networks have been developed that return the maximum energy recovery targets for industrial milk powder production. Comparison to industrial practice has shown that there is potential to economically increase specific heat recovery by at least 30 % with a specific cost improvement of about 9 % for the most energy efficient HENs in New Zealand milk powder plants. Spray dryer exhaust air heat recovery is necessary to achieve maximum energy recovery and

should be matched to preheat the dryer inlet air stream. Heat exchangers are sized based on typical values of  $\Delta T_{cont}$ . HEN solutions may be improved by optimising the HEN area allocation so that total annual cost is minimised.

# Chapter 4

## Cost optimal area allocation in milk powder plant HENs

---

### 4.1. Introduction

A key element of PA is the concept of a minimum approach temperature,  $\Delta T_{min}$  (or  $\Delta T_{cont}$ ). The  $\Delta T_{min}$  concept, in conjunction with the composite curve diagram, enables heat recovery and utility targets to be set, pinch temperatures to be identified, and effective HENs to be designed. This was demonstrated in Chapter 3 for the milk powder plant. However this strength of PA can also be a weakness. The  $\Delta T_{min}$  constraint for nearly all problems results in non-cost optimal HEN area allocation due to often substantial differences in utility costs, stream heat transfer film coefficients, Heat Exchanger (HE) types and flow arrangements, HE capital costs, and approach temperatures. To an extent the  $\Delta T$  contribution concept for individual streams, in place of a global  $\Delta T_{min}$ , was developed to account for large differences in film coefficients, although optimal area allocation is not ensured by this method. Simple methods for  $\Delta T_{min}$  relaxation through dual minimum approach temperatures, where one  $\Delta T_{min}$  is selected for heat recovery targeting and the other  $\Delta T_{min}$  is applied to individual exchangers, have also been proposed (Shenoy, 1995). In addition, the literature also contains pure computer programming based optimisation techniques but lacks a fundamental and generalised equation based method for optimising the area allocation within HEN structures.

The contribution of this chapter is the development a novel method for cost-optimal area allocation within a HEN structure. The method is applied to the MER networks for evaporator/CIP zones of the milk powder plant to obtain cost optimal area allocation, and is named the Cost Derivative Method (CDM). The intention is for this method to be applied after HEN structures are developed by PDM or some other approach. The approach attempts to add, remove and shift area to recovery

exchangers (RE) where the greatest cost benefit is returned. Effectiveness–number of transfer units relationships for sizing exchangers (Kays and London, 1998) forms an essential part of the method. The CDM method is currently only applicable to direct heat integration networks (MER A and B, Figure 3-7, from Chapter 3) and, therefore, cannot be applied to the liquid coupled loop HE system that is proposed to recover heat from the spray dryer exhaust. As a result the spray dryer zone is left out of the CDM optimisation. In addition to the milk powder plant, the new method is also applied to one literature non-diary case study to demonstrate its effectiveness.

## **4.2. Derivation of the Cost Derivative Method for cost optimal area allocation**

This section presents the derivation of fundamental equations that may be applied to a HEN to optimally allocate HE area (and duty) so that the total annual cost of the system is minimised. The scope of the derivation includes both utility and capital cost but ignores pumping and piping costs. The intention is for this method to be applied to a HEN during the design stage. Significant structural change to the heat recovery side of the HEN is not considered.

Necessary conditions for optimal area allocation are derived by focusing on how incrementally adding area to a single HE affects Total annual Cost ( $TC$ ). The overall goal is to identify which HEs can economically afford more area, whereas other HEs may need to reduce in area because the heat recovery cost savings are insufficient to justify the capital expenditure. A challenge in this approach is to accurately account for the several flow-on effects that occur from changing the area of one HE in a network.

### **4.2.1. Derivative of a HEs total cost function**

Consider the design of a large HEN containing several Recovery Exchangers (RE) and Utility Exchangers (UE) where  $RE_1$  is the match between hot stream “x” and cold stream “y”.

The total annual cost,  $TC$ , of the HEN, ignoring piping and pumping costs, is

$$TC = CC_{RE} + CC_{ut} + UC \quad (4-1)$$

where  $CC$  is the annualised capital cost, and subscript  $ut$  refers to utility. Each cost component is comprised of fixed and variable costs. If the area,  $A$ , of  $RE_1$  is increased by  $\Delta A$ , then the resulting change in total annual cost, i.e.  $\Delta TC$ , is

$$\Delta TC = \Delta CC_1 + \sum \Delta CC_{ut} - \sum \Delta S_{ut} \quad (4-2)$$

where  $S$  is the annual utility savings due to heat recovery and subscript 1 refers to the stream match between streams  $x$  and  $y$ .

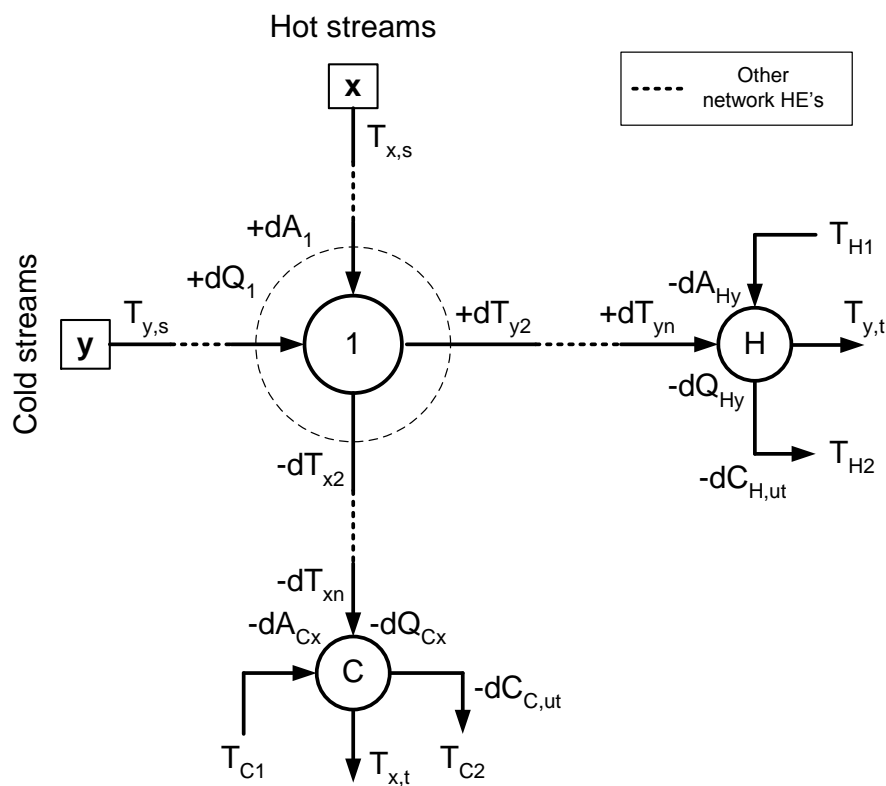


Figure 4-1: Impact of increasing the area of recovery exchanger 1 by  $dA$ .

Figure 4-1 illustrates the effects of increasing the area of  $RE_1$  by a very small amount, i.e.  $dA$ , on the exit temperatures from  $RE_1$ , which propagates to downstream REs. As the change in stream temperatures,  $dT_{y2}$  and  $dT_{x2}$ , flows on to the next network RE, it affects the REs duty and outlet temperatures. Eventually the change temperature propagates to a UE affecting is required utility load and design area.

After dividing by  $dA_1$  and converting to derivative form, Eq. 4-2 is rewritten

$$\frac{dTTC}{dA_1} = \frac{dCC_1}{dA_1} + \sum \frac{dCC_{ut(i)}}{dA_1} - \sum \frac{dS_{ut(i)}}{dA_1} \quad (4-3)$$

By setting  $dTTC/dA_1$  to zero the cost “optimum” area for  $RE_1$  may be solved. To find the solution to Eq. 4-3 each differential element is now analysed.

The incremental annualised heat recovery savings in Eq. 4-3 is the product of the annual utility price,  $p$ , ( $\$/kW \cdot y$ ) and the change in utility consumption,  $dQ_{ut(i)}$ ,

$$\sum \frac{dS_{ut(i)}}{dA_1} = \sum \left( -p_{ut(i)} \frac{dQ_{ut(i)}}{dA_1} \right), \text{ where } p_{ut} = \hat{p}_{ut} t \quad (4-4)$$

In Eq. 4-4,  $\hat{p}$  is the specific utility price ( $\$/kWh$ ) and  $t$  is the plant production hours per year (h/y). After applying the chain rule to  $dQ_{ut(i)}/dA_1$  and recognising that the new term  $dQ_1/dA_1$  is the constant for all UEs, Eq. 4-4 becomes

$$\sum \frac{dS_{ut(i)}}{dA_1} = \frac{dQ_1}{dA_1} \sum \left( -p_{ut(i)} \frac{dQ_{ut(i)}}{dQ_1} \right) \quad (4-5)$$

We may choose to (newly) define the heat duty flow-on factor,  $\theta$ , as the ratio of the reduction in duty of  $UE_i$  to the increase in duty of  $RE_1$ ,

$$\theta_1^{ut(i)} \equiv \frac{-dQ_{ut(i)}}{dQ_1} \quad (4-6)$$

The negative sign in Eq. 4-6 is included so that positive values for  $\theta$  represent an increase in heat recovery and a reduction in utility use. Substituting Eq. 4-6 into 4-5 gives

$$\sum \frac{dS_{ut}}{dA_1} = \frac{dQ_1}{dA_1} \sum (p_{ut(i)} \theta_1^{ut(i)}) \quad (4-7)$$

The other derivative terms in Eq. 4-3 are related to capital cost. The general annualised HE capital cost formula is

$$CC = FC + bA^n \quad (4-8)$$

where  $FC$  is a fixed cost,  $b$  is a positive constant and  $n$  is a positive constant less than unity. In the context of this study coefficients  $FC$  and  $b$  are annualised to take into account the time value of money. Taking the derivative of Eq. 4-8 with respect to area gives

$$\frac{dCC}{dA} = bnA^{n-1} \quad (4-9)$$

Eq. 4-9 may be applied directly to the RE capital cost component in Eq. 4-3. However, to apply Eq. 4-9 to the UE capital cost component requires application of the chain rule, as presented in Eq. 4-10, since  $dA_1 \neq dA_{ut(i)}$ .

$$\sum \frac{dCC_{ut(i)}}{dA_1} = \sum \left( \frac{dCC_{ut(i)}}{dA_{ut(i)}} \cdot \frac{dA_{ut(i)}}{dQ_{ut(i)}} \cdot \frac{dQ_{ut(i)}}{dQ_1} \cdot \frac{dQ_1}{dA_1} \right) \quad (4-10)$$

Eq. 4-11 is obtained by substituting Eq. 4-6 and 9 into Eq. 4-10 and once again recognising that  $dQ_1/dA_1$  is the same for all UEs.

$$\sum \frac{dCC_{ut(i)}}{dA_1} = -\frac{dQ_1}{dA_1} \sum \left( \frac{(bnA^{n-1})_{ut(i)} \theta_1^{ut(i)}}{dQ_{ut(i)}/dA_{ut(i)}} \right) \quad (4-11)$$

Each component of Eq. 4-3 has now been analysed. Substituting Eq. 4-7, 9, and 11 into Eq. 4-3 and simplifying gives

$$\frac{dTC}{dA_1} = (bnA^{n-1})_1 - \frac{dQ_1}{dA_1} \sum \left( \theta_1^{ut(i)} \left( p_{ut(i)} + \frac{(bnA^{n-1})_{ut(i)}}{dQ_{ut(i)}/dA_{ut(i)}} \right) \right) \quad (4-12)$$

By setting  $dTC/dA$  to zero and rearranging, Eq. 4-12 becomes

$$(bnA^{n-1})_1 = \frac{dQ_1}{dA_1} \sum \left( \theta_1^{ut(i)} \left( p_{ut(i)} + \frac{(bnA^{n-1})_{ut(i)}}{dQ_{ut(i)}/dA_{ut(i)}} \right) \right) \quad (4-13)$$

Eq. 4-13 represents the cost to savings trade-off where the left hand side is the incremental RE capital cost and the right hand side is the incremental heat recovery and UE capital savings. Three elements in Eq. 4-13 that need further analysis to be able to solve for area are: (1)  $dQ_1/dA_1$ , (2)  $dQ_{ut(i)}/dA_{ut(i)}$  and (3)  $\theta$ .

## 4.2.2. Analysis of $dQ/dA$ for HEs

### 4.2.2.1. Case 1: Heat recovery exchangers

When area is added to a heat recovery exchanger, the duty increases and the outlet temperatures change, whereas the stream flow rates are constant. The expression for  $dQ/dA$  is obtained by substituting the definitions for  $Q$  and  $A$  from the  $\epsilon$ -NTU design method (Kays and London, 1998) while assuming the overall heat transfer coefficient ( $U$ ), the difference in inlet temperature of the streams ( $\Delta T_{max}$ ) and the flow rates of the streams, are unaffected by the additional area. As a result Eq. 4-14 is obtained.

$$\frac{dQ}{dA} = U\Delta T_{max} \frac{d\epsilon}{dNTU} \quad (4-14)$$

The term  $d\epsilon/dNTU$  is specific to a HE flow arrangement. The derivative of the counterflow  $\epsilon$ -NTU relationship is

$$\frac{d\epsilon}{dNTU} = (1 - \epsilon)(1 - \epsilon C^*), \quad [0 \leq C^* \leq 1] \quad (4-15)$$

### 4.2.2.2. Case 2: Utility heat exchangers

The second case of  $dQ/dA$  is for UEs where a change in inlet temperature of a process stream affects the required utility duty, utility flow rate and exchanger area. For a UE, the outlet temperature of the process stream is typically a fixed (target) temperature and the inlet and outlet temperatures of the utility are also fixed. In cases where a target temperature is soft, the temperature provides a degree of freedom in defining the problem. It's important to note that the derivation (presented in Appendix C) uses temperature effectiveness,  $P$ , in place of effectiveness,  $\epsilon$ , because the stream with  $C_{min}$  is not always obvious. P-NTU relationships are the same as  $\epsilon$ -NTU relationships. The  $dQ/dA$  expression for utility exchangers is

$$\frac{dQ}{dA} = \frac{U\Delta T_{max}}{1 - P_p} \frac{dP_p}{dNTU_p}, \quad \text{where} \quad P_p = \frac{\Delta T_p}{\Delta T_{max}}, \quad R_p = \frac{C_p}{C_{ut}} \quad (4-16)$$

The counterflow solution for  $dP_p/dNTU_p$  is

$$\frac{dP_p}{dNTU_p} = \frac{P_p(1-P_p)(1-R_p)}{\frac{P_p}{1-P_p R_p} - \frac{R_p}{1-R_p} \ln \left| \frac{1-P_p R_p}{1-P_p} \right|}, \quad [0 \leq R_p \neq 1] \quad (4-17a)$$

$$\frac{dP_p}{dNTU_p} = (1-P_p)^2, \quad [R_p = 1] \quad (4-17b)$$

### 4.2.3. Heat duty flow-on factor

#### 4.2.3.1. Origin, propagation and termination of the heat duty flow-on effect

The heat duty flow-on factor,  $\theta$ , as defined in Eq. 4-6 needs to be determined to find the minimum total annual cost solution of a network. In this section, a derivation based on the  $\epsilon$ -NTU (and P-NTU) method is presented to demonstrate how network specific equations for  $\theta$  may be quickly formulated.

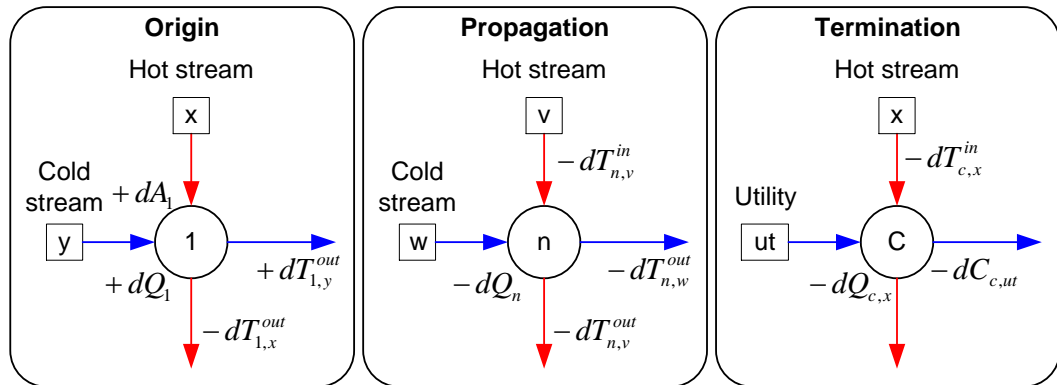


Figure 4-2: Analysis of heat duty flow-on through HENs.

#### Origin of heat duty flow-on “effect”

When  $dA$  is added to  $RE_1$ , the change in outlet temperature of hot stream  $x$  (Eq. 4-18a) and cold stream  $y$  (Eq. 4-18b) are

$$dT_{1,x}^{out} = -\frac{dQ_1}{C_x}, \quad x \in \text{hot streams} \quad (4-18a)$$

$$dT_{1,y}^{out} = \frac{dQ_1}{C_y}, \quad y \in \text{cold streams} \quad (4-18b)$$

The change in outlet temperature of streams x and y from RE<sub>1</sub> propagates through the network affecting the inlet temperatures to and duties of downstream recovery exchangers.

### Heat duty flow-on through downstream heat recovery exchangers

Now consider recovery exchanger n, RE<sub>n</sub>, that is positioned at the intersection of two other streams, v and w, which is downstream of RE<sub>1</sub> and illustrated in Figure 4-2. It is important to note that the change in inlet temperature for stream v is  $dT_{n,v}$ , whereas for stream w the change in inlet temperature,  $dT_{n,w}$ , is zero.

The total duty of RE<sub>n</sub> is

$$Q_n = (\varepsilon C_{\min} \Delta T_{\max})_n \quad (4-19)$$

The derivative of Eq. 4-19 with respect to temperature, recognising  $\varepsilon$  and  $C_{\min}$  are constants, is

$$dQ_n = (\varepsilon C_{\min})_n dT_{n,v}^{in}, \quad \text{where } dT_{n,v}^{in} = d(\Delta T_{\max}) \quad (4-20)$$

The change inlet and outlet temperatures of stream v to/from RE<sub>n</sub> are related by energy balance

$$dT_{n,v}^{out} = dT_{n,v}^{in} - \frac{dQ_n}{C_v} \quad (4-21)$$

Substituting Eq. 4-20 into Eq. 4-21 and simplifying gives

$$dT_{n,v}^{out} = dT_{n,v}^{in} (1 - P_{n,v}), \quad \text{where } P_{n,v} = \frac{(\varepsilon C_{\min})_n}{C_v} \quad (4-22)$$

Using temperature effectiveness,  $P$ , in the above equation enables useful simplification. Eq. 4-22 may be modified to account for stream splits. Consider if stream v is split into  $i$  number of streams and each branch passes through RE<sub>n1</sub>, ..., RE<sub>ni</sub>, then the change in temperature before and after the stream split is

$$dT_{n,v}^{out} = dT_{n,v}^{in} - \frac{1}{C_v} \sum_{i_0=1}^i dQ_{n(i)} \quad (4-23)$$

By substituting Eq. 4-20 into Eq. 4-23 and simplifying gives

$$dT_{n,v}^{out} = dT_{n,v}^{in} \left( 1 - \sum_{i_0=1}^i \beta_{v(i)} P_{n,v(i)} \right), \quad \text{where } P_{n,v(i)} = \frac{(\varepsilon C_{\min})_{n(i)}}{C_{v(i)}}, \quad \beta_{v(i)} \equiv \frac{C_{v(i)}}{C_v} \quad (4-24)$$

In Eq. 4-24,  $\beta$  is the split fraction. Eq. 4-24 is correct for splits on either hot or cold streams.

The next part of the analysis focuses on how the outlet temperature of stream w is affected (Figure 4-2). The energy balance for stream w is

$$dT_{n,w}^{out} = dT_{n,w}^{in} + \frac{dQ_n}{C_w} \quad (4-25)$$

Since  $dT_{n,w}^{in}$  is nil, then substituting Eq. 4-20 into Eq. 4-25 simplifies to

$$dT_{n,w}^{out} = dT_{n,v}^{in} P_{n,w}, \quad \text{where } P_{n,w} = \frac{(\varepsilon C_{\min})_n}{C_w} \quad (4-26)$$

It is important to note that the values of  $P_{n,v}$  and  $P_{n,w}$  always fall between zero and one, which implies that the heat duty and temperature flow-on effects from RE<sub>1</sub> are dampened as the change in temperature propagates through the HEN.

### Termination of heat duty flow-on effect

Eventually the change in exchanger duties and temperatures propagates to a UE (if required), where utility stream flow rates are adjusted to ensure the process stream's target temperature is achieved (Figure 4-2). Changes in heat duty from RE<sub>1</sub> may propagate along multiple different downstream paths to the same UE. Each flow-on path may be treated independently and summed to find the combined effect on utility use. We now consider how the change in inlet temperatures to the UEs on streams x and y affect its duty, assuming these  $dT$ 's are caused by  $j$  number of flow-on paths. The change in utility duty for the heater and cooler may be expressed as

$$dQ_{c,x} = C_x \sum_{j_0=1}^j dT_{c,x(j)}^{in}, \quad x \in \text{hot streams} \quad (4-27a)$$

$$dQ_{h,y} = -C_y \sum_{j_0=1}^j dT_{h,y(j)}^{in}, \quad y \in \text{cold streams} \quad (4-27b)$$

### Steps for deriving complete heat duty flow-on factor equations

Eq. 4-18, 24, 26 and 27 provide a framework to construct formulas for individual heat duty flow-on factors for a RE/UE match. The steps for constructing equations for  $\theta$  are:

1. Identify flow-on pathways between selected RE<sub>n</sub> (origin) and UE<sub>ut</sub> (termination)
2. For one pathway, write the energy balance for UE<sub>ut</sub> using Eq. 4-27
3. Move toward the RE using flow-on pathway by substituting in Eq. 4-24 or 26 for  $dT$
4. Once the RE is reached, apply Eq. 4-18 for RE<sub>n</sub>.
5. Rearrange to form an equation for  $\theta$  as defined in Eq. 4-6 for the flow-on path.
6. If applicable, repeat steps 2 – 5 for other flow-on pathways
7. Sum equations for the different pathways to find  $\theta$ .

Examples of constructing equations for  $\theta$  are provided in Appendix C.

#### 4.2.3.2. General principles for finding the heat duty flow-on factor

The general formulas presented in previous section are the foundation for finding heat duty flow-on factors. In addition to these equations, there are a few general principles that are useful for forming equations for the heat duty flow-on factor and implementing the factor as part of a computer program.

The generalised formula for a heat duty flow-on factor is

$$\theta_n^{ut} = \frac{-dQ_{ut}}{dQ_n} = \pm \sum \left( \frac{C_{ut,p(i)}}{C_{n,s(i)}} G_i \right) \quad (4-28)$$

where subscript  $ut,p$  refers to the process stream being cooled/heated by utility,  $n,s$  refers initial stream that the heat duty flow-on effect is propagated along, and  $i$  refers to the selected heat duty flow-on pathway. Function  $G$  is used to describe the heat duty flow-on effect along a pathway with an unspecified number and arrangement of REs such that

$$dT_{G_i}^{out} = G_i dT_{G_i}^{in}, \quad \text{where } G_i = \Pi(P_j, 1 - P_j) \quad (4-29)$$

For the general case, the inlet temperature to  $G$  is from  $RE_n$ , i.e. the RE where  $dA$  is added, and the outlet temperature from  $G$  is the inlet temperature of the process stream to  $UE_{ut}$ .

Heat duty flow-on factors for a single pathway may be positive or negative. This sign may be determined using the rules in Table 4-1. For example, if the heat duty flow-on effect is propagated from the origin RE along a hot stream to a hot utility, then the sign of heat duty flow-on factor is negative, i.e. utility increases.

**Table 4-1: Sign of heat duty flow-on factor. Positive is increased heat recovery, negative is increased utility use.**

	Hot stream (origin RE)	Cold stream (origin RE)
Hot utility	-	+
Cold utility	+	-

The heat duty flow-on factor of  $RE_1$  often has common flow-on pathways with other REs to some downstream  $UE_{ut}$  as illustrated in Figure 4-3.

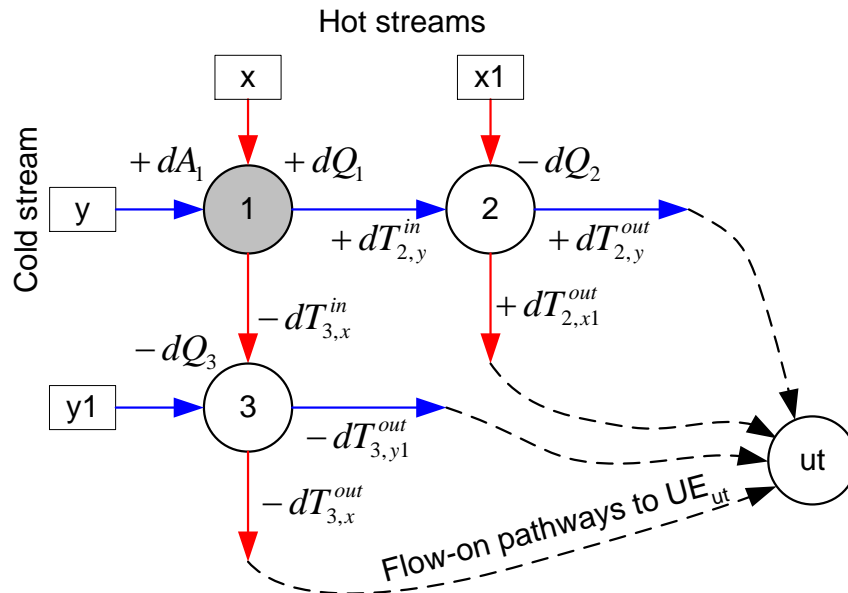


**Figure 4-3: Heat duty flow-on pathways.**

In general, the heat duty flow-on factor for  $RE_1$  to  $UE_{ut}$  is

$$\theta_1^{ut} = \theta_{1(x)}^{ut} + \theta_{1(y)}^{ut} \quad (4-30)$$

which is the sum of the heat duty flow-on effects along streams x and y. The heat duty flow-on factor for pathways along streams x and y may be related to the heat duty flow-on factors for downstream REs 2 and 3.

$$\theta_{1(x)}^{ut} = \left( 1 - \sum_{i_0=1}^i \beta_{x(i)} P_{3,x(i)} \right) \theta_{3(x)}^{ut} - P_{3,y1} \theta_{3(y1)}^{ut}, \quad \text{where } \theta_3^{ut} = \theta_{3(x)}^{ut} + \theta_{3(y1)}^{ut} \quad (4-31a)$$

$$\theta_{1(y)}^{ut} = \left( 1 - \sum_{i_0=1}^i \beta_{y(i)} P_{2,y(i)} \right) \theta_{2(y)}^{ut} - P_{2,x1} \theta_{2(x1)}^{ut}, \quad \text{where } \theta_2^{ut} = \theta_{2(y)}^{ut} + \theta_{2(x1)}^{ut} \quad (4-31b)$$

Relating the heat duty flow-on factor of RE<sub>1</sub> to the heat duty flow-on factor of downstream REs 2 and 3 (Figure 4-3) is very useful from a practical computer programming implementation point of view. By effective use of these equations, one may eliminate the need to derive complete heat duty flow-on factor equations from every RE to every UE in a network. Proofs for Eq. 4-31a and b are provided in Appendix C.

#### 4.2.3.3. Heat duty flow-on for closed loops – a special case

The idea of heat loops in a HEN is a well-known PA concept. In many cases it is advantageous to break a heat loop to reduce the number of HE units often as a trade-off for reduced heat recovery. Figure 4-4 is a schematic of two simple HENs that contain a non-self-interacting loop (i.e. open loop) (a) and a self-interacting loop (i.e. closed loop) (b). Arrows are included to highlight the important heat duty flow-on pathways.

Figure 4-4 illustrates the differences between an open loop and closed loop in the context of a HEN. In Figure 4-4a, the heat duty flow-on effects do not interact with itself whereas in Figure 4-4b the heat loop interacts with itself. In a so-called closed heat loop, adding dA to one of the REs affects at least one of the inlet temperatures to the same RE. Self-interacting closed heat loops presents an interesting challenge for determining an exact equation for the heat duty flow-on factor. In addition, interacting loops also presents a significant process control issue due to the closed loop feedback that occurs for disturbances in temperature or flow rate in any RE forming the loop.

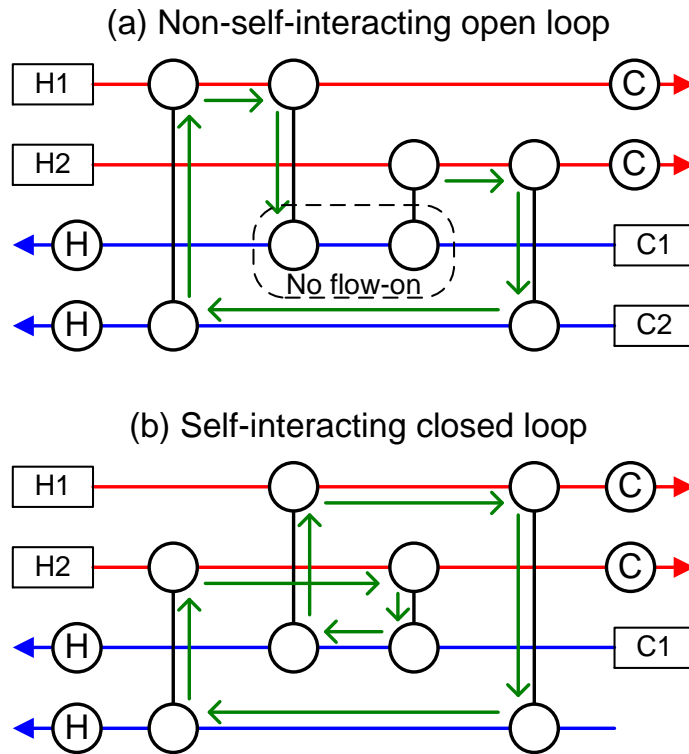


Figure 4-4: Non-self-interacting open heat loops (a) and self-interacting closed heat loops (b).

For the closed loop situation, it is necessary to clarify the definition of the heat duty flow-on factor, i.e. the ratio of  $dQ_{ut}$  to  $dQ_1$ . Normally when  $dQ_1$  is calculated the  $dQ$  solely occurs due the increase in area and HE effectiveness. However, when there is a closed heat loop, the heat duty change flows around the loop affecting the inlet temperature to  $RE_1$ , which implies

$$dQ_1 = dQ_{1(eff)} + \varepsilon_1 C_{\min,1} d(\Delta T_{\max,1}), \quad \text{where } dQ_{1(eff)} = C_{\min,1} \Delta T_{\max,1} d\varepsilon_1 \quad (4-32)$$

One portion of  $dQ_1$  is directly attributed to the change in HE effectiveness, whereas the second portion of  $dQ_1$  is due to the change in an inlet temperature to  $RE_1$ . To be consistent with the previous cost derivatives, the heat duty flow one factor for closed loops is based on  $dQ_{1(eff)}$ , i.e.  $-dQ_{ut}/dQ_{1(eff)}$ , rather than the actual  $dQ$  for  $RE_1$ .

Figure 4-5 presents four generalised HEN cases where the heat duty flow-on factor is affected by a closed heat loop. For each case in Figure 4-5,  $dA$  is added to  $RE_1$ , which is the match between streams  $s$  and  $t$ . Streams  $s$  and  $t$  are labelled so that the heat duty flow-on effect primarily flows along stream  $s$  to  $UE_{ut}$ . Circles in Figure 4-5 represent individual HEs whereas rectangular boxes represent a

function  $G$  that describes the heat duty flow-on effect through an unspecified number and arrangement of REs (Eq. 4-29). Table 4-2 presents the generalised heat duty flow-on factors relating to the four situations outlined in Figure 4-5. The derivations of these equations are presented in Appendix C.

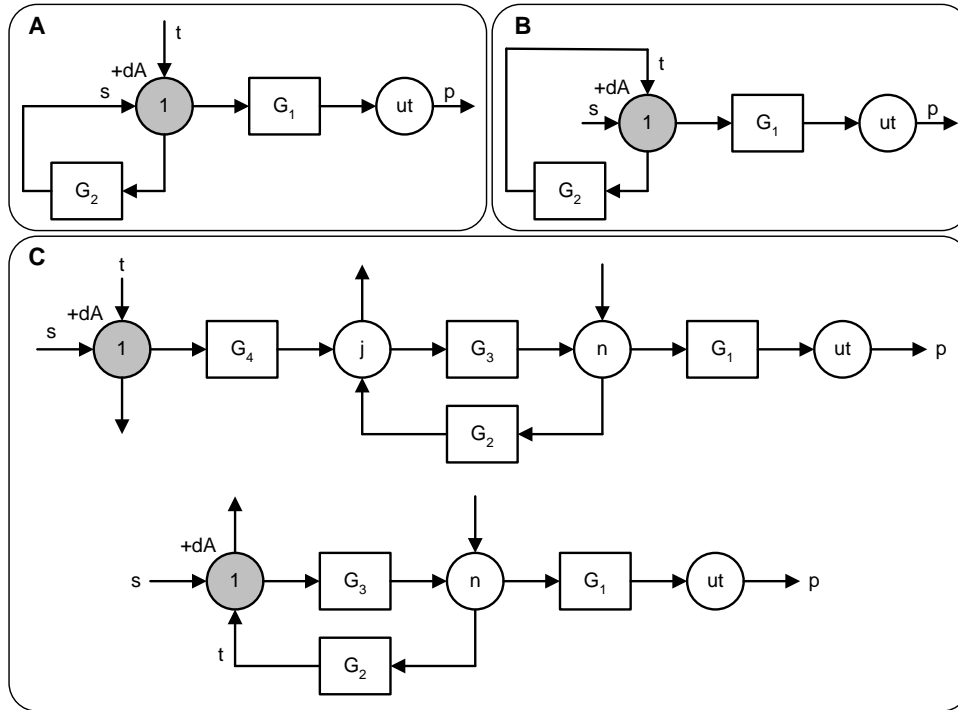


Figure 4-5: Heat duty flow-on in three general self-interacting closed heat loops.

Table 4-2: General formulas for heat duty flow-on factors in interacting closed heat loops where  $G_L$  is the function describing the closed loop and  $G_{OL}$  is the function describing the open loop. Refer to Appendix C for examples.

Position of RE <sub>1</sub>	General Formula
(A) "Corner" of a closed loop	$\theta_1^{ut} = \pm \frac{C_{ut,p}}{C_{1,s}} G_1 \left( \frac{P_{1,s} - G_L}{P_{1,s}(1 - G_L)} \right) \quad (4-33)$
(B) "Edge" of a closed loop	$\theta_1^{ut} = \pm \frac{C_{ut,p}}{C_{1,s}} G_1 \left( \frac{(1 - P_{1,t}) - G_L}{(1 - P_{1,t})(1 - G_L)} \right) \quad (4-34)$
(C) Upstream or in other positions of a closed loop	$\theta_1^{ut} = \pm \frac{C_{ut,p}}{C_{1,s}} \frac{G_{OL}}{1 - G_L} \quad (4-35)$

It is interesting to note that Eq. 4-35 bears some resemblance to the general formula for closed loop transfer functions in process control. The ratio of heat capacities at the front of the equation is analogous to a proportionality constant.

In process control the numerator is the closed loop function and the denominator is one plus the open loop function.

The term  $1 - G_L$  appears on the denominator of all three generalised equations in Table 4-2. Since  $G_L$  must be a positive value less than unity, it is deduced that the presence of the closed heat loop tends to amplify the heat duty flow-on factor. It maybe, therefore, possible to find a situation where an individual heat duty flow-on factor is greater than one, although the sum of individual heat duty flow-on factors to all heaters or coolers must collectively be less than one.

#### 4.2.3.4. Overall heat duty flow-on factor

It is useful to define the overall heat duty flow-on factor,  $\theta$ ,

$$\theta_1 \equiv \sum \theta_1^{h(i)} = \sum \theta_1^{c(i)} \quad (4-36)$$

where subscript 1 refers to the RE and superscripts  $h$  and  $c$  refer to the heaters and coolers. Using Figure 4-3, the overall heat duty flow-on factor may be also described in terms of downstream flow-on factors,

$$\theta_1 = 1 - \sum_{i_0=1}^i (\beta_{y(i)} P_{2,y(i)} \theta_{2(i)}) - \sum_{j_0=1}^j (\beta_{x(j)} P_{3,x(j)} \theta_{3(j)}) \quad (4-37)$$

The derivation of Eq. 4-37 is presented in Appendix C.

Two important properties of the heat duty flow-on factor are:

- (1) The heat duty flow-on factor is nearly always independent of the area of the RE where heat duty flow-on effect originates, i.e.  $RE_n$ .
- (2) The overall heat duty flow-on factor has the limits of -1 and 1 where negative overall heat duty flow-on factors indicate that a stream match is actually detrimental to network heat recovery.

Since  $\theta$  for  $RE_n$  is nearly always independent of the area of  $RE_n$ , i.e. its own area, it follows that the heat recovery,  $Q_{add}$ , unique to  $RE_n$  is

$$Q_{add} = \theta_{RE} Q_{RE}, \quad \text{where } Q_{RE} = Q_{net} + Q_{add} \quad (4-38)$$

In the above equation,  $Q_{add}$  is the portion of  $RE_n$ 's duty that goes to increasing the total network heat recovery and  $Q_{net}$  is the portion of  $RE_n$ 's duty that is substituting heat recovery from other REs in the network. Such a breakdown of a REs duty assumes the area and effectiveness of all other REs in the network is constant. When the heat duty flow-on factor is negative, it follows that  $Q_{add}$  is also negative even though  $Q_{net}$  and  $Q_{RE}$  may both be positive. Eq. 4-38 does not hold true in the case of a RE in a closed heat loop where the HE area for  $RE_n$  does affect the heat duty flow-on factor.

#### **4.2.4. Modifications for minimum HEN total annual cost**

Calculating a solution based on the cost optimum areas for each individual RE (i.e. the solution to Eq. 4-13 as presently interpreted) in the network does not ensure the overall minimum total cost for the entire HEN. Two common HEN situations where such is the case are:

1. The size of REs are constrained by a stream's target temperature
2. A small duty UE may be eliminated by shifting the utility load to REs or other UEs, thus saving a significant fixed installation fixed cost

To illustrate the first situation, consider the simple HEN in Figure 4-6. The cost optimum areas of the two REs are calculated and applied. However the target temperature of stream Y is exceeded and as a result the area of  $RE_2$  is scaled back such that  $dTC/dA$  is less than zero.

The second situation is encountered when the final temperature of a process stream (after heat recovery) does not quite reach its target temperature and requires the installation of a small UE, which incurs a significant fixed capital cost. In this situation it is sometimes possible to obtain a lower total cost solution by increasing the area of REs in the network and eliminating the need of the UE. However there is a tension between eliminating UEs to reduce capital cost and the controllability of a network (Young et al., 2006).

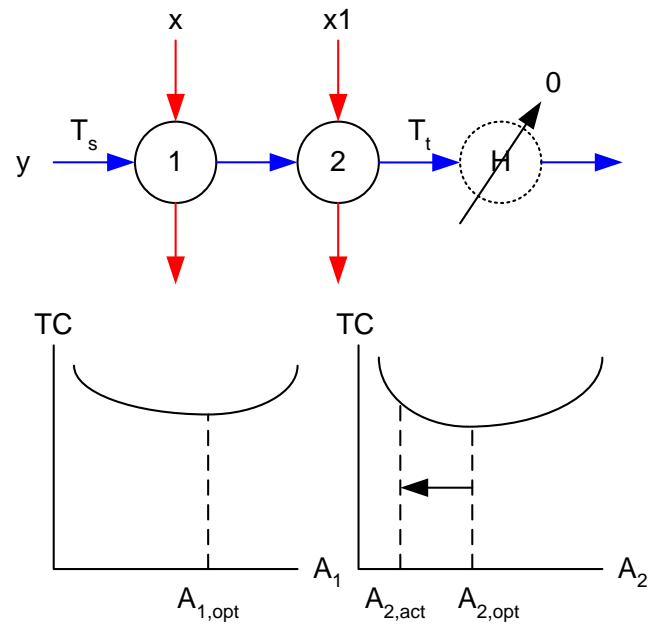


Figure 4-6: The impact of target temperature constraints on HE sizing.

#### 4.2.4.1. Recovery exchangers as terminal recovery exchangers

When a stream is able to thermodynamically and economically reach its target temperature with heat recovery, the final RE on the stream may be viewed as a pseudo UE. In Figure 4-6, RE<sub>2</sub> is unable to achieve its optimum area because of the target temperature constraint on stream y. As a result RE<sub>2</sub> may be treated as a UE such that its area is sized to obtain the remaining required duty. The final RE on a stream not needing utility, e.g. RE<sub>2</sub> on stream y, is referred to as a Terminal Exchanger (TE) to distinguish these exchangers from regular REs and UEs.

Figure 4-7 presents two general cases of how changes in area on two upstream REs (1 and 3) affect the duty and outlet temperatures from a TE (2). In case A,  $dA$  is added to RE<sub>1</sub>, which lessens the required duty on TE<sub>2</sub>. In turn, the area of TE<sub>2</sub> is reduced saving some capital cost, but no additional utility savings on stream y are gained. In case B,  $dA$  is added to RE<sub>3</sub>, which affects the inlet temperature to TE<sub>2</sub>. The change in  $\Delta T_{max}$  for TE<sub>2</sub> affects the required area and capital cost of TE<sub>2</sub> although the duty of TE<sub>2</sub> remains constant. In Appendix C, these two cases are analysed in detail and expressions for the capital cost savings, i.e.  $dCC/dA$ , and the heat duty flow-on factor for TEs are obtained, which may be used to reinterpret Eq. 4-7 for utility cost savings and Eq. 4-11 for capital cost savings resulting from adding  $dA$  to a RE. The summary of the detailed analysis is presented in Table 4-3.



Table 4-3: Expression for terminal recovery exchangers for two cases presented in Figure 4-7.

Objective	Case A	Case B
$\frac{dCC_{TE}}{dA_{RE}}$	$\frac{dCC_2}{dA_1} = -\frac{dQ_1}{dA_1} \frac{(bnA^{n-1})_2 \theta_1^2}{(dQ_2/dA_2)_{TE}}$	$\frac{dCC_2}{dA_3} = -\frac{dQ_3}{dA_3} \frac{(bnA^{n-1})_2 \theta_3^2}{(dQ_{2,x1}^{in}/dA_2)_{TE}}$
$\left(\frac{dQ}{dA}\right)_{TE}$	$\frac{dQ_2}{dA_2} = \frac{U \Delta T_{\max}}{1 - P_{2,y}} \frac{dP_y}{dNTU_y}$	$\frac{dQ_{2,x1}^{in}}{dA_2} = \frac{U \Delta T_{\max}}{P_{x1}} \frac{dP_{x1}}{dNTU_{x1}}$ where $dQ_{2,x1}^{in} = C_{x1} dT_{2,x1}^{in}$
$\left(\frac{dP}{dNTU}\right)_{TE}$	$\frac{dP_y}{dNTU_y} = (1 - P_y)(1 - P_y R_y)$	$\frac{dP_{x1}}{dNTU_{x1}} = (1 - P_{x1})(1 - P_{x1} R_{x1})$
$dT_{TE}^{out}$	$dT_{2,x1}^{out} = \frac{C_y}{C_{x1}} dT_{2,y}^{in}$	$dT_{2,x1}^{out} = dT_{2,x1}^{in}$
$\theta_{RE}^{TE}$	$\theta_1^2 = G_1$	$\theta_3^2 = G_3$
$\theta_{RE}^{UE}$	$\theta_1^{c,x1} = -G_1 G_2$	$\theta_1^{c,x1} = G_3 G_2$

#### 4.2.5. Solutions accounting for future utility and capital price ratio changes

For purposes of capital cost estimation, utility prices ( $p$ ) and capital cost coefficients ( $k$ ) are normally indexed to a particular base year. Indices,  $l$ , are a non-dimensional way of presenting trends in price for various commodities. Eq. 4-13 may be modified to include utility price ( $l_{ut}$ ) and capital cost ( $l_{cap}$ ) indices using the same base year and index,  $l_0$ ,

$$\left(\frac{l_{cap}}{l_0} bnA^{n-1}\right)_1 = \frac{dQ_1}{dA_1} \sum \left( \theta_1^{ut(i)} \left( \frac{l_{ut}}{l_0} p_{ut(i)} + \frac{l_{cap} (bnA^{n-1})_{ut(i)}}{I_0 \frac{dQ_{ut(i)}}{dA_{ut(i)}}} \right) \right) \quad (4-39)$$

which is multiplied by  $l_0/l_{cap}$  to obtain

$$(bnA^{n-1})_1 = \frac{dQ_1}{dA_1} \sum \left( \theta_1^{ut(i)} \left( \frac{l_{ut}}{l_{cap}} p_{ut(i)} + \frac{(bnA^{n-1})_{ut(i)}}{I_0 \frac{dQ_{ut(i)}}{dA_{ut(i)}}} \right) \right) \quad (4-40)$$

Eq. 4-40 demonstrates the importance of the ratio of utility to capital cost. If the initial value  $I_{ut}/I_{cap}$  is unity, then inputting values greater than one represents the fact that utility prices tend to rise over time whereas capital is paid for immediately. Higher utility to capital cost ratios result in HEN solutions with increased heat recovery due to increased justifiable capital cost.

### 4.3. Application of the Cost Derivative Method

The conditions arising from the previous derivations may be applied to find a cost optimal solution for area allocation for a given HEN structure. In this study, the CDM has been applied in an Excel™ Spreadsheet. A flow diagram of the method is provided in Figure 4-8. For the case studies analysed, the initial HEN structures were generated using the PDM and supplied as the main input, together with stream and cost data, into the CDM. Previously applied  $\Delta T_{min}$  constraints from the PDM are removed, although HE duties and areas may be used as initial values prior to optimisation. In the model, zero duty UEs are added to streams not requiring utility to ensure target temperatures are met while the model iterates through to find an overall solution.

The spreadsheet iteratively solves for the cost optimal area allocation in a HEN. In the spreadsheet, the value of  $dQ/dA$  from Eq. 4-8 for each HE is determined based on some initial sizing values (obtained in this case from the PDM solution). Using Eq. 4-14 and 4-15 together with  $dQ/dA$ , the required effectiveness of the recovery exchanger is calculated, from which the NTU and HE area is determined. The new HE areas and duties are now used to recalculate  $dQ/dA$  forming an iterative loop. After a few iterations, the changes to the calculated areas are negligible and a solution is found. If the solution contains a limiting target temperature and/or a small duty UE that can be thermodynamically removed, the total cost of the solution may be potentially reduced by identifying some REs as TEs. TEs are not sized according to Eq. 4-13 but according to the remaining duty required for a stream to achieve its target temperature. It is important to note that Eq. 4-15 may be substituted with the first derivate of the  $\epsilon$ -NTU relationship applicable to the specific HE type. These relationships are given in Appendix B.

Solutions to the CDM were obtained in less than a few seconds. In practice, the CDM may be repeated for different RE network structures and the minimum cost solutions compared to decide on the final network design.

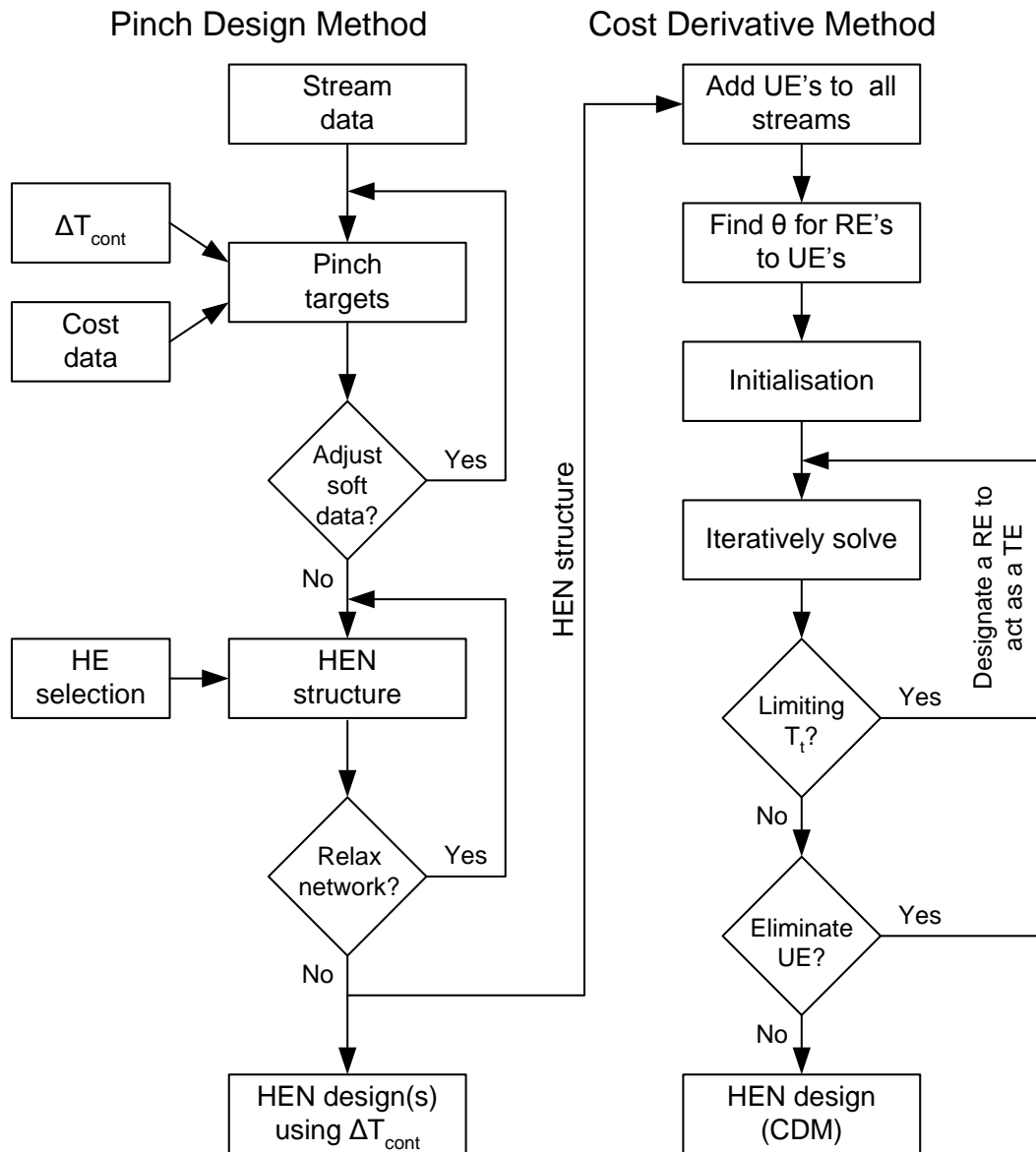


Figure 4-8: Flow sheet of Pinch Design Method and Cost Derivative Method.

## 4.4. Milk powder plant case study

In this section, the CDM solutions for area allocation in MER A and B are presented and compared to the PDM solutions from Chapter 3. The current CDM is only applicable to direct heat recovery exchangers and not indirect heat recovery systems, e.g. liquid coupled loops. As a result the area allocation in the other HENs presented in Chapter 3, which involves significant amounts of indirect heat exchange, has not been optimised. In particular focus is given to the evaporator and CIP zones for MER A and B where heat recovery is direct. The optimisation is based on the utility prices and capital cost functions presented in Table 3-3 of Chapter 3.

### 4.4.1. Comparison of the CDM and PDM solutions

A feature of MER A is the split of the milk stream to match with COW and the condenser vapour (Figure 3-7). The stream split fraction is a degree of freedom that may be utilised to minimise total annual cost,  $TC$ , of HEN of the evaporator and CIP zones. Figure 4-9 presents  $TC$  of the PDM and CDM solutions for milk split fractions between 0.0 and 0.2, where the fraction is for the milk/condenser match. For the PDM, a slight improvement (1.5 %) is gained over the original solution. The CDM applies a significant lower milk split fraction while attempting to optimally allocate HEN area and the CDM solution ( $\$5.56/t_p$ ) gives a 5.8 % total cost reduction compared to the original solution ( $\$5.91/t_p$ ).

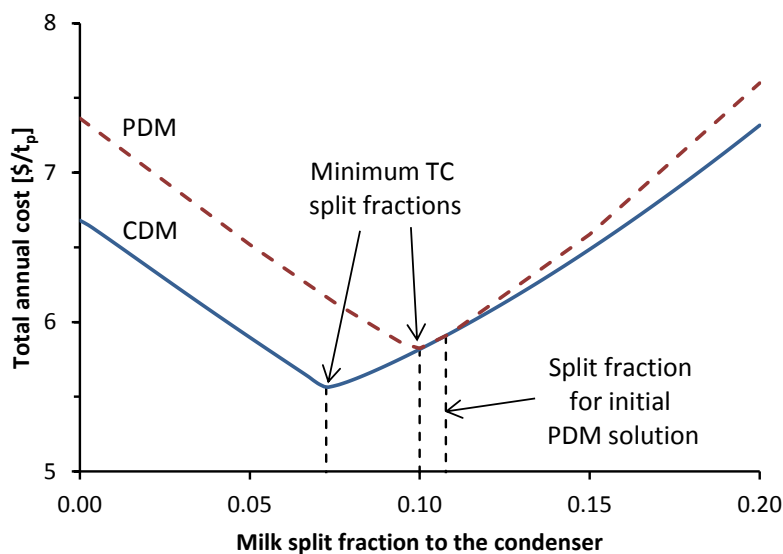


Figure 4-9: Optimising the milk split fraction to milk/condenser vapour match.

Figure 4-10 compares the HE area solutions for the PDM and CDM of MER A. The lower milk split fraction in the CDM is reflected in the allocation of area and duty in the HEN. The duty of the RE<sub>1</sub> is increased by 229 kW whereas RE<sub>2</sub> is decreased by 298 kW in the CDM compared to the PDM (Table 4-4). The economic balance in the CDM favoured increasing the duty of RE<sub>3</sub> by 298 kW in compensation for the reduction in duty on the RE<sub>2</sub>. The CDM solution viewed the CIP/condenser match as a terminal recovery exchanger. In general the selection of  $\Delta T_{cont}$  in the PDM appears to have been conservative as indicated by the lower  $\Delta T_{LM}$ 's in the CDM and the negative  $dTC/dA$  values. For this particular HEN, the heat duty flow-on factors for all the heat recovery exchangers were all unity due to the split and the temperature effectiveness ( $P$ ) of the condensing fluid being close to zero, i.e. no temperature change.

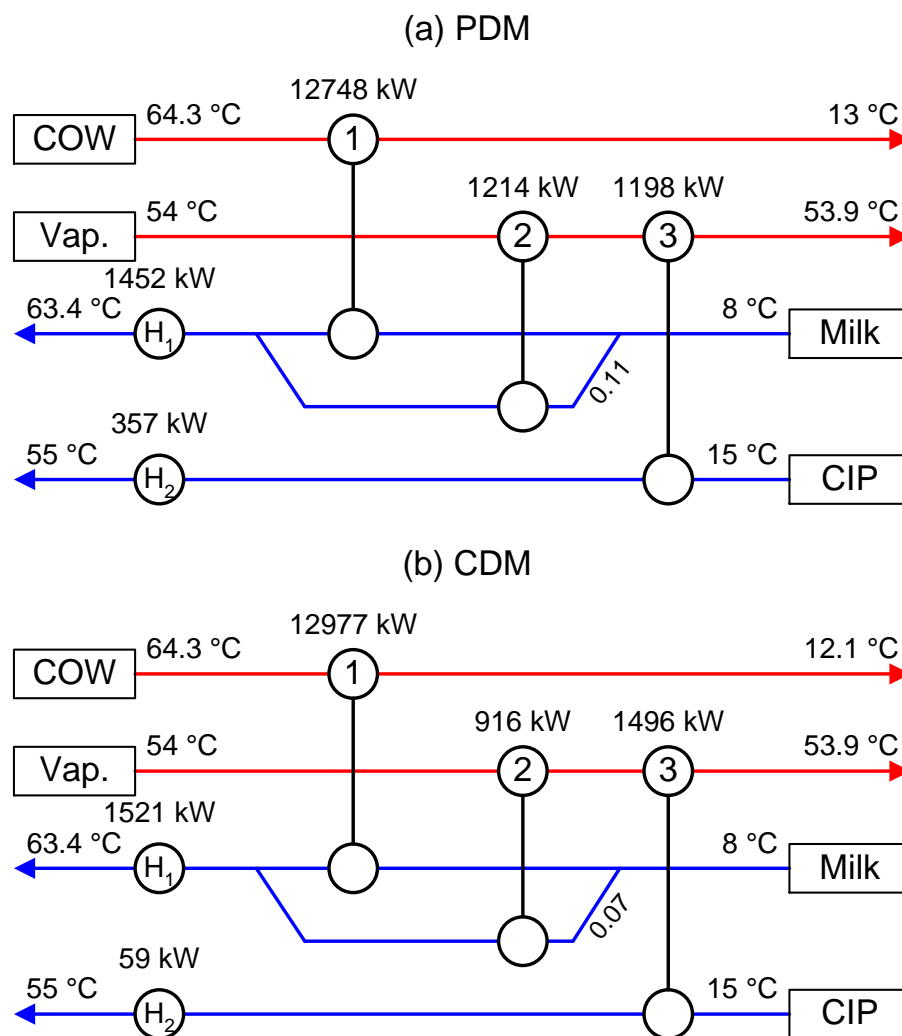


Figure 4-10: Heat exchanger network design solutions of the PDM and CDM for MER A. Duties based on a milk powder plant producing 23 t<sub>p</sub>/h.

Table 4-4: A detailed comparison of PDM and CDM solutions for MER A.

HE	Duty [kW]		Area [m <sup>2</sup> ]		$\Delta T_{LM}$ [°C]		$\Sigma\theta$		$dT/dA$ [\$/kW·y]	
	PDM	CDM	PDM	CDM	PDM	CDM	PDM	CDM	PDM	CDM
1	12748	12977	1275	1297	5.0	5.0	1.00	1.00	-21	0
2	1214	916	42	58	19.1	10.6	1.00	1.00	-219	0
3	1198	1496	41	114	19.7	8.8	1.00	1.00	-225	0
H <sub>1</sub>	1452	1521	25	26	29.2	29.3				
H <sub>2</sub>	357	59	19	7	9.6	4.5				

The CDM solution for MER B reduced total cost by 5.4 % from \$5.45 /t<sub>p</sub> for the PDM to \$5.16 /t<sub>p</sub>. These two solutions are compared in Figure 4-11. In the CDM, there is a significant shift of 279 kW from RE<sub>B</sub> to RE<sub>D</sub> compared to the PDM. This allows a rebalance and increase in total duty for the cyclic matches between milk/COW streams. As a result the duty of RE<sub>C</sub> increases by 1003 kW, although at the expense of a 549 kW reduction on RE<sub>A</sub>. It is important to note that the final temperatures of the COW stream in the two CDM solutions are slightly different.

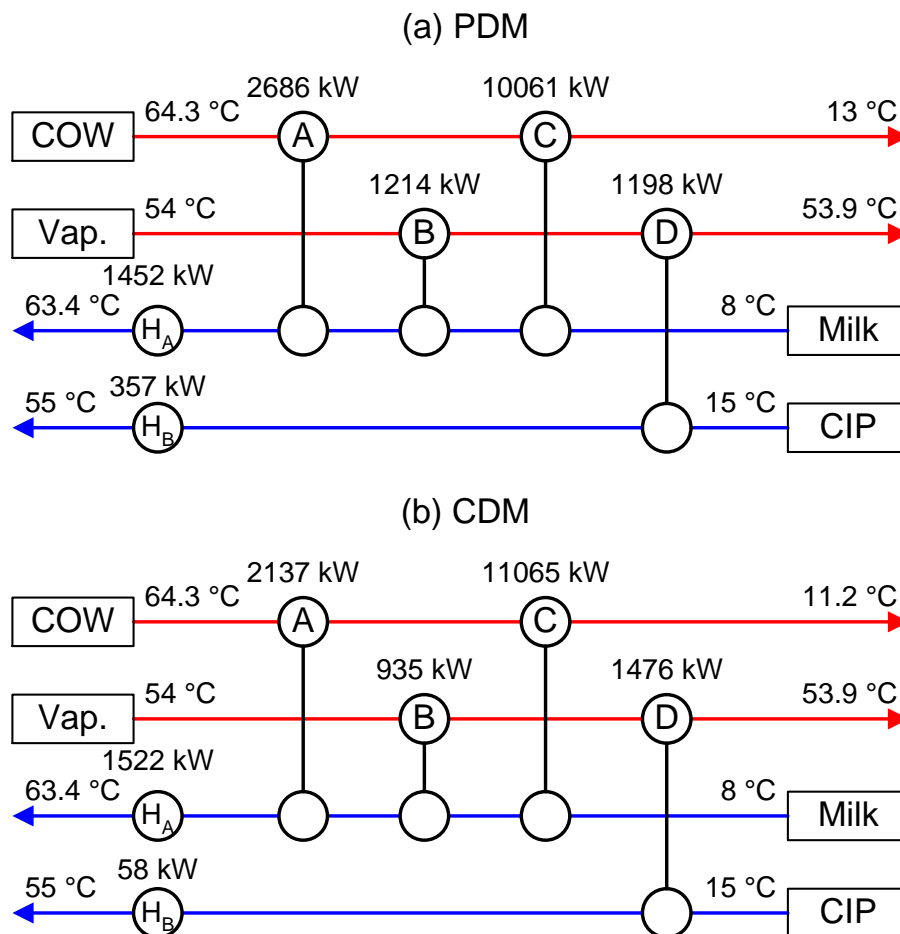


Figure 4-11: Heat exchanger network design solutions of the PDM and CDM for MER B. Duties based on a milk powder plant producing 23 t<sub>p</sub>/h.

A detailed comparison including duty, area, log-mean temperature difference, heat duty flow-on factor and  $dTC/dA$  for individual HEs is presented in Table 4-5. Although the duty of RE<sub>B</sub> is less in the CDM, its area is increased by 34 % to compensate for a lower  $\Delta T_{LM}$ . The  $\Delta T_{LM}$  of RE<sub>A</sub> and RE<sub>C</sub> are also lower requiring significantly more area on RE<sub>C</sub> to deliver an increase in duty. The heat duty flow-on factors for the PDM and CDM are similar. RE<sub>D</sub> is identified as a terminal recovery exchanger and the cyclic match on the milk stream forms an interacting closed heat loop. Like the PDM for MER A, the selection of  $\Delta T_{cont}$  generally appears to have been too conservative as indicated by the negative  $dTC/dA$  values whereas the  $dTC/dA$  values for the CDM are zero.

**Table 4-5: A detailed comparison of PDM and CDM solutions for MER B.**

HE	Duty [kW]		Area [m <sup>2</sup> ]		$\Delta T_{LM}$ [°C]		$\Sigma\theta$		$dTC/dA$ [\$/kW·y]	
	PDM	CDM	PDM	CDM	PDM	CDM	PDM	CDM	PDM	CDM
A	2686	2137	241	211	5.6	5.1	0.72	0.76	-600	0
B	1214	935	108	145	7.5	4.3	0.56	0.56	-1232	0
C	10061	11065	723	1063	7.0	5.2	0.31	0.26	118	0
D	1198	1476	41	94	19.7	10.4	1.00	1.00	-3594	0
H <sub>A</sub>	1452	1277	25	22	29.2	28.8				
H <sub>B</sub>	357	79	19	8	9.6	5.0				

#### 4.4.2. Solutions based on different utility-capital cost ratios

The relationship between utility and capital costs is dynamic. Utility prices are normally expected to rise although new discoveries of resources can lead to dramatic reductions in price due to increased confidence in long term energy supply. A prime example of this has been the rapid growth of shale oil and gas recovery in the United States and Canada. On the other hand, cost estimation invariably involves significant errors even with the best available data. It is important, therefore, to test a wide range of utility-capital ratios (i.e.  $I_{ut}/I_{cap}$  from Eq. 4-40) to understand the impact on the final solution.

Figure 4-12 presents the results for total area and the degree of heat integration for utility-capital ratios between 0.05 and 1.95. A utility-capital ratio of unity is the solution for the current costs. The degree of heat integration is defined in Eq. 3-1 and is based on a maximum heat recovery of 16401 kW for the evaporator and CIP

sections of the milk powder plant (excludes the spray dryer zone), which was obtained using Pinch targeting with  $\Delta T_{min} \rightarrow 0^\circ\text{C}$ . For the entire range of utility-capital ratios, Figure 4-12 shows the MER B solutions, which uses a cyclic match to preheat the milk instead of a split, result in slightly more heat recovery than MER A, but at the expense of slightly increased total area.

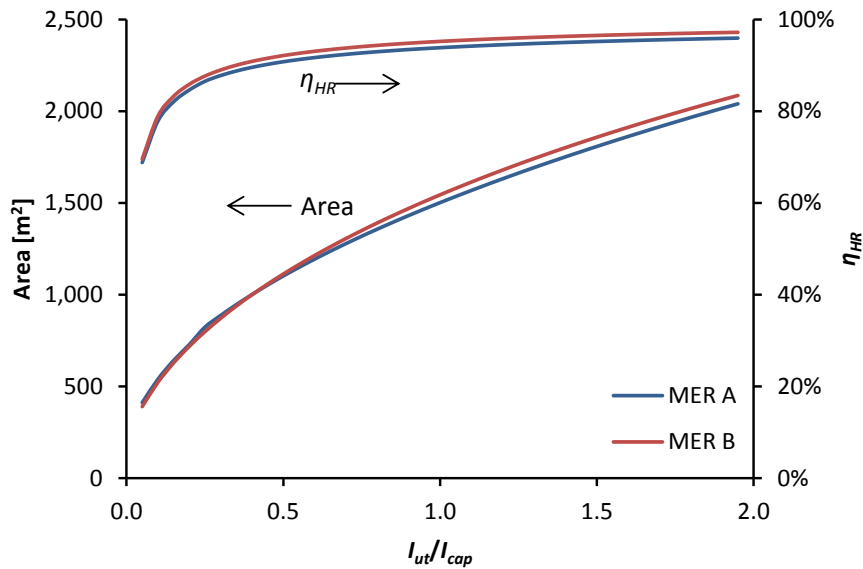


Figure 4-12: The impact of the utility-capital ratio on the total area and heat recovery of the CDM solution for MER A and B.

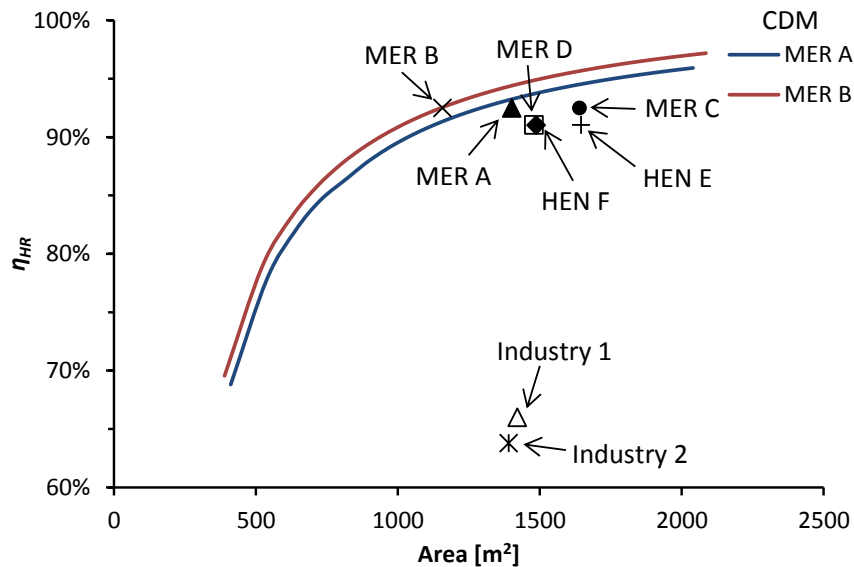


Figure 4-13: Degree of heat integration versus total HE area for CDM solutions and PDM networks from Chapter 3.

A direct comparison between the degree of heat integration and area for the CDM and PDM solutions is presented in Figure 4-13. This representation of the data highlights that MER B also give a more area efficient solution compared to MER A

for the same level of heat recovery. This better area efficiency will also tend to result in lower total cost solutions.

## 4.5. Simple distillation case study (non-dairy)

Process and utility stream data for the simple distillation process from Gundersen (2000) are given in Table 4-6. Heat exchangers are assumed to be counterflow and exchanger capital costs are estimated using

$$CC = 4000 + 500A^{0.83} \quad (4-41)$$

**Table 4-6: Process and utility stream data for a simple distillation process from Gundersen (2000).**

Stream	Code	$T_s$ [°C]	$T_t$ [°C]	$C$ [kW/°C]	$Q$ [kW]	$h$ [kW/m <sup>2</sup> ·°C]	$p$ [\$/y·kW]
Reactor outlet	H1	270	160	18	1980	0.5	
Product	H2	220	60	22	3520	0.5	
Feed	C1	50	210	20	3200	0.5	
Recycle	C2	160	210	50	2500	0.5	
Steam	HU	250	249			2.5	200
Cooling water	CU	15	20			1.0	20

To select an initial (pre-design) value of  $\Delta T_{min}$ , Gundersen applied a super targeting approach to calculate  $\Delta T_{min} = 10$  °C. As a result the HEN structure in Figure 4-14 is based on  $\Delta T_{min} = 10$  °C. This work also calculates a post-network synthesis optimisation of  $\Delta T_{min}$  of 12.5 °C to further minimise total cost. The CDM is applied to the HEN structure in Figure 4-14 taken from Gundersen (2000) to solve for near cost optimal area allocation.

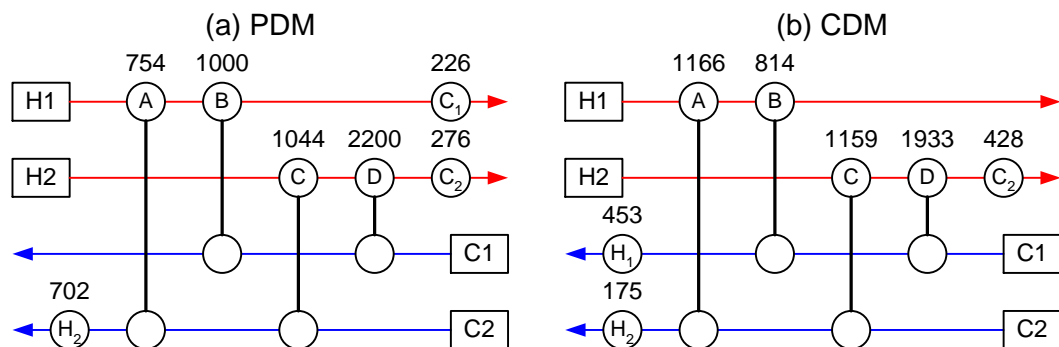


**Figure 4-14: Heat exchanger network for a distillation process using the PDM with  $\Delta T_{min} = 12.5$  °C and the CDM. Duties are in kW.**

The CDM solution achieves a similar level of heat recovery to the PDM solutions although the CDM solution has one less cooler and one extra heater than the PDM.

Table 4-7 compares the duty, area, log-mean temperature difference ( $\Delta T_{LM}$ ), overall heat duty flow-on factor ( $\Sigma\theta$ ) and  $dTC/dA$ , for each HE in the two solutions. In both solutions  $RE_D$  has the highest duty with the PDM assigning a duty of 2200 kW and the CDM allocating 1933 kW. As suggested by the positive value for  $dTC/dA$  of \$111 /kW · y for  $RE_D$  in the PDM solution, the additional HE duty and area allocated to  $RE_D$  in the PDM solution compared to the CDM solution comes at the expense of increased total cost.

**Table 4-7: A detailed comparison of PDM ( $\Delta T_{min} = 12.5$  °C) and CDM solutions for the distillation process.**

HE	Q [kW]		A [m <sup>2</sup> ]		$\Delta T_{LM}$ [°C]		$\Sigma\theta$		$dTC/dA$ [\$/kW·y]	
	PDM	CDM	PDM	CDM	PDM	CDM	PDM	CDM	PDM	CDM
A	754	1166	51	119	60	39	0.15	0.23	21	0
B	1000	814	264	210	15	16	1.00	1.00	4	0
C	1044	1159	179	254	23	18	0.77	0.71	-126	0
D	2200	1933	516	312	17	25	0.24	0.31	111	0
H <sub>1</sub>	0	453	0	22	--	50				
H <sub>2</sub>	702	175	36	10	46	41				
C <sub>1</sub>	226	0	5	0	149	--				
C <sub>2</sub>	276	428	17	25	49	52				

Interestingly the duty of  $RE_A$  in the PDM is only 65 % of the duty of  $RE_A$  in the CDM solution; yet the value of  $dTC/dA$  is positive for the PDM and zero for the CDM, which may appear counterintuitive. However one should note the significant difference in the overall heat duty flow-on factor,  $\Sigma\theta$ , which may be applied to calculate  $Q_{add}$  (Eq. 4-38). Only 115 kW for  $RE_A$  in the PDM is additional heat recovery ( $Q_{add}$ ) compared to 266 kW for the CDM solution. In calculating the CDM solution,  $RE_B$  is a terminal recovery exchanger due to utility  $C_1$  being nil. Using the concept of the final RE on some streams as a TE, it was possible to achieve  $dTC/dA$  of zero for all REs in the CDM solution and obtained the lowest total cost.

The PDM and CDM solutions are compared to four solutions for the same problem generated by Non-Linear Programming, Superstructure, Hyperstructure and Synheat computer programming HEN synthesis methods (Table 4-8) given in Escobar and Trierweiler (2013). The CDM solution requires 11 % less HEN area, recovers a similar quantity of heat, and saves 7.6 % of the total cost when compared to the PDM with  $\Delta T_{min} = 12.5$  °C. The programming synthesis methods

developed new HEN structures that reduced total cost. Even so, for this case study the CDM obtained the lowest total cost using the same structure as the PDM. The programming methods also increased network complexity as indicated by the increased number of stream splits and exchanger units, whereas the CDM focuses solely on cost optimal area allocation within a HEN. However the programming methods were constrained to obtain the same heat recovery target as the PDM with  $\Delta T_{min} = 10$  °C and, as a result, the total costs of programming methods do not necessarily represent the best solution the method could find without such a constraint.

**Table 4-8: Comparison of heat integration solutions for the distillation process. Non-Linear Programming (NLP), Superstructure, Hyperstructure and Synheat solutions are taken from Escobar & Trierweiler (2013).**

	CDM	PDM ( $\Delta T_{min}$ opt.)	PDM	NLP	Super- structure	Hyper- structure	Synheat model
$\Delta T_{min}$ (°C)	7.3	12.5	10.0	10.0	10.0	6.9	9.9
RE	4	4	4	4	4	4	5
UE	3	3	3	3	2	2	2
Splits	0	0	0	2	2	4	3
$\Sigma A$ (m <sup>2</sup> )	952	1,067	1,244	1,170	1,148	1,105	1,065
$Q_r$ (MW)	5,072	4,998	5,100	5,100	5,100	5,100	5,100
CC (\$/y)	222,037	235,242	261,486	251,120	247,842	232,927	239,047
UC (\$/y)	134,139	150,396	128,000	128,000	128,000	128,000	128,000
<b>TC (\$/y)</b>	<b>356,176</b>	<b>385,638</b>	<b>389,486</b>	<b>379,120</b>	<b>375,842</b>	<b>360,927</b>	<b>367,047</b>

## 4.6. Method limitations and future developments

In this section a few of the limitations of the CDM are highlighted knowing that future work may resolve some of the issues.

- Optimisation methods rely on obtaining accurate stream data, utility prices, and capital cost functions. Gaining an additional 5 % cost savings through optimisation can only be translated to actual industrial savings by supplementing the optimisation with quality information.
- The method does not deal with synthesis of the HEN. It is possible to apply the CDM to families of HENs generated using PA or another synthesis technique.
- Solutions to the CDM are calculated iteratively. Like most programming synthesis methods, there is substantial incentive to automate procedures

and algorithms to find the best solution for a given method. The CDM may be implemented in software such as Excel™, Matlab™, GAMS™ to automatically iterate and solve the necessary equations.

- The method looks at only the variable cost components of the total cost function. To an extent, the method overcomes this problem by viewing some REs as a terminal recovery exchanger that is required to recover sufficient heat for the stream to reach its target temperature.
- Stream split fractions are optimised individually, which increases the degrees of freedom.
- Heat transfer film coefficients and HE pressure drop are assumed independent of HE area. These assumptions are made because the trade-off between heat transfer and pressure drop is strongly dependent on the physical HE dimensions, which in most cases is undetermined at the time of designing the network. If the information is available, correlations between overall/individual stream film coefficients and area may be included by making the necessary adjustments to the derivation of  $dQ/dA$ . A correlation between pumping costs, i.e. pressure drop, and area may also be added to the overall cost derivative. This is an area of future development of the method.
- The controllability of a network is not considered in the present method. The CDM attempts to optimally allocate area based on a number of simplified constraints and often eliminates the need of some utility exchangers. However by doing so, the network solution may encounter control difficulties. For example if the solution increases the UEs or decreases the number of heat loops, there is an increase in the degrees of freedom resulting in improved control. Future work may look at how the controllability of a HEN and the cost of process control can be included in the overall optimisation. One possible method is to incorporate a controllability index (Westphalen et al., 2003) to identify solutions with serious control issues so that these issues may be resolved.

## **4.7. Conclusion**

This chapter successfully derives an optimisation method for minimising total cost for a HEN through optimal area allocation. New fundamental equations presented provide interesting insight to the HEN problem. The method is applied to the milk powder plant and distillation case studies to demonstrate its broad applicability. The MER networks from Chapter 3 are optimised such that total cost for the evaporator and CIP sections of the milk powder plant is reduced by 5.8 % for MER A and 5.4 % for MER B compared to the PDM solutions. In the distillation case study, a total cost savings of 7.6 % is generated and the CDM betters four programming methods applied to the same problem presented in literature. Cost reductions between 5 – 6 % may appear trivial; however, the CDM has much wider appeal since the CDM is generally applicable. In industries such as oil refining where energy represents a larger portion of the total production cost and the scale is a couple of magnitudes larger, a 5 - 6 % savings can be in the order of tens of millions rather than tens of thousands.



# Chapter 5

## Increasing total site heat integration in large multi-plant dairy factories

### 5.1. Introduction

New Zealand milk powder plants are often clustered on the same site with other dairy processes presenting the opportunity for inter-plant heat integration to improve overall site energy efficiency. Difficulties associated with plant and stream variability and availability and distance between heat sources and heat sinks can be overcome by using indirect heat integration technologies, such as a low-temperature HRL system as shown in Figure 5-1. The HRL concept has common hot and cold supply/return lines for all sources and sinks acting like a closed utility system. There is also the option of heat storage as a buffer to counter short-term differences in heat supply and demand. Heat exchangers on a HRL are controlled to return fluid to the storage tanks at a desired set-point temperature.

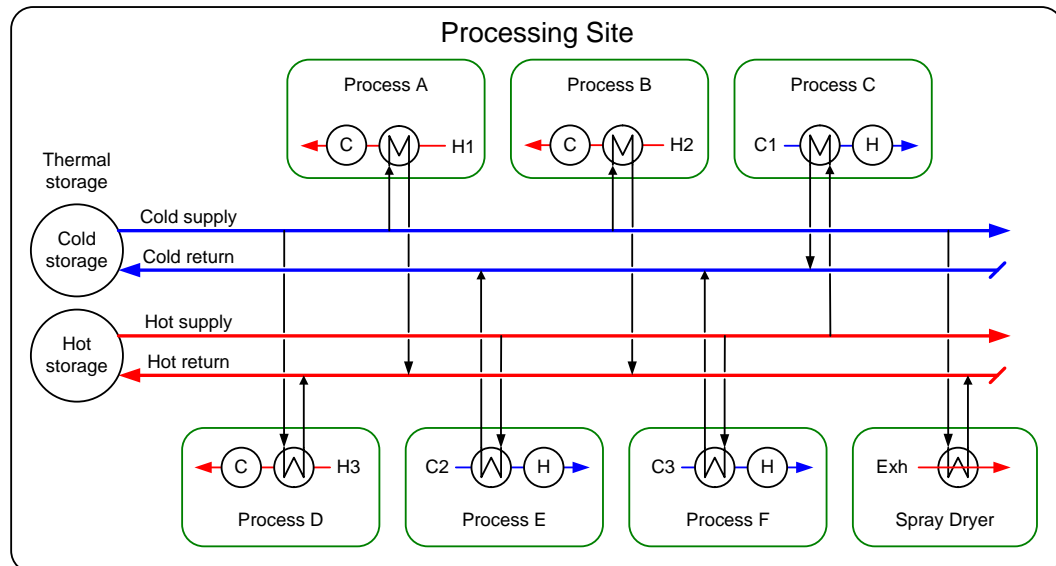


**Figure 5-1: Heat recovery loop network including the milk powder plant spray dryer.**

Heat from the spray dryer exhaust air in milk powder plants may be indirectly integrated with other on-site dairy processes using a HRL system. Detailed analysis of a stand-alone milk powder plant in Chapter 3 concluded that the spray dryer

exhaust air is best matched indirectly to preheat the dryer inlet air via a liquid coupled loop heat exchanger system. This solution requires the installation of two air-to-water compact heat exchangers in the exhaust and inlet ducts, which is capital intensive. Supplying heat recovery from the spray dryer exhaust air to a HRL presents itself as an attractive, less expensive option for large multi-plant sites since it only requires one air-to-water heat exchanger.

Total site heat integration using a HRL with storage also gives rise to the possibility of solar heating as an additional source. The economics of solar heating systems are often poor due to the significant infrastructure required to not only collect radiation heat, but also to store the heated fluid overnight (Quijera and Labidi, 2013). Seeing that HRLs already have most of the infrastructure needed for solar heating there exists a nexus between the two concepts that may be utilised for their mutual advantage.

This chapter investigates the feasibility of integrating the spray dryer exhaust heat and solar thermal heat with other common dairy processes using a HRL. Stream data for the analysis has been extracted from a local dairy factory. Traditional HRL design methods for batch and semi-continuous processes have successfully applied a composite curve approach for designing HRLs with a Constant Temperature Storage (CTS) system where the set-point of hot and cold return temperatures are common for the hot side and cold side of the loop (Krummenacher and Favrat, 2001; Sadr-Kazemi and Polley, 1996; M. R. W. Walmsley et al., 2013b). In addition to the constant temperature storage approach, this chapter reports the development of a novel method, also based on the composite curve for targeting and designing a HRL, but with a Variable Temperature Storage (VTS) system for improved heat recovery where the set-point of hot and cold return temperatures may differ for each heat exchanger on the loop. The idea of using a variable temperature storage system has been described in literature for batch processes based on mixed-integer non-linear computer programming (Chen and Ciou, 2009).

## **5.2. Targeting, design and modelling methodologies for HRLs**

### **5.2.1. Targeting and design methods for inter-plant heat integration via a HRL based on average data**

In this section a graphical Pinch based method for targeting inter-plant heat recovery across multiple semi-continuous plants is presented using a adapted method to that proposed by Kruppenacher and Favrat (2001) and Sadr-Kazemi and Polley (1996) for batch processes. Like traditional PA, the composite curves form an integral part of the targeting procedure. After zonal or intra-plant heat integration is targeted and heat exchanger networks are designed, streams that still require hot or cold utility are potential candidates for inter-plant integration at the Total Site level (Klemeš et al., 1997).

Inter-plant integration is complicated by the semi-continuous operation of dairy processes. A dairy process often has a number of different operating states such as on product, off product, and CIP. Variations in production rate, process demand, and season also have an effect on the flow rate and temperature of some process streams. M. R. W. Walmsley et al. (2013b) demonstrated that an effective method for representing variable stream flow rates for designing a HRL is basing the design on daily time averaged flow rates, which include times in a day when a process is on, off or being cleaned, as opposed to the peak flow rates or median flow rates (Figure 5-2). Time average values should only be taken across times when a plant is in regular operation and not shut down for an extended number of days or weeks. Daily time averaged stream data can then be used to draw hot and cold composite curves that show the daily average heating and cooling enthalpy deficits in each temperature range. How the composite curves are brought together and pinched is dependent on the operation – constant or variable temperature – of the storage system.

When targets are obtained from composite curves based on time average stream data, the target is for the daily average heat recovery. The targets assume intermediate loop fluid storage is continuously available, which is not always the

case in practice. Composites curves based on typical plant operating values may also be useful in understanding the real time balances between sources and sinks. Time averaged flow rates are less than or equal to average stream flow rates while on-product (often referred to as plant design values), therefore determining heat recovery targets from design flows often over predicts what can be recovered especially if there are streams with high flow rates but only operate for a few hours each day.

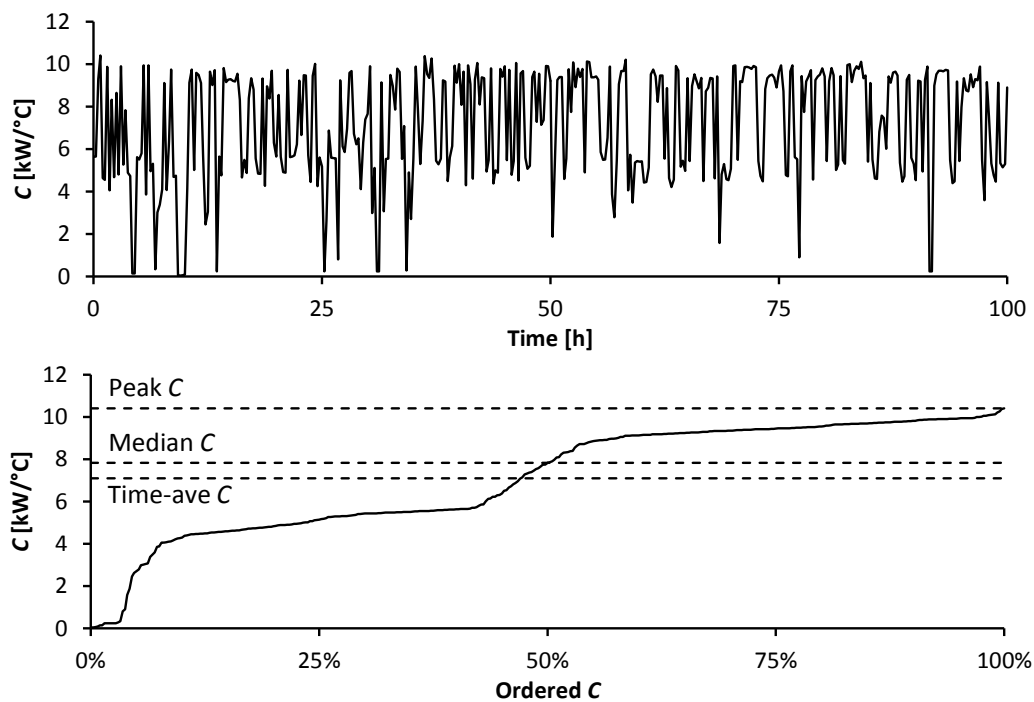


Figure 5-2: Example raw and ordered heat capacity flow rate of a stream. Data taken from M. R. W. Walmsley et al. (2013b).

The algorithms for targeting and designing CTS and VTS HRLs have been developed and implemented into an Excel™ spreadsheet. This targeting and design tool is automated so that a wide range of designs may be generated based on time average stream data.

### 5.2.1.1. Constant temperature HRL storage design procedure

For the case of constant temperature storage, composite curves may be shifted by a full  $\Delta T_{min}$  or by  $\Delta T_{cont,pro} + \Delta T_{cont,loop}$  since the heat recovery is indirect through an intermediate fluid. A pinch occurs between a limiting supply temperature of a stream and the opposite composite curve as shown in Figure 5-3. The limiting supply temperature for the hot composite curve is the lowest supply temperature

of a hot stream and the limiting supply temperature for the cold composite curve is the highest supply temperature of a cold stream. The limiting supply temperatures constrain the feasible storage temperature ranges for operating a CTS HRL. The supply temperatures of the streams forming the composite curves may be circled to clearly show when a pinch occurs. Once pinched, targets for indirect heat recovery may be calculated. The hot and cold storage temperatures can also be determined directly from the pinched composite curves, and a sloped line drawn to span the overlapping heat recovery region represents the average heat capacity flow rate of the HRL intermediate loop fluid. The pinched storage temperature ( $T_{lh}$ ) is fixed while the other storage temperature ( $T_{lc}$ ) may be varied within a small range without violating the  $\Delta T_{min}$  constraint. Assuming vertical integration between the hot and cold composite curves,  $T_{ho}$  is the outlet temperature of hot streams and  $T_{co}$  is the outlet temperature of the cold streams.

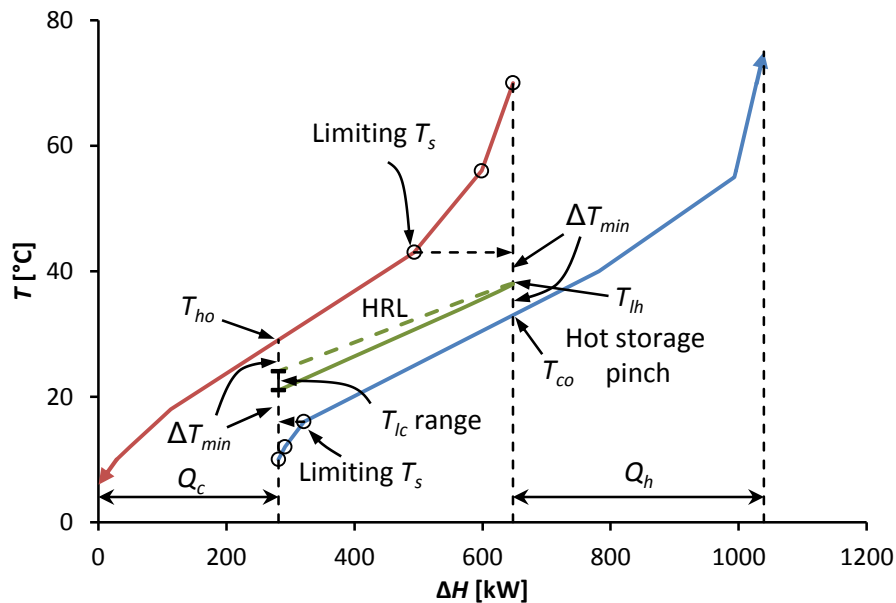


**Figure 5-3: Inter-plant composite curve for indirect heat recovery using a HRL with CTS. Steam data given in M. R. W. Walmsley et al. (2013b).**

After identifying the HRL storage temperatures on the composite curve, heat exchanger areas are calculated using the time average stream data as was recommended by M. R. W. Walmsley et al. (2013b) for improved heat recovery per unit of area. For constant temperature storage operation, the storage temperatures become the control set-points for the outlet temperature of the loop fluid from heat exchangers on the HRL. Each heat exchanger in the HRL

system receives fluid from one storage temperature and is controlled to return the fluid to the other storage tank at its temperature. Designs for a range of heat recovery levels are obtained by selecting new values for  $\Delta T_{min}$ , which leads to new heat exchanger area requirements and new hot and cold storage temperatures.

A comprehensive example of this targeting and design method for HRLs with constant temperature storage is available in Chapter 20 of the Handbook of Process Integration (M. R. W. Walmsley et al., 2013a).

### 5.2.1.2. Variable temperature HRL storage design procedure

This section outlines a novel method for targeting and designing a HRL operated using a Variable Temperature Storage system (Figure 5-4). The approach is also based on the daily time-average composite curve and implemented into an Excel™ spreadsheet.

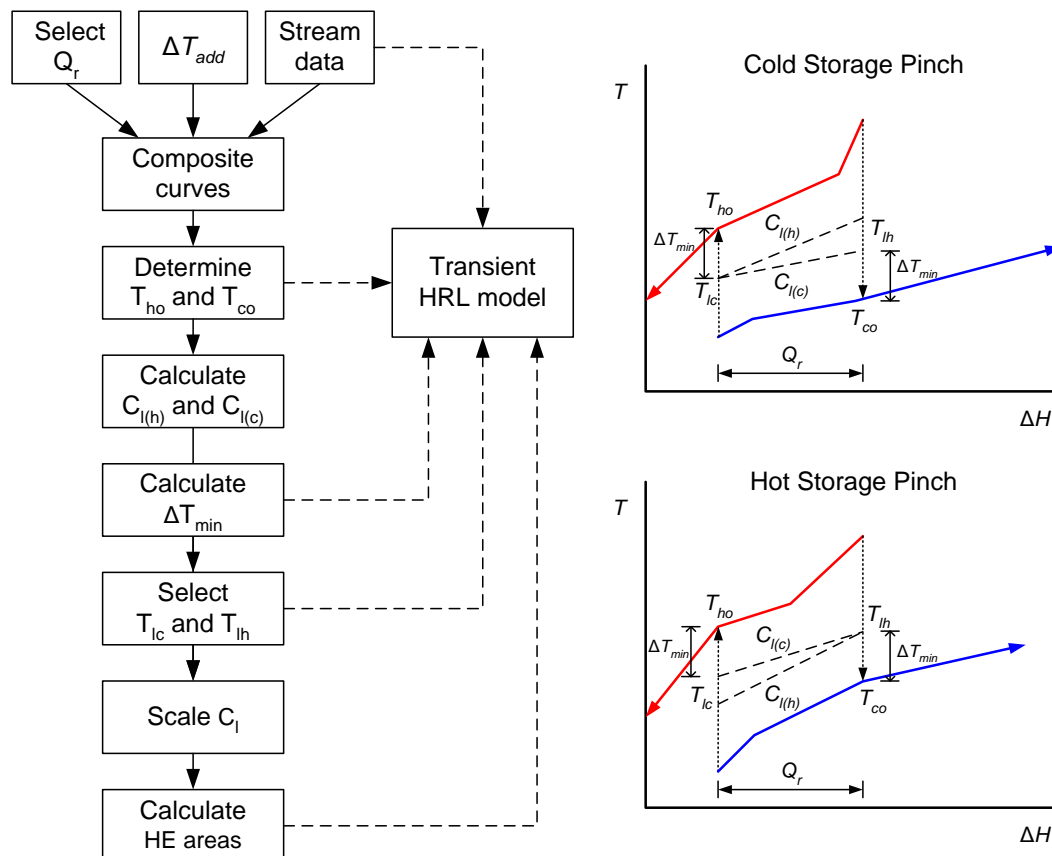


Figure 5-4: Procedure for targeting and designing a HRL with VTS.

The targeting and design procedure varies from traditional PA in that the cold composite curve is shifted under the hot composite curve by a selected feasible  $Q_r$ . After  $Q_r$  is selected, the composite curves are shifted together to determine the minimum exchanger approach temperature,  $\Delta T_{min}$ . In this method  $\Delta T_{min}$  and  $\Delta T_{cont}$  is no longer an input variable and therefore a modified method is needed to apply  $\Delta T_{cont}$  for different stream types to account for large differences in film coefficients between streams, e.g. gas versus liquid streams. Where necessary individual streams are shifted by  $\Delta T_{add}$  prior to the construction of the composite curve to penalise streams with poor heat transfer coefficients such that

$$T_{s(i)}^* = T_{s(i)} \pm \Delta T_{add} \quad (5-1a)$$

$$T_{t(i)}^* = T_{t(i)} \pm \Delta T_{add} \quad (5-1b)$$

where the sign depends on whether the stream is a hot or cold stream. In this study,  $\Delta T_{add}$  for condensing vapour and liquid streams is zero since the respective heat transfer coefficients for these stream types are typically high whereas  $\Delta T_{add}$  for gaseous streams is 10 °C since gas streams normally have very low film coefficients (T. G. Walmsley et al., 2013b). This same approach for penalising gaseous streams, i.e. the dryer exhaust, maybe applied in the CTS method. The composite curve is, therefore, partially shifted and the actual minimum approach temperature of a heat exchanger is  $\Delta T_{min} + \Delta T_{add}$ .

With the composite curves overlapping by  $Q_r$ , the hot stream outlet temperature, i.e.  $T_{ho}$ , and the cold stream outlet temperature, i.e.  $T_{co}$ , is determined assuming vertical heat integration as shown in Figure 5-4. For the same heat recovery level these two outlet temperatures for the CTS and VTS methods are the same. Once these temperatures are found, the limiting combined loop flow rates based on the individual hot streams or the cold streams, i.e.  $C_{l(h)}$  and  $C_{l(c)}$ , are calculated using

$$C_{l(h)} = \sum_{i=1}^{n_h} \frac{Q_i}{T_{s(i)}^* - T_{ho}}, \quad \text{where } Q_i = C_i (T_{s(i)}^* - \max(T_{ho}, T_{t(i)}^*)) \quad (5-2a)$$

$$C_{l(c)} = \sum_{i=1}^{n_c} \frac{Q_i}{T_{co} - T_{s(i)}^*}, \text{ where } Q_i = C_i (\min(T_{co}, T_{t(i)}^*) - T_{s(i)}^*) \quad (5-2b)$$

where  $n_h$  is the number of hot streams and  $n_c$  is the number of cold streams. If  $C_{l(h)} < C_{l(c)}$ , then the pinch is at the cold storage whereas if  $C_{l(h)} > C_{l(c)}$ , then the pinch is at the hot storage. In some cases  $C_{l(h)} = C_{l(c)}$  and both hot and cold storages are pinched. Streams that start outside the vertical overlapping region of the composite curves are not included in the calculation of the limiting heat capacity flow rate. The limiting hot and cold heat capacity flow rates define the minimum and maximum average flow rate boundaries for the VTS HRL system.

As demonstrated in Figure 5-4,  $T_{ho}$  is related to  $T_{co}$  through  $\Delta T_{min}$  and the minimum loop temperature difference,  $\Delta T_{L,min}$ ,

$$T_{co} + \Delta T_{min} = T_{ho} - \Delta T_{min} + \Delta T_{L,min} \quad (5-3)$$

where the minimum loop temperature difference is a function of the heat recovery level divided by the maximum limiting combined loop flow rate

$$\Delta T_{L,min} = \frac{Q_r}{\max(C_{l(h)}, C_{l(c)})} \quad (5-4)$$

These equations are rearranged to find an expression for  $\Delta T_{min}$  for a selected  $Q_r$ .

$$\Delta T_{min} = \frac{1}{2} \left( T_{ho} - T_{co} + \frac{Q_r}{\max(C_{l(h)}, C_{l(c)})} \right) \quad (5-5)$$

The feasible range of average storage temperatures may be calculated using

$$T_{co} + \Delta T_{min} \leq T_{lh} \leq T_{ho} - \Delta T_{min} + \frac{Q_r}{C_{l(h)}} \quad (5-6a)$$

for the hot storage temperature,  $T_{lh}$ , and

$$T_{co} + \Delta T_{min} - \frac{Q_r}{C_{l(c)}} \leq T_{lc} \leq T_{ho} - \Delta T_{min} \quad (5-6b)$$

for the cold storage temperature,  $T_{lc}$ .

The designer may choose the average temperature of the non-pinned storage temperature within the range defined in the above equations. The selection may attempt to minimise total heat exchanger area or minimise the loop flow rate; or, one may simply take the mid-point temperature between the upper and lower temperature bounds. With the average storage temperatures ( $T_{lh}$  and  $T_{lc}$ ) and the outlet temperature of the process streams ( $T_{ho}$  and  $T_{co}$ ) decided, the combined average loop flow rate may be calculated

$$C_{l,ave} = \frac{Q_r}{T_{lh} - T_{lc}} \quad (5-7)$$

Focus is now given to the design of individual heat exchangers in the HRL system. For each heat exchanger, the inlet and outlet temperatures of the process stream and the hot and cold supply temperatures of the loop fluid have been determined. However, the flow rate of the loop through an individual exchanger is not yet known and nor is the outlet (return) temperature of the loop for an individual heat exchanger. As a result an additional equation is needed to fully define each heat exchanger. This equation is based on heat and mass flow rate conservation such that the loop flow rate through a heat exchanger is

$$C_{l(i)} = \frac{Q_i}{T_{s(i)}^* - T_{ho}} \left( \frac{C_{l,ave}}{C_{l(h)}} \right), \quad \text{where } i \in \text{hot streams} \quad (5-8a)$$

$$C_{l(i)} = \frac{Q_i}{T_{co} - T_{s(i)}^*} \left( \frac{C_{l,ave}}{C_{l(c)}} \right), \quad \text{where } i \in \text{cold streams} \quad (5-8b)$$

In the above equations, the heat capacity ratio provides a scaling factor for the limiting flow rate for an individual match. Applying the above equations ensure that the average heat and mass flow rates balance. Using the design heat capacity flow rate for a heat exchanger, the outlet/return temperature of the loop fluid may be calculated.

$$T_{l(i),sp} = T_{lh} - (T_{s(i)}^* - T_{ho}) \frac{C_{l(h)}}{C_{l,tot}}, \quad \text{where } i \in \text{hot streams} \quad (5-9a)$$

$$T_{l(i),sp} = T_{lc} + (T_{co} - T_{s(i)}^*) \frac{C_{l(c)}}{C_{l,tot}}, \quad \text{where } i \in \text{cold streams} \quad (5-9b)$$

This outlet temperature becomes a temperature set point for the control of the loop fluid through the exchanger. Each heat exchanger will have its own temperature set point returning fluid to the storage tank, which then mixes together. Hence, the HRL has a variable temperature storage system. With each heat exchanger fully defined, its area may be determined using the  $\epsilon$ -NTU heat exchanger design equations (Kays and London, 1998). All design parameters of the variable temperature storage HRL are now defined.

## 5.2.2. Method for transient modelling of actual Heat Recovery Loop performance

An Excel™ based spreadsheet tool has also been developed to simulate the transient performance of a HRL. The tool uses the loop temperature control set points and heat exchanger areas targeted from the steady state design to step-wise calculate the level and temperature of the hot and cold storage tanks. With historical or representative transient stream data, the model may be applied to estimate actual heat recovery for defined volumes of storage. When a stream falls short of its target temperature or storage is unavailable, utility is consumed. In the model, the capacity of the storage tanks and intermediate fluid properties such as density and heat capacity may be specified and the storage tank is assumed to be well-mixed. In this work, the intermediate fluid is water and the effect of storage capacity is investigated.

For this case study the model solves nearly 140,000 counter-current heat exchanger problems. Each problem has an unknown loop heat capacity flow rate, process stream outlet temperature and heat duty. Inlet loop temperatures to the heat exchanger are the same as the storage temperature from where it is withdrawn. Outlet loop temperatures are the control set point, which is specified in the design. Dynamics relating to process control are not modelled in the spreadsheet. Given a heat exchanger area and overall heat transfer coefficient ( $U$ ), the heat exchanger problems become fully defined. However to calculate the

unknowns neither the Log-Mean-Temperature-Difference ( $\Delta T_{LM}$ ) nor the  $\epsilon$ -NTU method may be applied. The  $\Delta T_{LM}$  method requires the temperatures in and out of the heat exchanger to be defined; whereas the  $\epsilon$ -NTU method requires both heat capacity flow rates to be known. Hence an iterative approach was implemented and a generalised solutions table (600 x 600) was generated by iteratively solving a simple, single heat exchanger model. Looking up the solution on the table then enabled the HRL model to solve quickly in about one minute avoiding the need to iteratively solve thousands of heat exchanger problems, which takes a few hours. To simplify the problem, all heat exchangers, regardless of type, are modelled as a counter current heat exchanger. Cross-flow heat exchangers applied to transfer heat to/from gaseous streams from/to liquid streams normally have multiple liquid passes (> 6) to produce a near counter flow arrangement (Kays and London, 1998).

Fluctuations in process stream flow rates and temperature, which are characteristic of semi-continuous processes, are successfully accounted for in the spreadsheet model. Heat exchanger areas are designed according to the time-average flow rate of the process stream. When the flow rate of a stream falls below the design point flow rate,  $U$  and  $Q$  are reduced, and when the flow rate is above,  $U$  and  $Q$  increase. To account for this in the modelling, individual  $U$  values are calculated from the corresponding film coefficients ( $h$ ) for the process and loop streams as a function of Reynolds number ( $Re$ ). Liquids are assigned a design film coefficient of  $4000 \text{ W}/^\circ\text{C}\cdot\text{m}^2$ ; vapours are assigned  $2400 \text{ W}/^\circ\text{C}\cdot\text{m}^2$ ; and gaseous flows are  $71 \text{ W}/^\circ\text{C}\cdot\text{m}^2$ . Film coefficients have been selected to match up with the overall heat transfer coefficients used in Chapter 3. Assuming the fluids have a constant viscosity, density, and heat capacity, the ratio of the instantaneous  $h$  to the design  $h_{dp}$  is related to the ratio of  $C$  through the Reynolds number, where  $a$  and  $n$  are constants specific to a heat exchanger design,

$$h = a \cdot Re^n \Rightarrow \frac{h}{h_{dp}} = \left( \frac{Re}{Re_{dp}} \right)^n \cong \left( \frac{C}{C_{dp}} \right)^n \quad (5-10)$$

The spreadsheet model developed for the transient study uses a value of 0.58 for  $n$ , which is specific to a plate heat exchanger (Wang et al., 2007) but is not out of the range of values for finned tube heat exchangers, 0.52 – 0.70, calculated from the correlations of Kays and London (1998). Constant  $a$  may be slightly dependent on fluid properties such as the Prandtl number, which is a function of temperature. In this work,  $a$  is assumed to be constant, as is often the case for liquids with relatively small temperature changes. Design point values are based on the average operating flow rate of a stream. Again, to avoid an iterative solution, a value for  $h$  of the loop side of the heat exchangers was required without first knowing the duty of the heat exchanger and  $C_{l(i)}$ . As a result, the loop side flow rate was approximated by

$$\frac{C_{l(i)}}{C_{pro(i)}} \cong \frac{C_{l(i),dp}}{C_{pro(i),dp}} \quad (5-11)$$

for the calculation of  $h$  and then  $U$ . In a simple test case, the difference between the estimated and calculated loop  $C$  values was found to be at most 3 %.

Included in the HRL model is solar heating based on recorded data from a local weather station. Solar collector efficiency and duty has been modelled using the design equations and constants given by Atkins et al. (2010a).

$$Q_s = A_s (\eta_0 G - a_1 (T_s - T_{amb}) - a_2 (T_s - T_{amb})^2) \quad (5-12)$$

where  $Q_s$  is the solar heating duty,  $\eta_0$  is the optical efficiency (0.764),  $A_s$  is the area of the solar collector,  $G$  is the solar irradiance,  $a_1$  (1.53 W/m<sup>2</sup>·°C) and  $a_2$  (0.0003 W/m<sup>2</sup>·°C<sup>2</sup>) are thermal loss coefficients,  $T_s$  is the average temperature of the collector, and  $T_{amb}$  is the ambient temperature. The values of  $\eta_0$ ,  $a_1$ , and  $a_2$  are specific to a solar collector.

### 5.2.3. Principles for integrating solar heating with HRLs

The integration of solar heating with HRLs is logical because both systems need thermal storage to account for their variable heat supply/demand throughout a day/night cycle. Figure 5-5 illustrates the effect of integrating solar heating into two general cases, which may be characterised by the location of the pinch.

In the first case (Figure 5-5a) the pinch is at the cold storage (CS) temperature indicating a lack of heat sources. As a result solar heating may be integrated as an additional heat source and either CTS or VTS control may be applied to operate the HRL. It is advantageous to further increase the area of the sink heat exchangers to ensure that the extra heating from solar is fully utilised by the HRL.

The second case (Figure 5-5b) is where the pinch is located around the hot storage temperature. Applying solar heating to produce hot water at the pinched hot storage temperature for CTS operation is totally ineffective and inappropriate. This is analogous to adding a hot utility to below the pinch temperature. For VTS operation with a hot storage pinch, the addition of solar heating is like adding a hot utility across the pinch that increases the site's required cooling duty but decreases the site's heating load. To generate benefits from adding solar, the HRL fluid temperature needs to be raised above the pinch temperature and some modifications to the HRL design may need to be made such as adding a third storage tank with the temperature level as indicated in Figure 5-5b.

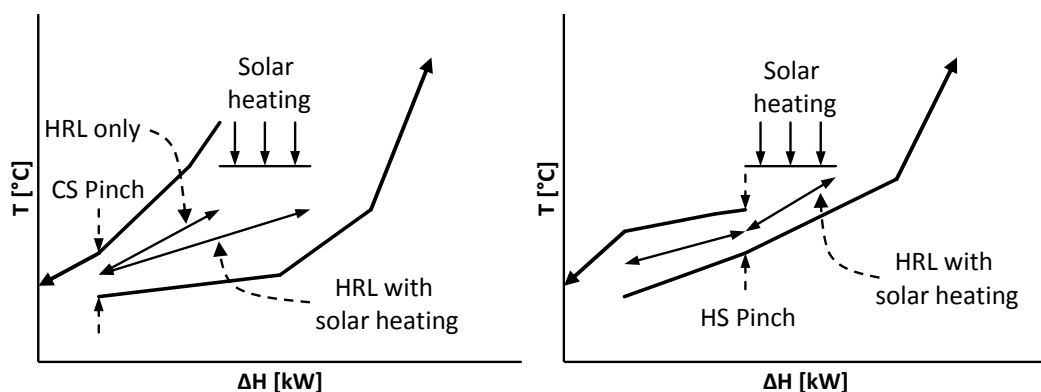


Figure 5-5: Composite Curves for the integration of solar heating with HRLs for processes with cold storage pinch (a) and hot storage pinch (b).

### 5.3. Data collection and characterisation

Stream data for four milk powder plants, four other dairy processes, site hot water and two utility units (e.g. compressor) have been obtained from a New Zealand dairy factory for a period of two months during peak processing at intervals of 10 minutes. Volumetric flow rates were measured by magnetic flow meters and recorded by the company's computer system whereas most temperatures were measured but not logged. As a result historical average temperatures have been used in most cases.

**Table 5-1: Extracted stream data including the spray dryer exhaust and solar heating.**

Stream	Type	$T_s$ [°C]	$T_t$ [°C]	Operating		Time-average	
				C [kW/°C]	Q [kW]	C [kW/°C]	Q [kW]
Dryer Exhaust A	HOT	75	55	143	2851	139	2785
Dryer Exhaust B	HOT	75	55	75	1497	73	1462
Dryer Exhaust C	HOT	75	55	45	898	44	877
Dryer Exhaust D	HOT	75	55	29	570	28	557
Utility Unit A	HOT	45	30	10	146	8	120
Utility Unit B	HOT	45	30	10	146	8	120
Casien A	HOT	50	20	33	999	22	647
Casien B	HOT	50	20	49	1477	32	956
Casien C	HOT	50	20	49	1485	32	962
Condenser	HOT	80	79	993	993	351	351
Cheese A	HOT	35	20	120	1797	98	1470
Cheese B	HOT	35	20	139	2074	114	1691
Solar Collector	HOT	85	-	-	-	-	-
Site Hot Water (SHW)	COLD	16	65	160	7827	160	7827
Milk Treatment A	COLD	10	50	104	4159	104	4159
Milk Treatment B	COLD	10	50	104	4159	104	4159
Milk Treatment C	COLD	11	50	116	4563	116	4563
Whey A	COLD	12	45	20	663	16	522
Whey B	COLD	14	45	11	340	9	267

Table 5-1 presents the stream data for the 18 process streams with the addition of a solar collector. Operating average and daily time average heat capacity flow rates are calculated and temperatures are averaged for while a stream is in operation. The daily time average values include periods when a stream is unavailable throughout a normal day's plant operation due to cleaning and off-product times. Duties based on both heat capacity flow rates are also presented.

The solar collector is assigned a supply temperature of 85 °C, and it is assumed that solar heating can heat the intermediate fluid up to 80 °C in evacuated tubes.

Some streams such as the condenser have a high operational duty (993 kW) but only operate for around 8 hours per day resulting in a time average duty of 351 kW. The condenser duty is plotted in Figure 5-6 using instantaneous values for a 72 hour period and ordered values for the entire two months. On the other hand, streams like site hot water are continuously available but its supply temperature and flow rate fluctuates noticeably as shown in Figure 5-7.

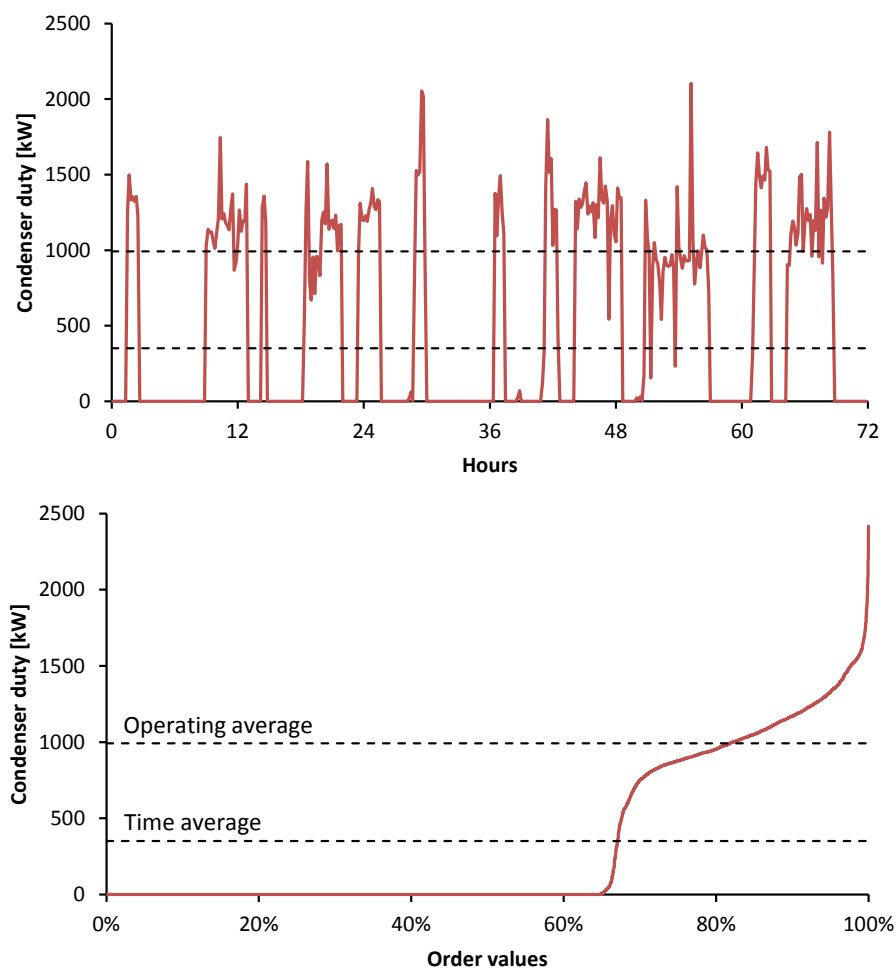
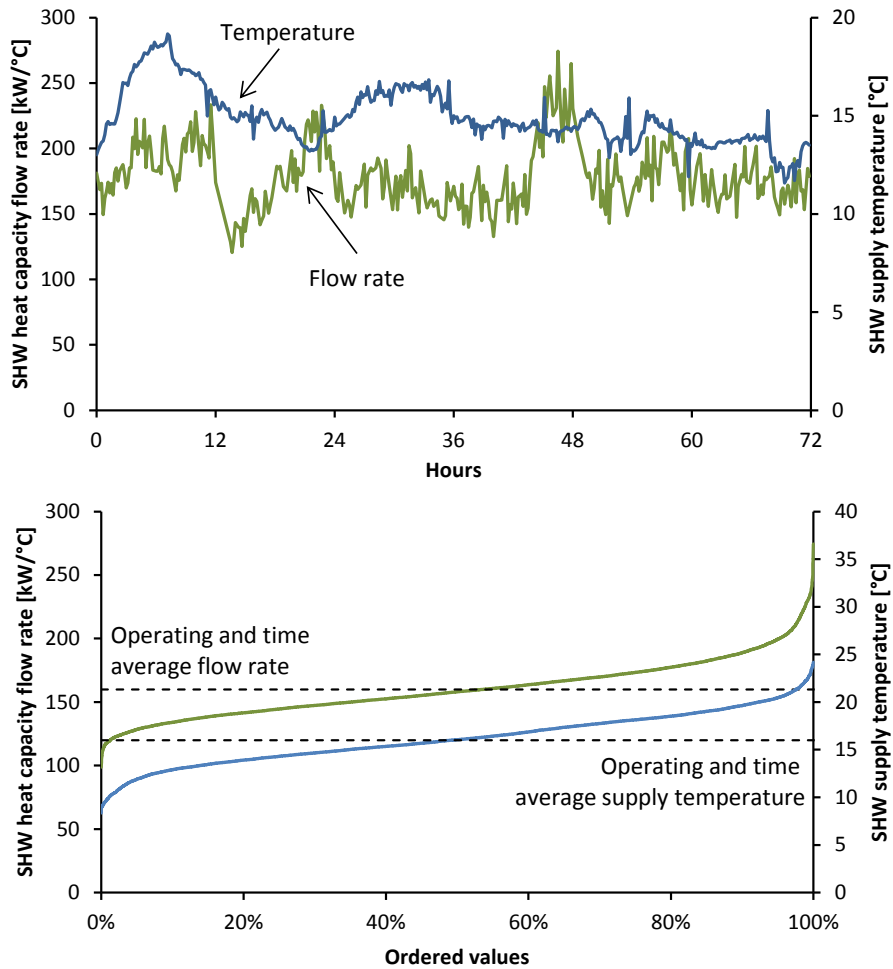


Figure 5-6: Condenser duty for a 72 hour period (a) and as ordered values for the entire two months (b).



**Figure 5-7: Site hot water supply temperature and heat capacity flow rate for a 72 hour period (a) and as ordered values for the entire two months (b).**

Solar irradiance and ambient temperature data recorded at a nearby weather station has been downloaded from New Zealand's National Climate Database (NIWA, 2013). Solar irradiance data for the entire two months is plotted in Figure 5-8 using time of day as the x-axis and showing the day average (0.43 kW/m<sup>2</sup>), day/night average (0.25 kW/m<sup>2</sup>) and the average of the daily peak (0.97 kW/m<sup>2</sup>).

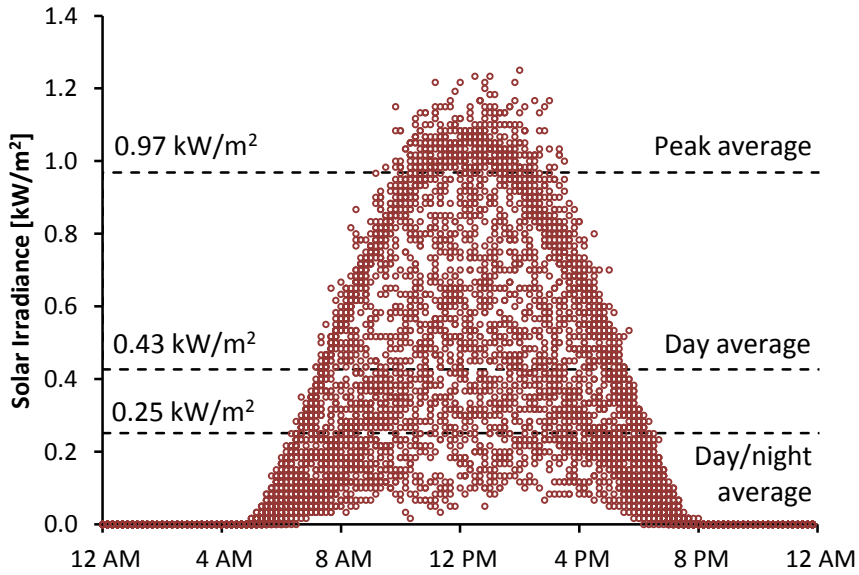


Figure 5-8: Solar irradiance recorded by closest weather station to the dairy factory (NIWA, 2013).

## 5.4. Steady state HRL targets and design

### 5.4.1. Site composite curves

The site's heating and cooling demand profiles may be determined using the stream data in Table 5-1 as shown in Figure 5-9. The dryer exhaust stream has been shifted by 10 °C to reflect its lower heat transfer film coefficient compared to other liquid and condensing vapour streams. The total heating requirement is 21.5 MW on average and the total cooling requirement is 12.0 MW on average.

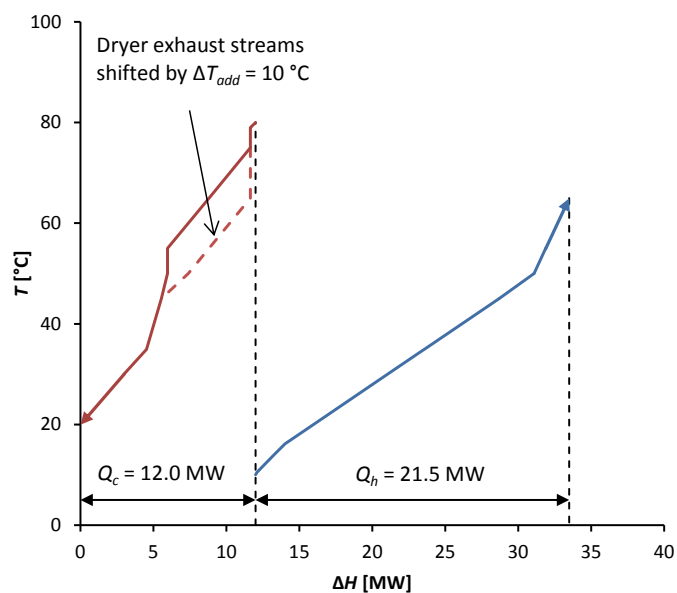


Figure 5-9: Time average composite curves of available streams for the HRL. Solar heating is not included.

### 5.4.2. Average heat recovery targeting for CTS

Average inter-plant heat recovery achieved by CTS HRL is targeted using a  $\Delta T_{min}$  of 5 °C. As a rule of thumb, liquid/liquid heat recovery using plate heat exchangers tend to be economic at a  $\Delta T_{min}$  of 5 °C as was demonstrated in Chapter 3 for the stand-alone milk powder plant. Figure 5-10 presents the pinched composite curves for targeting a CTS HRL showing a heat recovery of 8.3 MW. The pinch is around the cold storage temperature caused by Site Utility Unit A's and B's common supply temperatures.

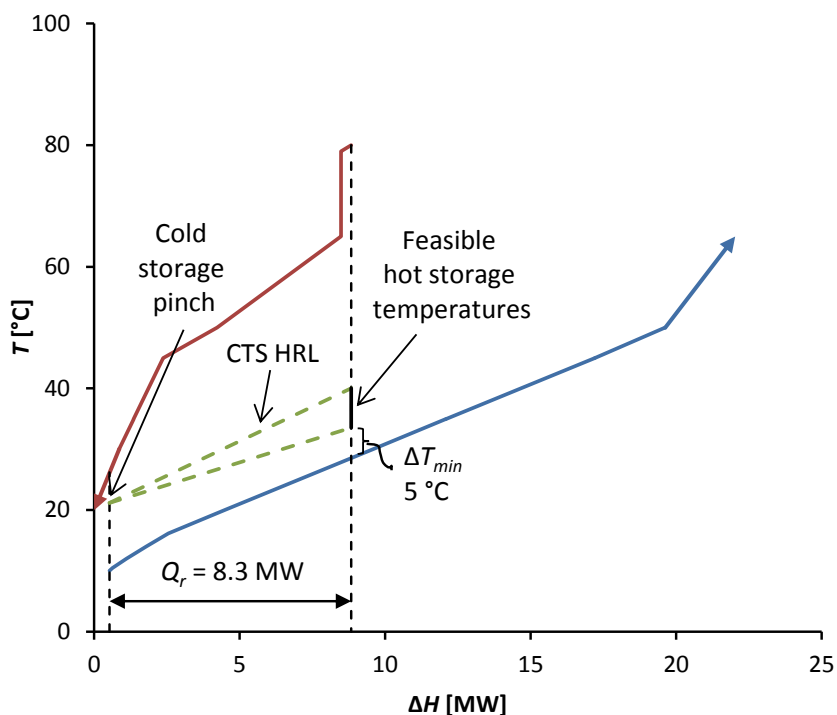


Figure 5-10: Heat recovery targeting for CTS based on a  $\Delta T_{min}$  of 5 °C. Cheese A and B removed from analysis.

Cheese A and B have been removed from the analysis and the composite curve in Figure 5-10 to increase heat recovery for a  $\Delta T_{min}$  of 5 °C. Cheese A and B have the lowest hot stream supply temperature and leaving these streams in the analysis would limit heat recovery to a maximum of 7.5 MW. Above a heat recovery of 7.5 MW, streams Cheese A and B would be encompassed in the overlap region of the composite curves causing a hot storage pinch and a  $\Delta T_{min}$  of less than 5 °C. In general, the stream causing a pinch is removed, which sometimes allows the composite curves to be further overlapped indicating increased heat recovery.

There is a small range of feasible temperatures for the non-pinned hot storage temperature. The effect of varying the hot storage temperature on total area and the loop flow rate is shown in Figure 5-11. At the hottest feasible hot storage temperature, the loop flow rate, pressure drop and pumping costs are minimised; whereas different cold storage temperature minimises total area. From experience, minimising the loop flow rate produces a more practical solution in terms of loop temperature difference and flow rate whereas optimising for the minimum area tends to make less of an impact as indicated by the flatness of the total area curve.

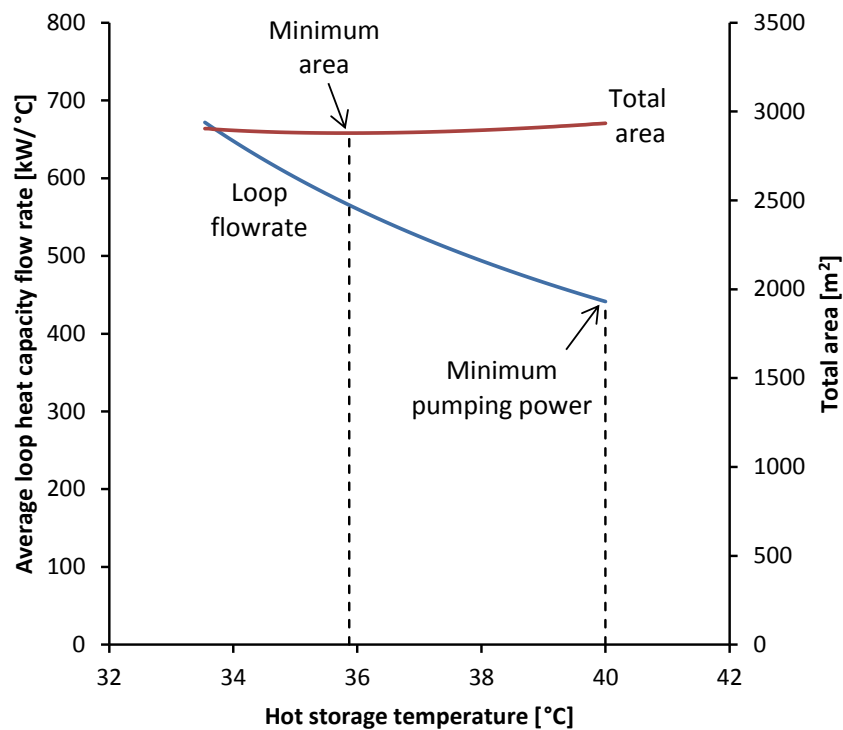


Figure 5-11: Effect of cold storage temperature selection on total area and loop flow rate for a CTS HRL based on a  $\Delta T_{min}$  of 5 °C.

### 5.4.3. Average heat recovery targeting for VTS

A heat recovery target for a VTS HRL is determined assuming a  $\Delta T_{min}$  of 5 °C as shown in Figure 5-12. The heat recovery target for the VTS approach is 11.3 MW, which is considerably higher than CTS approach. Figure 5-13 presents the effect of hot storage temperature selection where minimising area is at odds with minimising loop flow rate. The CTS method can also recover 11.3 MW, although it requires a lower  $\Delta T_{min}$  of 0.2 °C and hence a much larger total heat transfer area.

To better compare between the two methods, an understanding of the trade-off between heat recovery, total area and average loop flow rate across a broader range is needed.

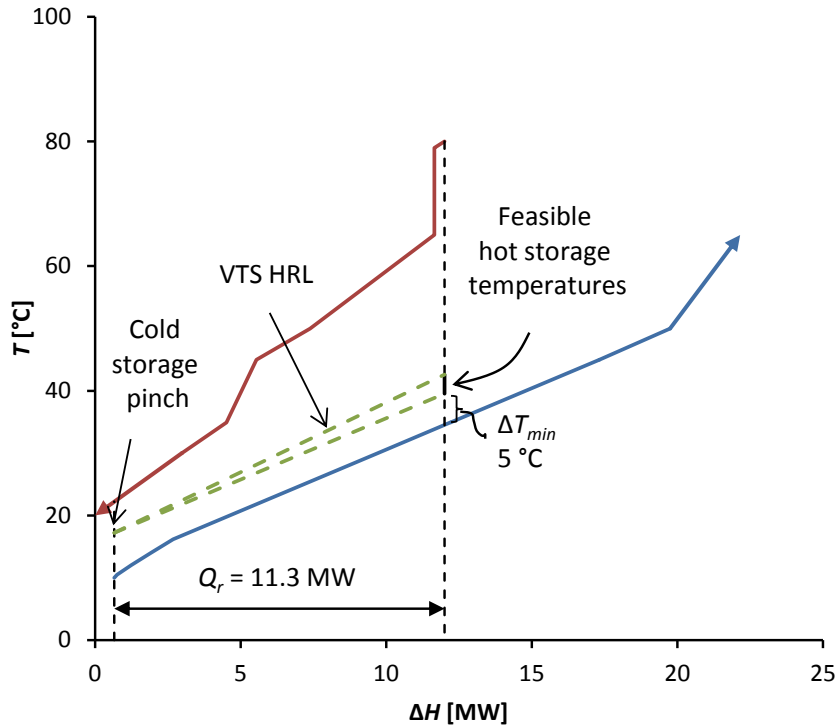


Figure 5-12: Heat recovery targeting for VTS based on a  $\Delta T_{min}$  of 5 °C.

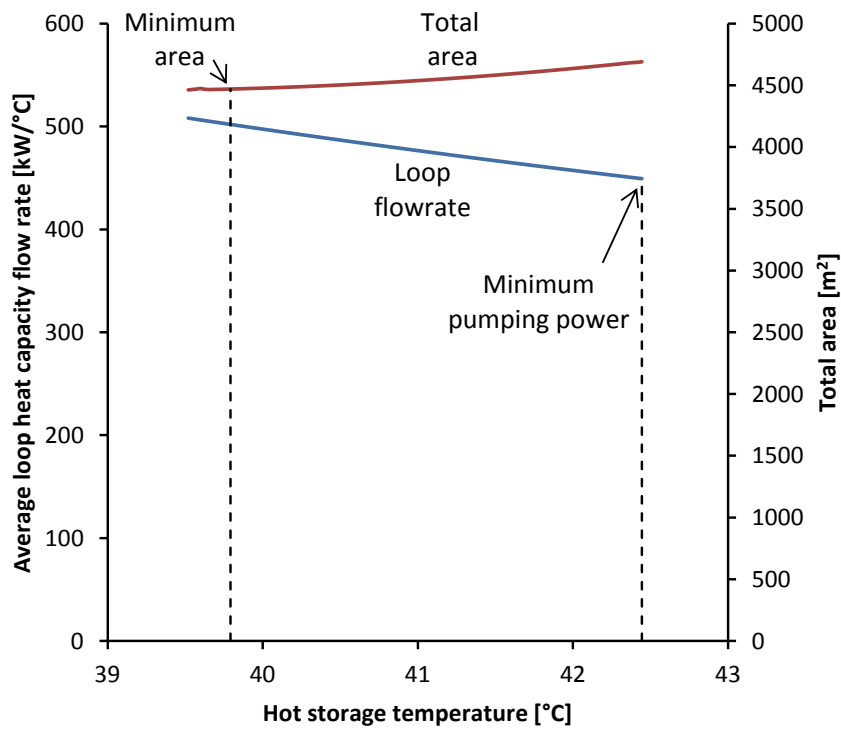


Figure 5-13: Effect of cold storage temperature selection on total area and loop flow rate for a VTS HRL based on a  $\Delta T_{min}$  of 5 °C.

#### 5.4.4. Heat recovery, total area and loop flow rate trade-off

In designing a HRL there is an acute trade-off between heat recovery, total area and the loop flow rate. Heat recovery delivers utility savings, heat exchanger area is a capital cost and the loop flow rate determines the pressure drop and pumping costs. The heat recovery performance of CTS and VTS HRLs are compared for a range of  $\Delta T_{min}$  values in Figure 5-14. In general the VTS method more effectively distributes temperature driving forces between heat exchangers resulting in higher  $\Delta T_{min}$  values compared to the CTS method. Discontinuities in this graph as well the other graphs in this section are caused by streams being added or removed from the HRL design. For a  $\Delta T_{min}$  of 5 °C, the VTS approach recovers 11.3 MW of heat compared to 8.3 MW for the CTS design.

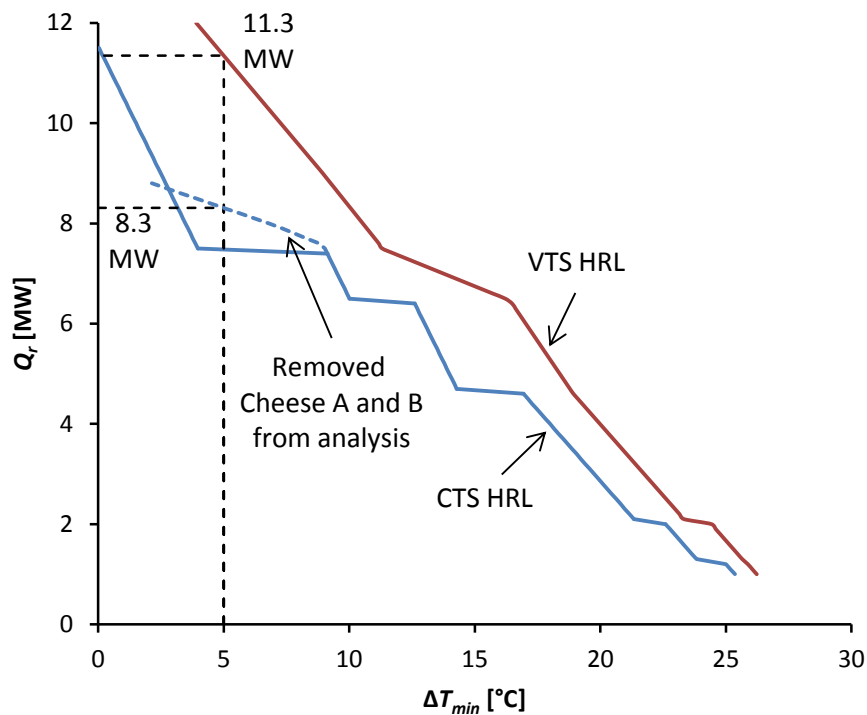


Figure 5-14: Heat recovery versus minimum approach temperature.

The heat recovery performance may also be plotted against total network area including the dryer exhaust heat exchanger area as shown in Figure 5-15 and total network area excluding the dryer exhaust heat exchanger area as shown in Figure 5-16. Black dotted lines are included that correspond to a  $\Delta T_{min}$  of 5 °C for the two design approaches. Below 9.9 MW of heat recovery the CTS approach for this problem provides better heat recovery per unit of area while the VTS

approach is advantageous above 9.9 MW of heat recovery if the dryer exhaust area is included. The maximum inter-plant heat recovery for the site, 12.0 MW, is feasible to achieve using the VTS method with a  $\Delta T_{min}$  of 3.9 °C, at which heat recovery level the composite curves for a threshold problem. The CTS storage has a maximum heat recovery of 11.5 MW with  $\Delta T_{min}$  approaching zero.

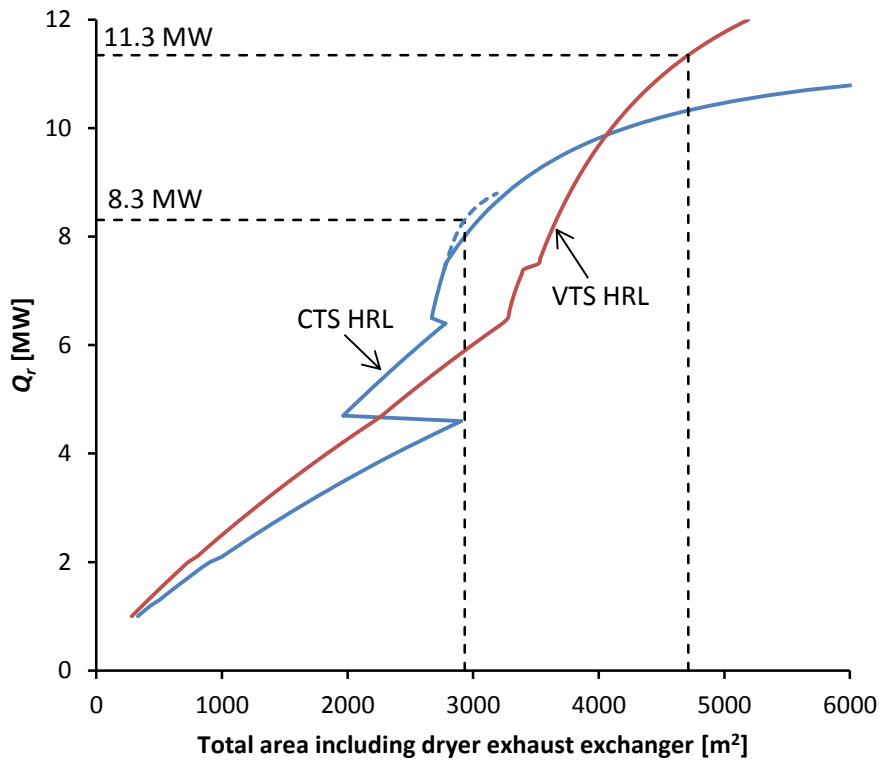


Figure 5-15: Heat recovery versus total area including the dryer exhaust exchanger.

The lower total area achieved by the CTS method below 9.9 MW of heat recovery is mostly due to lower inlet and outlet loop temperatures for the dryer exhaust heat exchangers. The lower loop temperatures for the CTS design improve the temperature driving force of heat exchangers on the hot side of the loop, which includes the dryer exhaust exchangers. At 9.9 MW of heat recovery the area required for dryer exhaust heat recovery comprises 50 % of the total HRL system area, which percentage is higher for heat recovery targets less than 9.9 MW. As a result heat recovery is plotted against the total area excluding the dryer exhaust heat exchangers as presented in Figure 5-16. This graph provides a different perspective on which design approach is better. In Figure 5-16, the VTS system gives substantially improved heat recovery per unit area for heat recovery greater

than 7.5 MW. Below a heat recovery of 7.5 MW, the total area is dominated by the area required for dryer exhaust heat recovery. As a result the CTS approach in Figure 5-15 appears to be better at the design stage due to lower loop temperatures maximising the temperature driving force for the dryer exhaust exchanger.

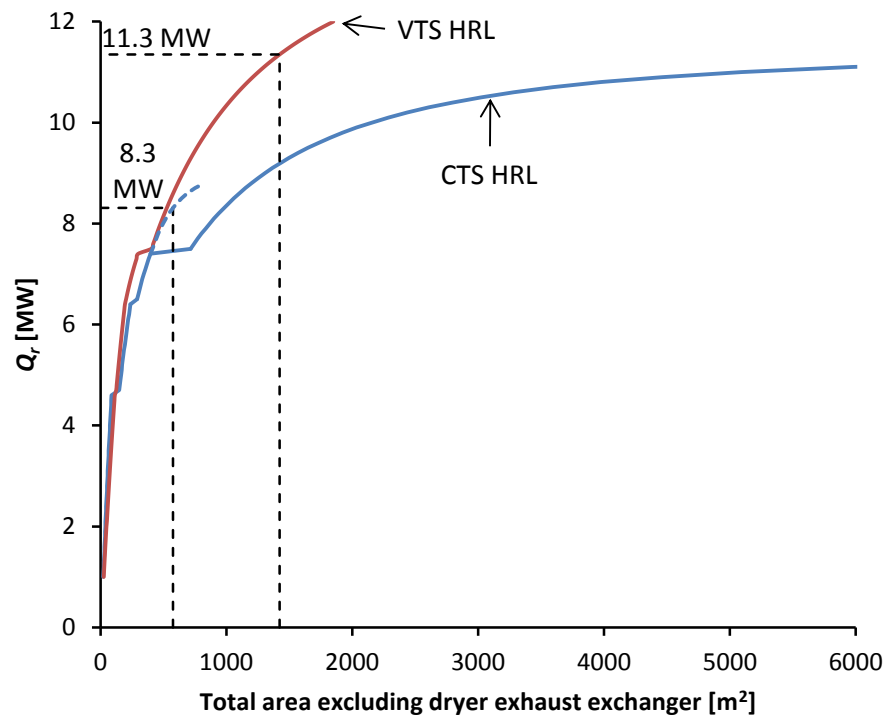


Figure 5-16: Heat recovery versus total area excluding the dryer exhaust exchanger.

The temperature difference between the hot and cold loop temperatures is a key factor affecting the required loop flow rate (Figure 5-17). Small temperature differences require large loop flow rates. When selecting the non-pinched storage temperature, the philosophy has been to minimise the loop flow rate, thus minimising pressure drop and pumping costs. Several additional curves for both CTS and VTS methods could be generated by selecting different non-pinched storage temperatures. When targeting site heat recovery below 5.2 MW, it is possible to remove the stream with the limiting supply temperature from the analysis and improve the final design. As a result Cheese A and B are removed for the CTS design to show this effect while also being able to achieve a  $\Delta T_{min}$  of 5 °C.

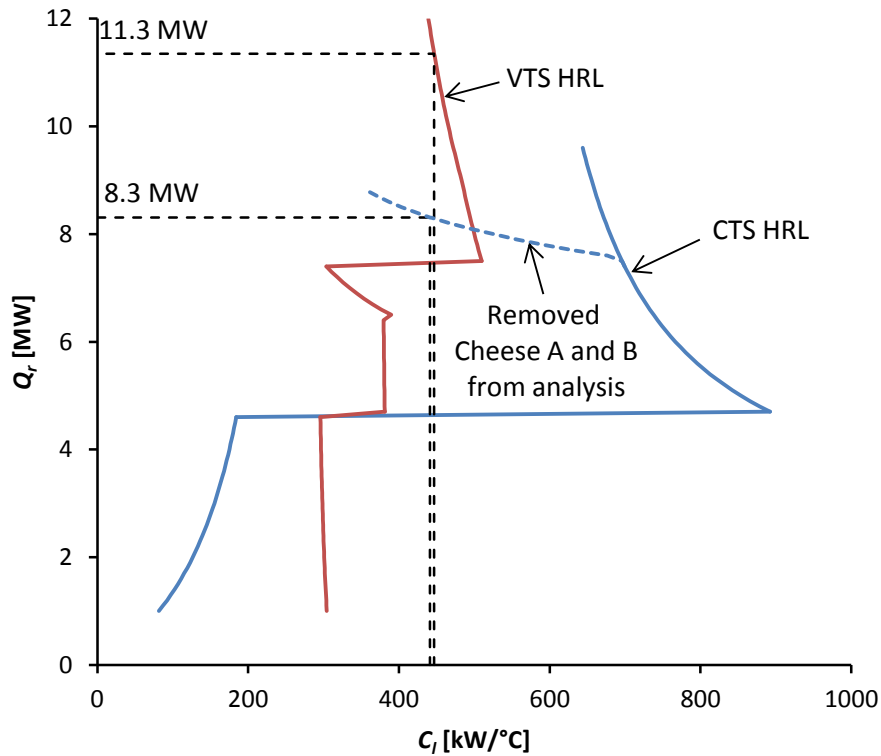


Figure 5-17: Heat recovery versus heat capacity flow rate of the loop.

#### 5.4.5. Integration of solar heating into the HRL design

The integration of solar heating with a HRL is beneficial when the pinch is around the cold storage temperature, which is the case for the CTS and VTS methods with a  $\Delta T_{min}$  of 5 °C. In this section, the maximum and practical integration of solar heating into the 5 °C  $\Delta T_{min}$  solutions is investigated.

Figure 5-18 shows the maximum amount of solar heat that can be integrated into the CTS HRL without violating the  $\Delta T_{min}$  constraint whereas Figure 5-19 is for a VTS HRL. For these cases the pinch at the hot storage tank is caused by the solar heating. For the CTS approach, the hot storage pinch is between the supply temperature of Utility Units A and B and the cold composite curve as a result of adding solar to the HRL. For the VTS approach, the second pinch is related to the limiting heat capacity flow rate of the loop based on the hot and cold streams, i.e.  $C_{l(h)}$  and  $C_{l(c)}$ . For a second pinch to occur it is necessary that  $C_{l(h)} = C_{l(c)}$ , where  $C_{l(h)}$  includes solar heating as a hot stream and  $C_{l(c)}$  is based on  $T_{co}$  after solar heating.

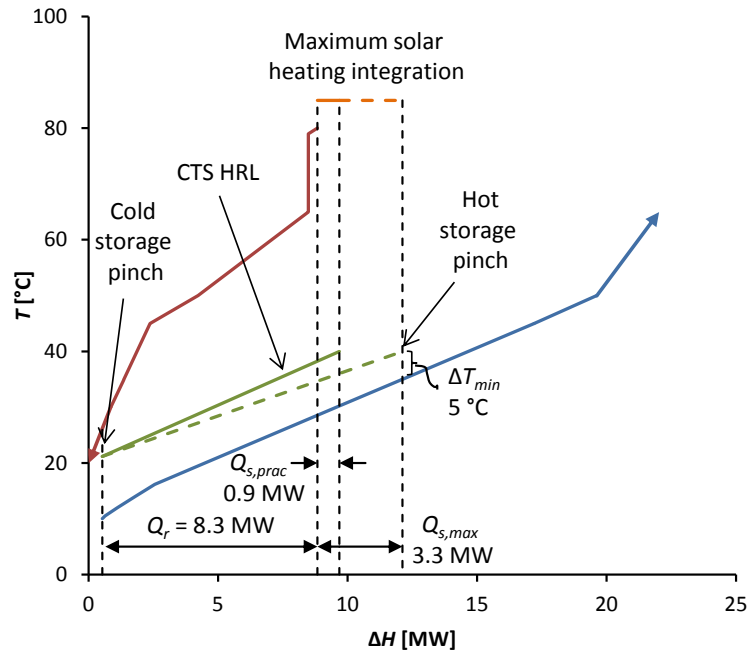


Figure 5-18: Maximum and practical average heat recovery and solar heating targets for a CTS HRL based on a  $\Delta T_{min}$  of 5 °C.

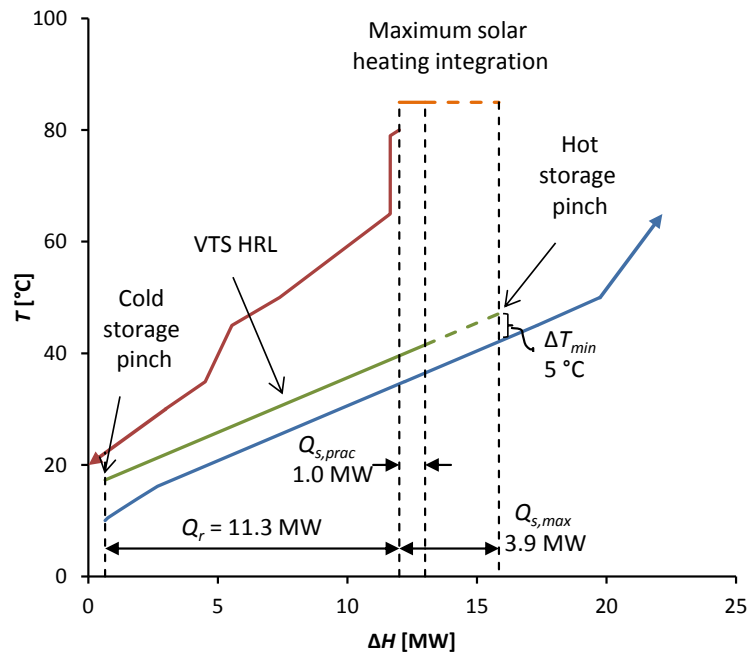


Figure 5-19: Maximum and practical average heat recovery and solar heating targets for a VTS HRL based on a  $\Delta T_{min}$  of 5 °C.

Achieving the maximum integration of solar heating is impractical due to the daily solar heating cycle requiring excessive thermal storage. By analysing the solar irradiance data it is found that 65 % of the day/night cycle is below the day/night irradiance average of 0.25 kW/m<sup>2</sup>. To account for the cyclic nature of solar availability an estimated 3000 m<sup>3</sup> of thermal storage is required whereas storage

for a HRL is typically less than 500 m<sup>3</sup>. If the outlet temperature of the solar collector was higher than 85 °C, which is the value used in this work, the amount of required storage could be lessened. There is an acute optimisation between solar collector temperature, collector heat loss and storage needs that may be analysed as part of future work.

A practical amount of solar heating that requires minimal storage can be calculated from  $Q_{s,max}$  assuming that  $Q_{s,max}$  is obtained by the daily average peak solar irradiance, for which there is sufficient sinks on average. As a result this maximum duty is scaled down by the ratio of day/night average to daily average peak solar irradiance ( $I$ ) to obtain a practical average duty of solar heating.

$$Q_{s,prac} = Q_{s,max} \frac{I_{s,ave}}{I_{s,peak}} \quad (5-13)$$

The practical amount of solar heating is estimated as 0.9 MW for the CTS design and 1.0 MW for the VTS design. Solar heating duty is a function of the collector area. If the solar collector size is based on the day/night solar irradiance average of 0.25 kW/m<sup>2</sup>, the collector would have insufficient area to achieve the desired average heating duty because the average irradiance value does not take into account the optical and heat losses of the collector. Preliminary analysis of the solar collector suggests that one square meter can average 0.178 kW for the day/night cycle. Without correctly taking into account optical and thermal losses the solar collector would be undersized by 30 % for this case and unable to meet its design duty. The solar collector needs to be 4776 m<sup>2</sup> for the CTS design and 5606 m<sup>2</sup> for the VTS design.

For solar heating, there is always a question of economic competitiveness. Since detailed analysis of solar heating fits in the fringes of the thesis aim as it relates to a HRL and displacing the use of fossil fuels for generating steam and not a focal point, the question of economic viability is viewed as out of scope for this work. Future work in this area should look at the economic optimisation of a HRL integrated with industrial solar, which may include the selection of the solar temperature as an additional degree of freedom.

### 5.4.6. Maximum energy recovery HRL designs

The design of a HRL requires the specification of heat exchanger areas and temperature control set points for the return temperature of the loop fluid to storage as provided in Table 5-2. These design values provide the details for the four HRL designs modelled using transient data. Other parameters such as the operating temperature of the storage units and the loop flow rate may be determined from these two specifications. Heat exchanger areas are sized based on the time average flow rate. Maximum heat recovery HRL designs are targeted to recover 8.3 MW for the CTS design and 11.3 MW for the VTS design with the option of integrating solar heating.

**Table 5-2: HRL design specifications.**

Stream	Loop temperature return set point [°C]				Area [m <sup>2</sup> ]			
	CTS	CTS with Solar	VTS	VTS with Solar	CTS	CTS with Solar	VTS	VTS with Solar
<i>Hot streams</i>								
Dryer Exhaust A	40.0	40.0	60.0	60.0	1156	1156	1613	1613
Dryer Exhaust B	40.0	40.0	60.0	60.0	607	607	847	847
Dryer Exhaust C	40.0	40.0	60.0	60.0	364	364	508	508
Dryer Exhaust D	40.0	40.0	60.0	60.0	231	231	323	323
Utility Unit A	40.0	40.0	40.0	40.0	9	9	7	7
Utility Unit B	40.0	40.0	40.0	40.0	9	9	7	7
Casien A	40.0	40.0	45.0	45.0	36	36	60	60
Casien B	40.0	40.0	45.0	45.0	53	53	89	89
Casien C	40.0	40.0	45.0	45.0	53	53	89	89
Condenser	40.0	40.0	75.0	75.0	5	5	10	10
Cheese A	40.0	40.0	29.9	29.9	0	0	125	125
Cheese B	40.0	40.0	29.9	29.9	0	0	144	144
Solar collector	40.0	40.0	80.0	80.0	0	4776	0	5606
Total Hot side HE area					2523	2523	3822	3822
Solar collector	40.0	40.0	80.0	80.0	0	4776	0	5606
<i>Cold streams</i>								
Site Hot Water	21.2	21.2	21.7	21.6	127	158	219	257
Milk Treatment A	21.2	21.2	14.7	14.8	85	100	205	230
Milk Treatment B	21.2	21.2	14.7	14.8	85	100	205	230
Milk Treatment C	21.2	21.2	15.3	15.3	94	111	221	249
Whey A	21.2	21.2	17.0	17.0	13	15	28	32
Whey B	21.2	21.2	19.2	19.2	7	8	14	16
Total Cold side HE area					411	494	890	1013

## 5.5. Transient modelling of HRL performance

### 5.5.1. HRL performance with 500 m<sup>3</sup> storage tanks

At any instance the combined heat recovery from the sources may not exactly match the combined heat transfer to the sinks. When that occurs there is a hot and cold imbalance. Most imbalances are short term only lasting for a couple of hours but it is possible that a long term imbalance is sustained for days when plants cease to run due to a lack of milk production from the farms. Short term imbalance is accommodated for by sizing sufficient thermal storage capacity in the HRL system. Long term imbalance results in one of the storage tanks becoming completely empty of fluid.

The instantaneous storage level and hot and cold storage temperatures across a 14 day period is presented in Figure 5-20 for the CTS design, Figure 5-21 for the CTS with solar design, Figure 5-22 for the VTS design and Figure 5-23 for the VTS with solar design. These plots demonstrate the real-time transient behaviour of dairy process streams and their associated heating and cooling demands impacting on the HRL operation. Even with 500 m<sup>3</sup> of thermal storage the hot storage tank can quickly fill or empty depending on the mix of streams available. The amount of thermal storage is related to the temperature difference of the hot and cold storage tanks (Table 5-3). A larger difference on average between the hot and cold storage tanks gives increased thermal density and capacity.

**Table 5-3: Average hot and cold storage temperatures and the associated impact on thermal storage density and capacity.**

Design	Average $T_{th}$ [°C]	Average $T_{lc}$ [°C]	$T_{th} - T_{lc}$ [°C]	Thermal storage density increase
CTS	40.0	21.2	18.8	-
CTS with solar	40.0	21.2	18.8	-
VTS	43.3	17.1	26.2	39 %
VTS with solar	44.6	17.1	27.5	46 %

The effect of adding solar heating to the HRL is visible in Figure 5-21 for the CTS design and Figure 5-23 for the VTS design. For the CTS system, the level of the hot storage tank rises and falls noticeably more than the design without solar. The rise

corresponds with daylight hours while the falls relate to night time and the lack of solar heating. The regular cyclic pattern of the hot storage temperature in Figure 5-23 for the VTS with solar design is caused by the day/night variations in solar availability. Shorter term variations result from the difference in mixed loop return temperatures from the various heat sources on the HRL. The amplitude of the temperature fluctuations is a function of the amount of hot fluid returned compared to the amount of hot fluid in storage.

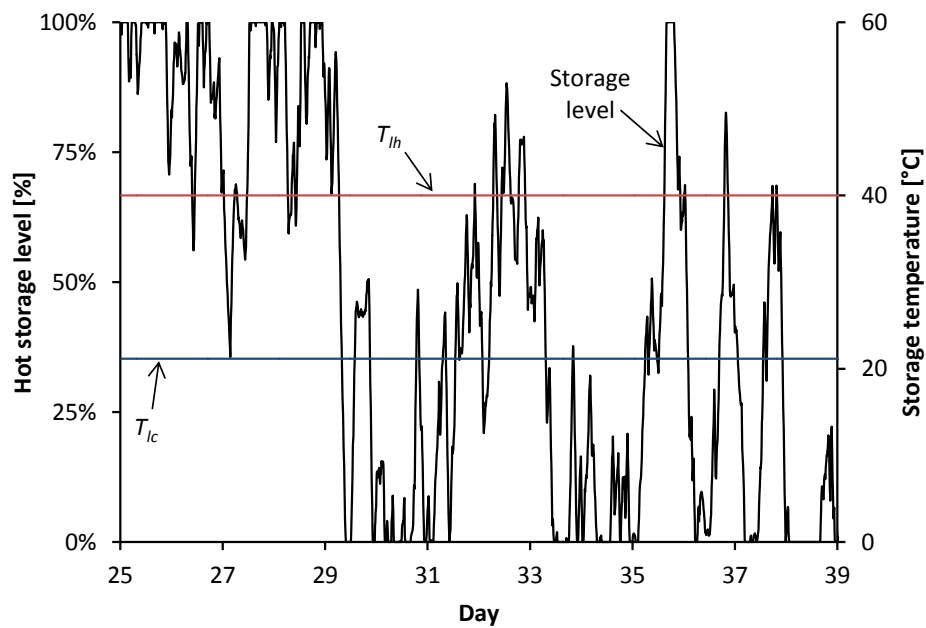


Figure 5-20: Thermal storage dynamics for CTS design using 500 m<sup>3</sup> hot and cold storage tanks.

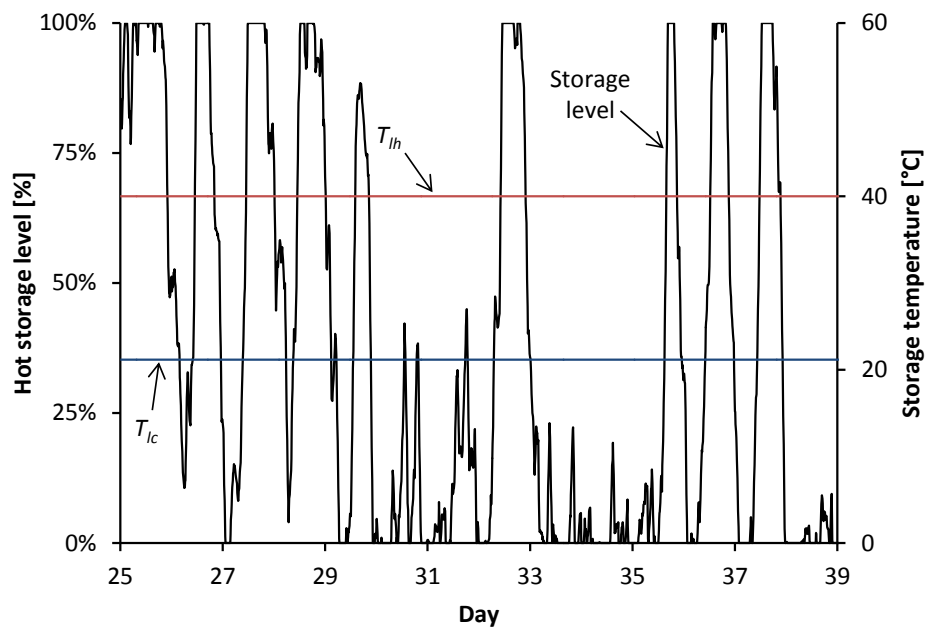


Figure 5-21: Thermal storage dynamics for CTS with solar heating design using 500 m<sup>3</sup> hot and cold storage tanks.

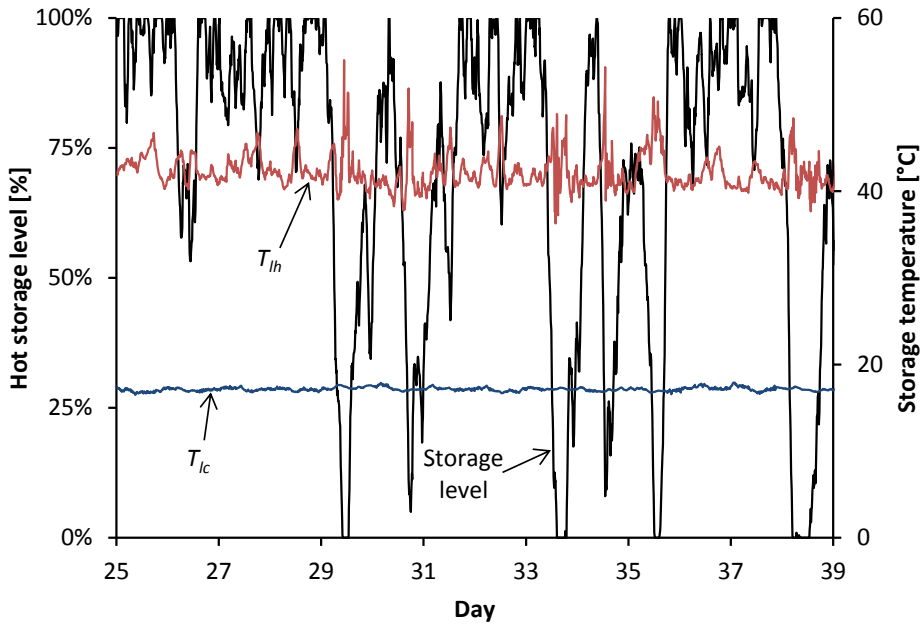


Figure 5-22: Thermal storage dynamics for VTS design using 500 m<sup>3</sup> hot and cold storage tanks.

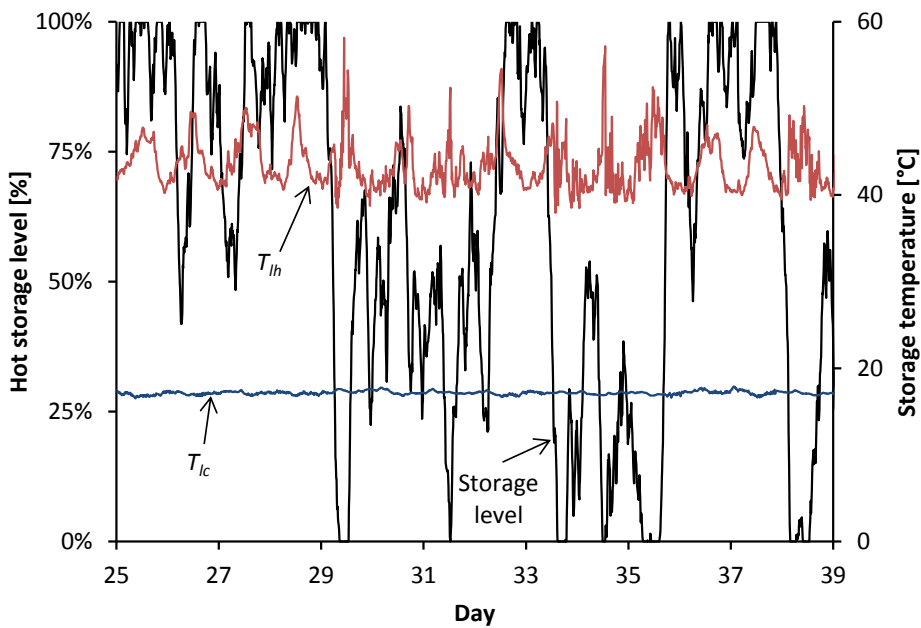


Figure 5-23: Thermal storage dynamics for VTS with solar heating design using 500 m<sup>3</sup> hot and cold storage tanks.

In contrast to the variable hot storage temperature, the cold storage temperature is fairly constant. Many of the sinks at the dairy factory are vital streams for the on-going site operation. These sinks include site hot water, which is constantly being used for washing, and milk treatment streams, which is a necessary process for treating the milk before it is processed into final products. The difference in supply temperature between the sinks is also small (10 – 16 °C).

The actual combined heat recovery and solar heating with 500 m<sup>3</sup> storage tanks is about 5 % less than the targeted values as shown in Table 5-4. The difference between these two values is a loss that can be attributed to three areas: (1) insufficient heat storage, (2) flow rate variability, and (3) temperature variability. These root causes for the drop in performance of the HRL compared to the targets is analysed in the next three sections.

**Table 5-4: Comparison of combined heat recovery and solar heating targets to actual modelled performance highlighting the root causes of the difference.**

Design	Combined heat recovery and solar heating [kW]		Root causes of performance reduction [kW]		
	Target	Actual	Insufficient heat storage	Flow rate variability	Temperature variability
CTS	8310 (100.0 %)	7872 (94.7 %)	223 (2.7 %)	166 (2.0 %)	49 (0.6 %)
CTS with solar	9160 (100.0 %)	8624 (94.1 %)	321 (3.5 %)	157 (1.7 %)	58 (0.6 %)
VTS	11347 (100.0 %)	10777 (95.0 %)	126 (1.1 %)	350 (3.1 %)	94 (0.8 %)
VTS with solar	12345 (100.0 %)	11700 (94.8 %)	121 (1.0 %)	350 (2.8 %)	174 (1.4 %)

### 5.5.2. Effect of storage volume on HRL performance

HRL performance has been modelled for storage capacities between 0 – 1000 m<sup>3</sup> (Figure 5-24) as well as the case of infinite storage capacity. HRL performance is characterised by the combination of heat recovery and solar heating that replaces the need for steam and hot water utility. With minimal storage the HRL system recovers a high percentage (92 – 94 %) of the heat recovery for the same design method with infinite storage. Issues relating to stream variability and availability on the required storage appear to be minimised by a number of sources and sinks on the HRL. As more sinks and sources are connected to the HRL, the degree of source to sink imbalance is reduced lessening the storage requirement. If there were only one source stream and one sink stream in the HRL, then the system would be out of balance whenever one stream is on while the other is off. But when a HRL system has multiple source/sink streams, the degree of imbalance is dampened by the fact the load is spread across more streams.

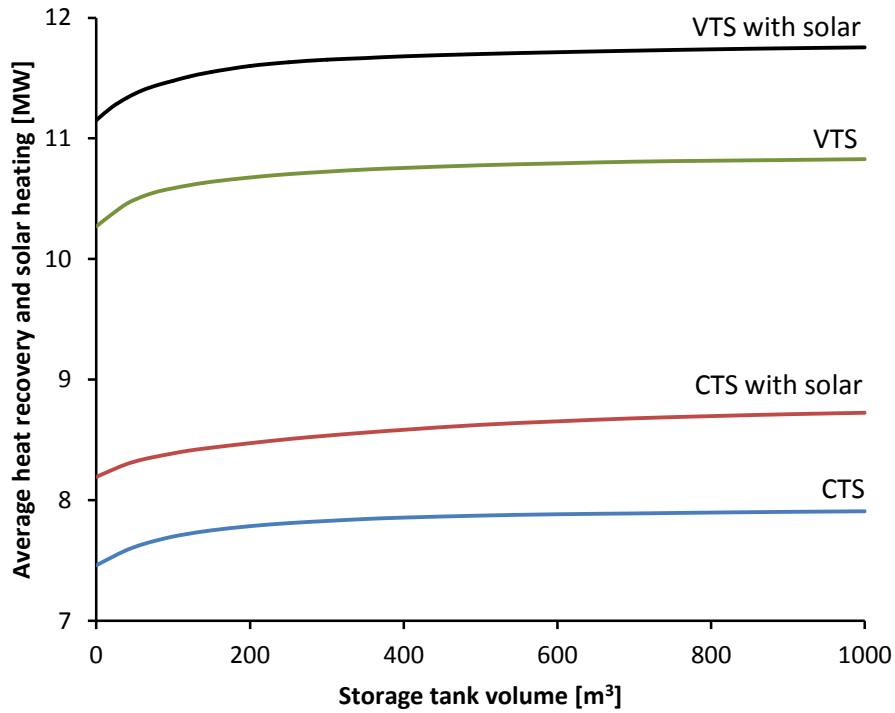


Figure 5-24: Effect of thermal storage volume on HRL performance.

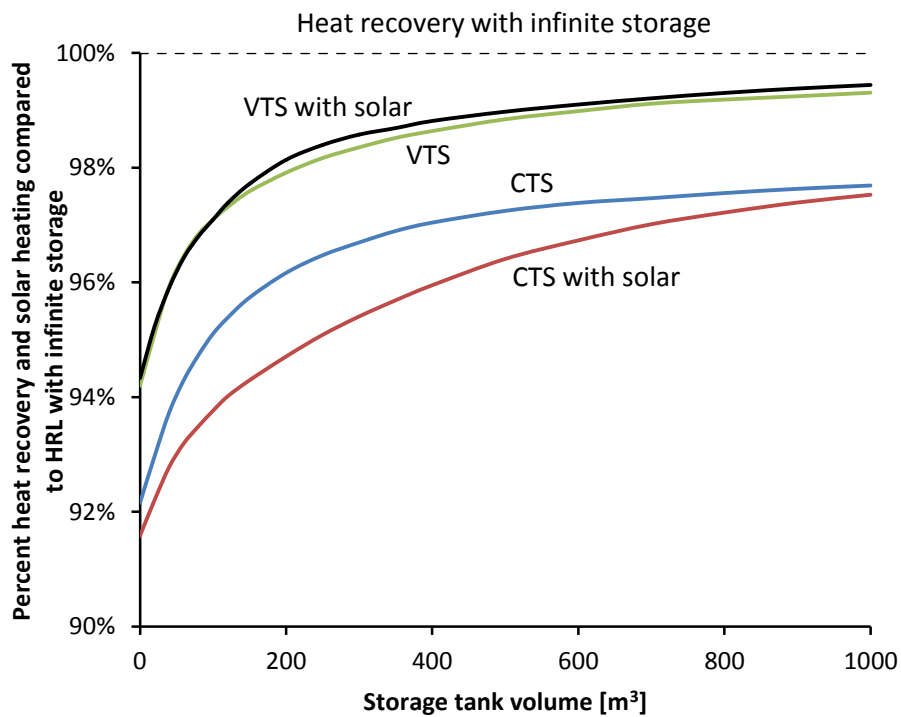


Figure 5-25: Effect of average thermal storage capacity on HRL performance as a percentage of the HRL performance with infinite storage.

Actual HRL performance for an effective thermal storage volume may also be characterised as a percentage of the HRL performance with infinite storage (Figure 5-25). The VTS designs require much less storage volume to achieve the

same HRL performance percentage as the CTS designs. The effective thermal storage energy densities in the VTS systems are higher due to a larger average temperature difference between hot and cold storage temperatures (Table 5-3).

### **5.5.3. Effect of off-design process flow rates on heat recovery**

As the process stream's flow rate changes, a simple feedback temperature control loop is used to adjust the flow rate of the loop to maintain a constant outlet (return) temperature of the loop fluid. When the process stream's flow rate is above its design value, the heat transfer film coefficients increase due to higher Reynolds numbers for the two fluids exchanging heat. This results in an increased pressure drop and  $\Delta T_{LM}$  due to a larger approach temperature. The duty of the exchanger is now greater than the design duty, although at the expense of increased pumping power. When the process stream's flow rate is below the design value,  $h$ ,  $U$ , pressure drop and the  $\Delta T_{LM}$  are decreased giving a reduced duty.

Figure 5-26 plots the actual heat exchanger duty against the heat capacity flow rate of Whey B (sink) using the CTS approach. The CTS design is analysed to remove any temperature variability effects. For Whey B the supply temperature is an assumed value and is constant for the entire analyse period. The difference between the actual points and the dashed diagonal line ( $n = 1.00$ , Eq. 5-10) represents the duty loss/gain caused by variable Whey B flow rates. The average actual duty was 117 kW while the time average targeted duty was 125 kW.

The degree to which the exchanger is above and below the targeted duty (diagonal line) is dependent on the  $n$  exponent in Eq. 5-10. The maximum value of  $n$  is unity. As  $n$  approaches unity, an increase or decrease in  $C$  above the design  $C$  of the process stream results in a proportional increase or decrease in  $U$  and a proportional increase or decrease in  $Q$ . As a result there is no reduction in temperature effectiveness based on the process stream with transient  $C$  values for  $n$  approaching unity as shown in Figure 5-27. This implies an important, and perhaps obvious result, that overall heat exchanger performance from transient process streams is always less efficient than from steady process streams with the

same time average flow rate and heat exchanger area because  $n$  is always significantly less than one in practice.

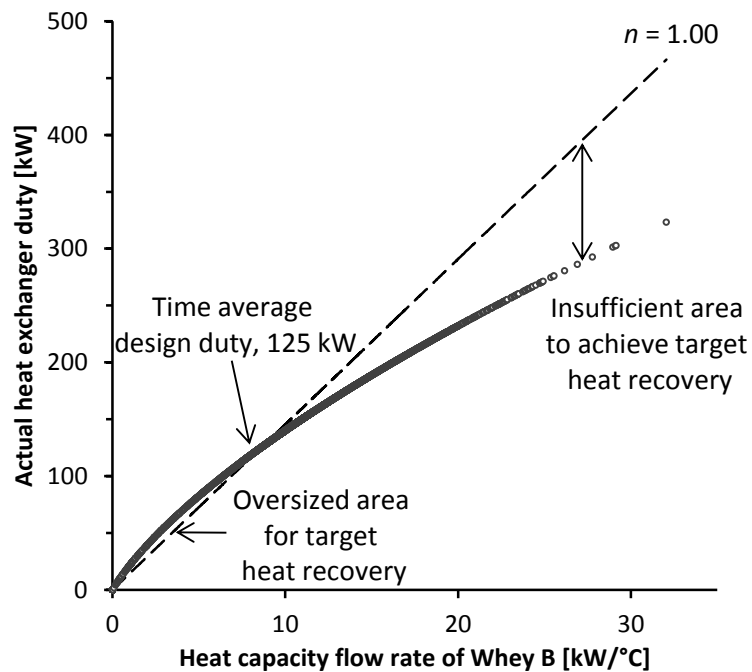


Figure 5-26: Actual duty versus heat capacity flow rate of Whey B for CTS design.

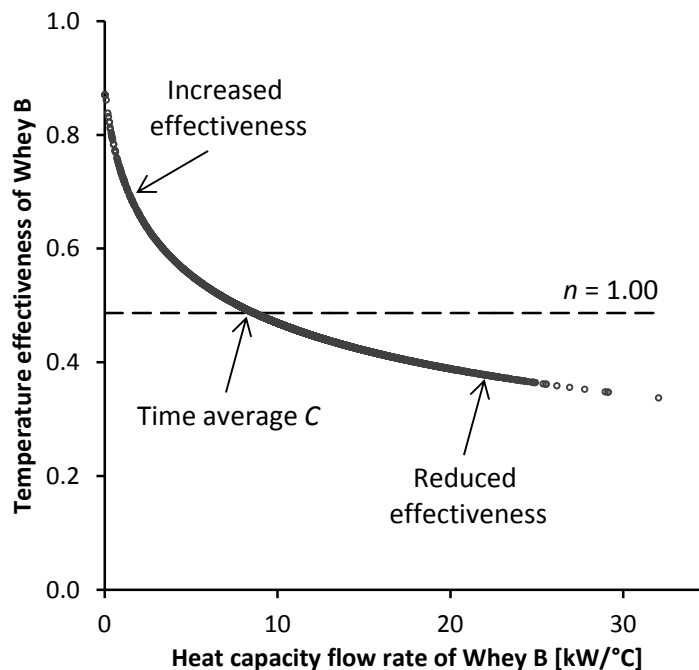


Figure 5-27: Temperature effectiveness versus heat capacity flow rate of Whey B for CTS design.

Figure 5-27 also shows that temperature effectiveness increases as the flow rate of the process stream is reduced. In essence, the heat exchanger is oversized for flow rates below the design value and undersized for flow rates above the design

value. It may appear that choosing a heat exchanger design with a high exponent  $n$  is advantageous. However the improved performance at higher flow rates will always come at the expense of increased pressure drop and pumping power, which has close to a squared relationship with velocity, which is proportional to flow rate.

#### **5.5.4. Effect of process supply temperature variability on heat recovery**

The third reason that the actual HRL performance is lower than the target is temperature variability. Figure 5-28 plots the temperature effectiveness of the Site Hot Water (SHW) heat exchanger against its inlet temperature. The CTS design is applied to illustrate the effect of process supply temperature variability on heat recovery, which ensures the supply and return temperatures of the HRL are constant. SHW is selected to demonstrate the effect of temperature variability because its inlet temperature is recorded and is known to fluctuate due to changing outside weather conditions as previously shown in Figure 5-7.

When the inlet temperature of SHW is less than the loop return set point temperature, the temperature effectiveness of the heat exchanger has some scatter. This scatter is caused by the fact the flow rate of the stream also has variability. To decouple the effects of flow rate variability and temperature variability, exponent  $n$  is set to unity eliminating the effect of flow rate variability from temperature effectiveness as shown by the red line. Low SHW inlet temperatures have high effectiveness and increased duty, whereas high inlet temperatures have low effectiveness and low duties. At times the actual effectiveness and heat exchanger duty are zero because the supply temperature of the process stream exceeds the return temperature set-point of the HRL fluid, which contributes to the amount of decrease HRL performance.

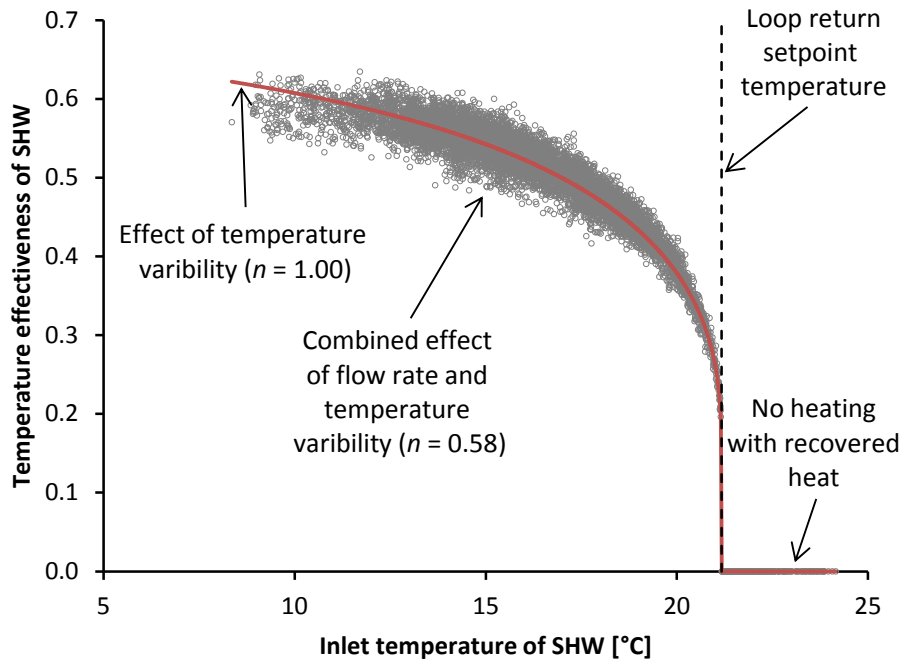


Figure 5-28: Temperature effectiveness versus inlet temperature of SHW for CTS design.

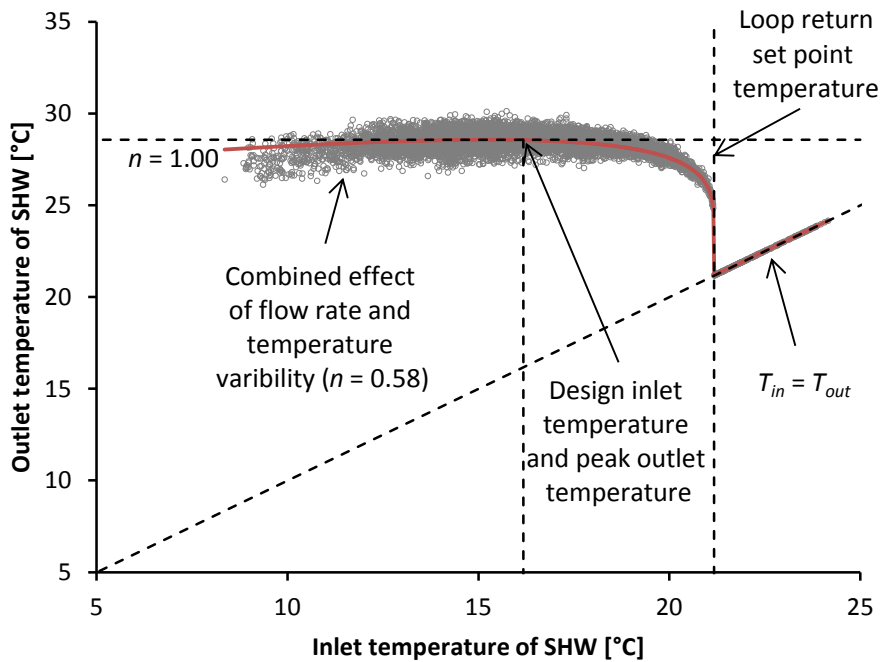


Figure 5-29: Outlet temperature versus inlet temperature of SHW for CTS design.

The effect of inlet temperature variability on heat exchanger performance can also be characterised by the outlet temperature of SHW as plotted in Figure 5-29. After decoupling the effects of flow rate and temperature variability by setting  $n$  to unity, it is noted that the peak outlet temperature of SHW is achieved when the inlet temperature is equal to the design value. This peak outlet temperature is same as the design outlet temperature. The gap between the red line in Figure 5-29 and

the design outlet temperature (28.5 °C) represents, therefore, the loss of duty due to inlet temperature variability for the SHW exchanger. However most (90 %) of the heat recovery loss tied up with the SHW exchanger is the result of high inlet temperatures causing the stream to be incompatible with the operation of the HRL.

### 5.5.5. The contribution of dryer exhaust heat recovery to improving HRL performance and site energy efficiency

The dairy factory has four milk powder plants. Dryer exhaust heat recovery from these plants contribute about 70 % of the heat recovery in the CTS designs and about 50 % of the heat recovery in the VTS designs (Table 5-5). Integrating the dryer exhaust with external operations to the milk powder plant is likely advantageous from a capital cost perspective. Dryer exhaust heat recovery represents the key that is able to unlock a new level of energy efficient dairy processing. Linking exhaust heat recovery into a VTS HRL with the added possibility of solar heating can reduce this site’s steam demand by 11.7 MW, which is utility cost savings of \$2.6 – \$4.0 million per annum.

**Table 5-5: Contributions to hot utility reduction assuming 500 m<sup>3</sup> of storage.**

Design	Dryer exhaust heat recovery [kW]	Other heat recovery [kW]	Solar heating [kW]	Total [kW]
CTS	5639	2233	0	7872
CTS with solar	5639	2134	851	8624
VTS	5644	5134	0	10777
VTS with solar	5643	5139	917	11700

## 5.6. Conclusion

Substantial heating and cooling savings can be gained in multi-plant dairy factories through better inter-plant heat integration via a HRL. The site chosen had available 12 source streams including four spray dryer exhausts and six sink streams. Added to the mix of streams was the option of solar heating. In this chapter, a new method for designing a HRL based on using a variable temperature storage system is presented.

Compared to the conventional HRL design based on a constant temperature storage system, this new method gives solutions with: (1) more effective distribution of temperature driving forces between heat exchangers resulting in higher  $\Delta T_{min}$  values for the same heat recovery, (2) lower average loop flow rates giving reduced pressure drop and pumping requirements, (3) increased average temperature difference between hot and cold storage temperatures increasing thermal storage density and capacity, and (4) requires less thermal storage. The dairy factory analysed lacked sufficient sources. The addition of the dryer exhausts as heat sources was a critical factor in gaining a heat recovery of 10.8 MW for the variable temperature storage design, of which 5.1 MW was contributed from exhaust heat recovery. Solar heating also proved to be a valuable source with the maximum addition of 0.9 MW of heating on average.

# Chapter 6

## A criterion for skim milk powder deposition on stainless steel surfaces

---

### 6.1. Introduction

Dryer exhaust heat recovery represents a potential step change in energy efficiency for the dairy industry regardless of whether the heat is used internally within the milk powder plant or externally in neighbouring processes. However industry concerns regarding milk powder fouling of a dryer exhaust heat exchanger need to be addressed.

The dryer exhaust air contains a low concentration of milk powder (2 – 20 mg/m<sup>3</sup>). In other unit operations such as the main drying chamber, fluidised beds and cyclones, the problem of milk powder fouling and deposition on equipment surfaces is well known (Boonyai et al., 2004). Dryer air temperatures, humidity and flow rates are normally manipulated to maximise drying capacity, while maintaining manageable levels of deposition, which must be cleaned after two to four weeks. Excessive build-up of deposits on dryer walls, transport ducts, and cyclones leads to plant down-time. Time on-product is highly valuable to the dairy industry, especially during the peak of the season. Exhaust heat recovery presents, therefore, another possible piece of equipment that could foul causing blockages and requiring additional unplanned process shut-downs.

Over the past few decades, milk powder fouling, deposition and stickiness has been the focus of numerous studies, e.g. (Chen et al., 1993; Hennigs et al., 2001; Intipunya et al., 2009; Kota and Langrish, 2006; Paterson et al., 2007a; Zuo et al., 2007). Even with all the fantastic effort that has been put into understanding milk powder stickiness and deposition, the literature review in Chapter 2 showed that there is a gap in the knowledge of an experimentally validated model that

successfully describes the adhesion of impacting milk powder particles on surfaces.

The contribution of this chapter is to develop and experimentally validate a suitable model to describe the adhesion of Skim Milk Powder (SMP) onto a flat stainless steel surface. Factors contributing to deposition that are studied include: air temperature and humidity, particle size and mass distribution, impact velocity and angle, and plate temperature. To describe these known effects, a simple elastic contact model with adhesion is derived and its constants solved by fitting the model to experimental data. Data from several literature sources are included when validating the model. This validated semi-empirical model is applied in Chapter 7 to understand deposition that occurs on fins and tubes and to predict where and how much deposition will occur in a dryer exhaust heat exchanger as part of Chapter 8.

## 6.2. Theory of particle-wall contact mechanics

In this section the derivation of a criterion is presented that describes the collision of an adhesive elastic sphere against a solid wall. The criterion is based on the works of Johnston, Kendall and Roberts (1971), Savkoor and Briggs (1977) and Thornton and Ning (1998) to describe the contact kinetics of an elastic particle impacting a rigid wall, in combination with the work of Williams et al. (1955) to describe the temperature dependency of the surface viscosity and adhesion energy of a particle. The combining of these two bodies of work has generated a functional and novel criterion that describes the attachment of variably adhesive particles, such as SMP.

The energy balance of a particle-surface collision is

$$E_{k,i} = E_{k,f} + W_a + E_{pd} + \Delta E_{rot} \quad (6-1)$$

where  $E_{k,i}$  and  $E_{k,f}$  are the initial and final kinetic energy of a particle colliding with a surface,  $W_a$  is the work of adhesion,  $E_{pd}$  is the energy of plastic deformation, and  $\Delta E_{rot}$  is change in rotational energy. If it is assumed that  $E_{pd}$  and  $\Delta E_{rot}$  are zero, then

a particle sticks when the incoming kinetic energy is less than the work of adhesion, which may be determined by

$$W_a = \int_{\delta_c}^0 F_n' d\delta \quad (6-2)$$

where  $F_n'$  is the equivalent normal force and  $\delta$  is the penetration depth.

Thornton and Ning (1998) applied numerical integration to find the equivalent expression

$$W_a = 0.9355 F_s \delta_{crit} \quad (6-3)$$

where  $F_s$  is the pull-off force (adhesion force) and  $\delta_{crit}$  is the critical (negative) penetration depth at which separation is imminent. Thornton and Ning (1998) then applied Eq. 6-3 to normal impacts and produced a model that describes sticking and restitution of a particle. In this work, we extend the application of Eq. 6-3 to sticking at non-normal impacts, but do not attempt to completely describe the rebound of a particle. It is at this point that the derivation now turns to the work of Savkoor and Briggs (1977) to described when an adhesive elastic sphere sticks at oblique impacts given known normal ( $F_n$ ) and tangential ( $F_t$ ) loadings. Savkoor and Briggs (1977) presented the following condition for sticking to occur

$$9\pi^2 r^2 \gamma_s^2 + 6F_n \pi r \gamma_s - \frac{Y^*}{4G^*} F_t^2 \geq 0 \quad (6-4)$$

where  $\frac{1}{Y^*} = \frac{1-\nu_1^2}{Y_1} + \frac{1-\nu_2^2}{Y_2}$ ,  $\frac{1}{G^*} = \frac{2-\nu_1^2}{G_1} + \frac{2-\nu_2^2}{G_2}$

In the above equation,  $\gamma_s$  is the surface adhesion bond strength,  $r$  is the particle radius,  $Y$  is Young's modulus,  $\nu$  is Poisson's ratio,  $G$  is the shear modulus and subscripts 1 and 2 refer to properties of the particle and surface. As a simplification, in this work it is assumed ratio of the normal and tangential forces are related through the normal impact angle and a proportionality constant  $B$ ,

$$\frac{F_t}{F_n} \approx \frac{dF_t}{dF_n} = -B \tan(\Theta_n) \quad (6-5)$$

The adhesion pull-off force,  $F_s$ , required to prevent particle detachment at the boundary between stick/rebound is found when Eq. 6-4 is set equal to zero

$$9\pi^2 r^2 \gamma_s^2 - 6F_s \pi r \gamma_s - \frac{Y^* B^2}{4G^*} \tan^2(\Theta_n) F_s^2 = 0, \quad \text{where } F_s = -F_n \quad (6-6)$$

which may be rearranged to make  $F_s$  the subject,

$$F_s = \frac{3}{2} \pi r \gamma_s \lambda, \quad \text{where } \lambda = 2 \left( 1 + \sqrt{1 + \frac{Y^* B^2}{4G^*} \tan^2(\Theta_n)} \right)^{-1} \quad (6-7)$$

Johnston, Kendall and Roberts (1971) derived the pull-off force for normal impacts

as  $F_{s(0)} = \frac{3}{2} \pi r \gamma_s$ , which solution is obtained by setting  $\Theta_n = 0$  in Eq. 6-7.

The solution to the critical penetration depth is (Thornton and Ning, 1998),

$$\delta_{crit} = \left( \frac{5\pi \gamma_s r^{1/2} \lambda}{8Y^*} \right)^{2/3} \quad (6-8)$$

Substituting Eq. 6-7 and 6-8 into Eq. 6-3 and simplifying gives

$$W_a = 6.913 \left( \frac{r^4 \gamma_s^5 \lambda^5}{Y^{*2}} \right)^{1/3} \quad (6-9)$$

For sticking, Eq. 6-9, the effective work of adhesion in the normal direction, must equal to or greater than the kinetic energy of the particle in the normal direction,

$$\frac{1}{2} m v_n^2 \leq 6.913 \left( \frac{r^4 \gamma_s^5 \lambda^5}{Y^{*2}} \right)^{1/3}, \quad \text{where } m = \frac{4}{3} \pi r^3 \rho \quad (6-10)$$

Eq. 6-11 is obtained by making  $\gamma$  the subject

$$\gamma_s \geq 0.2442 r \rho^{3/5} v_n^{6/5} Y^{*2/5} \left( 1 + \sqrt{1 + \frac{Y^* B^2}{4G^*} \tan^2(\Theta_n)} \right) \quad (6-11)$$

In this work the adhesion bond strength,  $\gamma_s$ , is related to  $T - T_g$ , i.e. particle surface stickiness, through viscosity. To link  $\gamma_s$  to  $T - T_g$ , the adhesion bond strength,  $\gamma_s$ ,

using the adhesion bond strength at the glass transition temperature as the basis is postulated to be proportional to the inverse of the ratio of the surface viscosity,  $\mu$ , of the particle using the viscosity at the glass transition temperature as the basis such that

$$\frac{\gamma_s}{\gamma_g} = a \left( \frac{\mu}{\mu_g} \right)^{-1} \quad (6-12)$$

where  $a$  is a dimensionless proportionality constant and subscript  $g$  refers to the property at the glass transition temperature. Viscosity is related to  $T - T_g$  as described by the WLF equation (see Chapter 2, Eq. 2-8). Combining the WLF equation and 6-12 and rearranging gives

$$\gamma_s = a \gamma_g 10^{\left( \frac{D_1 (T - T_g)}{D_2 + (T - T_g)} \right)} \quad (6-13)$$

By equating Eq. 6-11 and 6-13, a model is formed that describes the critical boundary between adhesion and rebound of particles.

$$0.2442 r \rho^{3/5} v_n^{6/5} Y^{*2/5} \left( 1 + \sqrt{1 + \frac{Y^* B^2}{4G^*} \tan^2(\Theta_n)} \right) = a \gamma_g 10^{\left( \frac{D_1 (T - T_g)_{crit}^*}{D_2 + (T - T_g)_{crit}^*} \right)} \quad (6-14)$$

Eq. 6-14 is rearranged to make  $T - T_g$  the subject to obtain

$$(T - T_g)_{crit}^* = \frac{D_2 \log \left( \frac{0.2442 r \rho^{3/5} v_n^{6/5} Y^{*2/5} \left( 1 + \sqrt{1 + \frac{Y^* B^2}{4G^*} \tan^2(\Theta_n)} \right)}{a \gamma_g} \right)}{D_1 - \log \left( \frac{0.2442 r \rho^{3/5} v_n^{6/5} Y^{*2/5} \left( 1 + \sqrt{1 + \frac{Y^* B^2}{4G^*} \tan^2(\Theta_n)} \right)}{a \gamma_g} \right)} \quad (6-15)$$

In its present form Eq. 6-15 is a theoretical description of the critical  $T - T_g$  conditions required for a particle to stick. The following experimental work was carried out to determine the constants  $a$ ,  $B$ ,  $D_1$ , and  $D_2$  in Eq. 6-15 and to validate the functional form of the model. It is important to note that the deposition model

derived encompasses a number of simplifications such as particles are assumed to be spherical, incoming rotational energy to the collision is zero, and plastic deformation is zero. These simplifications are considered to be of a low order of magnitude compared to effects of as particle size, velocity, etc.

## 6.3. Experimental methods

### 6.3.1. Particle gun operation

The particle gun is an experimental test that looks at deposition on a flat plate in an impingement jet (Paterson et al., 2007a). The particle gun delivers air at a controllable temperature (20 – 90 °C), relative humidity (0 – 100 %) and average jet velocity (0 – 40 m/s). It functions by bubbling compressed air through a temperature regulated hot water tank. Depending on the tank water temperature and pressure (regulators  $P_2$  and  $P_3$  in Figure 6-1), the air moisture content is controlled. Adjusting  $P_3$  controls the air flow rate exiting the tank.

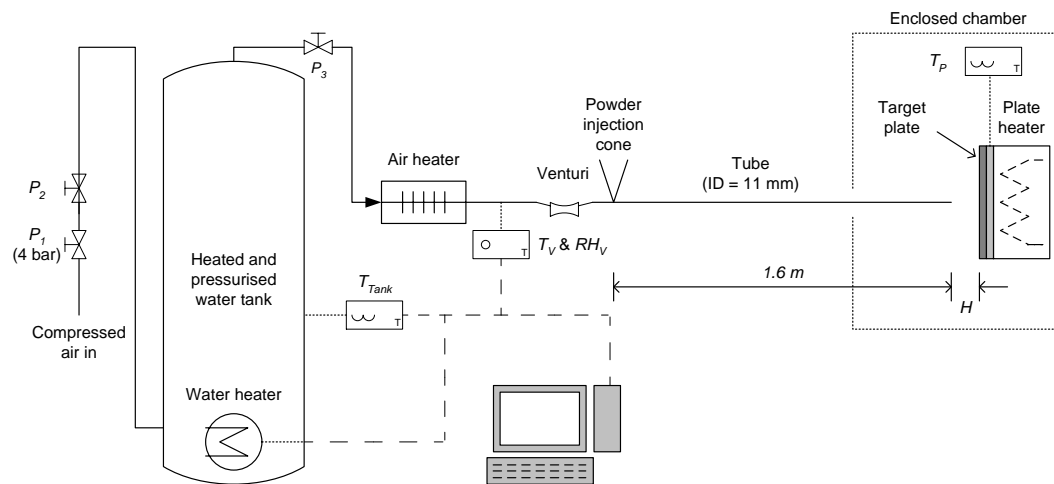


Figure 6-1: Schematic of the particle gun test apparatus.

After exiting the tank, moist air passes through a 400 W heater to reach the required temperature. Temperature ( $T_V$ ) and relative humidity ( $RH_V$ ) readings are logged immediately before a Venturi. Immediately following the Venturi, powder is injected through a cone with the aid of a little air suction. A tape heater is wrapped around the powder injection cone to eliminate condensation forming and to increase powder flowability into the air. The particle-laden air then develops along a 1.6 m insulated 11 mm tube (inside diameter), before impacting

a target plate. The particle surfaces are assumed to be in equilibrium with the air and impact the plate at the same speed as the jet (Paterson et al., 2007a). Air Reynolds numbers ranged from 4200 – 18800, indicating the air is fully turbulent.

Air temperature and relative humidity are logged before the Venturi. Using this temperature and relative humidity, the absolute humidity is calculated. Air temperature ( $T$ ) is also regularly measured at the end of the tube. By using a water mass balance around the Venturi, the air moisture content in the tube is calculated. This mass balance takes into account ambient air sucked in through the Venturi. Knowing  $T$  and the absolute humidity in the tube, the relative humidity ( $RH$ ) is also determined. At the time of impact with the plate, particles are estimated to have a surface temperature and water activity in equilibrium with  $T$  and  $RH$ . Plate temperature is measured using a K-type thermocouple slotted into a hole in the aluminium plate. A polished 304 stainless steel plate, 150 mm square, is used as the target plate. Jet velocity is measured using a 15 mm diameter impeller anemometer, 10 mm from the tube end. Anemometer readings are corrected through the aid of PIV analysis to give a more accurate average jet velocity across the 11 mm tube.

Tests performed analyse the effects of plate (or wall) temperature and particle size, velocity and impact angle on deposition and the minimum required  $T - T_g$ , which is a function of air temperature and relative humidity, to achieve deposition. For each test the amount of deposition at the centre of the collection is weighed, which helped reinforce the identification of critical  $T - T_g$  values.

### **6.3.2. Particle size distribution analysis**

Powders used in the deposition tests include agglomerated and non-agglomerated SMP. Bulk non-agglomerated SMP has a lower particle size distribution whereas agglomerated SMP has a high particle size distribution. These bulk powders were also mechanically sieved to create several size fractions (Table 6-1). By using both types of powder a wider range of particle size fractions were able to be obtained and tested than if only agglomerated or non-agglomerated powder was sieved. The various size fractions are identified by referring to the medium,  $d_{(0.5)}$ . Particle

size distributions were measured in iso-propanol using a Malvern Mastersizer 2000 according to the method outlined by Pisecky (1997).

**Table 6-1: SMP particle size distribution parameters used in deposition tests.**

<b>Agglomerated (Y/N)</b>	<b><math>d_{(0.1)}</math> (<math>\mu\text{m}</math>)</b>	<b><math>d_{(0.5)}</math> (<math>\mu\text{m}</math>)</b>	<b><math>d_{(0.9)}</math> (<math>\mu\text{m}</math>)</b>
N	18	30	57
N	31	51	87
N	32	61	140
N	39	104	202
Y	66	108	172
Y	101	170	285
Y	98	268	571
Y	164	303	532
Y	410	686	1159
Y	431	893	1488

### **6.3.3. Visualisation of impingement jet airflow patterns**

A PIV flow visualisation technique has been successfully applied to characterise the impingement jet air flow patterns of the particle gun set-up at average jet velocities of 8.0, 10.0, 15.0, 25.0 and 35.8 m/s. PIV uses a thin laser light sheet orientated parallel to the seeded gas or liquid flow. Dispersion of the light sheet caused by the seeded particles is captured by a camera fixed perpendicular to the sheet. Two images are taken in quick succession ( $\approx 10 \mu\text{s}$ ). These are compared and processed using cross correlation computer algorithms. From this analysis full velocity flow fields are obtained. For further information on PIV, refer to Raffel et al. (2007).

Impingement jet characteristic dimensions for the PIV analysis mirrored those used for the powder adhesion tests. Fine paraffin liquid particles were seeded into the air jet by a Flow Tracker 700 CE fluid atomiser at 1.5 bar. After impacting the wall, some particles were observed to stick to the plate, although enough remained in the air flow to capture the flow field in and around the jet. The light sheet was produced by a Nd:YAG laser (526 nm) and position in the jet centre,

parallel to the jet flow. A Nikon FlowSense 4M MKII camera with resolution 2048 x 2048 pixels was fixed perpendicular to and focused on the light sheet.

For analysis, 200 double frame images at 1 Hz and 10  $\mu$ s between frames are captured. These are analysed using an average cross correlation method with an interrogation area of 32 pixels square and an overlap of 50 % in both the horizontal and vertical directions. A No-DC filter, a peak height ratio filter and a moving average filter were successively applied to remove inconsistent vectors. Interpolation of the neighbouring vectors replaced deleted vectors. Maximum velocities in the jet's centre have been checked using a TSI 8386-M-GB hot wire anemometer.

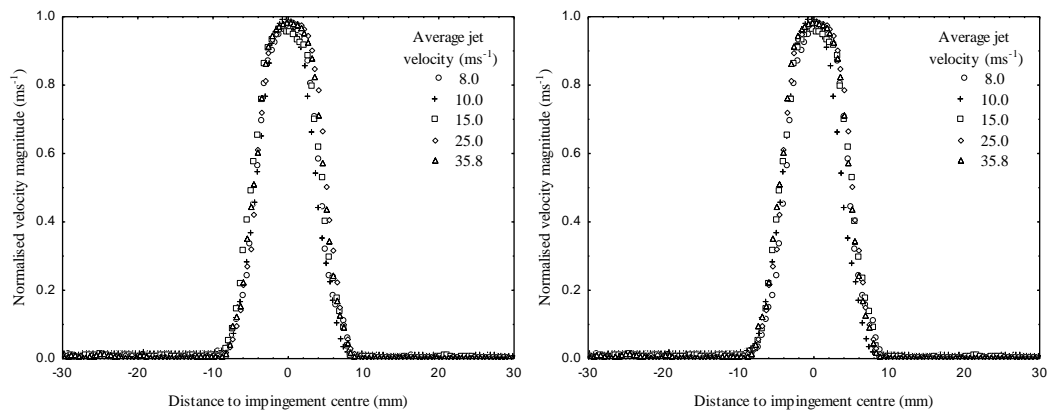


**Figure 6-2: Normalised velocity profile 10 mm (a) and 20 mm (b) away from and parallel to the plate obtained using PIV.**

For comparison of the different average jet velocities, profile cuts 10 mm and 20 mm away from the plate are plotted (Figure 6-2). Velocities have been normalised by dividing by the maximum velocity. Both normalised velocity profiles suggest the shape of the jet does not change significantly within the average velocity range of 8.0 to 35.8  $\text{ms}^{-1}$ . Therefore Figure 6-3 is representative of all average velocities. Results increased understanding of air flow interaction with the plate boundary. The normalised velocity contour plot, Figure 6-3, shows the jet spreads only a little before interacting with the plate. In the centre of the jet is a stagnation zone.

During deposition testing, the jet velocity was measured using an anemometer and correlated with the aid of PIV to ensure accurate estimate average jet velocity

and peak velocity (Figure 6-4). All reported jet velocities are the average velocity across the tube exit and they have been corrected using the equations shown in Figure 6-4. In most previous particle gun studies no correction was made to account for the difference in size (if there was one) between the jet and vane anemometer diameters (Paterson, 2011). Zhao (2009) also used PIV to successful correct anemometer readings.

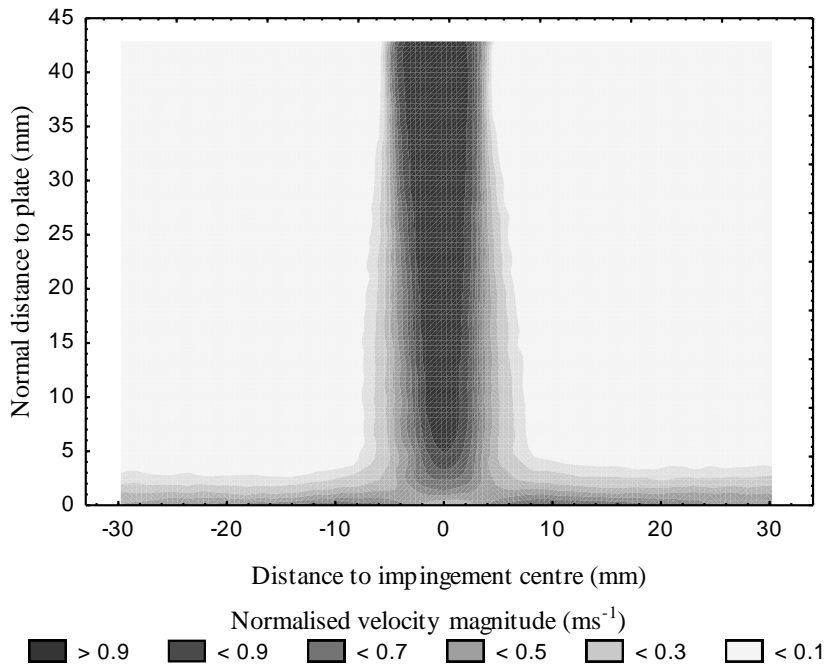


Figure 6-3: Normalised velocity magnitude contours of a normal impingement jet obtained using PIV.

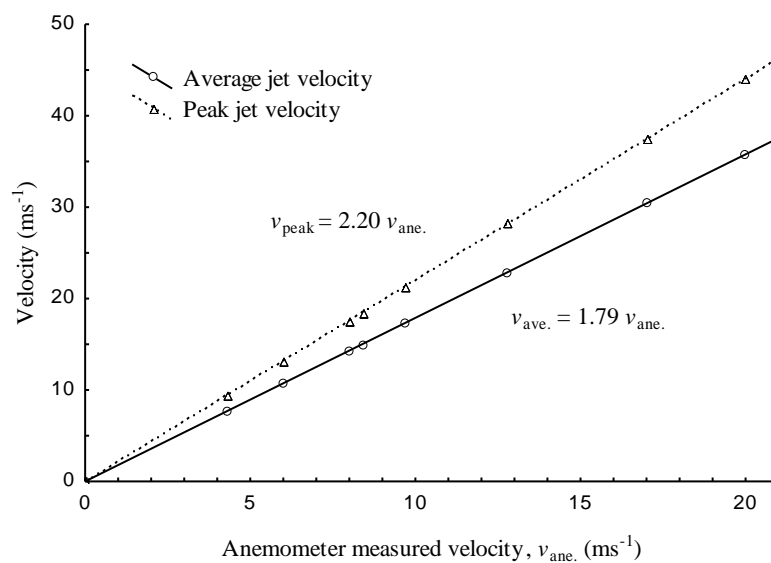
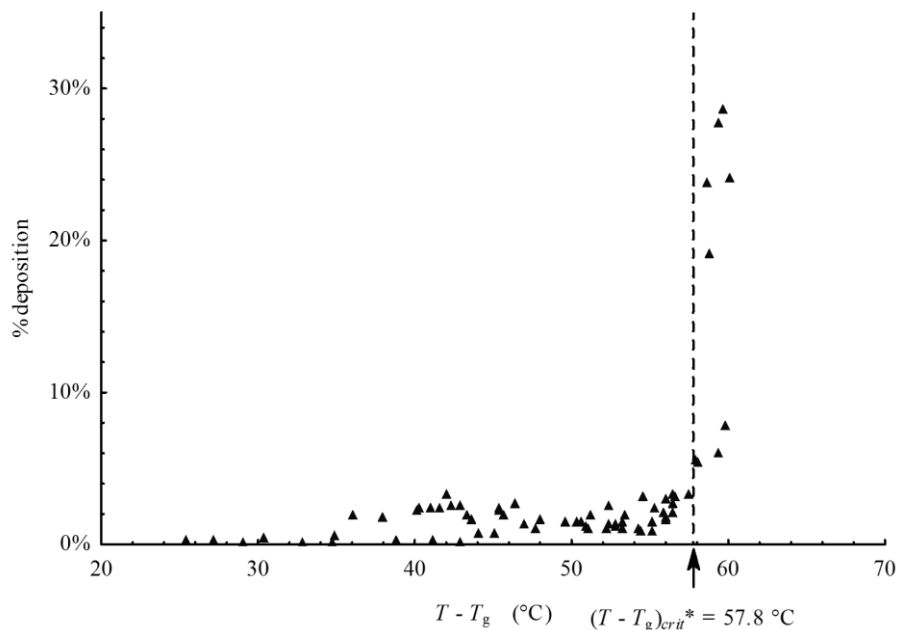


Figure 6-4: Correlation between PIV and 15 mm diameter anemometer velocities of a 11 mm air jet.

### 6.3.4. Determination of $(T - T_g)_{crit}^*$

The critical  $T - T_g$  is defined as the deposition onset point on a deposition % in the impingement zone versus  $T - T_g$  graph (Figure 6-5). Deposition % is the amount of powder deposited divided by the amount of powder injected into the test rig. Deposits located outside the impingement zone (approximately the size of the tube) are not included when measuring the deposition because the conditions, i.e. air temperature, humidity and velocity, causing the powder to stick is unknown and may significantly differ from the impingement jet conditions. Plots similar to Figure 6-5 were required to determine the critical  $T - T_g$  for each test condition reported in this work.



**Figure 6-5: Effect of  $T - T_g$  on the deposition % at the centre of the plate. Test conditions:  $d_{(0.5)}$  267  $\mu\text{m}$ , average jet velocity 15.0 m/s and normal impingement.**

$T - T_g$  or stickiness is a function of the combined effects of air temperature and relative humidity where  $T$  is taken as the air temperature (dry bulb) and  $T_g$  is calculated using the Gordon-Taylor equation presented in Chapter 2. Relative humidity and water activity are assumed to be the same. As will be shown, the critical  $T - T_g$  is affected by the plate temperature that a particle impacts. It is therefore necessary to make a correction for this effect when the plate ( $T_p$ ) and air ( $T$ ) temperatures are different. To account for this effect, the following linear relationship was experimental found

$$\left(T - T_g^*\right)_{T=T_p} = \left(T - T_g\right)_{T \neq T_p} + 0.26(T - T_p) \quad (6-16)$$

The determination of  $(T - T_g)_{crit}$  is a significant point of difference between this work and previous studies that have employed the particle gun test but included any deposit attached to the collection plate at the end of a run (Paterson et al., 2007a; Zhao, 2009). As a result, the  $(T - T_g)_{crit}$  calculated in this work are differentiated from previous definitions by using a \*.  $(T - T_g)_{crit}^*$  is standardised for plate temperature effects using Eq. 6-16 so that  $T = T_p$ .

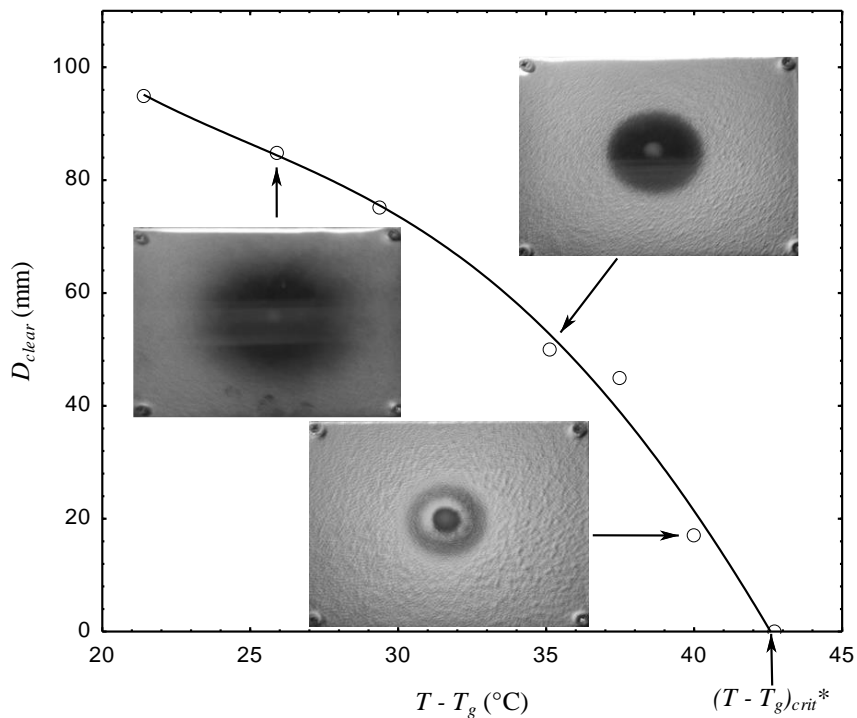


**Figure 6-6: Effect of  $T - T_g$  on the clear ring diameter. Test conditions:  $d_{(0.5)}$  61  $\mu\text{m}$ , normal impingement and jet velocity 15.0  $\text{ms}^{-1}$ , data from Zhao (2009).**

Using the data of Zhao (2009), Figure 6-6 is constructed to illustrate that significant deposition occurs outside the impingement zone at low  $T - T_g$  stickiness values before deposition is concentrated within the impingement zone. It is interesting to note that after heating the target plate to ensure the jet and plate are at the same temperature, the deposition at the periphery of the plate almost completely ceased. Controlling the plate temperature is also a clear point of difference between this work and previous works by Paterson et al. (Paterson et al., 2007a) and Zhao (2009).

## 6.4. Experimental deposition results

### 6.4.1. Effect of plate temperature on $(T - T_g)_{crit}^*$

Results show an increase in plate temperature relative to the jet temperature  $(T - T_p)$ , slightly increases  $(T - T_g)_{crit}^*$  and decreases deposition, for air and plate temperatures below 90 °C (Figure 6-7). Figure 6-7 shows trends for 15.0 and 25.0 m/s jet velocities and an estimate for a lower velocity of 5.4 m/s using the same slope. The estimate shows the relative influence of plate temperature compared to velocity.

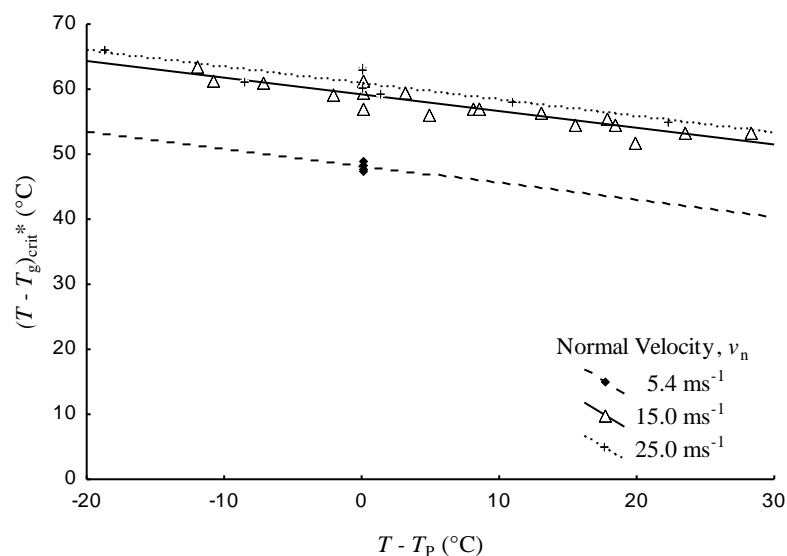


**Figure 6-7: Influence of plate temperature on  $(T - T_g)_{crit}^*$ . Test conditions:  $d_{(0.5)}$  267  $\mu\text{m}$  and normal impingement.**

When the plate and jet are different temperatures, the region in front of the plate has a temperature and relative humidity gradient. The interaction of this region on stickiness is complex. On a macro-scale, Figure 6-7 shows a linear relationship between  $T - T_p$  and  $(T - T_g)_{crit}^*$ . Since the relationship between  $T_g$  and RH is non-linear, the trend in Figure 6-7 suggests that the temperature gradient in front of the plate mostly affects the temperature at the surface of the particle; rather than its water activity.

The effect of plate temperature also has significant industrial application. Where processing equipment – dryers, transport ducts, cyclones and fluidised beds – are un-insulated and deposition is a key issue, one possible solution is to insulate the

walls. Insulation effectively increases the wall temperature, which increases  $(T - T_g)_{crit}^*$  and is likely to result in reduced deposition, e.g. Chen et al. (1993).

### 6.4.2. Effect of particle size distribution

Figure 6-8 shows that smaller particles having significantly lower  $(T - T_g)_{crit}^*$  values. This result is consistent with the well-known observation that smaller particles have greater agglomeration and deposition tendencies. Of particular note is the log scale applied to the  $d_{(0.5)}$  axis to yield a straight line for the data. In the formation of trend line equations,  $d_{(0.5)}$  is assumed to be equivalent to a uniform particle diameter,  $d_p$ .

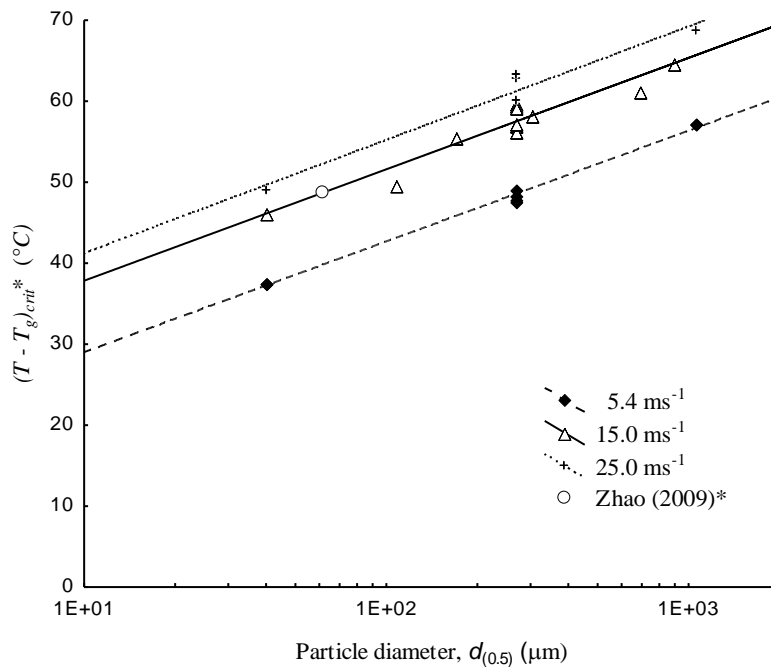


**Figure 6-8: Effect of particle size on  $(T - T_g)_{crit}^*$  in a normal impingement jet. Trends for 5.4 and 25.0 m/s are estimates.**

When Zhao (2009) published his results, focus was given to calculation of  $(T - T_g)_{crit}$  values where the deposition % was based on all deposits attached to the target plate. In this study, only deposits at the jet's central zone are included in the deposition %. Photographs of the deposition morphology were taken by Zhao, which has allowed the authors to reanalyse Zhao's results to obtain the data points in Figure 6-8 and later in Figure 6-9. Since Zhao did not control the temperature of the plate, corrections for a difference in temperature between the plate and jet (23  $^{\circ}\text{C}$ ) have also been carried out, as indicated using a \*, according to the slope of

the trend line in Figure 6-7. Walmsley et al. (2010) showed that without temperature control, the difference between the jet and plate temperatures, i.e.  $T - T_p$ , is 23.2 °C for the same set-up as Zhao. Figure 6-8 also shows trend estimates for 5.4 and 25.0 m/s, drawn using the same slope as the 15.0 m/s trend line and offset by the few data points measured. It is worthy to note that work by Paterson and co-workers did not focus on the effect of particle size.

### 6.4.3. Effects of impact velocity and angle on $(T - T_g)_{crit}^*$

In general, higher particle impact velocities, as a result of higher air flow, result in less deposition. In this analysis it is assumed that particles impact with the same velocity and angle as the jet is positioned relative to the target plate. When the jet is at an angle, then both a normal component and tangential velocity component arise. The effect of normal velocity on  $(T - T_g)_{crit}^*$  is presented in Figure 6-9. Of particular note is the log scale on the  $v_n$  axis applied to obtain a straight line. Trend lines for particle size distributions 100 and 500  $\mu\text{m}$  have been estimated using offsets shown in Figure 6-8.

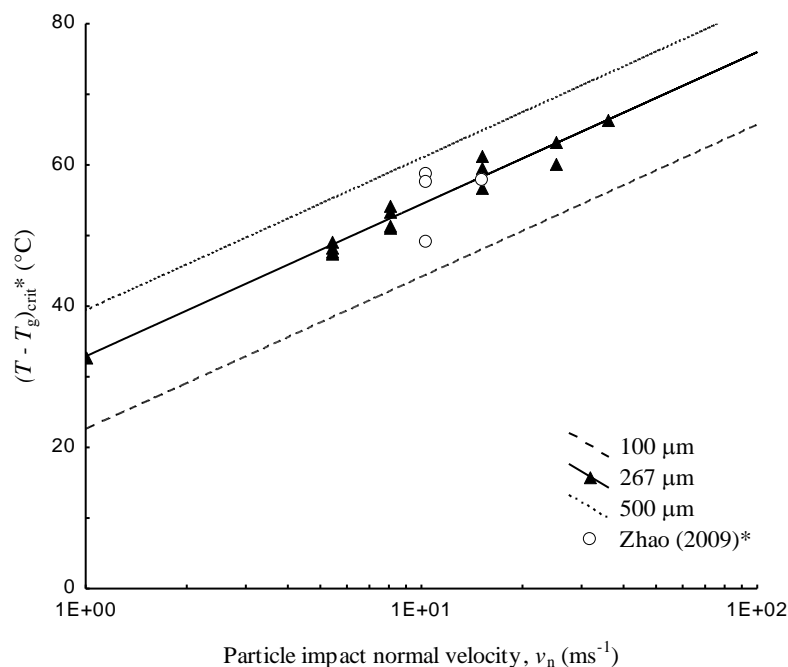


**Figure 6-9: Effect of normal particle impact velocity on  $(T - T_g)_{crit}^*$  with normal impingement, i.e. an impact angle of zero degrees.**

The effect of tangential velocity is reported by Murti et al. (2010) and Walmsley et al. (2010), although both studies used original definition of  $(T - T_g)_{crit}$

rather than the newly defined  $(T - T_g)_{crit}^*$ . However the trends are the same. Figure 6-10 shows that increasing the impact angle for a constant velocity magnitude requires an increase in  $(T - T_g)_{crit}^*$  for particles to stick. Alternatively, it may be rephrased that particles impacting at non-normal angles at the same velocity magnitude are less likely to stick. Konstandopulos (2006) reports that for non-normal impacts there may also exist a critical impact angle beyond which no deposition occurs. However due to operational limitations of the experimental test the applicability of Konstandopulos' observation could not be ascertained.

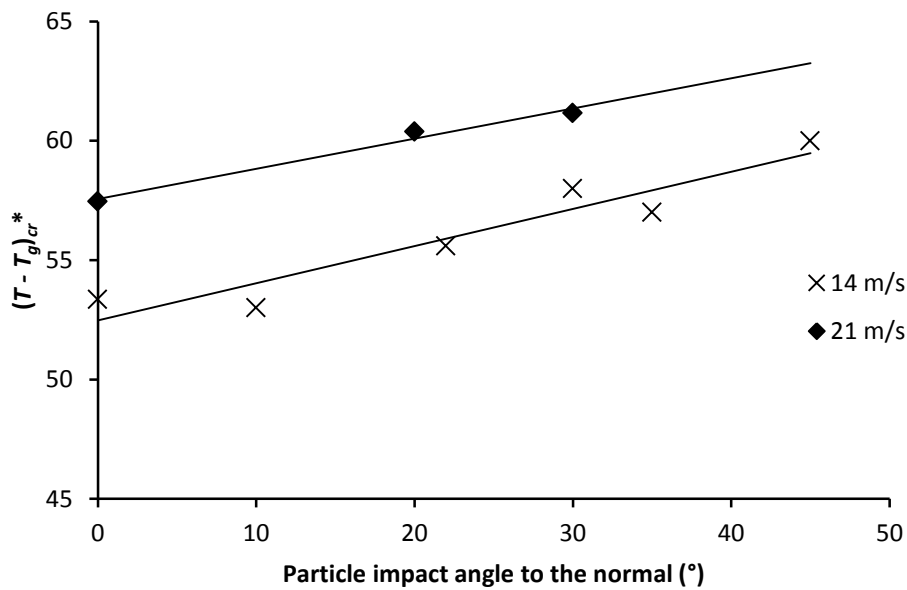


Figure 6-10: Effect of impact angle on  $(T - T_g)_{crit}^*$ . Particle size  $d_{(0.5)}$  100  $\mu\text{m}$ .

## 6.5. Validation of deposition criterion

The experimental and literature data are applied to Eq. 6-15 to determine the constants in the model. Materials properties for SMP and stainless steel are provided in Table 6-2. Materials properties (other than density) for SMP are difficult to locate in literature; consequentially, data for lactose is used in its place. Surface tension energy at the glass transition temperature is estimated from measurements for stainless steel and lactose taken at low humidity.

**Table 6-2: Mechanical properties and constants of stainless steel and amorphous lactose (Murti, 2006; Perkins et al., 2007; Zhang et al., 2006).**

Material property	Stainless steel	SMP (Lactose)
Particle density, $\rho$ (kg/m <sup>3</sup> )	N/A	1050
Shear modulus, $G$ (GPa)	73.9	3.49
Young's modulus, $Y$ (GPa)	193	3.57
Poisson's ratio, $\nu$	0.305	0.120
Surface tension at low humidity, $\gamma_{g1}$ (J/m <sup>2</sup> )	0.0520	0.0574
$Y^*$ (GPa)		3.56
$G^*$ (GPa)		0.83
$\gamma_g$ (J/m <sup>2</sup> ) for $T < T_g$		0.109

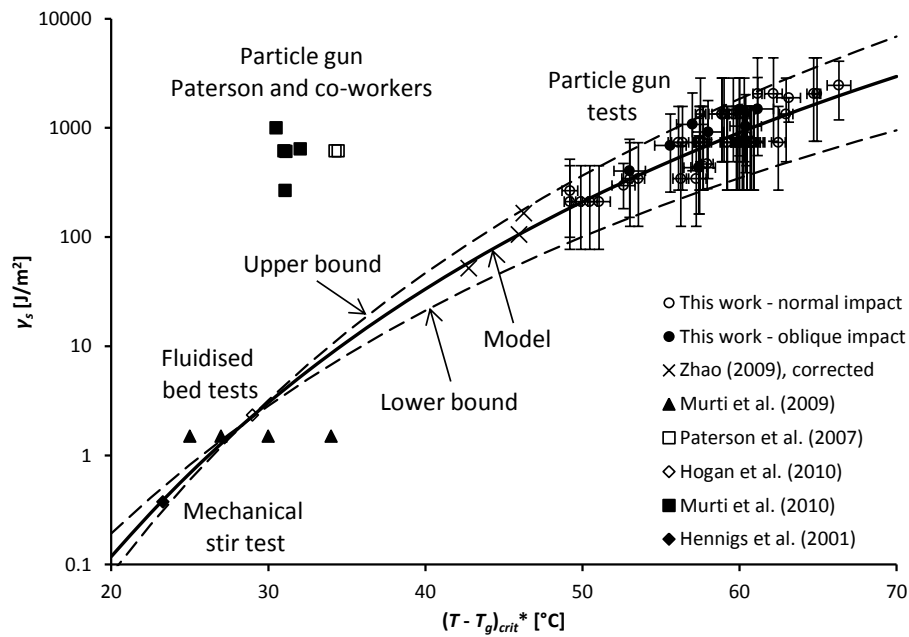


**Figure 6-11: Combined effect of particle size, impact angle and velocity on deposition. The work of Zhao is corrected (\*) for plate temperature effects.**

With estimates for the materials properties in Eq. 6-15, the remaining unknowns are constants  $a$ ,  $B$ ,  $D_1$ , and  $D_2$ . These constants are found by plotting  $\log(\gamma_s)$  against  $(T - T_g)_{crit}^*$  adjusted for  $T - T_p = 0$ . In addition to data collected in this work Figure 6-11 includes: fluidised bed deposition data from Murti et al. (2009) and Hogan and O'Callaghan (2010); mechanical stir test data from Hennigs et al. (2001), and particle gun test data corrected from Zhao (2009), Paterson et al. (2007a), and Murti et al. (2010). Vertical bars indicating the degree of uncertainty

in Figure 6-11 are estimated from the distribution of particle sizes and impact velocities of the particles and the horizontal uncertainty bars are estimated from non-stick/stick test conditions. By applying a least squares approach in tandem with Excel™ Solver the constants in Eq. 6-15 are solved and are given in Table 6-3. Constants for the upper and lower bounds are obtained using the estimated errors for the experimental data in this work.

**Table 6-3: Constants for SMP deposition model.**

Constant	Model	Upper bound	Lower bound
$a$	$7.7 \times 10^{-6}$	$1.2 \times 10^{-4}$	$8.9 \times 10^{-7}$
$B$	9.7	10.4	9.9
$D_1$	14.5	12.2	16.2
$D_2$ [°C]	36.4	38.5	34.8

## 6.6. Conclusion

In this chapter the key factors that cause milk powder to attach to walls or plates have been experimentally investigated. These factors include air temperature and humidity, plate temperature, particle size, and impact velocity and angle. Using standard solutions to the contact mechanics problem of a spherical adhesive elastic particle impacting a rigid plate, a semi-empirical criterion is successfully derived and fitted to literature and experimental data. One potential application of the model is to predict the critical angle at which deposition will cease for curved surfaces such as round tubes, assuming the other variables can be estimated.

# Chapter 7

## Thermal and hydraulic performance analysis of fins and tubes

---

### 7.1. Introduction

Milk powder fouling can significantly degrade the thermal and hydraulic performance of milk spray dryer exhaust heat recovery systems as has been observed in industrial settings, such as boilers (Stehlík, 2011), power stations, Heating, Ventilation and Cooling (HVAC) systems (Bell and Groll, 2011), to name only a few. As fouling initiates and grows, it provides additional resistance to fluid flow increasing the system pressure drop placing added electrical load on fans or pumps to maintain a desired flow rate. A fouling layer is also a thermal barrier to heat transfer degrading the overall heat transfer film coefficient and heat exchanger duty.

The dryer exhaust air contains a low concentration of milk powder ( $2 - 20 \text{ mg/m}^3$ ). At low temperature and high humidity, milk powder is sticky increasing its propensity to deposit on heat exchanger surfaces. The quantity of powder exiting through the exhaust is also an important factor for determining the rate of deposition and the concentration varies depending on the efficiency of separation operations (e.g. baghouse and/or cyclones) upstream of a heat recovery system (Gabites et al., 2007). Spray dryers typically have to keep within resource consent emission levels that are determined by local municipal and district councils.

This chapter focuses on understanding the practical limits to dryer exhaust heat recovery when fouling is taken into account. Critical air conditions leading to fouling and deposition on more complex geometries in cross-flow is determined for round, elliptical and turned square tubes, and fins. For each test the air temperature and absolute humidity is selected to mimic various locations within an exhaust heat recovery system. The chapter reports the development of a novel

lab based test similar to the particle gun but at a larger scale. The experimentally validated model describing the deposition of milk powder on stainless steel surfaces from Chapter 6 is compared to the larger scale experimental results.

## 7.2. Methods

### 7.2.1. Test rig operation

The experimental setup for this chapter is shown in Figure 7-1. The test rig allows milk powder to be added to an air stream of controlled temperature and humidity. This powder laden air flow is then contacted in cross-flow with various geometries. The air temperature is controlled using three separate thermal operations. First a plate-fin liquid to air heat exchanger circulates heated water to preheat air. The air is drawn in by a fan and blown along the test duct. A small amount of direct steam injection further increases the temperature of the air while achieving the target humidity. Finally an electric heater connected to a Variable Speed Drive (VSD) is used as a trimming element to adjust the final temperature of the air stream.

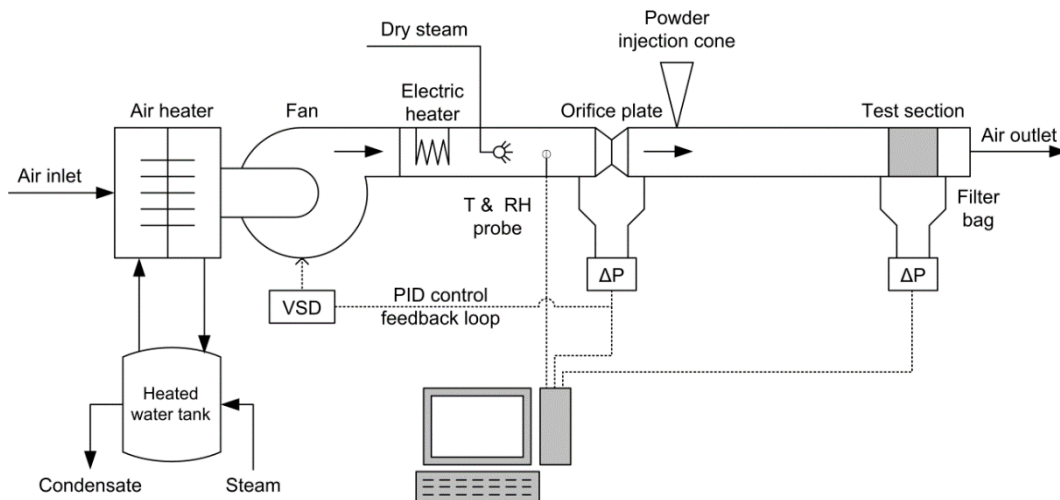


Figure 7-1: Deposition test rig schematic.

An orifice plate in the duct provides a pressure drop which is related to the air velocity in the air duct and used to control the fan speed via a PID feedback loop to ensure a constant flow rate through the system as fouling on the tubes occurred. This also creates a region of low pressure immediately behind the plate where milk powder is injected, aided by a little suction induced by the orifice plate.

The powder laden airflow then travels through the test duct where fully developed turbulent flow is to be achieved before contact with the deposition surfaces. To control the rate of powder injection, a bottle full of powder is mechanically tapped. On average, powder was added at 2.4 – 3.8 g/min and test durations ranged from 20 to 80 minutes depending on the rate of deposition.

By adjusting the direct steam injection valve, it was attempted in the tests to achieve an absolute humidity of 50 – 60 g H<sub>2</sub>O/kg dry air as this relates directly to the moisture content in industrial milk spray dryer exhausts. The process of setting up the initial temperature and humidity of the test system took anywhere up to three hours. Rigorous start-up and operation procedures for the equipment were established to prevent condensation on the test section. In the event that condensation was evident, the results were invalidated. Preventing condensation is a key reason why it often took several hours to achieve the desired conditions because temperature and humidity increased had to be done by small increments. Once the desired values were achieved and steadied, powder was added. The time for separate tests varied depending on the rate of deposition.

Throughout the course of the tests, deposition, pressure drop across the tube, and air temperature and humidity are visually observed and/or monitored. In general a test would be stopped when the pressure drop across the tube reached a constant level. Temperature and relative humidity were logged at one second intervals and  $T - T_g$  was calculated for each interval and averaged for the entire test period. Two standard deviations of the temperature and relative humidity data for each test are used to estimate uncertainty in  $T - T_g$ . At the conclusion of each test the test assembly was removed from the duct and photographs were taken to show the deposition morphology from various angles.

### **7.2.2. Bare tube test set-up**

Round (25.4 mm), elliptical (22 mm x 39 mm), and turned square (25.4 mm x 25.4 mm) tubes were housed horizontally in a cross-flow fashion in a section with transparent acrylic walls enabling visual inspection of the test. Each tube was tested individually using various temperatures (46 °C to 62 °C) to achieve a range

of stickiness levels,  $T - T_g$ . Average duct velocities of 4.5 and 6.5 m/s are used in the tests.

Photographs looking down the tubes were taken at regular intervals in an attempt to observe the growth of deposition over time. These images, depending on the clarity of the deposition layer, were later analysed to measure the location of deposition on each tube. Based on the photos, measurements and the tube geometry, the average location for the edge of the fouling layer was calculated using MatLab™. This result was then compared with flow simulation Computational Fluid Dynamics (CFD) results (Figure 7-2) to determine the wall shear stress at that location where deposition ceased. CFD model included a single tube in an 80 mm square duct (same as the experimental) using the modelling parameters outlined by Walmsley et al. (2012b).

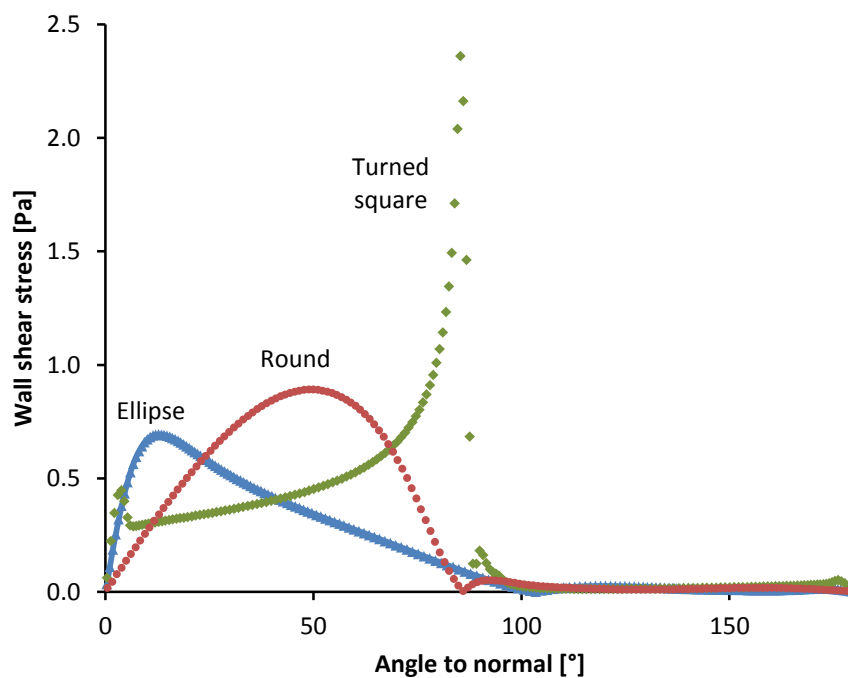


Figure 7-2: Wall shear stress for round (a), elliptical (b) and turned squared (c) tubes using CFD. Refer to Walmsley et al. (2012b) for CFD model parameters.

### 7.2.3. Fin bank test set-up

A fin bank has been subjected to conditioned air flow with entrained milk powder and the resulting deposition and its effects are analysed (Figure 7-3). The fin bank is a stack of 0.6 mm parallel aluminium plates that are evenly spaced and act in a similar manner to the fins in a finned tube heat exchanger. The fin pitch is 13.5 fins

per inch, which is similar to standard compact air recuperators, and the gap between the fins is 1.3 mm. The fin bank, therefore, represents an extreme case for fouling due to the closeness of the fins. The air flow rate in all tests has been kept constant at 28.8 L/s, which is an average face velocity,  $u_\infty$ , of 4.5 m/s.

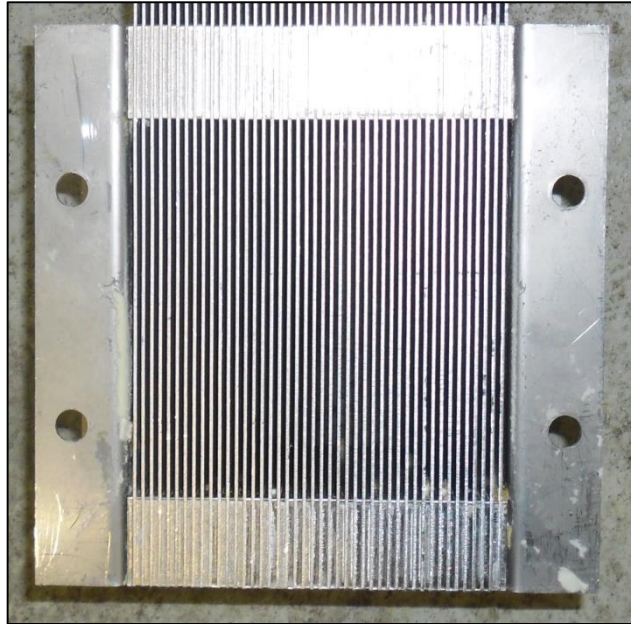


Figure 7-3: Photograph of fin bank.

#### 7.2.4. Particle size distribution

Non-agglomerated Skim Milk Powder is used in all tests. The particle size distribution was measured in iso-propanol using a Malvern Mastersizer 2000 according to the method of Pisecky (1997). By cumulative volume fraction, the mid diameter of the powder,  $d(50\%)$ , was measured as  $104\ \mu\text{m}$ ;  $d(10\%) = 39\ \mu\text{m}$  and  $d(90\%) = 202\ \mu\text{m}$ .

#### 7.2.5. Determination of $T - T_g^*$

Particle stickiness or  $T - T_g^*$  is defined in the same manner as Chapter 6 where  $T$  is taken as the air temperature (dry bulb) and  $T_g$  is calculated using the Gordon-Taylor equation presented in Chapter 2. Wall temperature effects on  $T - T_g$  are accounted for using Eq. 6-16 from Chapter 6.

## 7.3. Experimental results for single tubes in cross-flow

### 7.3.1. Fouling coverage and location

The stickiness of the milk powder, as quantified by  $T - T_g^*$ , influenced the coverage and morphology of deposits around the front of the tubes. Figure 7-4 shows photographs of three tests performed on the round tube. Results are organised so that the top photographs are for the lowest  $T - T_g^*$  condition progressively down to the bottom photograph for the highest  $T - T_g^*$  condition. Increasing the stickiness of the powder is observed to significantly increase the fouling coverage around the front of the tube and the powder layer thickness.

The side angle photographs show the growth of the fouling layer near the wall. An air flow separation point on the front of the round tube is suggested by the deposits attached to the duct wall. Very little deposition was observed during any of the tests on the rear of the tubes. For each the test conditions the wall of the ducting is seen to make an impact on the amount of deposition near the wall. Since the velocity profile is likely to be fully developed after travelling along a relatively long straight duct, air velocities near the duct wall are slower than in the centre of the duct. As a result the particle impact velocity near the wall is slower increasing the chance for particles to deposit.

The elliptical tube required higher  $T - T_g^*$  values to result in similar deposition amount and coverage levels as the round tube for the same bulk air velocity as shown in Figure 7-5. In terms of milk powder fouling properties the elliptical tube is, therefore, favourable over the round tube. The low fouling property of elliptical tubes has been demonstrated for tube bundles by researchers in other fields. For example, Bouris et al. (2005) applied both experimental and numerical approaches to conclude elliptical tube bundles were less susceptible to fouling.

Another benefit associated with the elliptical tube is the lower gas side flow resistance resulting in a lower pressure drop. Walmsley et al. (2012b) numerically evaluated the performance of round and elliptical tube bundles. In the models the same hydraulic air-side diameter and frontal free-flow area for the two sets of

tube bundles are constant so that the comparison between the tube geometries was fair. Their models suggested that the pressure drop across an elliptical tube bundle is about half of the pressure across a round tube bundle for the same air side heat transfer coefficient. In terms of compactness, the round tube bundle required about 30 % less volume (and heat transfer area) than the elliptical tube bundle to achieve the same heat transfer, but experienced a 150 % greater pressure drop.

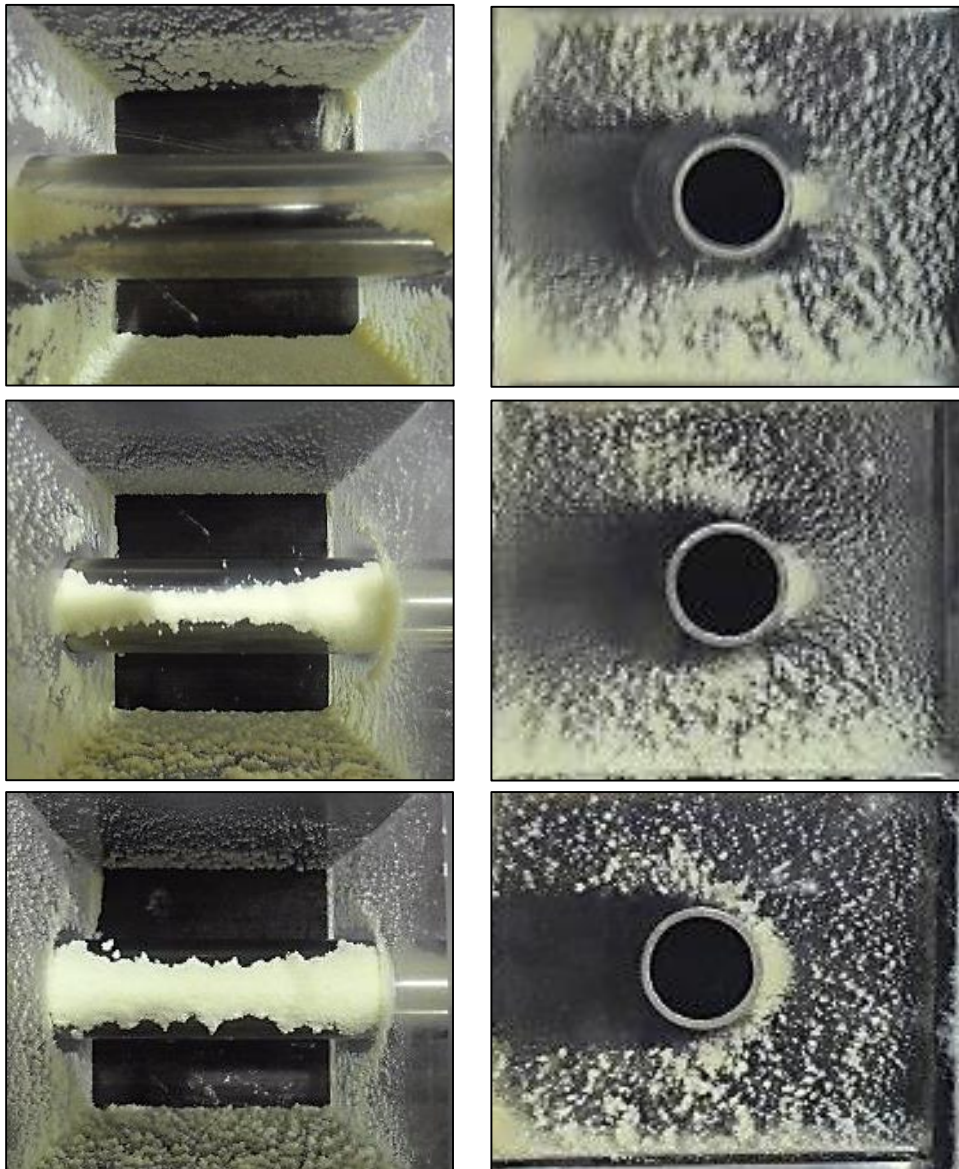
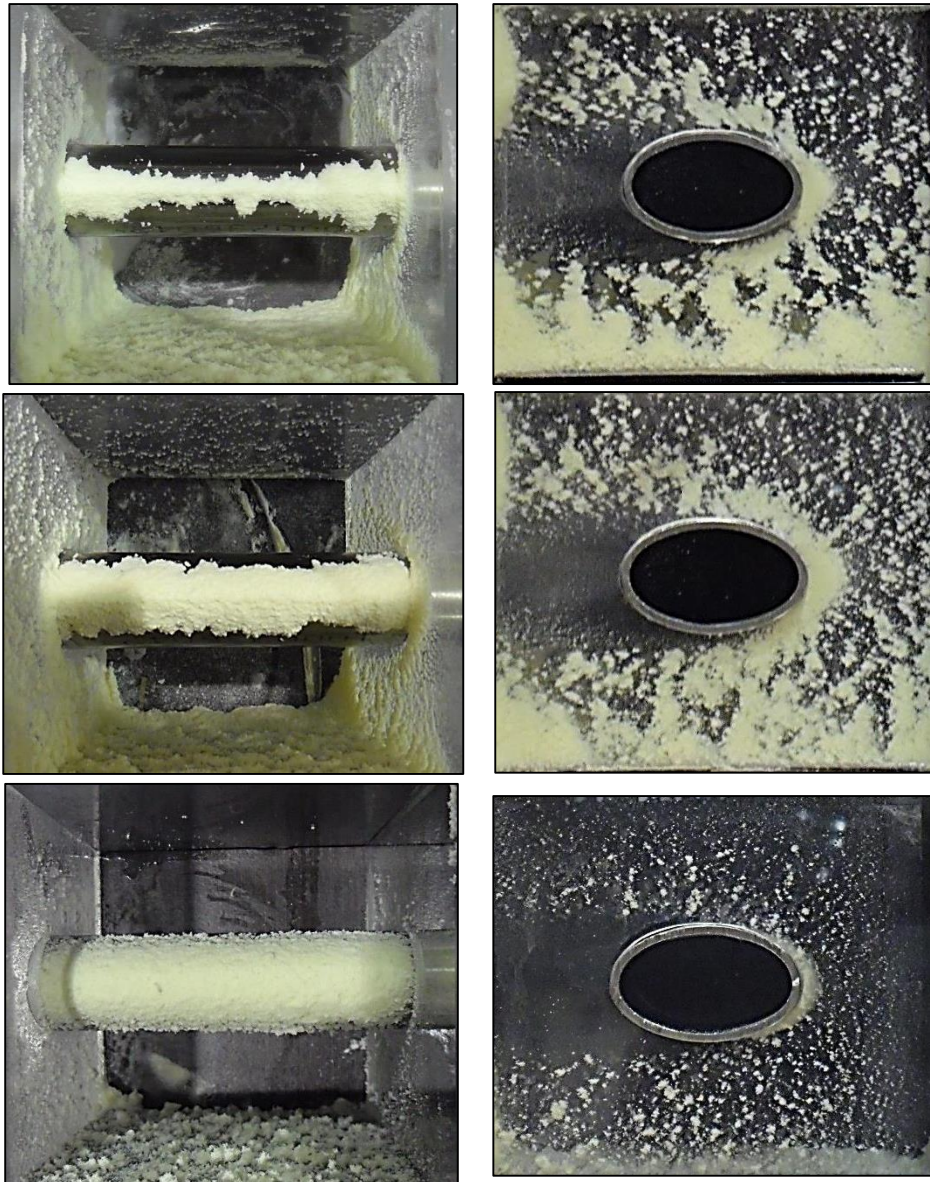


Figure 7-4: The effect of increasing stickiness on the frontal deposition for round tube. From top,  $T - T_g^*$  conditions are 43.3, 47.6 and 52.6 °C. Photographs were taken at the end of the test.



**Figure 7-5: The effect of increasing stickiness on the frontal deposition for elliptical tubes. From top,  $T - T_g^*$  conditions are 50.0, 54.8 and 62.5 °C. Photographs were taken at the end of the test.**

The turned square geometry is characterised by two flat 45° angled sides facing the airflow. It was noticed in testing the turned square tube that no partial deposition occurred at intermediate  $T - T_g$  values, as was seen for the round and elliptical tubes. Instead, there was either very little deposition (Figure 7-6 left), or a fouling layer completely covering the front face of the tube (Figure 7-6 right). This result is consistent with the idea that the impact angle is critical factor determining deposition since the sides of the turned square are flat faces at an angle of 45°. The small amount of deposition in Figure 7-6 (left) near the wall is likely the result of wall slowing the air velocity. The air velocity near the wall is

slower than in the centre of the duct resulting in particle impacts at a slower velocity.

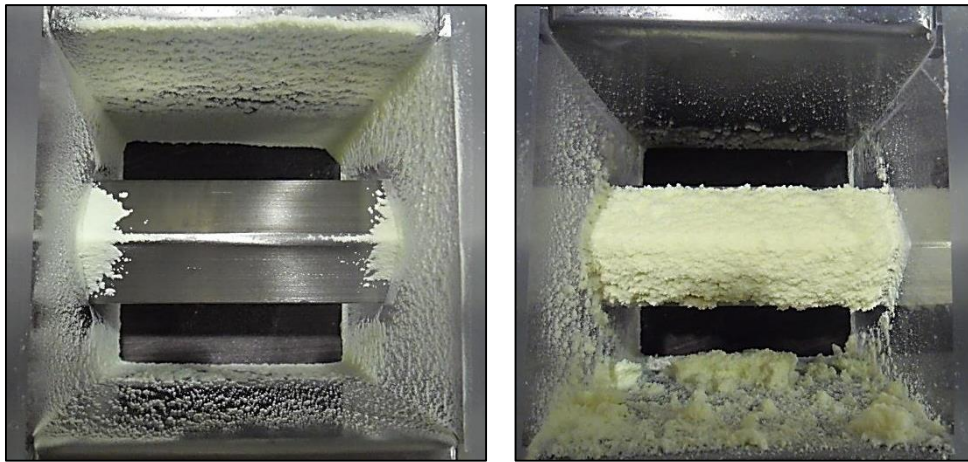


Figure 7-6: The effect of increasing stickiness on the frontal deposition for turned square tube.  $T - T_g^*$  conditions are 56.7 °C (left) and 61.2 °C. Photographs were taken at the end of the test.

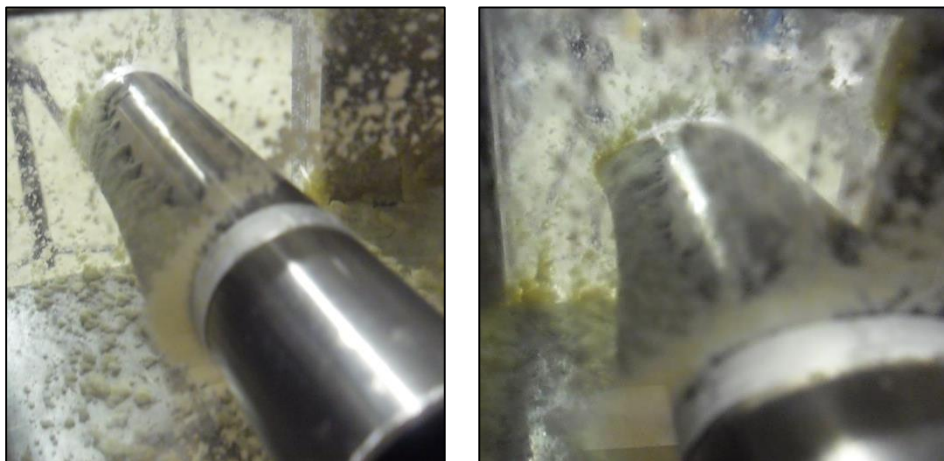


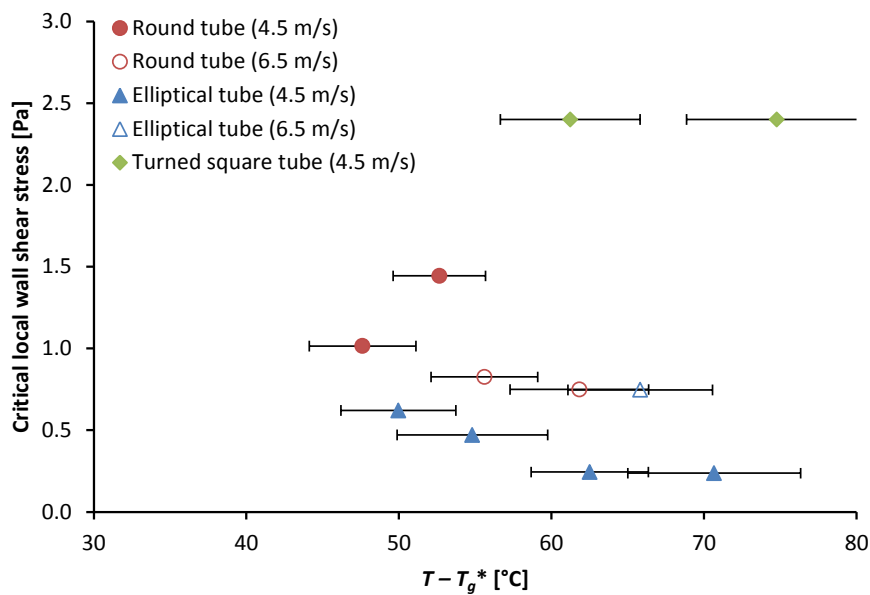
Figure 7-7: Deposition morphology on round and elliptical tubes.  $T - T_g^*$  conditions are 52.6 °C (left) and 54.8 °C. Photographs were taken at the end of the test.

Figure 7-7 presents photographs of the deposition morphology for round tube and elliptical tube. The surface of the deposition on the front of the tubes typically had a small rounded peak that extended on an angle back to the tube at which point deposition ceased. The angled sides of the deposition were flat but rough. Deposition growth and peak was greatest near the duct walls.

### 7.3.2. Critical wall shear stress and impact angle

The initial focus of the analysis is to investigate how the local wall shear stress around the profile of various tubes influences particulate deposition. Three observations were expected in relation to this concept. First, it was expected that

increasing  $T - T_g^*$  would require a higher wall shear stress to prevent deposition. Second, if wall shear stress is a determining factor for deposition, then it is expected that there is a clear correlation between wall shear stress and  $T - T_g^*$  that may be independent of the tube geometry and average bulk air flow velocity. Third, it was expected that deposition may favour the rear facing side of the tube as shown by Paz et al. (2012) for particulate deposition on tube bundles fouled by a diesel exhaust, which has already been shown to not be the case for milk powder deposition on tubes.



**Figure 7-8: Critical local wall shear stress plotted against  $T - T_g^*$  for round, elliptical, and turned square tubes.**

Based on these hypotheses a unique critical wall shear stress should exist for each  $T - T_g^*$  value. To test this hypothesis, the local wall shear stress at the location on the tube where deposition ceased is plotted against  $T - T_g^*$  for round, elliptical and turned square tubes in Figure 7-8. Results show no clear correlation for the tests performed at various face velocities. This lack of correlation suggests that the size and momentum of the milk powder particles is sufficient to break through the shear layer around the tubes with little impact. In addition, deposition at the rear of the tube was observed to be minimal. These results imply that the transport regime and mechanism of the bulk of the particles is not diffusion controlled as was the case for Paz et al. (2012). An underlying reason for the difference between this work and Paz et al. is the particle relaxation time. The

literature review in Chapter 2 presented analysis of the particle relaxation time for milk powder suggesting the transport and deposition mechanism of milk powder in heat exchangers is particle inertia moderated indicating particles respond slowly to changes in velocity flow field changes. On the other hand the particle relaxation time in the work of Paz et al. was between 0.1 and 1 s indicating particle transport is turbulent diffusion-eddy impaction controlled.

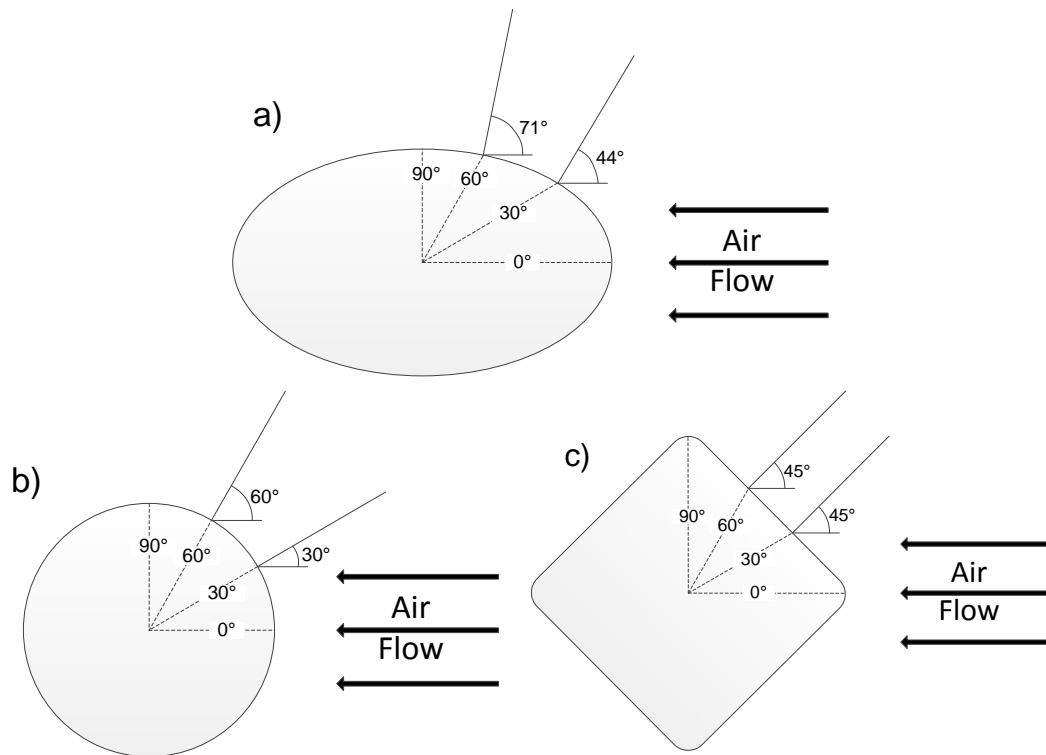


**Figure 7-9: Schematic showing how the impact angle is defined and how it changes for: a) elliptical tubes; b) round tubes; c) turned square tubes.**

In the situation where particle motion does not deviate from that of the bulk fluid, particles impact the tube surface at an angle approximately equal to that of the bulk flow. The critical impact angle may be defined as the angle between the bulk flow direction and the normal to the tube surface at the point where deposition terminates. The general concept of a critical impact angle was originally suggested by Konstandopoulos (2006). Figure 7-9 illustrates how the critical impact angle to the normal is estimated for deposition on the elliptical, round and square tubes. For the round tube this is merely the angle of the polar coordinate at the surface location. For the elliptical tube the angle varies from that of the polar coordinate

as illustrated in Figure 7-9a. For the square tube the angle remains constant at 45° (considering only the positive angles).

Figure 7-10 plots the critical impact angle relative to the direction of the airflow against particle stickiness,  $T - T_g^*$ . Vertical and horizontal bars in Figure 7-10 represent the uncertainty of the measurements. Uncertainty in  $T - T_g^*$  was the result of fluctuating temperature and humidity measurements. The uncertainty in the critical impact angle is due to the non-uniform deposition along the length of the tube. When the uncertainty is taken into account, the deposition model for Chapter 6 appears to be sufficiently representative of the experimental data for single tubes in cross-flow. At  $T - T_g^*$  below 65 °C, the model provides a close match to the critical impact angle with the exception of the turned square tube; whereas at higher  $T - T_g^*$  the model over predicts the critical impact angle.

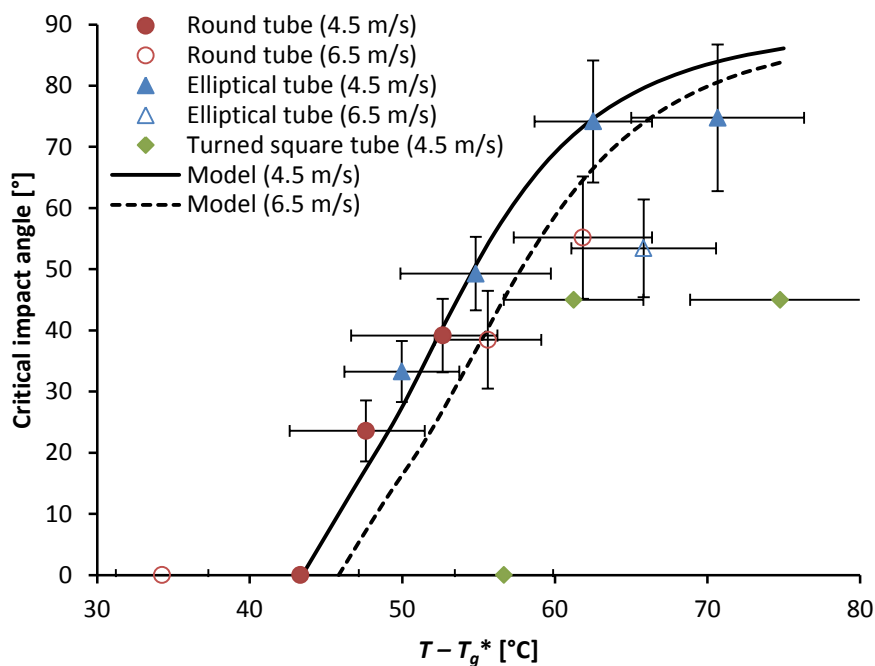


**Figure 7-10: Estimated critical impact angle for the round, elliptical and turned square tubes. Models assume a particle size of 104  $\mu\text{m}$ .**

In the case of the turned square tube, it was found that either the entire face of the tube was clean or fouled. Increasing  $T - T_g^*$  after the tube fouled therefore gave an apparent “critical” impact angle of 45 ° since there was no impacts at angles greater than 45 °. The minimum measured  $T - T_g^*$  required to cause the turned square tube to foul was 61.2 °C and the maximum measured  $T - T_g^*$  giving

no fouling was 56.7 °C. The critical combination of  $T - T_g^*$  and impact angle lies, therefore, between 56.7 °C and 61.2 °C for the turned square tube. The model predicts a  $T - T_g^*$  value of 53.6 °C. If the  $T - T_g^*$  uncertainty is taken into account, the measured  $T - T_g^*$  may be as low as 53.4 °C, which marginally encompasses the model.

### 7.3.3. Modelled fouling coverage

Since the deposition model from Chapter 6 is representative of critical impact angle as shown in Figure 7-10, the model is applied to estimate the deposition coverage of the frontal tube face and area for a range of  $T - T_g^*$  values. Figure 7-11 predicts the frontal face deposition on the front of the tubes as would be viewed from the perspective of the airflow. Figure 7-12 estimates the deposition area coverage for the three tube geometries. The definitions of the two deposition coverage's are clearly drawn as inserts on the respective figures. It can be seen that for any given  $T - T_g^*$  the round tube is expected to have a higher level of fouling coverage in terms of the frontal face and frontal area than the ellipse.

In contrast to the round and elliptical tubes, the square tube only has the single impact angle of 45° as discussed previously. When  $T - T_g^*$  exceeds 53.6 °C the entire frontal faces of the turned square are full of deposition. In designing an dryer exhaust recuperator, one may think the turned square tube is advantageous from a fouling point of view so long as air exiting the recuperator system is warm enough to have a  $T - T_g^*$  below 53.6 °C. However a key disadvantage of the square tube is its poor external flow behaviour. Of the three tubes tested, the square tube had the highest measured bare tube pressure drop by more than twice that of the round tube. Using CFD models, Walmsley et al. (2012b) showed the performance of a turned square tube requires 2.5 times the pressure drop of the round tube and 5.4 times the pressure drop of the elliptical tube, to achieve the same heat transfer duty.

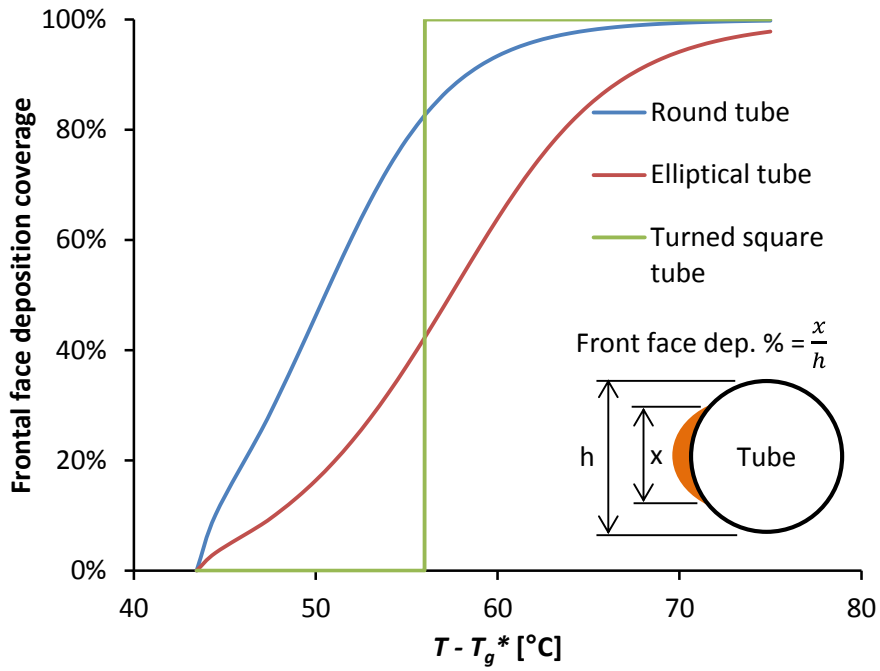


Figure 7-11: Predicted frontal face deposition coverage versus  $T - T_g^*$  using the deposition model based on an air velocity, i.e. particle impact velocity, of 4.5 m/s.

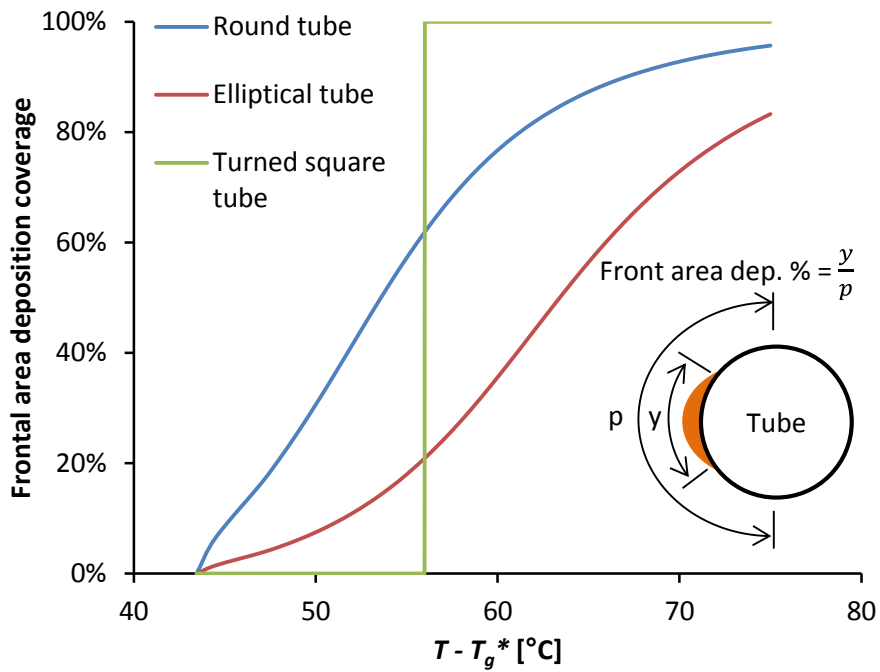
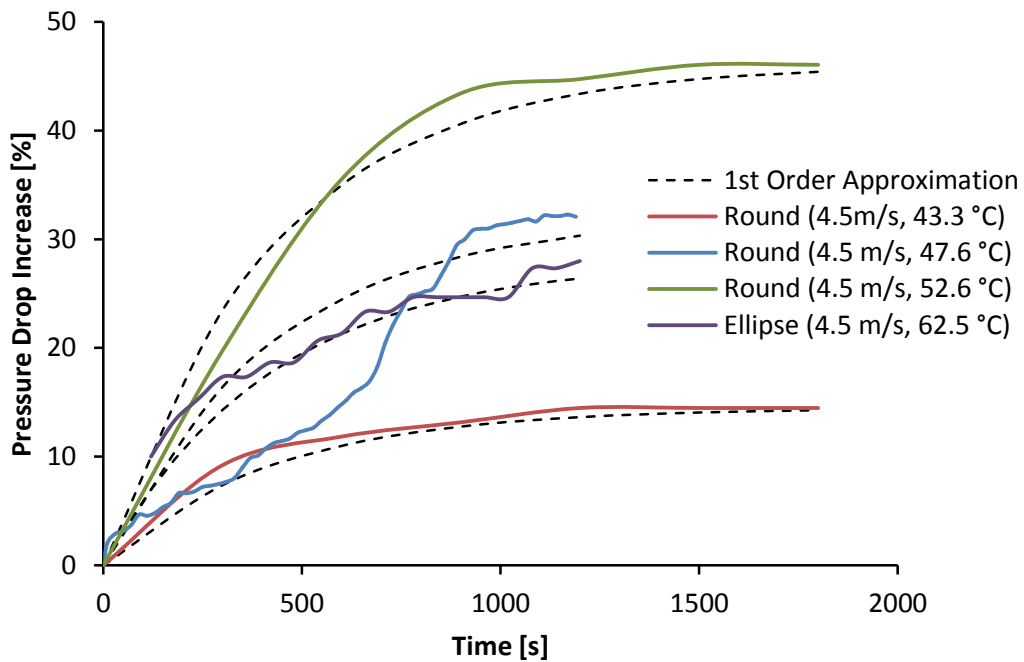


Figure 7-12: Predicted frontal area deposition coverage versus  $T - T_g^*$  using the deposition model based on an air velocity, i.e. particle impact velocity, of 4.5 m/s.

### 7.3.4. Pressure drop

The fouling growth rate and pressure drop across the tube are related. Figure 7-13 plots the increase in pressure drop as a percentage for three stickiness levels for the round tube and one stickiness level for the elliptical tube. The data suggests the rate of pressure drop and, therefore, fouling build-up is dependent on the stickiness level, with higher stickiness conditions resulting in faster growth.



**Figure 7-13: Pressure drop over time across a single round tube for three levels of stickiness showing a first order exponential approximation with a time constant of 420 s.**

A first order exponential approximation of the pressure drop increase with time is also plotted in Figure 7-13 using the general equation

$$\Delta P(\%) = \Delta P_{final}(\%) \left( 1 - \exp\left(-\frac{t}{\tau_f}\right) \right) \quad (7-1)$$

where  $t$  is the time from the start of the test and  $\tau_f$  is the time constant for the fouling, which is estimated as 420 s. This time constant was similar for the round and elliptical tubes. Since the powder concentration is fairly low and it is unexpected to significantly influence the airflow profiles, it may be assumed that the supply of powder to heat exchanger surfaces is a key limiting factor for the rate of deposition. On the other hand the air velocity and stickiness of the powder determines the equilibrium amount powder attached to a tube. As a result the

final pressure drop increase is a function of stickiness whereas the time constant is a function of powder concentration. For different concentrations of powder the equivalent time constant for the pressure drop rise is estimated using

$$\tau_{f,2} = \tau_{f,1} \frac{c_{b,1}}{c_{b,2}} \quad (7-2)$$

The final pressure drop increase percentages are plotted against  $T - T_g^*$  in Figure 7-14. The round and elliptical tubes both experience increases in pressure drop with increasing  $T - T_g^*$ . As  $T - T_g^*$  increases, the deposition coverage around the tubes grows adding resistance to the airflow. For the same  $T - T_g^*$  the pressure drop increase for the round tube is greater than for the elliptical tube. This conclusion reinforces the idea that the coverage of the frontal deposition for the round tube is greater than for the elliptical tube at the same  $T - T_g^*$ .

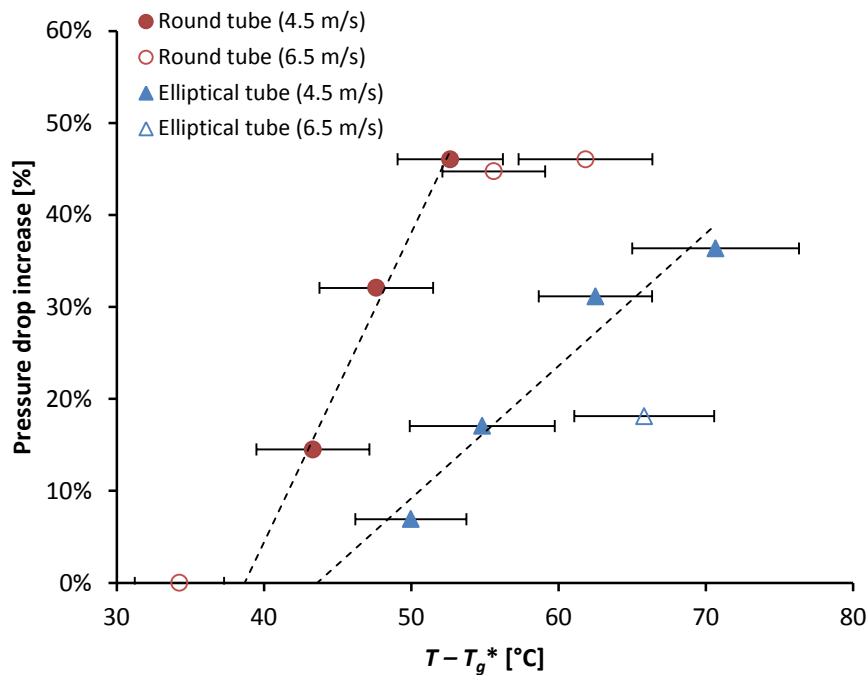


Figure 7-14: Final pressure drop versus  $T - T_g^*$  for the round and elliptical tubes.

## 7.4. Experimental results for parallel plates

### 7.4.1. Pressure drop analysis of the fin bank

The pressure drop across the fin bank is related to the average duct air velocity immediately prior to the fin bank,  $u_\infty$ , and the fraction of open frontal area,  $\varphi$  as shown in Figure 7-15. To understand this relationship and to form an empirical model, tests are carried out at high temperatures (about 60 °C) using different open area fractions. No powder is injected, rather sticky tape is applied to block off known amounts of frontal area. With no additional blocking, the fin bank alone is an open area fraction of 0.67, for a fin pitch of 13.5 fins per inch.

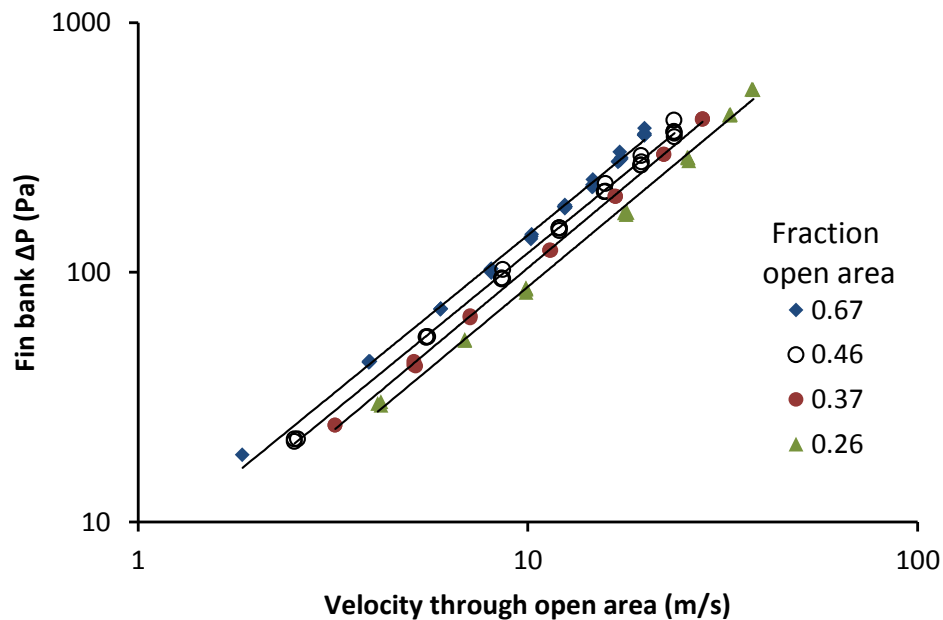


Figure 7-15: Pressure drop across the fin bank for different open area fractions.

The velocity through the open area of the fins,  $u_\varphi$ , may be defined using the average duct air velocity and the open area fraction,  $u_\varphi = u_\infty/\varphi$ . Results in Figure 7-15 were measured by changing the fan speed, which varied the air flow rate in the duct, and measuring the pressure drop across the fins using an angled water manometer. The average velocity in the duct is measured using a 75 mm diameter vane anemometer. The velocity through the open area is calculated from the measured air flow rate and the known open area fraction. Each air flow rate has been tested at least three times.

Figure 7-15 shows that the pressure drop is strongly influenced by the velocity through the fin bank and weakly influenced by the fraction of open area. The plot is presented in a log-log form with the trend lines being power-law fits. A slight curve in the data can be seen with the greatest percentage difference being at the lower velocity range. Since the slopes of the power equations in Figure 7-15 are the very similar, an empirical model for the pressure drop can be constructed based on the average face velocity (duct velocity) and the open area fraction.

$$\Delta P = 8.90 \frac{u_{\infty}^{1.29}}{\phi^{0.77}}, \quad [0.26 < \phi < 0.67 \quad \text{and} \quad 1.2 < u_{\infty} < 9.8 \text{ m/s}] \quad (7-3)$$

Eq. 7-2 is applied to deposition results, where the pressure drop and face velocity are known, to work out an estimate of the open area fraction and velocity through the open area.

#### 7.4.2. Powder deposition on the fin bank

Results from the deposition tests presented in Figure 7-16 show the pressure drop across the fin bank increased over time as powder deposited. The pressure drop curve followed a typical asymptotic model with the rate of pressure drop increase diminishing over time as suggested in general particulate fouling models (Shah and Sekulić, 2003). Photographs of the frontal deposition on the fin bank at the end of each test are presented in Figure 7-17. Open area fractions are estimated using Eq. 7-2. Deposition mostly occurred in the lower half of the face of the fin bank with very minor deposition inside and at the rear of the fin bank. This affinity is due to gravity causing particles to settle out of the air flow. As a result a greater share of the injected powder passes through the bottom half of the fin bank. Deposition and blocking tended to initiate at the bottom of the fin bank face before moving up the face until the net deposition rate was close to zero.

For high temperatures and low relative humidity, the amount of deposition was minimal (Figure 7-17A). As the air temperature was reduced, the amount of fouling slowly increased (B and C). A decrease in air temperature resulted in an increase in particle stickiness due to a significant increase in the air relative humidity and a subsequent fall in  $T_g$ . The net effect on  $T - T_g^*$  was an increase in temperature

difference. A further drop in the air temperature resulted in a rapid rise in pressure drop and reduction in open frontal area. The concept of a critical stickiness observed by Paterson et al. (2007a) and many others, e.g. (Boonyai et al., 2004; Intipunya et al., 2009), can also be seen for the fouling of the fin bank considered in this study.

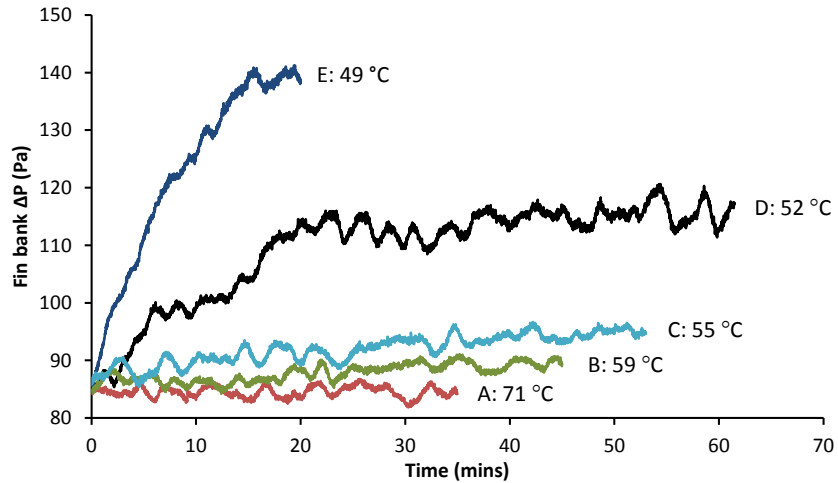


Figure 7-16: Pressure drop across the fin bank over time. Air temperatures as labelled with air moisture content constant at 60 g/kg.

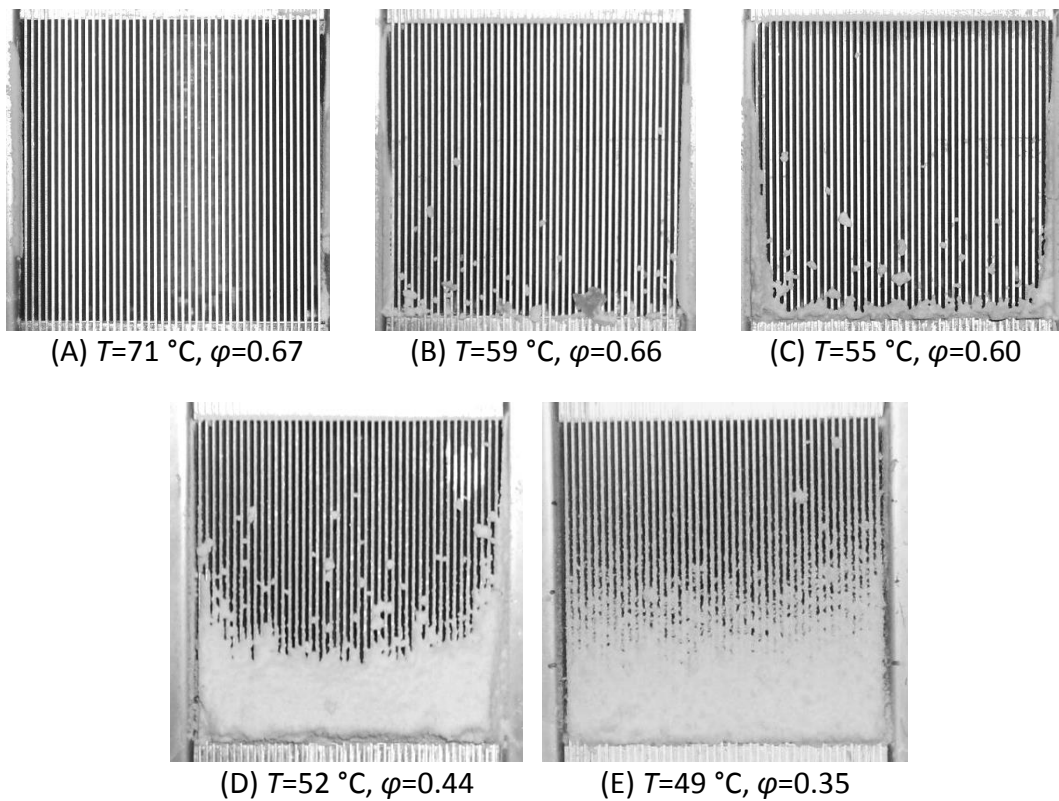


Figure 7-17: Photographs of frontal fouling for various air temperatures and a constant air moisture content of 60 g/kg. Photos were taken at the end of each test.

Particularly apparent in tests D and E is the distinctive asymptotic pressure drop. At this equilibrium, the rate of deposition and the rate of removal are similar, which indicates the amount of open area remains fairly constant. Powder may deposit on top or over powder, but the open area to the flow is unchanged. The reduction in frontal free flow area results in high velocities through the open sections of the fin bank. The increase in velocity simultaneously causes an increase in the rate of deposit removal. Blocked areas of the fin bank may then temporarily reopen. This dynamic deposit/removal process is one contributor to the oscillations in pressure drop in Figure 7-16. Oscillations in the air flow rate, and subsequently the pressure drop, also resulted from the PID control loop.

### 7.4.3. Critical pressure drop, velocity and stickiness

The pressure drop asymptotes from Figure 7-16 are plotted against powder stickiness,  $T - T_g$ , as shown in Figure 7-18. The critical  $T - T_g$  value after which deposition initiates is identified as  $(T - T_g)_{crit}^*$  and has a value of approximately 37 °C. This  $(T - T_g)_{crit}^*$  value is very close to the particle gun test results of Patterson et al., where  $(T - T_g)_{crit}^*$  was 37.5 °C, although the reported velocity of the particle gun air jet was considerably higher at 20 m/s and the powder tested was Whole Milk Powder. The closeness of  $(T - T_g)_{crit}^*$  values is probably mere coincidence.

Applying Eq. 7-2, estimates for the velocity through the open area of the partially fouled fin bank are plotted against particle stickiness,  $T - T_g$ , in Figure 7-19. In essence, Figure 7-19 represents an equilibrium and critical condition, where the  $u_\phi$  is a function of  $T - T_g$ . For a given face velocity, the curve in Figure 7-19 can be used to predict a critical  $T - T_g$  above which deposition will begin to close off small sections of the fin bank. For example, if the face velocity was 6.7 m/s instead of 4.5 m/s as in the tests, then the initial velocity through the open area would be 10 m/s as indicated by  $u_{\phi}^*$  and the expectation would be that significant deposition would not occur until  $T - T_g$  is greater than about 75 °C. The equation of the linear trend line in Figure 7-19 is

$$v_{\phi}^* = 0.11 (T - T_g)_{crit}^* + 1.48 \quad (7-4)$$

Eq. 7-3 may be applied to predict the critical  $T - T_g^*$  at which significant deposition will be initiated. For a given absolute humidity, this critical  $T - T_g^*$  may be converted into a temperature to provide a limit to the exhaust heat recovery.

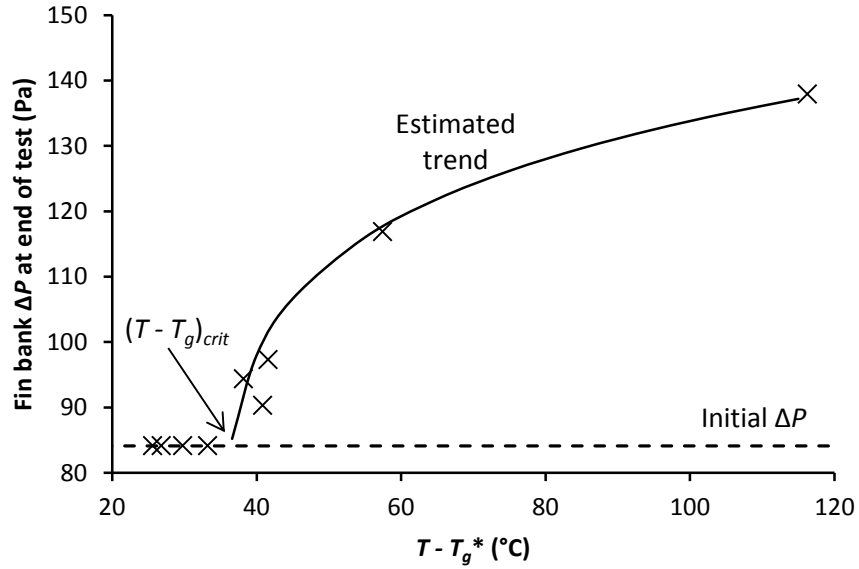


Figure 7-18: The relationship of fin bank pressure drop and particle stickiness,  $T - T_g^*$ .

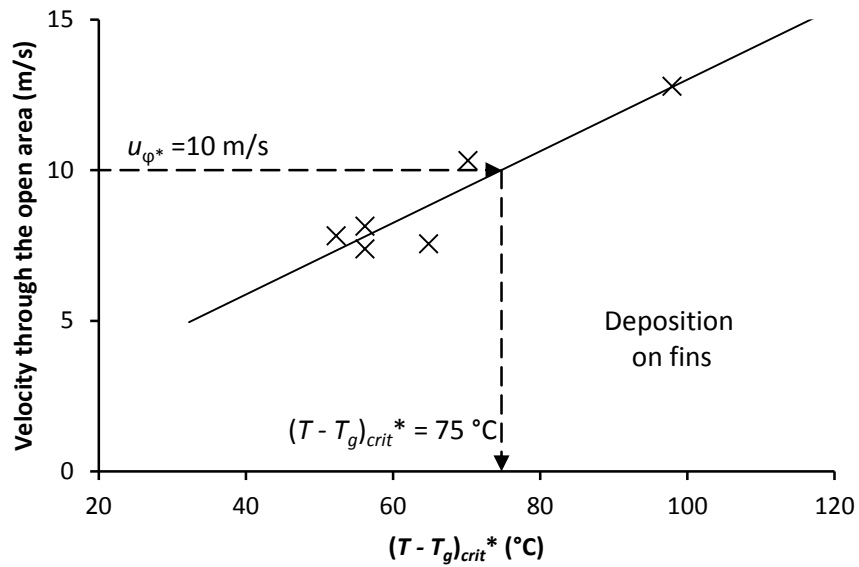


Figure 7-19: The impact of particle stickiness,  $T - T_g$ , on the equilibrium velocity through the open area of the fin bank.

## 7.5. Application of experimental results

In the case of milk powder deposition on tubes, the deposition model from Chapter 6 adequately predicts the deposition coverage around a tube. Importantly the particle impact angle in the model is taken to be the angle between the bulk air flow direction and the normal to a localised position on the tube's surface. Applying the deposition models predicts the impact angle at which deposition ceases and therefore the frontal area that will foul for a given tube shape. This model may also be applied to large scale tubular heat exchangers to predict deposition coverage around a tube.

Fouling on the front of compact finned tube heat exchangers applied to exhaust heat recovery in industrial spray dryers is demonstrated to be an important issue. The pressure drop across the lab scale fin bank was shown to increase by as much 65 %. A similar percentage increase in pressure drop for an industrial heat recovery system may be expected if the exhaust air is driven below 49 °C in the recuperator and sufficient time passes for powder to deposit.

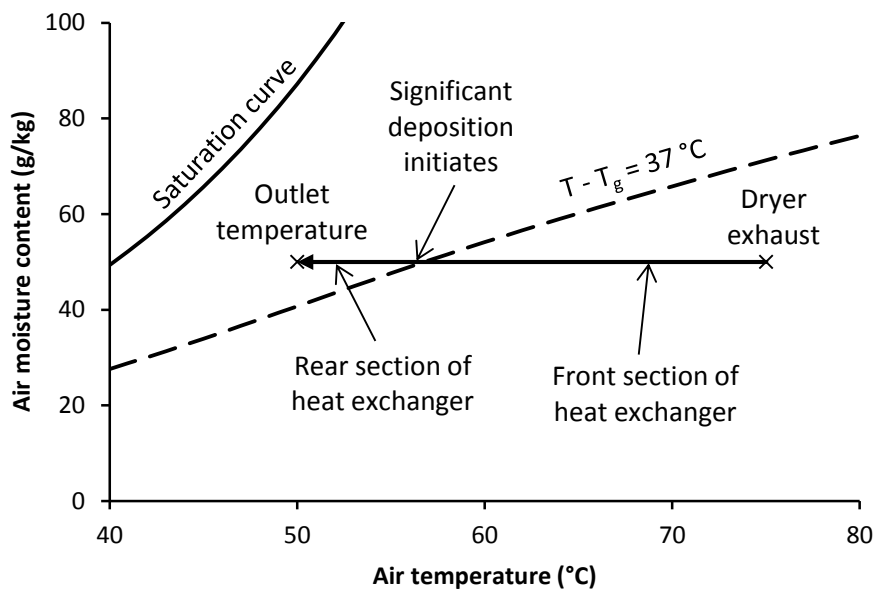


Figure 7-20: Psychrometric plot of the effect of exhaust heat recovery.

Figure 7-20 shows the relationship between exhaust heat recovery and stickiness,  $T - T_g^*$ , using a psychrometric plot. The critical stickiness line corresponds to a velocity through the open area of 5.8 m/s, which is calculated from an average heat exchanger face velocity of 4 m/s. As heat from the exhaust dryer air (75 °C) is

recovered, air conditions cross the stickiness line,  $T - T_g = 37\text{ }^\circ\text{C}$ , at an air temperature of  $56\text{ }^\circ\text{C}$  depending on the absolute humidity of the exhaust air. Below  $56\text{ }^\circ\text{C}$  the exhaust finned tube heat exchanger is likely to experience significant fouling on the frontal face of the fins. Tube rows at the rear of the heat exchanger will experience increased fouling due to increased stickiness as the air temperature drops causing an increase in relative humidity.

## **7.6. Conclusion**

Deposition results for tubes indicate milk powder deposition occurs in the particle inertia moderated regime and is not strongly influenced by local wall shear stress for average duct velocities of 4.5 and 6.5 m/s. Deposition mostly occurs on the front face of the round, elliptical and turned square tubes and decreases around each tube until a critical impact angle to the surface of the tube and deposition ceases. None of the tube geometries contained significant deposition on the rear side of the tube. The critical impact angle maybe described by the deposition model from Chapter 6 and is independent of tube shape. Elliptical tube is shown to be naturally low fouling due to the shape of the tube.

Results show that milk powder deposition can cause a rise in the pressure drop across the fin bank by as much as 65 %. The pressure drop across the fin bank is strongly related to the fraction of open area available for air to pass through and the average face velocity. The stickiness level of milk powder is a determining factor in the severity of deposition and pressure drop increase. Application of the results to industry may inform the design of a recuperator to intentionally limit the amount of heat recovery to avoid sticky conditions thus preventing high levels of fouling on the frontal face of fins.



## Chapter 8

# Thermo-economic assessment tool for industrial milk spray dryer exhaust to inlet air heat recovery systems

---

### 8.1. Introduction

Economic profit is the ultimate driver behind implementation of heat recovery projects. Acquiring approval for capital expenditure is often a competitive process where various projects are compared and ranked before final selection is determined. By its very nature exhaust heat recovery may appear less attractive than other liquid heat recovery projects due to the expense associated with heat recovery from a low temperature gaseous flow. Chapter 3 clearly demonstrated gaseous exhaust heat recovery is essential to achieving maximum heat recovery and minimum utility consumption.

Figure 8-1 explains the design challenge and potential optimisation associated with spray dryer exhaust heat recovery. The up-side down triangle represents the possible exhaust heat exchanger solutions. On the one hand exhaust heat exchangers with a greater number of tube rows can recover more heat but this increases both pressure drop and fouling. Fewer tube rows recover less heat with lower fouling and pressure drop. The air face velocity on the heat exchanger is also important and may be manipulated by changing the duct dimensions. High air velocities reduce fouling and improve heat transfer but also increase pressure drop. Lower air velocities have the opposite effect. Finding the right balance between heat recovery, fouling, and pressure drop is chiefly governed by the number of tube rows of the heat exchanger, the face velocity and the geometry of the heat exchanger surface. These parameters are important degrees of freedom that may be manipulated to maximise the economic benefit of an exhaust heat recovery project.

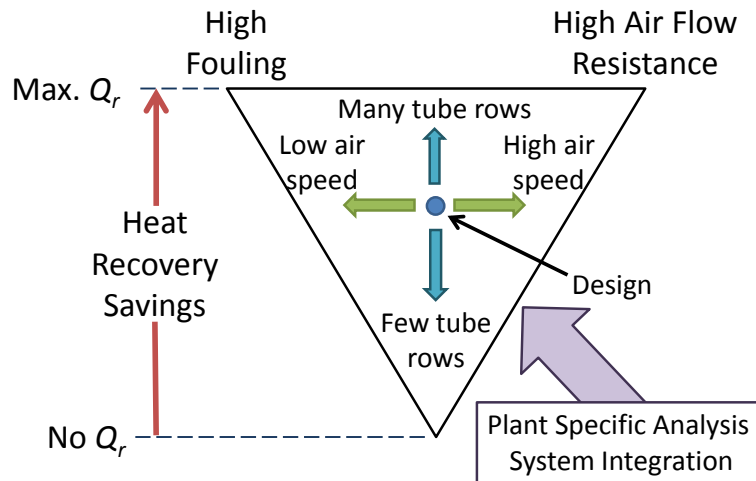


**Figure 8-1: The exhaust heat exchanger design challenge.**

This chapter reports the development of a thermo-economic assessment tool for modelling a dryer exhaust-to-inlet air indirect heat recovery system so that key economic indicators such as Net Present Value (NPV) and Internal Rate of Return (IRR) may be calculated and maximised. Incorporated into the tool is an estimate of the fouling on the heat exchanger surface based on the milk powder deposition model presented in Chapter 6. Literature correlations for the Colburn  $j$  factor and Fanning friction factor  $f$  of various heat transfer surfaces are built into the tool to model the heat exchanger system. In the tool, user defined parameters include heat exchanger geometry, heat exchanger surface type, exhaust and inlet air conditions including the particulate concentration, utility prices, and capital cost equations.

## **8.2. Method for modelling indirect exhaust heat recovery system**

### **8.2.1. Heat transfer and friction factor modelling**

#### **8.2.1.1. Heat exchanger system user defined inputs**

The exhaust-inlet liquid coupled loop heat recovery model is set-up to allow user-defined inputs for the design and modelling parameters of the heat recovery system. Figure 8-2 is a screenshot from the spreadsheet of the key design parameter inputs. Dimensions of the heat exchangers are calculated based on air mass flow rate in conjunction with the heat exchanger face velocity for the height

and width, and the number of tube rows for the depth. The model arbitrarily uses a height to width ratio of 1:1, i.e. square face, although it is possible to adjust this ratio elsewhere in the spreadsheet. The user has the option of inputting a specific loop flow rate or allowing the tool to calculate the optimum loop flow rate. In Figure 8-2, the tube type number refers to a particular tube geometry and arrangement. Each tube geometry and arrangement has been assigned a number and a new tube type maybe selected by inputting a number or from a drop down menu.

<b>User Defined Design Parameters</b>			
	<b>Exh. HX</b>	<b>Inlet HX</b>	
Air Mass Flow Rate	76	56	kg/s
Temperature In	75.0	15.0	°C
Abs Humidity	50.0	10.0	g/kg
Face Velocity	4.0	4.0	m/s
Tube Type	19	6	
Tube Rows	10	6	
Number of Passes	10	6	
Loop Flow Rate	Optimum		kg/s

Figure 8-2: Screenshot of heat exchanger user defined parameters in spreadsheet tool.

### 8.2.1.2. Governing heat transfer equations based on effectiveness

The model uses the effectiveness-NTU approach to solve the liquid coupled loop system from Kays and London (1998). The governing overall effectiveness ( $\epsilon_0$ ) relationship for the performance of LCHE systems is

$$\frac{1}{\epsilon_0} = \frac{C_{\min,o}/C_{\min,c}}{\epsilon_c} + \frac{C_{\min,o}/C_{\min,h}}{\epsilon_h} + \frac{C_{\min,o}}{C_l} \quad (8-1)$$

Each heat exchanger has the option to contain multiple fluid passes to produce a near counter flow heat exchanger arrangement for enhanced heat transfer but at the expense of pumping power. Kays and London provide the following relationship for determining the effectiveness of a multi-pass heat exchanger unit based on  $n$  number of passes and an effectiveness of a pass,  $\epsilon_p$ , defined by the applicable  $\epsilon$ -NTU relationship, which is the unmixed-unmixed cross-flow relationship for this situation. The unmixed-unmixed cross-flow correlation is

selected because there is very little transverse mixing on both the air and water sides within a pass of a finned tube heat exchanger.

$$\varepsilon = \frac{\left(\frac{1 - \varepsilon_p C^*}{1 - \varepsilon_p}\right)^n - 1}{\left(\frac{1 - \varepsilon_p C^*}{1 - \varepsilon_p}\right)^n - C^*} \quad (8-2)$$

The model contains a circular referencing/calculation system so that once the heat exchanger outlet temperatures are known, the air and water properties update and the system resolves. Air properties are called from the commercial Excel™ add-in package @Air ([www.techwareeng.com](http://www.techwareeng.com)). Water properties are called from built-in spreadsheet functions powered by the open source XSteam tables ([www.x-eng.com](http://www.x-eng.com)), which are based on IAPWS IF97 steam and water properties.

Once the model finds a solution, the quality of the solution is checked. The model checks to ensure the temperatures in and out of the heat exchangers are thermodynamically feasible and the duties of the two heat exchangers are the same. The model ensures the number of passes is valid for the number of tube rows. Warning messages appear and are recorded when heat transfer and/or friction factor correlation limits are exceeded.

### **8.2.1.3. Heat transfer and pressure drop heat exchanger surface characteristics**

Heat transfer and friction factor correlations have been formulated using the tabulated data presented in Kays and London (1998) for staggered finned and bare tube banks and the data in Walmsley et al. (2012b) for bare circular and elliptical tube geometries. A power law based equation provided sufficiently high correlation for the data of most tube types and arrangements. Correlations for bare and finned tubes and plain plate air-water geometries are built into the spreadsheet. Table 8-1 provides the essential heat exchanger surface design variables such as tube diameter, tube/plate arrangements, etc.

**Table 8-1: Heat exchanger geometry information. Key for heat exchanger surface codes: C – circular (round); E – elliptical; B – bare; F – finned; KL – Kays and London (1998); W – Walmsley et al. (2012b); numbers and other letters refer to the specific surface arrangement.**

Source	Code	$d_o$ mm	$d_i$ mm	$x$ tube/plate mm	$d_{h,air}$ mm	$\sigma_{air}$ $m^2/m^2$	$\alpha$ $m^2/m^3$	$S_T$ mm	$S_L$ mm	Fin pitch fins/m	$x_{fin}$ mm	$d_{fin}$ mm	$\Phi$ $m^2/m^2$
<i>Bare tube - staggered arrangement</i>													
KL	CB-1.5:1.25-3/8	9.5	6.2	1.7	7.6	0.333	175	14.3	11.9				
W	CB-1.5:1.25 (CFD)	20.0	16.7	1.7	15.9	0.333	84	30.0	25.0				
W	CB-2:1 (CFD)	20.0	16.7	1.7	25.5	0.500	79	40.0	20.0				
W	EB-1.5:1.25 (CFD)	30.8	27.5	1.7	15.9	0.333	84	30.0	38.5				
W	EB-2:1 (CFD)	25.9	22.6	1.7	25.5	0.500	79	40.0	30.8				
<i>Circular finned tube - staggered arrangement</i>													
KL	CF-7.34	9.7	7.2	1.2	4.8	0.538	459	24.8	20.3	289	0.460	23.4	0.892
KL	CF-8.72	9.7	7.2	1.2	3.9	0.524	535	24.8	20.3	343	0.460	23.4	0.910
KL	CF-8.72c	10.7	8.2	1.2	4.4	0.494	446	24.8	20.3	343	0.480	23.4	0.876
KL	CF-7.0-5/8J	16.4	13.1	1.7	6.7	0.449	269	31.3	34.3	276	0.250	28.5	0.830
KL	CF-8.7-5/8J (A)	16.4	13.1	1.7	5.5	0.443	324	31.3	34.3	343	0.250	28.5	0.862
KL	CF-8.7-5/8J (B)	16.4	13.1	1.7	11.7	0.628	216	46.9	34.3	343	0.250	28.5	0.862
KL	CF-9.05-3/4J (A)	19.7	16.4	1.7	5.1	0.455	354	39.5	44.5	356	0.305	37.2	0.917
KL	CF-9.05-3/4J (B)	19.7	16.4	1.7	8.2	0.572	279	50.3	44.5	356	0.305	37.2	0.917
KL	CF-9.05-3/4J (C)	19.7	16.4	1.7	13.6	0.688	203	69.2	44.5	356	0.305	37.2	0.917
KL	CF-9.05-3/4J (D)	19.7	16.4	1.7	4.8	0.537	443	69.2	20.3	356	0.305	37.2	0.917
KL	CF-9.05-3/4J (E)	19.7	16.4	1.7	6.4	0.572	354	50.3	34.9	356	0.305	37.2	0.917
KL	CF-8.8-1.0J (A)	26.0	22.7	1.7	5.9	0.439	299	49.8	52.4	346	0.305	44.1	0.825
KL	CF-8.8-1.0J (B)	26.0	22.7	1.7	13.2	0.642	191	78.2	52.4	346	0.305	44.1	0.825
<i>Plain plate</i>													
KL	2.0 T			0.3	14.5		250	19.1	304.8	79	0.813		0.606
KL	3.01 T			0.3	10.8		323	19.1	304.8	119	0.813		0.706
KL	3.97 T			0.3	8.6		392	19.1	304.8	156	0.813		0.766
KL	5.3 S			0.3	6.1		617	11.9	304.8	209	0.152		0.719
KL	6.2 B			0.3	5.5		669	10.3	304.8	244	0.254		0.728
KL	9.03 SB			0.3	4.6		801	6.4	304.8	356	0.203		0.888
KL	11.1 B			0.3	3.5		1024	12.2	304.8	437	0.203		0.854
KL	14.77 ST			0.3	2.6		1378	8.4	304.8	582	0.152		0.844
KL	15.08 SB			0.3	2.7		1358	6.4	304.8	594	0.152		0.870
KL	19.86 ST			0.3	1.9		1841	10.6	304.8	782	0.152		0.849

In practice the average heat transfer coefficient varies from row-to-row in a finned tube heat exchanger (Kays and London, 1998). Literature correlations are corrected for the row effect so that the reported Nusselt ( $Nu$ ) or  $j$  factor correlation is based on a heat exchanger with infinite rows. There are two methods to account for the row-effect on the heat transfer coefficient: (1) adjust the heat transfer coefficient and (2) use row specific  $\epsilon$ -NTU relationships. The approach taken in this work is to apply row specific  $\epsilon$ -NTU relationships from Engineering Science Data Unit (ESDU) 86018 cited by Wang et al. (2000).

#### 8.2.1.4. Loop flow rate optimisation

The approach applied in the Excel tool to optimise a LCHE system is to select areas for the exhaust and inlet air heat exchangers. The tool then determines the near optimum loop flow rate using Eq. 2-6 from Chapter 2. With a known loop flow rate,  $C_l$ , and heat exchanger areas, the loop temperatures of a LCHE system may be calculated using the temperature effectiveness of the exhaust and inlet exchangers. Temperature effectiveness is obtained from the unmixed-unmixed

cross-flow P-NTU (or  $\epsilon$ -NTU) relationship, which is given in Appendix C. The respective formulas for the hot and cold loop temperatures are

$$T_{lc} = \frac{P_h C_h (1 - P_{c(l)}) T_{h1} + P_c C_c T_{c1}}{P_h C_h (1 - P_{c(l)}) + P_c C_c} \quad (8-3)$$

$$T_{lh} = \frac{P_h C_h T_{h1} + P_c C_c (1 - P_{h(l)}) T_{c1}}{P_h C_h (1 - P_{c(l)}) + P_c C_c} \quad (8-4)$$

The derivations for the loop temperature equations based on using the optimum loop flow rate are presented in Appendix D.

## 8.2.2. Modelling fouling and its effects on heat transfer and pressure drop

### 8.2.2.1. Fouling build-up

Figure 8-3 shows the inputs to the model that relate to the build-up of fouling. Elsewhere in the spreadsheet the user may also input a particle size distribution. Using these parameters the spreadsheet applies the deposition model from Chapter 6 to estimate the amount of powder that sticks for each time step. The method for estimating the amount of deposition is explained in Figure 8-4. After entering the required inputs, the spreadsheet calculates the overall heat recovery system duty and estimates the air temperature profile within the exhaust heat exchanger based on a constant average heat transfer coefficient for each tube row, which results in a constant NTU for all tube rows.

Fouling and Cleaning Parameters		
Concentration	3.5	mg/m <sup>3</sup>
Run time	672	h
Time Step	5.0	h
Wash Length	1.0	h
Start Clean?	TRUE	
Optimum Clean?	FALSE	

Figure 8-3: Screenshot of fouling and cleaning user defined parameters from spreadsheet tool.

The temperature profile is used to calculate a critical impact angle (Eq. 6-14) for each combination of tube row and particle size, which may be translated into a

probability of sticking assuming a uniform particle impact distribution across the frontal face of a tube. The probability of sticking is the probability that a particle which impacts a tube will stick. The probability of impact is the probability that a particle will impact a tube. The probability of impact is assumed constant and equal to one minus the frontal free-flow area. There is opportunity in future work to input a probability of impact that is particle size specific. In practice smaller particles are expected to have lower probabilities due to the smaller particle relaxation times as was discussed in Chapter 2.

The product of the probabilities of impact and sticking give the percentage of particle mass entering a row that will deposit. This process of calculating the mass deposited is repeated for each combination of particle size fraction and tube row within a single time-step. The effect of the fouling build-up on  $R_f$  and  $f$  is discussed in detail in the next two sections. For each new time-step, the performance of the heat recovery system and the exhaust heat exchanger temperature profile is recalculated. Once the run-time is complete, the model uses the cumulative heat recovery savings and costs to estimate the payback, NPV and IRR for the system.

The spreadsheet tool incorporating the fouling model required 2.5 h on average to complete the analysis for one heat exchanger design using a time step of 5 h for a total cycle of 672 h. The fouling model was computed on an Intel™ i7 3.4 GHz processor. Test cases were used to determine the appropriate time step as to minimise its impact on the final solution.

The fouling build-up model makes several simplifications and assumptions. Uniform distribution along the length of each tube is assumed although in practice the particle distribution, which is often related to the airflow distribution, may be mal-distributed causing a non-uniform profile along the length of a tube. Deposition is also likely to be heavier near the heat exchanger outer walls as shown in the experimental work of Chapter 7. The probability of impact is constant for all rows and particle sizes. The probability of sticking has no respect for the surface condition and assumes the probability of a particle sticking to the tube wall is similar to a particle sticking to a particle. This simplification is supported by the

work of Nijdam and Langrish (2006), who found pre-coating the inside of a dryer with powder had little effect on the rate of deposition build-up.

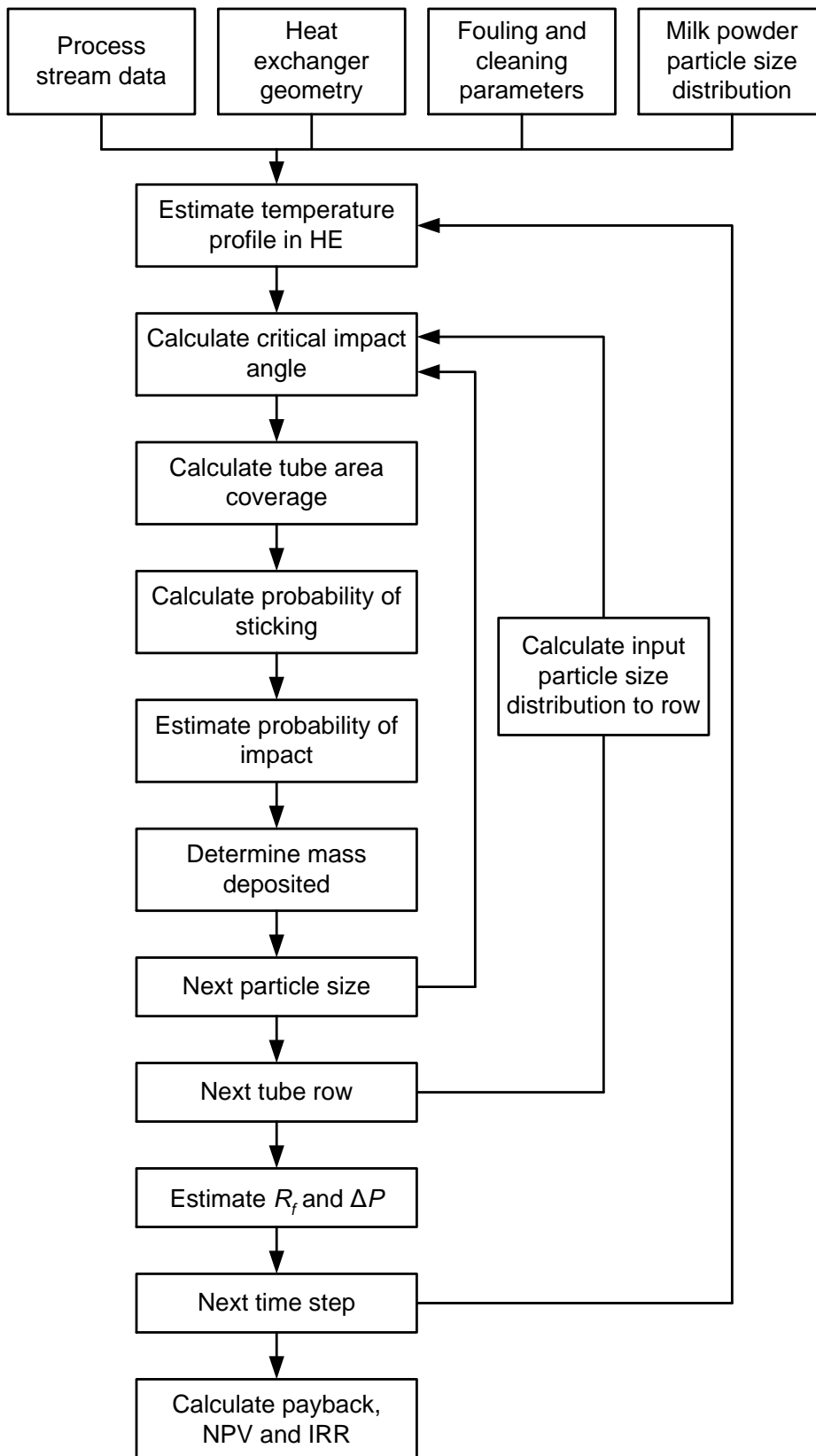
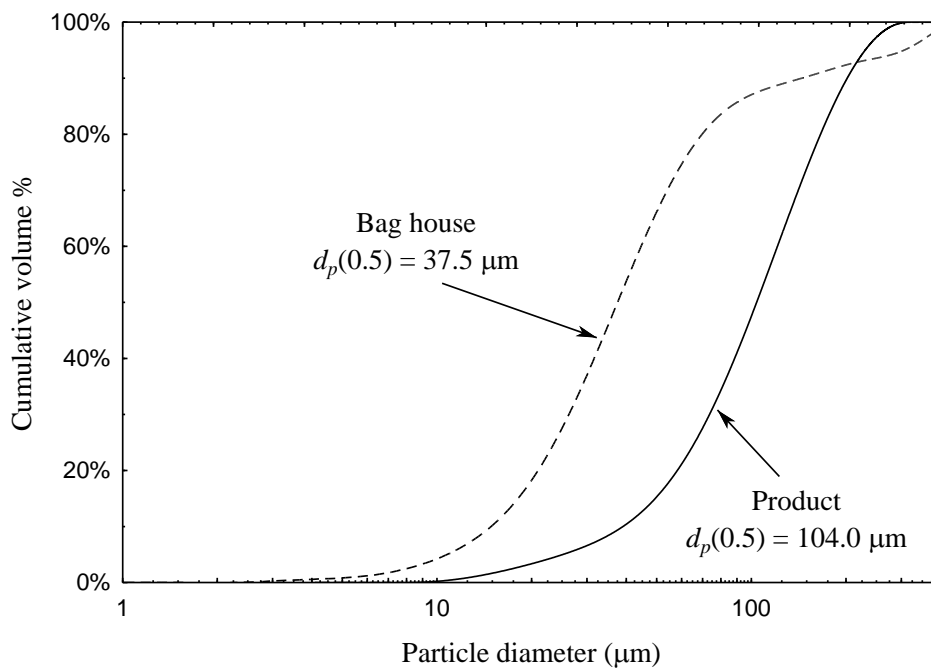


Figure 8-4: Heat exchanger fouling model flow diagram.

### 8.2.2.2. Particle size distribution

Figure 8-5 shows the particle size distributions of SMP product compared to the size distribution collected in the bag house, which is assumed to be similar to the size distribution emitted out the exhaust duct. The average particle size for bag house powder is significantly lower than bulk product, but the distributions span similar size ranges. The baghouse powder particle size distribution is entered into the spreadsheet tool as an input to the fouling model.



**Figure 8-5: Particle size distribution of baghouse and bulk product SMP.**

The particle size distributions in Figure 8-5 were experimentally obtained using a light ray diffraction method using such instruments as a Malvern Mastersizer. Commonly food powders are added to a solvent and analysed. The standard method for analysis of milk powders is to place a small sample in isopropanol and test every two minutes until readings are constant (Nijdam and Langrish, 2006; Pisecky, 1997).

### 8.2.2.3. The effect of fouling on heat transfer

#### Fouling on tubes

Fouling affects heat transfer due to adding a layer of resistance. If the fouling was assumed to be perfectly uniform in thickness around a circular tube, the resistance due to fouling may be estimated using

$$R_{f,tube} = \frac{r_{tube}}{k_f} \ln\left(\frac{r_f}{r_{tube}}\right) \quad (8-5)$$

where  $R_{f,tube}$  is the fouling resistance using the air-side tube area as the basis,  $k_f$  is the thermal conductivity of the foulant layer,  $r_f$  is the radius of the fouling and  $r_{tube}$  is the outside radius of the tube. As a simplification, it is assumed that the fouling build-up on the front of the tubes add a layer of thermal resistance approximately equal to the same volume of fouling uniformly spread around the outside of the tube. Thermal conductivity is taken as  $0.1 \text{ W/}^\circ\text{C} \cdot \text{m}$  (MAF Quality Management, 1996).

The heat transfer resistance due to milk powder deposition on the front of the tube is difficult to estimate without simplification. The presence of deposits in a heat exchanger are likely to significantly influence the airflow profile and the overall bulk average air velocity in the heat exchanger. The fouling layer acts as a thermal resistance, but it also improves  $h$  and  $A$  by channelling the air flow, which increases the average velocity in the heat exchanger, and enlarging the surface contact area between the air and the tube with fouling.

#### Fouling on fins

Fouling on the frontal face of fins has been shown to add little in the way of heat transfer resistance in other industries. Fouling does impact on the air flow resistance and, therefore, the velocity and distribution of the air flow experienced inside the heat exchanger. The added pressure drop can cause a reduction in the volumetric flow rate if the capacity of the fan has reached its zenith. The reduction in air flow through a heat exchanger has been shown to be the root cause of

decreases in heat duty for particulate fouling on the frontal face of fins (Bell and Groll, 2011).

In this work, attempts are made to stay in heat recovery regions where powder deposition on the frontal face of fins is avoided. Chapter 8 presented a relationship between the velocity through the open area and milk powder stickiness. Using this relationship limits are placed on the outlet temperature of the exhaust heat exchanger, which is the point of greatest powder stickiness, to minimise the likelihood of fouling on the frontal face of fins. As a result only fouling on the frontal face of the tube is considered in the model. Future work may look in detail at the accuracy of this assumption between testing finned tubes of various pitches.

#### **8.2.2.4. The effect of fouling on pressure drop**

The effect of fouling pressure drop is estimated based on the experimental pressure drop data for single bare tubes in cross-flow from Chapter 7. Differentiating Eq. 8-1 with respect to time gives

$$\frac{d(\Delta P(\%))}{dt} = \frac{\Delta P_{final}(\%)}{\tau_f} \exp\left(-\frac{t}{\tau_f}\right) \quad (8-6)$$

For a small time step the change in pressure drop may be numerically estimated using

$$\Delta(\Delta P(\%)) = \frac{\Delta P_{final}(\%)}{\tau_f} \exp\left(-\frac{t}{\tau_f}\right) \Delta t \quad (8-7)$$

The above equation is applied to estimate how the pressure drop of the exhaust heat exchanger increases overtime. The time constant in Eq. 8-13 is determined using Eq. 7-2 from Chapter 7, which is applied to scale the time constant to industrial situations with much lower powder concentration. Experimental results yielded a time constant of 420 s based on a powder concentration of 1.8 g of powder per kg of air. Linear equations relating the final asymptotic value for the percent pressure drop increase to stickiness are obtained from the data presented in Figure 7-14. These equations are specific to the tube shape.

### 8.2.3. Utility and capital costing

Utility and capital cost estimates are made based on the parameters presented in Figure 8-6. Capital cost equations are built into the spreadsheet and use the cost factor as a Lang factor. Based on these inputs together with the performance predictions, the spreadsheet calculates the cost benefit analysis shown in Figure 8-7.

User Defined Cost Parameters		
Target Inlet Temp	200	°C
Steam Price	\$ 30	/t
Electricity Price	\$ 120	/MWh
$\eta_{\text{Pump/Fan}}$	0.60	
Cost for Cleaning	\$ 5,000	/wash
Production Hours	5000	h/y
Utility Price Rise	5%	/y
Discount Rate	15%	/y
Accounting Period	10	y
Cost Factor	3.37	

Figure 8-6: Screenshot of utility, capital and miscellaneous user defined parameters.

The literature and industrial documentation has very few capital cost estimation equations for finned tube heat exchangers. Furthermore the few equations that are present do not differentiate between heat exchangers with different fin pitches and tube or fin thickness and instead total area is used to estimate a capital cost. As a result the costs of the heat exchangers have been estimated using two different methods. HE cost method A is based on calculating the total mass of stainless steel and aluminium required to make the heat exchangers multiplied by individual forming factors that reflect how easy a material will shape. Added to the material and forming costs is the cost of welding the heat exchanger together, which is dependent on the number of tubes in each exchanger, and the cost of putting fins on a tube. The sum of the various cost components relating to the construction of the heat exchanger is multiplied by a Lang factor of 3.5 (Bouman et al., 2005). HE cost method B is based on the total area of the heat exchanger using the equation presented in Table 3-3 of Chapter 3. When payback, NPV and IRR are calculated, the spreadsheet uses the higher of the two HE cost estimates

(either HX Cost A or HX Cost B). Electrical power includes additional electricity consumed by the inlet fan for the new inlet exchanger, by the exhaust fan for the fouled exhaust heat exchanger, and by the water pump.

Cost/Benefit		
Estimated Savings	1289	kW
Steam Savings	\$290,001	/y
Inlet Air Heat Req.	10,667	kW
%Main Air Heater Duty	12.1%	
Electrical Power	44	kW
Electrical Cost	\$26,242	/y
Cleaning Cost	\$ 0	/y
Profit	\$ 263,759	/y
HX Cost A	\$ 521,423	/y
HX Cost B	\$ 339,528	/y
Pump & Fan Cost	\$ 33,669	/y
Total Capital Cost	\$555,092	
Payback	2.10	y
Net Present Value	\$ 1,099,282	
IRR	54%	

Figure 8-7: Screenshot of cost/benefit analysis results.

### 8.2.4. Macros for modelling a range of design inputs

The spreadsheet tool has a simple flexible macro built-in to enable the user to test a range of heat exchanger design parameters. Figure 8-8 is a screenshot of the interface that allows input of which parameter is to be tested, and the range and step size for the parameter. The user also specifies the heat exchanger which the parameter refers to (exhaust or inlet). There are the options to allow the model to calculate the optimum loop flow rate and determine the IRR, which many companies use as a key economic indicator for a heat recovery project.

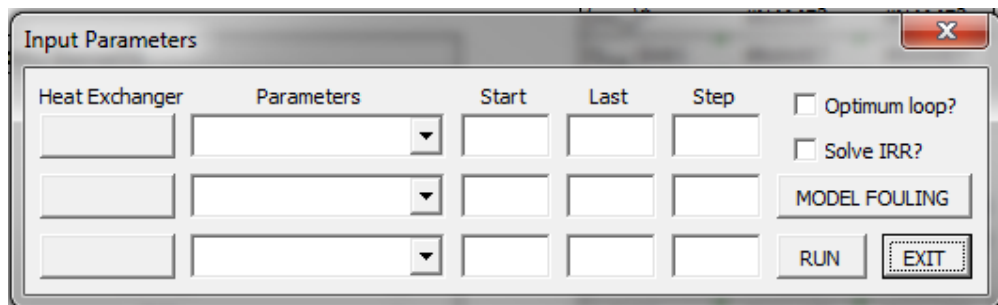


Figure 8-8: Interface for setting up a user defined macro for testing a range of inputs.

### **8.3. Exhaust heat recovery industrial case study**

The case study for modelling exhaust heat recovery is the same plant as studied in Chapter 3. The exhaust air temperature is 75 °C with a humidity of 48 g/kg before heat recovery flowing at 153 kg/s on a dry air basis. The inlet air is drawn in at 15 °C on average with a humidity of 10 g/kg at 117 kg/s on a dry air basis. The exhaust air flow includes air flow through the dryer and fluidised beds whereas the inlet air flow is only for the dryer.

In the analysis, a steam cost of \$45 /MWh and an electricity price of \$120 /GWh are used. The plant is assumed to operate for 5000 h per year and the dryer is washed every four weeks. At a minimum it is hoped that the exhaust heat exchanger will not require cleaning while the dryer is on product. Project economics are calculated using a typical industrial discount rate of 15 % and an accounting period of 10 years. Utility prices are assumed to rise at a constant rate of 5 % per year.

#### **8.3.1. Modelling heat exchanger performance with fouling**

Heat exchanger performance has been modelled for a four week period with estimates for fouling build-up and its associated effects based on the experimental data gathered in Chapters 6 and 7. Figure 8-9 plots one case where the inlet heat exchanger has 12 tube rows and the exhaust exchanger has 14 tube rows.

With no fouling, the finned tube exhaust heat exchanger recovered 3.2 MW, which is equivalent to a 14.4 % reduction in steam use for the main dryer air heater. The duty of the finned tube exhaust exchanger system fell to 3.0 MW at the end of the dryer production cycle. The finned round tube had the greatest amount of deposition resulting in an 8 % reduction in heat recovery, which is similar heat transfer reductions experienced in boilers (Stehlík, 2011), and an increase in pressure drop for the exhaust exchanger of 5 %, which is very modest. The bare round tube exhaust heat exchanger began with a duty of 2.7 MW, which fell to 2.6 MW at the end of the dryer run, and a pressure drop increase of 2 %. The elliptical bare tube experienced very little fouling resulting in only a small change to its heat recovery and pressure drop.

The exhaust exchanger with bare round tube recovers 17 % less heat than with finned round tube. Fouling on the bare round tube is expected to be less than for the finned tube because the average temperatures experienced in the exhaust heat exchanger are higher due to less heat recovery compared to the finned round tube. The elliptical bare tube has a 41 % lower pressure drop and a 3 % higher heat recovery compared to the bare round tube. The elliptical tube is also low fouling as was shown in Chapter 7 and is not expected to have much fouling after four weeks.

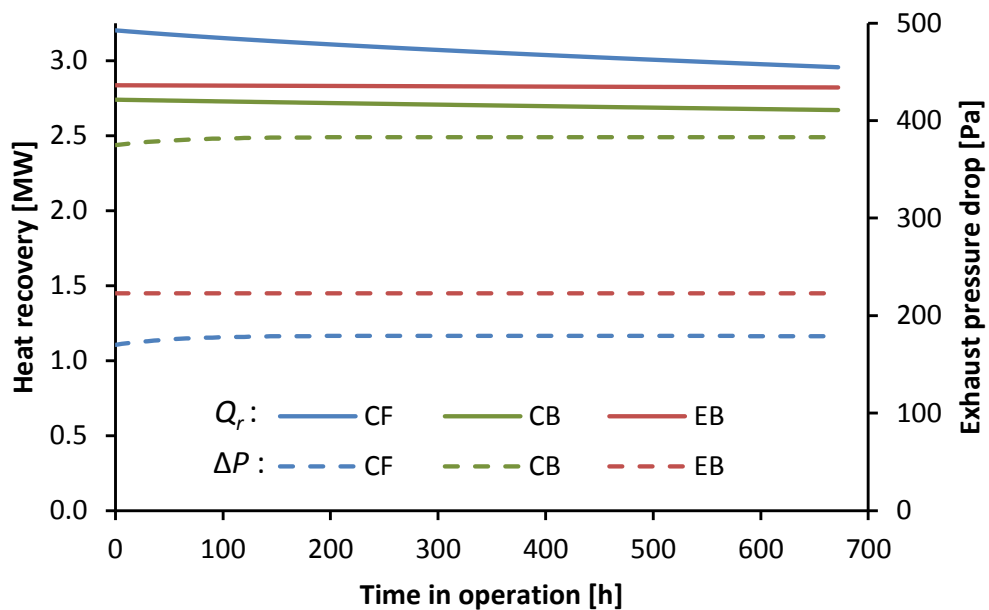


Figure 8-9: Estimated heat recovery and pressure drop for a period of four weeks. Exhaust heat exchanger with 14 tube rows of either finned round tube (CF-9.05-3/4J (C)), bare round tube (CB-1.5:1.25 (CFD)) and elliptical tube (EB-1.5:1.25 (CFD)). Inlet heat exchanger with 12 tube rows of finned round tube (CF-9.05-3/4J (C)). Both heat exchangers have a face velocity of 4 m/s.

### 8.3.2. Optimisation of the liquid coupled loop heat exchanger system

The fouling with its associated effects has been modelled for a range of tube geometries (finned round tube, bare round tube and elliptical tube), number of tube rows in the exhaust exchanger (4 – 40), and face velocities for the exhaust heat exchanger (2 – 8 m/s). In total over 25,000 time steps were modelled and the economics of the exhaust heat recovery system was analysed in terms of NPV and IRR based on average heat recovery and pressure drop values.

Figure 8-10 plots the results for a finned round tube, bare round tube and elliptical round tube using the number of tube rows in the exhaust exchanger as the independent variable on the x-axis. Results show it is possible to design an economically favourable heat recovery system with payback times of about 2 years with IRR values greater than 50 %. The inlet heat exchanger has 12 tube rows, which could also be a variable to optimise. For Figure 8-10 the face velocity of the heat exchanger is set at 4.0 m/s. Each point in Figure 8-10 takes into account fouling which overtime lowers heat recovery and increases pressure.

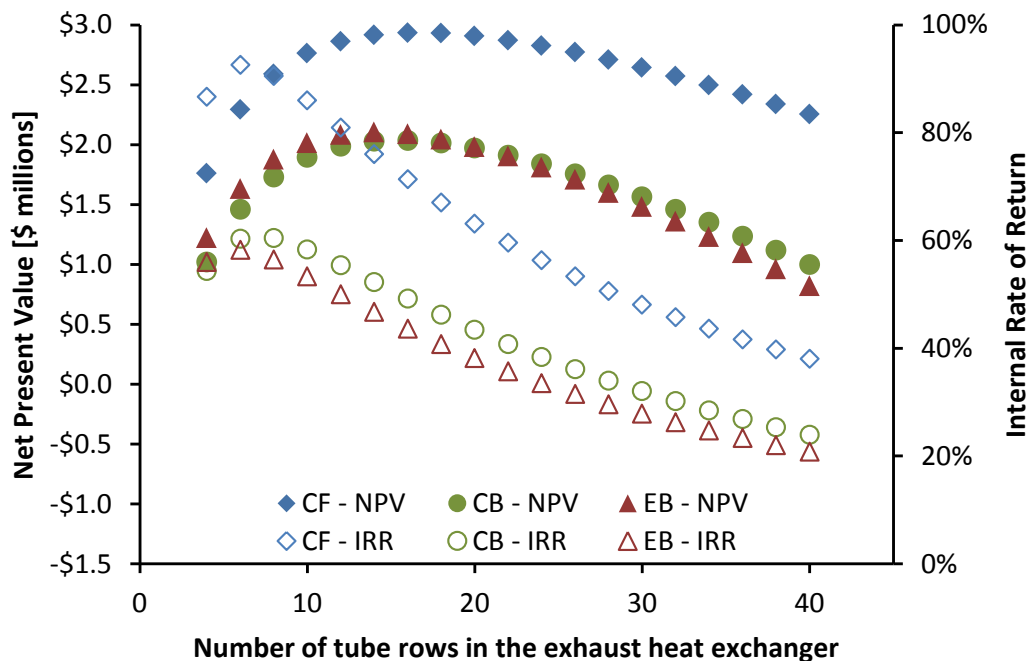


Figure 8-10: Number of exhaust tube rows versus NPV and IRR at 4 m/s air velocity for finned round tube (CF-9.05-3/4J (C)), bare round tube (CB-1.5:1.25 (CFD)) and elliptical tube (EB-1.5:1.25 (CFD)).

Based on IRR a designer would select 4 – 6 tube rows for the exhaust exchanger whereas NPV indicates 12 – 14 tube rows is most profitable. This difference is important because IRR gives a good indication of the short-term payback of a project and NPV focuses on the long-term profit. As expected the finned tube exhaust heat exchanger offers better IRR and NPV values compared to the bare tubes. The finned tube arrangement was selected over the other finned tube geometries in Kays and London (1998) because of its high Goodness factor ( $j/f$ ).

The model results may be also plotted using the exhaust outlet temperature as the x-axis as shown in Figure 8-11. The deposition results on the frontal face of fins

from Chapter 7 suggest fouling on the fins initiates and accolades for exhaust temperatures below about 55 °C for an absolute humidity of 48 g/kg. In this particular case, the peak of the IRR and NPV curves all occur before 55 °C, which indicates deposition on the front of the fins should not occur. Figure 8-11 shows the heat recovery savings achieved by basing the design on NPV is over 40 % higher than basing the design on IRR.

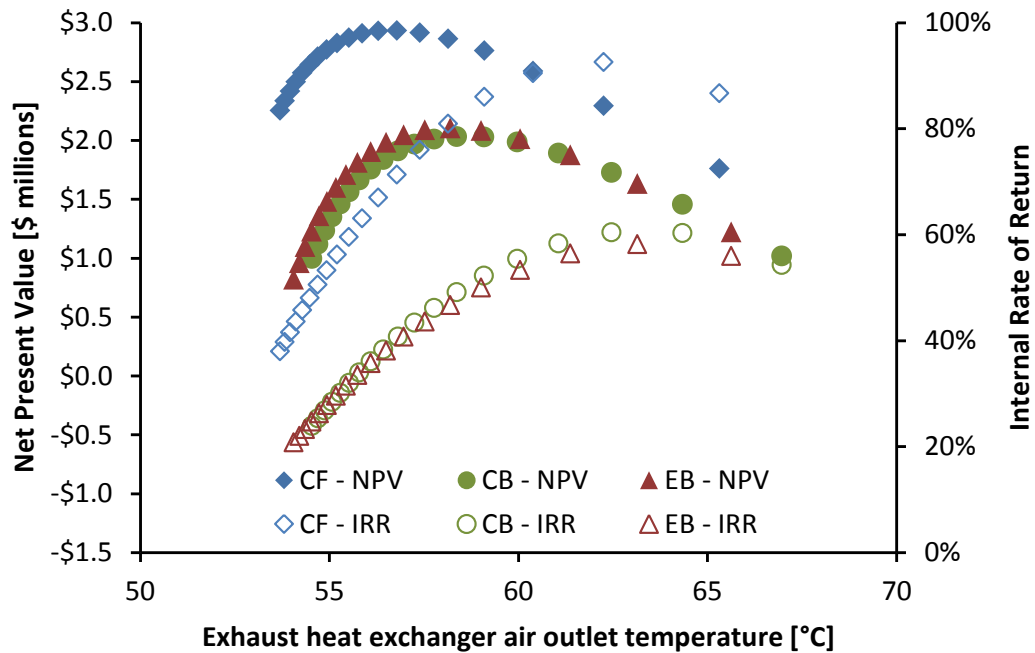


Figure 8-11: Exhaust outlet temperature versus NPV and IRR at 4 m/s air velocity for finned round tube (CF-9.05-3/4J (C)), bare round tube (CB-1.5:1.25 (CFD)) and elliptical tube (EB-1.5:1.25 (CFD)). Inlet air temperature to exhaust heat exchanger is 75 °C.

Face velocity of the exhaust air heat exchanger is another important design parameter. Fluid velocity is often a parameter that is manipulated to reduce heat exchanger fouling at the expense of increased pressure drop. Figure 8-12 plots the peak IRR and NPV values for the three heat exchanger geometries. In all cases the number of rows to achieve the peak IRR value compared to the peak NPV value is different. IRR analysis suggests a face velocity of about 6 m/s is advantageous whereas the NPV values support the selection of 4 m/s. Some dairy plants in New Zealand have a minimum threshold of an IRR of 50 % for an energy project to be actioned. Based on the results, the best LCHE system would use a finned tube heat exchanger to recover heat from the exhaust air with a face velocity of 4 m/s and 14 tube rows. For this system the NPV is NZ\$2.9 million and an IRR of 71 %.

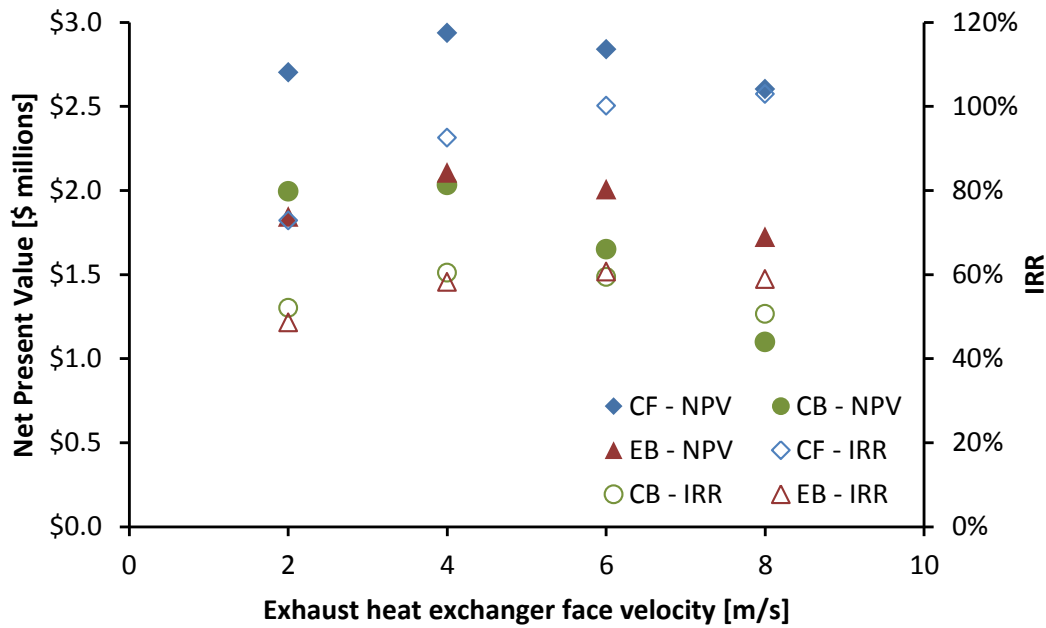


Figure 8-12: Heat exchanger face velocity versus the peak NPV and IRR values for a bare round tube exhaust heat exchanger and finned tube inlet heat exchanger.

## 8.4. Importance of site selection for dryer exhaust heat recovery

The economics for dryer exhaust heat recovery are highly site specific. The operation, equipment, and construction are slightly different for each milk powder plant and spray dryer. The purpose of this section is to highlight some of the important factors that require consideration for industrial implementation of exhaust heat recovery in New Zealand milk powder plants by drawing upon personal experience and observation.

1. **Inlet air temperature and humidity to the dryer:** the temperature and humidity of the ambient is location specific. The temperature of the inlet air as the designated heat sink provides essential temperature driving to recovery exhaust heat, which is directly related to the size of the exhaust heat exchanger. The inlet temperature will vary during a day/night and over the production season. Less humidity air is advantageous in terms of dryer capacity, but it also has a lower heat capacity flow rate, which means less recovered heat and steam is needed to raise the temperature of the air to approximately 200 °C.

2. **Exhaust air temperature and humidity:** dryers with higher exhaust temperatures are better candidates for energy recovery due to a larger potential temperature driving force. For the same exhaust air outlet temperature after heat recovery, exhaust air with an additional 5 °C can result in 30 % extra heat recovery. Humidity is also an important factor because it affects the stickiness of the milk powder and, therefore, the amount of fouling. For ease of exhaust heat recovery, a lower humidity is desirable, but from an overall dryer efficiency perspective, lower exhaust temperatures at high humidity maximise the drying capacity of the air.
3. **Inlet and exhaust fan capacity:** for existing sites it is important to understand where the inlet and exhaust fans are operating on the respective fan curves. Fans with sufficient spare capacity do not require replacement, which for retrofits is likely to be a significant cost. Where fans are likely pressure drop constrained, it is smarter to design the exhaust and inlet heat exchangers to meet a pressure drop target rather than a heat recovery target.
4. **Existing pre-heaters using utility:** at many sites steam is used to preheat air entering the building to 30 – 35 °C. These heat exchangers are typically a few rows deep with a large frontal area and a low face velocity. Re-piping an existing inlet preheater exchanger to use heat from the dryer exhaust is likely the most economical opportunity for some sites.
5. **Existing heat recovery to dryer inlet air:** some sites use waste heat from flue gas from the boiler or hot COW water to preheat the dryer inlet air. Because exhaust heat recovery is heating in similar temperature ranges, the full benefits of both heat recovery systems are not achievable.
6. **Re-usable existing ducting:** if possible it is desirable to avoid the costs of fabricating and installing large sections of new ducting.
7. **Price of energy:** heating costs can vary by 30 – 50% from site to site depending on the fuel source and the conversion efficiency. Sites in the South Island of New Zealand typically burn relatively cheap coal for process heat whereas North Island sites mostly use natural gas, which may be in shortage in the coming decades causing price increases.

8. **Operating and production hours:** heat recovery savings is directly proportional to the hours of production per year.
9. **Space:** the building housing the dryer needs to have the room for a heat recovery system. Modifications to buildings are very costly and risky potentially causing product contamination.
10. **Inlet air heater bottleneck:** where the inlet air heater is the bottleneck to increased production, exhaust heat recovery would provide additional duty to allow for more airflow into the dryer and additional dryer capacity. In this case, exhaust heat recovery may prevent the need for increasing the capacity of the existing steam boiler to meet the higher process heat demand.
11. **Bag filters:** efficient removal of milk particles from the exhaust air stream can decrease the risk and potential for exchanger fouling.
12. **Good attitude to change:** the site needs a good attitude to change, particularly when a technology is being implemented for the first time.

## 8.5. Conclusion

Exhaust heat recovery is economically justifiable based on current technology and utility and capital prices. The profitability of an exhaust heat recovery project is closely dependent on the size of the exhaust heat exchanger and its face velocity. Results from the model indicate that 4 m/s face velocity is a good trade-off between reducing fouling while maintaining an acceptable pressure drop. IRR analysis suggests the exhaust heat exchanger should contain only a few rows of tube (4 – 6 rows) whereas NPV analysis favours a larger exhaust heat exchanger with 12 -14 rows. The spreadsheet tool has flexibility to be applied to any milk powder plant to optimise the economics of an exhaust heat recovery system. Site selection for the first exhaust heat recovery projects is important to determine the sites with the greatest economic benefit.

# Chapter 9

## Conclusions and recommendations for future work

---

### 9.1. Conclusions

New Zealand milk powder plants can economically increase heat recovery by nearly 20 %. Stand-alone milk powder plants have a low pinch temperature of 10.5 °C, which is strongly influenced by the selection of the exhaust air target temperature. Additional heat recovery from liquid and vapour streams associated with the evaporator system can increase heat recovery by 6.9 % and the balance of the heat recovery increase comes from the dryer exhaust air. For stand-alone plants exhaust heat recovery is best applied to preheat the inlet dryer air using a liquid coupled loop heat exchanger system.

The economics of heat exchanger networks can be improved through optimisation of the area allocation using a novel Cost Derivative Method (CDM). By optimising the liquid and vapour sections of the milk powder plant MER networks using the CDM, the total cost was reduced by 5.8 % for MER A and 5.4 % for MER B compared to the Pinch Design Method solutions. In the distillation case study, a total cost savings of 7.6 % was obtained and the CDM solution betters four programming methods applied to the same problem.

Heat Recovery Loops (HRL) with a variable temperature storage system can be applied to multi-plant dairy factories to significantly improve inter-plant heat recovery. Exhaust heat recovery can play an integral part in supplying heat to neighbouring plants through a HRL. A novel method for designing a HRL with a variable temperature storage system is developed for improved heat recovery. Realistic heat recovery targets for a HRL can be generated using transient modelling of historical data. Industrial solar can be effectively integrated into a

HRL to take advantage of infrastructure common with HRLs, e.g. pumps, pipes and storage.

Severe milk powder fouling in an exhaust heat recovery system can be avoided by smart selection of the outlet temperature of the exhaust air leaving an exhaust heat exchanger. The propensity of milk powder to deposit on heat exchanger surfaces is strongly affected by the air temperature. As the air temperature in an exhaust heat exchanger drops, the stickiness of milk powder is increased. For skim milk powder, an exhaust heat exchanger outlet temperature above 55 °C is shown to minimise particulate fouling.

A semi-empirical criterion for predicating the deposition of milk powder on rigid surfaces has been developed. Milk powder deposition tests on tubes and fins confirm the applicability of the deposition model for non-flat surfaces. Milk powder deposition mostly occurs on the front face of round, elliptical and turned square tubes and very little deposition on the rear of the tubes confirming milk powder deposition is inertia moderated. Elliptical tube is naturally low fouling while also having a better heat transfer to pressure drop ratio compared to standard round tube.

The economics of exhaust heat recovery are favourable for large industrial spray dryers. With an optimised exhaust heat recovery system based on finned round tube for a 23.5 t/h plant, the spreadsheet tool estimates a simple payback time of less than 1.6 years, a net present value of nearly NZ\$2.9 million and an internal rate of return of 71 %.

## **9.2. Recommendations for future work**

### **Further development of the Cost Derivative Method**

The CDM, which uses the first derivative of the total cost function to optimally allocate network to minimise cost, have many areas that may be improved and extended. Some of the CDM concepts, such as the heat duty flow on factor, may prove valuable to be integrated with programming synthesis methods to

formulate network structure. The CDM may be extended to help optimise the selection of soft data, such as the target temperature of discharge streams.

At present the CDM only uses the first derivative of the total cost function to minimise cost. It is possible to also take a second derivative of the total cost function to confirm that a local minimum on the total cost function is found. The second derivative of the cost function may be useful to understand the nature of the first derivative of the total cost function and identify what may cause an additional local minimum/maximum to be generated for a specific network structure and stream data.

The CDM could include functions for variables that are assumed constant, such as the heat transfer film coefficient for individual streams. Such inclusion would require the designer to pre-determine some of the geometric aspects of each individual heat exchanger as to use the appropriate relationship between film coefficient and velocity as commonly expressed by the Reynolds number. For example plate heat exchangers have standard heights and widths and chevron angles. With these geometric parameters pre-defined, it is possible to establish how the number of plates affects the channel velocity, Re number and ultimately the film coefficient.

### **Further development of the HRL design method**

At present the HRL is designed on average data. Alternatively it may be possible to use historic, transient plant data as the basis of design framework to better select storage temperatures, heat exchanger areas, etc. The CDM may be extended to apply to optimum area allocation in HRLs and may be included as part of a wider design framework. An investigation into the best number of storage temperature levels for the large dairy site case may be performed. The controllability of HRLs as a system needs attention.

Details such as the position of utility exchangers in the HRL system and storage bypass may be looked into for further cost reductions. Present industrial HRLs contain a significant amount of redundant area for the times when storage is completely full of cold fluid or hot fluid. A different approach may be to place one

utility exchanger on each of the HRL supply fluid streams and require a minimum temperature quality fluid be distributed to the hot and cold sides of the network. Some streams to be included on the HRL may have installed balance tanks to even out flow variability, which would give control and heat exchanger performance benefits. In this work, industrial solar is integrated as if it was an extra heat source, but it is possible for solar to be integrated as a temperature and enthalpy booster for selected sink streams.

### **The next steps of the experimental milk powder deposition work**

Milk powders other than SMP may be tested for their individual stickiness characteristics. The clean-ability of fouled heat exchanger surfaces may be investigated. One difficulty faced with lab-scale testing exhaust heat exchanger fouling is the exact same conditions of the exhaust air and heat exchanger surface cannot be easily simulated. There is an issue with injecting very small particle sizes into the conditioned airflow without some manner agglomeration between particles occurring. The concentration of powder in the air flow is considerably higher for the lab test in order to accelerate the fouling rate and shorten the length of a test from a few weeks to a few hours. Generating a large quantity of hot, humid air for long periods of time is also costly. As a result further research in this area may be best directed to pilot scale in-plant implementation where a portion of actual dryer exhaust air is ducted to pass through a small heat exchanger. Such a set-up could be used to better understand the fouling as well as the trade-off between heat exchanger size and gas velocity, and their associated impacts on fouling, heat transfer, and pressure drop.

### **Further development of the thermo-economic assessment tool for exhaust air heat recovery**

There remain many questions around the accuracy of the cost estimations and the effects of fouling. Cost functions for finned tube heat exchangers are notoriously difficult to find in literature and equally as difficult to obtain from industry. This is partially due to the fact that economics and costs are constantly changing and affected by the state of the market.

## References

---

- Abd-Elhady, M.S., Rindt, C.C.M., Wijers, J.G., Van Steenhoven, A.A., Bramer, E.A., van der Meer, T.H., 2004. Minimum gas speed in heat exchangers to avoid particulate fouling. *International Journal of Heat and Mass Transfer* 47, 3943–3955. doi:10.1016/j.ijheatmasstransfer.2004.03.024
- Ahmad, S., Hui, D.C.W., 1991. Heat recovery between areas of integrity. *Computers & Chemical Engineering* 15, 809–832.
- Ahmad, S., Smith, R., 1989. Targets and design for minimum number of shells in heat exchanger networks. *ChERD* 67, 481–494.
- Ait-Ali, M.A., Wilde, D.J., 1980. Optimal area allocation in multistage heat exchanger systems. *Journal of Heat Transfer* 102, 199–201. doi:10.1115/1.3244260
- Atkins, M.J., Walmsley, M.R.W., Morrison, A.S., 2010a. Integration of solar thermal for improved energy efficiency in low-temperature-pinch industrial processes. *Energy* 35, 1867–1873. doi:10.1016/j.energy.2009.06.039
- Atkins, M.J., Walmsley, M.R.W., Neale, J.R., 2010b. The challenge of integrating non-continuous processes – milk powder plant case study. *Journal of Cleaner Production* 18, 927–934. doi:10.1016/j.jclepro.2009.12.008
- Atkins, M.J., Walmsley, M.R.W., Neale, J.R., 2011. Integrating heat recovery from milk powder spray dryer exhausts in the dairy industry. *Applied Thermal Engineering* 31, 2101–2106. doi:10.1016/j.applthermaleng.2011.03.006
- Atkins, M.J., Walmsley, M.R.W., Neale, J.R., 2012a. Process integration between individual plants at a large dairy factory by the application of heat recovery loops and transient stream analysis. *Journal of Cleaner Production* 34, 21–28. doi:10.1016/j.jclepro.2012.01.026
- Atkins, M.J., Walmsley, M.R.W., Walmsley, T.G., Fodor, Z., Neale, J.R., 2012b. Minimising Energy Use in Milk Powder Production using Process Integration Techniques. *Chemical Engineering Transactions* 29, 1507–1512. doi:10.3303/CET1229252
- Axelsson, E., Olsson, M.R., Berntsson, T., 2008. Opportunities for process-integrated evaporation in a hardwood pulp mill and comparison with a softwood model mill study. *Applied Thermal Engineering* 28, 2100–2107. doi:10.1016/j.applthermaleng.2008.01.011
- Bagajewicz, M., Rodera, H., 2000. Energy savings in the total site heat integration across many plants. *Computers & Chemical Engineering* 24, 1237–1242. doi:10.1016/S0098-1354(00)00318-5
- Bagajewicz, M., Rodera, H., 2002. Multiple plant heat integration in a total site. *AIChE Journal* 48, 2255–2270. doi:10.1002/aic.690481016
- Becker, H., Vuillermoz, A., Maréchal, F., 2011. Heat pump integration in a cheese factory. *Chemical Engineering* 25, 195.
- Bell, I.H., Groll, E.A., 2011. Air-side particulate fouling of microchannel heat exchangers: Experimental comparison of air-side pressure drop and heat transfer with plate-fin heat exchanger. *Applied Thermal Engineering* 31, 742–749. doi:10.1016/j.applthermaleng.2010.10.019

- Bell, L.N., Labuza, T.P., 2000. Moisture sorption: practical aspects of isotherm measurement and use. American Association of Cereal Chemists, St. Paul, USA.
- Bhandari, B., Howes, T., 2005. Relating the stickiness property of foods undergoing drying and dried products to their surface energetics. *Drying Technology: An International Journal* 23, 781. doi:10.1081/DRT-200054194
- Biegler, L.T., Grossmann, I.E., Westerberg, A.W., Kravanja, Z., 1997. Systematic methods of chemical process design. Prentice Hall, Upper Saddle River, NJ.
- Boonyai, P., Bhandari, B., Howes, T., 2004. Stickiness measurement techniques for food powders: a review. *Powder Technology* 145, 34–46. doi:10.1016/j.powtec.2004.04.039
- Boonyai, P., Howes, T., Bhandari, B., 2006. Applications of the cyclone stickiness test for characterization of stickiness in food powders. *Drying Technology: An International Journal* 24, 703.
- Bouman, R.W., Jensen, S.B., Wake, M.L., Earl, W.B., 2005. Process capital cost estimation for New Zealand 2004. Society of Chemical Engineers New Zealand, Wellington, New Zealand.
- Bouris, D., Konstantinidis, E., Balabani, S., Castiglia, D., Bergeles, G., 2005. Design of a novel, intensified heat exchanger for reduced fouling rates. *International Journal of Heat and Mass Transfer* 48, 3817–3832. doi:10.1016/j.ijheatmasstransfer.2005.03.026
- Bouris, D., Papadakis, G., Bergeles, G., 2001. Numerical evaluation of alternate tube configurations for particle deposition rate reduction in heat exchanger tube bundles. *International Journal of Heat and Fluid Flow* 22, 525–536. doi:10.1016/S0142-727X(01)00110-2
- Brilliantov, N., Albers, N., Spahn, F., Pöschel, T., 2007. Collision dynamics of granular particles with adhesion. *Phys. Rev. E* 76, 051302. doi:10.1103/PhysRevE.76.051302
- Brilliantov, N., Spahn, F., Hertzsch, J.M., Pöschel, T., 1996. Model for collisions in granular gases. *Phys. Rev. E* 53, 5382–5392. doi:10.1103/PhysRevE.53.5382
- Brooks, G.F., 2000. The sticking and crystallisation of amorphous lactose (M. Tech.). Massey University, Palmerston North, New Zealand.
- Buma, T.J., 1965. The true density of spray milk powders and of certain constituents. *Netherlands Milk and Dairy Journal* 19, 249–265.
- Chatterjee, R., 2004. Characterising stickiness of dairy powders (M. Tech.). Massey University, Palmerston North, New Zealand.
- Chen, C.L., Ciou, Y.J., 2009. Design of indirect heat recovery systems with variable-temperature storage for batch plants. *Ind. Eng. Chem. Res.* 48, 4375–4387. doi:10.1021/ie8013633
- Chen, X.D., Lake, R., Jebson, S., 1993. Study of milk powder deposition on a large industrial dryer. *Food and Bioproducts Processing: Transactions of the Institution of Chemical Engineers, Part C* 71, 180–186.
- Chen, X.D., Rennie, P.R., Mackereth, A.R., 2004. Combined Influences of Humidity and Temperature upon the Inter-Particle Stickiness of a Whole Milk Powder. *International Journal of Food Properties* 7, 499.

- Chen, X.D., Rutherford, L., Lloyd, R.J., 1994. Preliminary results of milk powder deposition at room temperature on a stainless steel surface mimicking the ceiling of a spray dryer. *Food and Bioproducts Processing* 72, 170–175.
- Davies, R.M., 1949. The Determination of Static and Dynamic Yield Stresses Using a Steel Ball. *Proceedings of the Royal Society of London. Series A. Mathematical and Physical Sciences* 197, 416–432. doi:10.1098/rspa.1949.0073
- Dhole, V.R., Linnhoff, B., 1993. Total site targets for fuel, co-generation, emissions, and cooling. *Computers & chemical engineering* 17, S101–S109.
- Douglas, J., 1988. *Conceptual Design of Chemical Processes*. McGraw-Hill, New York, USA.
- Downton, G.E., Flores-Luna, J.L., King, C.J., 1982. Mechanism of stickiness in hygroscopic, amorphous powders. *Industrial & Engineering Chemistry Fundamentals* 21, 447–451. doi:10.1021/i100008a023
- El-Halwagi, M.M., 2006. *Process Integration*. Academic Press, San Diego, USA.
- Escobar, M., Trierweiler, J.O., 2013. Optimal heat exchanger network synthesis: A case study comparison. *Applied Thermal Engineering* 51, 801–826. doi:10.1016/j.applthermaleng.2012.10.022
- Fodor, Z., Klemeš, J.J., Varbanov, P.S., Walmsley, M.R.W., Atkins, M.J., Walmsley, T.G., 2012. Total site targeting with stream specific minimum temperature difference. *Chemical Engineering Transactions* 29, 409–414. doi:10.3303/CET1229069
- Furman, K.C., Sahinidis, N.V., 2001. Computational complexity of heat exchanger network synthesis. *Computers & Chemical Engineering* 25, 1371–1390. doi:10.1016/S0098-1354(01)00681-0
- Furman, K.C., Sahinidis, N.V., 2002. A Critical Review and Annotated Bibliography for Heat Exchanger Network Synthesis in the 20th Century. *Ind. Eng. Chem. Res.* 41, 2335–2370. doi:10.1021/ie010389e
- Gabites, J.R., Abrahamson, J., Winchester, J.A., 2007. Fines Loadings in Milk Powder Plants with Washable Baghouses. *Food and Bioproducts Processing* 85, 315–321. doi:10.1205/fbp07064
- Gordon, M., Taylor, J.S., 1952. Ideal copolymers and the second-order transitions of synthetic rubbers. i. non-crystalline copolymers. *J. Appl. Chem.* 2, 493–500. doi:10.1002/jctb.5010020901
- Gorji-Bandpy, M., Yahyazadeh-Jelodar, H., Khalili, M., 2011. Optimization of heat exchanger network. *Applied Thermal Engineering* 31, 779–784. doi:10.1016/j.applthermaleng.2010.10.026
- Goršek, A., Glavič, P., Bogataj, M., 2006. Design of the optimal total site heat recovery system using SSSP approach. *Chemical Engineering and Processing: Process Intensification* 45, 372–382. doi:10.1016/j.cep.2005.10.003
- Goula, A.M., Karapantsios, T.D., Adamopoulos, K.G., 2007. An Advanced Centrifugal Technique to Characterize the Sticking Properties of Tomato Pulp during Drying. *Drying Technology: An International Journal* 25, 599.
- Greenwood, J.A., Johnson, K.L., 1981. The mechanics of adhesion of viscoelastic solids. *Philosophical Magazine A* 43, 697–711.

- Guha, A., 2008. Transport and deposition of particles in turbulent and laminar flow. *Annual Review of Fluid Mechanics* 40, 311–341.
- Gundersen, T., 2000. *A Process Integration PRIMER*. SINTEF Energy Research, Trondheim, Norway.
- Hanneman, H., Robertson, L.J., 2005. Heat recovery systems, in: *Energy Use in Dairy Processing*. Presented at the IDF World Dairy Summit, International Dairy Federation, Brussels, Belgium.
- Haque, M.K., Roos, Y.H., 2004. Water Plasticization and Crystallization of Lactose in Spray-dried Lactose/Protein Mixtures. *Journal of Food Science* 69, FEP23–FEP29. doi:10.1111/j.1365-2621.2004.tb17863.x
- Hayashi, H., Handa, M., 1974. The True Particle Density of Milk Powder by the Beakman Air Comparison Pycnometer. Presented at the XIX International Dairy Congress, p. 524.
- Hennigs, C., Kockel, T.K., Langrish, T.A.G., 2001. New measurements of the sticky behavior of skim milk powder. *Drying Technology: An International Journal* 19, 471. doi:10.1081/DRT-100103929
- Hertz, H., 1881. On the contact of elastic solids. *J. reine angew. Math* 92, 156–171.
- Hertz, H., 1896. *Miscellaneous papers*. McMillan, London, UK.
- Hill, V.L., Craig, D.Q.M., Feely, L.C., 1998. Characterisation of spray-dried lactose using modulated differential scanning calorimetry. *International Journal of Pharmaceutics* 161, 95–107. doi:10.1016/S0378-5173(97)00334-7
- Hogan, S.A., O’Callaghan, D.J., 2010. Influence of milk proteins on the development of lactose-induced stickiness in dairy powders. *International Dairy Journal* 20, 212–221. doi:10.1016/j.idairyj.2009.11.002
- Holmberg, R.B., 1975. Heat transfer in liquid-coupled indirect heat exchanger systems. *Journal of Heat Transfer* 97, 499–503.
- Hui, C.Y., Baney, J.M., Kramer, E.J., 1998. Contact Mechanics and Adhesion of Viscoelastic Spheres. *Langmuir* 14, 6570–6578. doi:10.1021/la980273w
- Intipunya, P., Shrestha, A., Howes, T., Bhandari, B., 2009. A modified cyclone stickiness test for characterizing food powders. *Journal of Food Engineering* 94, 300–306. doi:10.1016/j.jfoodeng.2009.03.024
- Jegla, Z., Kilkovský, B., Stehlík, P., 2010. Calculation Tool for Particulate Fouling Prevention of Tubular Heat Transfer Equipment. *Heat Transfer Engineering* 31, 757–765. doi:10.1080/01457630903500932
- Johari, G.P., Hallbrucker, A., Mayer, E., 1987. The glass-liquid transition of hyperquenched water. *Nature* 330, 552–553. doi:10.1038/330552a0
- Johnson, K.L., 1987. *Contact mechanics*. Cambridge University Press, Cambridge, UK.
- Johnson, K.L., 1996. Continuum mechanics modeling of adhesion and friction. *Langmuir* 12, 4510–4513.
- Johnson, K.L., 1998. Mechanics of adhesion. *Tribology International* 31, 413–418.
- Johnson, K.L., Greenwood, J.A., 1997. An adhesion map for the contact of elastic spheres. *Journal of Colloid and Interface Science* 192, 326–333.
- Johnson, K.L., Kendall, K., Roberts, A.D., 1971. Surface Energy and the Contact of Elastic Solids. *Proceedings of the Royal Society of London. A. Mathematical and Physical Sciences* 324, 301–313. doi:10.1098/rspa.1971.0141

- Jouppila, K., Roos, Y.H., 1994. Water Sorption and Time-Dependent Phenomena of Milk Powders. *Journal of Dairy Science* 77, 1798–1808. doi:10.3168/jds.S0022-0302(94)77121-6
- Jung, S.-H., Lee, I.-B., Yang, D.R., Chang, K.S., 1994. Synthesis of maximum energy recovery networks in batch processes. *Korean J. Chem. Eng.* 11, 162–171. doi:10.1007/BF02697461
- Kakaç, S., Liu, H., 2002. Heat exchangers: selection, rating, and thermal design. CRC, London, UK.
- Kays, W.M., London, A.L., 1998. Compact Heat Exchangers, 3rd ed. Krieger Pub. Co., Malabar, USA.
- Kemp, I.C., 2005. Reducing Dryer Energy Use by Process Integration and Pinch Analysis. *Drying Technology: An International Journal* 23, 2089.
- Kemp, I.C., 2007. Pinch analysis and process integration: a user guide on process integration for the efficient use of energy. Butterworth-Heinemann, Oxford, UK.
- Kemp, I.C., Deakin, A.W., 1989. Cascade analysis for energy and process integration of batch processes. Part 1. Calculation of energy targets. *Chemical Engineering Research and Design* 67, 495–509.
- Kemp, I.C., MacDonald, E., 1987. Energy and process integration in continuous and batch processes. I. *Chem. E. Symp. Ser.* 105, 185–200.
- Kemp, I.C., MacDonald, E., 1988. Application of pinch technology to separation, reaction and batch processes. *ICHEME Symposium Series* 109, 239–257.
- Kim, E.H.J., Chen, X.D., Pearce, D., 2005. Effect of surface composition on the flowability of industrial spray-dried dairy powders. *Colloids and Surfaces B: Biointerfaces* 46, 182–187. doi:10.1016/j.colsurfb.2005.11.005
- Klemeš, J.J. (Ed.), 2013. Handbook of process integration: Minimisation of energy and water use, waste and emissions. Woodhead Publishing, Cambridge, UK.
- Klemeš, J.J., Dhole, V.R., Raissi, K., Perry, S.J., Puigjaner, L., 1997. Targeting and design methodology for reduction of fuel, power and CO<sub>2</sub> on total sites. *Applied Thermal Engineering* 17, 993–1003. doi:10.1016/S1359-4311(96)00087-7
- Klemeš, J.J., Friedler, F., Bulatov, I., Varbanov, P., 2010. Sustainability in the process industry: integration and optimization. McGraw-Hill, New York, USA.
- Klemeš, J.J., Smith, R., Kim, J.K., 2008. Handbook of water and energy management in food processing. Woodhead Publishing, Cambridge, UK.
- Kockel, T.K., Allen, S., Hennigs, C., Langrish, T.A.G., 2002. An experimental study of the equilibrium for skim milk powder at elevated temperatures. *Journal of Food Engineering* 51, 291–297. doi:10.1016/S0260-8774(01)00070-X
- Konstandopoulos, A.G., 2006. Particle sticking/rebound criteria at oblique impact. *Journal of Aerosol Science* 37, 292–305. doi:10.1016/j.jaerosci.2005.05.019
- Kota, K., Langrish, T.A.G., 2006. Fluxes and Patterns of Wall Deposits for Skim Milk in a Pilot-Scale Spray Dryer. *Drying Technology: An International Journal* 24, 993–1001.

- Kralj, A.K., Glavič, P., Kravanja, Z., 2002. Waste heat integration between processes. *Applied Thermal Engineering* 22, 1259–1269.
- Kralj, A.K., Glavič, P., Kravanja, Z., 2005. Heat integration between processes: Integrated structure and MINLP model. *Computers & Chemical Engineering* 29, 1699–1711. doi:10.1016/j.compchemeng.2005.01.006
- Krummenacher, P., Favrat, D., 2001. Indirect and mixed direct-indirect heat integration of batch processes based on Pinch Analysis. *International Journal of Thermodynamics* 4, 135–143.
- Kudra, T., 2003. Sticky Region in Drying—Definition and Identification. *Drying Technology: An International Journal* 21, 1457.
- Kukulka, D.J., Smith, R., Fuller, K.G., 2011. Development and evaluation of enhanced heat transfer tubes. *Applied Thermal Engineering* 31, 2141–2145. doi:10.1016/j.applthermaleng.2011.01.024
- Lazar, M.E., Brown, A.H., Smith, G.S., Wang, F.F., Lindquist, F.E., 1956. Experimental production of tomato powder by spray drying. *Food Technology* 129–134.
- Lee, I.B., Reklaitis, G.V., 1995. Optimal scheduling of cyclic batch processes for heat integration-I. Basic formulation. *Computers and Chemical Engineering* 19, 883–905.
- Lin, S.X.Q., Chen, X.D., Pearce, D., 2005. Desorption isotherm of milk powders at elevated temperatures and over a wide range of relative humidity. *Journal of Food Engineering* 68, 257–264. doi:10.1016/j.jfoodeng.2004.05.036
- Linnhoff, B. (Ed.), 1982. *User guide on process integration for the efficient use of energy*. Pergamon Press, Oxford, UK.
- Linnhoff, B., 1993. Pinch analysis : a state-of-the-art overview : Techno-economic analysis. *Chemical engineering research & design* 71, 503–522.
- Linnhoff, B., Ashton, G.J., Obeng, E.D.A., 1988. Process integration of batch processes. *Understanding process integration II*. 221.
- Linnhoff, B., Dhole, V.R., 1993. Targeting for CO<sub>2</sub> emissions for Total Sites. *Chemical Engineering & Technology* 16, 252–259. doi:10.1002/ceat.270160407
- Linnhoff, B., Flower, J.R., 1978. Synthesis of heat exchanger networks: I. Systematic generation of energy optimal networks. *AIChE Journal* 24, 633–642. doi:10.1002/aic.690240411
- Linnhoff, B., Hindmarsh, E., 1983. The pinch design method for heat exchanger networks. *Chemical Engineering Science* 38, 745–763.
- Lloyd, R.J., Chen, X.D., Hargreaves, J.B., 1996. Glass transition and caking of spray-dried lactose. *International Journal of Food Science & Technology* 31, 305–311. doi:10.1046/j.1365-2621.1996.00352.x
- Lovell-Smith, J.E.R., Baldwin, A.J., 1988. Energy Saving Opportunities in Dairy Manufacturing Plant. *New Zealand Journal of Dairy Science and Technology* 23, 61–74.
- MAF Quality Management, 1996. *Physical Properties of Dairy Products*, 3rd ed. MAF Quality Management, Hamilton, New Zealand.
- Mercer, A.C., 1986. Improving the energy efficiency of industrial spray dryers. *Journal of Heat Recovery Systems* 6, 3–10. doi:10.1016/0198-7593(86)90166-9

- Mikkelsen, J., 1998. Thermal-energy storage systems in batch processing (PhD thesis). Technical University of Denmark, Lyngby, Denmark.
- Minton, P.E., 1986. Handbook of Evaporation Technology. Noyes Publications, New Jersey, USA.
- Morrison, A.S., Walmsley, M.R.W., Neale, J.R., Burrell, C.P., Kamp, P.J.J., 2007. Non-continuous and variable rate processes: Optimisation for energy use. *Asia-Pacific Journal of Chemical Engineering* 2, 380–387.
- Murti, R.A., 2006. The effect of lactose source on the stickiness of dairy powders (M.Enginering). Massey University, Palmerston North, New Zealand.
- Murti, R.A., Paterson, A.H.J., Pearce, D., Bronlund, J.E., 2009. Stickiness of skim milk powder using the particle gun technique. *International Dairy Journal* 19, 137–141. doi:10.1016/j.idairyj.2008.09.001
- Murti, R.A., Paterson, A.H.J., Pearce, D., Bronlund, J.E., 2010. The influence of particle velocity on the stickiness of milk powder. *International Dairy Journal* 20, 121–127. doi:10.1016/j.idairyj.2009.08.005
- Navarro, H.A., Cabezas-Gómez, L., 2005. A new approach for thermal performance calculation of cross-flow heat exchangers. *International Journal of Heat and Mass Transfer* 48, 3880–3888. doi:10.1016/j.ijheatmasstransfer.2005.03.027
- Neale, J.R., 2014. Personal communication.
- New Zealand Energy Use: Industrial and trade sector 2012 [WWW Document], 2013. Statistics NZ. URL [http://www.stats.govt.nz/browse\\_for\\_stats/industry\\_sectors/Energy/EnergyUseSurvey\\_HOTP2009revised.aspx](http://www.stats.govt.nz/browse_for_stats/industry_sectors/Energy/EnergyUseSurvey_HOTP2009revised.aspx) (accessed 2.17.14).
- Nijdam, J.J., Langrish, T.A.G., 2005. An Investigation of Milk Powders Produced by a Laboratory-Scale Spray Dryer. *Drying Technology: An International Journal* 23, 1043. doi:10.1081/DRT-200060208
- Nijdam, J.J., Langrish, T.A.G., 2006. The effect of surface composition on the functional properties of milk powders. *Journal of Food Engineering* 77, 919–925. doi:10.1016/j.jfoodeng.2005.08.020
- NIWA, 2013. The National Climate Database [WWW Document]. The National Climate Database. URL <http://cliflo.niwa.co.nz/> (accessed 11.10.13).
- Obeng, E.D.A., Ashton, G.J., 1988. On pinch technology based procedures for the design of batch processes. *Chemical Engineering Research & Design* 66, 255–259.
- Olsen, D., Wellig, B., 2011. Practical Heat Integration Analysis In The Process Industries. Presented at the World Engineers' Convention, Geneva, Switzerland.
- Omar, A.M.E., Roos, Y.H., 2007. Water sorption and time-dependent crystallization behaviour of freeze-dried lactose-salt mixtures. *LWT - Food Science and Technology* 40, 520–528. doi:10.1016/j.lwt.2005.12.006
- Ozkan, N., Walisinghe, N., Chen, X.D., 2002. Characterization of stickiness and cake formation in whole and skim milk powders. *Journal of Food Engineering* 55, 293–303. doi:10.1016/S0260-8774(02)00104-8
- Ozmen, L., Langrish, T.A.G., 2002. Comparison of glass transition temperature and sticky point temperature for skim milk powder. *Drying Technology: An International Journal* 20, 1177. doi:10.1081/DRT-120004046

- Ozmen, L., Langrish, T.A.G., 2003. An experimental investigation of the wall deposition of milk powder in a pilot-scale spray dryer. *Drying Technology* 21, 1253–1272.
- Palzer, S., 2005. The effect of glass transition on the desired and undesired agglomeration of amorphous food powders. *Chemical Engineering Science* 60, 3959–3968. doi:10.1016/j.ces.2005.02.015
- Papadakis, S.E., Bahu, R.E., McKenzie, K.A., Kemp, I.C., 1993. Correlations for the equilibrium moisture content of solids. *Drying Technology: An International Journal* 11, 543. doi:10.1080/07373939308916843
- Papageorgiou, L.G., Shah, N., Pantelides, C.C., 1994. Optimal Scheduling of Heat-Integrated Multipurpose Plants. *Industrial & Engineering Chemistry Research* 33, 3168–3186. doi:10.1021/ie00036a036
- Paterson, A.H.J., 2011. Personal communication.
- Paterson, A.H.J., Bronlund, J.E., Zuo, J.Y., Chatterjee, R., 2007a. Analysis of particle-gun-derived dairy powder stickiness curves. *International Dairy Journal* 17, 860–865. doi:10.1016/j.idairyj.2006.08.013
- Paterson, A.H.J., Brooks, G.F., Bronlund, J.E., Foster, K.D., 2005. Development of stickiness in amorphous lactose at constant T-Tg levels. *International Dairy Journal* 15, 513–519. doi:10.1016/j.idairyj.2004.08.012
- Paterson, A.H.J., Zuo, J.Y., Bronlund, J.E., Chatterjee, R., 2007b. Stickiness curves of high fat dairy powders using the particle gun. *International Dairy Journal* 17, 998–1005. doi:10.1016/j.idairyj.2006.11.001
- Paz, C., Suárez, E., Eiris, A., Porteiro, J., 2012. Experimental evaluation of the critical local wall shear stress around cylindrical probes fouled by diesel exhaust gases. *Experimental Thermal and Fluid Science* 38, 85–93. doi:10.1016/j.expthermflusci.2011.11.011
- Perkins, M., Ebbens, S.J., Hayes, S., Roberts, C.J., Madden, C.E., Luk, S.Y., Patel, N., 2007. Elastic modulus measurements from individual lactose particles using atomic force microscopy. *International Journal of Pharmaceutics* 332, 168–175. doi:10.1016/j.ijpharm.2006.09.032
- Pettersson, F., 2005. Synthesis of large-scale heat exchanger networks using a sequential match reduction approach. *Computers & Chemical Engineering* 29, 993–1007. doi:10.1016/j.compchemeng.2004.11.001
- Pisecky, I., 1997. Handbook of milk powder manufacture. Niro A/S, Copenhagen, Denmark.
- Polley, G.T., Panjeh Shahi, M.H., Jegede, F.O., 1990. Pressure drop considerations in the retrofit of heat exchanger networks. *ChERD* 68, 211–220.
- Pourali, O., Amidpour, M., Rashtchian, D., 2006. Time decomposition in batch process integration. *Chemical Engineering and Processing: Process Intensification* 45, 14–21. doi:10.1016/j.cep.2005.06.002
- Quijera, J.A., Labidi, J., 2013. Pinch and exergy based thermosolar integration in a dairy process. *Applied Thermal Engineering* 50, 464–474. doi:10.1016/j.applthermaleng.2012.06.044
- Rademacher, B., Walenta, W., Kessler, H.G., 1995. Contamination during pasteurization [of milk] by biofilms of thermophilic streptococci, in: *Heat Treatments and Alternative Methods*. Presented at the IDF Symposium, International Dairy Federation, Vienna, Austria.

- Raffel, M., Willert, C.E., Wereley, S.T., Kompenhans, J., 2007. Particle Image Velocimetry: A Practical Guide, 2nd ed. Springer, New York, USA.
- Reay, D., 1982. A selection of heat recovery applications illustrated by means of case studies. *Journal of Heat Recovery Systems* 2, 401–418. doi:10.1016/0198-7593(82)90028-5
- Robertson, L.J., Baldwin, A.J., 1993. Process integration study of a milk powder plant. *Journal of Dairy Research* 60, 327–338.
- Rodera, H., Bagajewicz, M.J., 1999. Targeting procedures for energy savings by heat integration across plants. *AIChE Journal* 45, 1721–1742.
- Rogers, L.N., Reed, J., 1984. The adhesion of particles undergoing an elastic-plastic impact with a surface. *J. Phys. D: Appl. Phys.* 7, 677. doi:10.1088/0022-3727/17/4/007
- Roos, Y.H., 2002. Importance of glass transition and water activity to spray drying and stability of dairy powders. *Le Lait* 82, 10. doi:10.1051/lait:2002025
- Sadr-Kazemi, N., Polley, G.T., 1996. Design of energy storage systems for batch process plants. *Chemical engineering research & design* 74, 584–596.
- Savkoor, A.R., Briggs, G.A.D., 1977. The effect of tangential force on the contact of elastic solids in adhesion. *Proceedings of the Royal Society of London. A. Mathematical and Physical Sciences* 356, 103–114.
- Schmitt, E.A., Law, D., Zhang, G.G.Z., 1999. Nucleation and crystallization kinetics of hydrated amorphous lactose above the glass transition temperature. *J. Pharm. Sci.* 88, 291–296. doi:10.1021/js980387s
- Seider, W.D., Seader, J.D., Lewin, D.R., Widagdo, S., 2009. *Product and process design principles: synthesis, analysis, and evaluation*, 3rd Edition. ed. John Wiley and Sons, New York, USA.
- Shah, K.R., Sekulić, D.P., 2003. *Fundamentals of Heat Exchanger Design*. Wiley & Sons, Hoboken, USA.
- Shenoy, U.V., 1995. *Heat exchanger network synthesis: process optimization by energy and resource analysis*. Gulf Professional Publishing, Houston, USA.
- Siddique, M., Khaled, A.R.A., Abdulhafiz, N.I., Boukhary, A.Y., 2010. Recent Advances in Heat Transfer Enhancements: A Review Report. *International Journal of Chemical Engineering* 2010, 1–28. doi:10.1155/2010/106461
- Sieniutycz, S., Jeżowski, J., 2009. *Energy optimization in process systems*. Elsevier Science.
- Silalai, N., Roos, Y.H., 2010. Roles of Water and Solids Composition in the Control of Glass Transition and Stickiness of Milk Powders. *Journal of Food Science* 75, E285–E296. doi:10.1111/j.1750-3841.2010.01652.x
- Singhvi, A., Shenoy, U.V., 2002. Aggregate Planning in Supply Chains by Pinch Analysis. *Chemical Engineering Research and Design, Techno-Economic Analysis* 80, 597–605. doi:10.1205/026387602760312791
- Smith, R., 2000. State of the art in process integration. *Applied Thermal Engineering* 20, 1337–1345. doi:10.1016/S1359-4311(00)00010-7
- Smith, R., 2005. *Chemical process design and integration*. John Wiley and Sons, New York, USA.
- Smith, R., Jones, P.S., 1990. The optimal design of integrated evaporation systems. *Heat Recovery Systems and CHP* 10, 341–368. doi:10.1016/0890-4332(90)90086-Y

- Statistics NZ, 2013. Infoshare [WWW Document]. Statistics New Zealand. URL [www.stats.govt.nz/infoshare/Default.aspx](http://www.stats.govt.nz/infoshare/Default.aspx) (accessed 1.31.13).
- Stehlík, P., 2011. Conventional versus specific types of heat exchangers in the case of polluted flue gas as the process fluid – A review. *Applied Thermal Engineering* 31, 1–13. doi:10.1016/j.applthermaleng.2010.06.013
- Stoltze, S., Lorentzen, B., Petersen, P.M., Qvale, B., 1993. A Simple Technique for Analyzing Waste-Heat Recovery with Heat-Storage in Batch Processes, in: Pilavachi, D.P.A. (Ed.), *Energy Efficiency in Process Technology*. Springer, Netherlands, pp. 1063–1072.
- Stoltze, S., Mikkelsen, J., Lorentzen, B., Peterson, P.M., Qvale, B., 1995. Waste-Heat Recovery in Batch Processes Using Heat Storage. *Journal of energy resources technology* 117, 142.
- Tan, R.R., Foo, D.C.Y., 2007. Pinch analysis approach to carbon-constrained energy sector planning. *Energy* 32, 1422–1429. doi:10.1016/j.energy.2006.09.018
- Thomsen, M.K., Jespersen, L., Sjostrom, K., Risbo, J., Skibsted, L.H., 2005. Water Activity–Temperature State Diagram of Amorphous Lactose. *Journal of Agricultural and Food Chemistry* 53, 9182–9185. doi:10.1021/jf0508394
- Thornton, C., Ning, Z.M., 1998. A theoretical model for the stick/bounce behaviour of adhesive, elastic-plastic spheres. *Powder Technology* 99, 154–162. doi:10.1016/S0032-5910(98)00099-0
- Tiwari, S., Maurya, D., Biswas, G., Eswaran, V., 2003. Heat transfer enhancement in cross-flow heat exchangers using oval tubes and multiple delta winglets. *International Journal of Heat and Mass Transfer* 46, 2841–2856. doi:10.1016/S0017-9310(03)00047-4
- Towler, G.P., Mann, R., Serriere, A.J.-L., Gabaude, C.M.D., 1996. Refinery Hydrogen Management: Cost Analysis of Chemically-Integrated Facilities. *Ind. Eng. Chem. Res.* 35, 2378–2388. doi:10.1021/ie950359+
- Varbanov, P.S., Klemeš, J.J., 2011. Integration and management of renewables into Total Sites with variable supply and demand. *Computers & Chemical Engineering* 35, 1815–1826. doi:10.1016/j.compchemeng.2011.02.009
- Vaselenak, J.A., Grossmann, I.E., Westerberg, A.W., 1986. Heat integration in batch processing. *Industrial & Engineering Chemistry Process Design and Development* 25, 357–366.
- Verdurmen, R.E.M., van Houwelingen, G., Gusing, M., Verschueren, M., Straatsma, J., 2006. Agglomeration in Spray Drying Installations (The EDECAD - Project): Stickiness Measurements and Simulation Results. *Drying Technology: An International Journal* 24, 721.
- Wallack, D.A., King, C.J., 1988. Sticking and Agglomeration of Hygroscopic, Amorphous Carbohydrate and Food Powders. *Biotechnology Progress* 4, 31–35. doi:10.1002/btpr.5420040106
- Walmsley, M.R.W., Atkins, M.J., Walmsley, T.G., 2013a. Application of Heat Recovery Loops to Semi-continuous Processes for Process Integration, in: *Handbook of Process Integration (PI)*. Woodhead Publishing, Cambridge, UK.
- Walmsley, M.R.W., Walmsley, T.G., Atkins, M.J., Kamp, P.J.J., Neale, J.R., 2014. Minimising carbon emissions and energy expended for electricity

- generation in New Zealand through to 2050. *Applied Energy* In Press. doi:10.1016/j.apenergy.2014.04.048
- Walmsley, M.R.W., Walmsley, T.G., Atkins, M.J., Neale, J.R., 2013b. Methods for improving heat exchanger area distribution and storage temperature selection in heat recovery loops. *Energy* 55, 15–22. doi:10.1016/j.energy.2013.02.050
- Walmsley, M.R.W., Zhao, S.X., Walmsley, T.G., Neale, J.R., Atkins, M.J., Hoffmann-Vocke, J., 2010. Modelling Deposition of Amorphous Based Particles in an Impingement Jet, in: 19th International Congress of Chemical and Process Engineering. Presented at the CHISA, Prague, CZ.
- Walmsley, T.G., Walmsley, M.R.W., Atkins, M.J., Fodor, Z., Neale, J.R., 2012a. Optimal Stream Discharge Temperatures for a Dryer Operation Using a Thermo-Economic Assessment. *Chemical Engineering Transactions* 29, 403–408. doi:10.3303/CET1229252
- Walmsley, T.G., Walmsley, M.R.W., Atkins, M.J., Hoffman-Vocke, J., Neale, J.R., 2012b. Numerical Performance Comparison of Different Tube Cross-Sections for Heat Recovery From Particle-Laden Exhaust Gas Streams. *Procedia Engineering* 42, 1476–1490. doi:10.1016/j.proeng.2012.07.527
- Walmsley, T.G., Walmsley, M.R.W., Atkins, M.J., Neale, J.R., 2013a. Fouling and pressure drop analysis of milk powder deposition on the front of parallel fins. *Advanced Powder Technology* 24, 780–785. doi:10.1016/j.apt.2013.04.004
- Walmsley, T.G., Walmsley, M.R.W., Atkins, M.J., Neale, J.R., 2013b. Improving energy recovery in milk powder production through soft data optimisation. *Applied Thermal Engineering* 61, 80–87. doi:10.1016/j.applthermaleng.2013.01.051
- Walmsley, T.G., Walmsley, M.R.W., Zhao, S., Neale, J.R., Atkins, M.J., 2010. Effect of Angle on Particle Deposition in an Impingement Jet, in: 17th Australasian Fluid Mechanics Conference. Presented at the 17th Australasian Fluid Mechanics Conference, Auckland, New Zealand.
- Wang, C.C., Webb, R.L., Chi, K.Y., 2000. Data reduction for air-side performance of fin-and-tube heat exchangers. *Experimental Thermal and Fluid Science* 21, 218–226. doi:10.1016/S0894-1777(00)00005-4
- Wang, J.F., Cleland, D.J., 2011. Heat pump heat recovery options for dryers in the food industry. Presented at the 23rd IIR International Congress of Refrigeration, Prague, CZ.
- Wang, L., Sundén, B., Manglik, R.M., 2007. Plate heat exchangers: design, applications and performance. *Wit Pr/Computational Mechanics*.
- Wang, Y.P., Smith, R., 1994. Wastewater minimisation. *Chemical Engineering Science* 49, 981–1006. doi:10.1016/0009-2509(94)80006-5
- Webb, R., Kim, N.H., 2005. Principles of enhanced heat transfer, 2nd ed. ed. Taylor & Francis, Boca Raton, USA.
- Westergaard, V., 2010. Milk Powder Technology, 5th Edition. ed. GEA Niro, Copenhagen, Denmark.
- Westphalen, D.L., Wolf Maciel, M.R., 2000. Pinch analysis of evaporation systems. *Brazilian Journal of Chemical Engineering* 17, 525–538. doi:10.1590/S0104-66322000000400017

- Westphalen, D.L., Young, B.R., Svrcek, W.Y., 2003. A Controllability Index for Heat Exchanger Networks. *Ind. Eng. Chem. Res.* 42, 4659–4667. doi:10.1021/ie020893z
- Williams, M.L., Landel, R.F., Ferry, J.D., 1955. The Temperature Dependence of Relaxation Mechanisms in Amorphous Polymers and Other Glass-forming Liquids. *Journal of the American Chemical Society* 77, 3701–3707. doi:doi:10.1021/ja01619a008
- Woo, M.W., Daud, W.R.W., Tasirin, S.M., Talib, M.Z.M., 2009. Controlling food powder deposition in spray dryers: Wall surface energy manipulation as an alternative. *Journal of Food Engineering* 94, 192–198. doi:10.1016/j.jfoodeng.2008.10.001
- Wu, C.Y., Thornton, C., Li, L.Y., 2003. Coefficients of restitution for elastoplastic oblique impacts. *Advanced Powder Technology* 14, 435–448.
- Xu, T., Flapper, J., 2011. Reduce energy use and greenhouse gas emissions from global dairy processing facilities. *Energy Policy* 39, 234–247. doi:10.1016/j.enpol.2010.09.037
- Yee, T.F., Grossmann, I.E., 1990. Simultaneous optimization models for heat integration—II. Heat exchanger network synthesis. *Computers & Chemical Engineering* 14, 1165–1184. doi:10.1016/0098-1354(90)85010-8
- Yee, T.F., Grossmann, I.E., Kravanja, Z., 1990a. Simultaneous optimization models for heat integration—I. Area and energy targeting and modeling of multi-stream exchangers. *Computers & Chemical Engineering* 14, 1151–1164. doi:10.1016/0098-1354(90)85009-Y
- Yee, T.F., Grossmann, I.E., Kravanja, Z., 1990b. Simultaneous optimization models for heat integration—III. Process and heat exchanger network optimization. *Computers & Chemical Engineering* 14, 1185–1200. doi:10.1016/0098-1354(90)80001-R
- Young, B.R., Tellez, R., Svrcek, W.Y., 2006. Towards Integrated Process and Control System Synthesis for Heat-Integrated Plants. *The Canadian Journal of Chemical Engineering* 84, 219–229. doi:10.1002/cjce.5450840209
- Zamora, J.M., Grossmann, I.E., 1998. A global MINLP optimization algorithm for the synthesis of heat exchanger networks with no stream splits. *Computers & Chemical Engineering* 22, 367–384. doi:10.1016/S0098-1354(96)00346-8
- Zhang, F., Busnaina, A.A., Fury, M.A., Wang, S.Q., 2000. The removal of deformed submicron particles from silicon wafers by spin rinse and megasonics. *Journal of Elec Materi* 29, 199–204. doi:10.1007/s11664-000-0142-0
- Zhang, J.X., Ebbens, S., Chen, X.Y., Jin, Z., Luk, S., Madden, C., Patel, N., Roberts, C.J., 2006. Determination of the Surface Free Energy of Crystalline and Amorphous Lactose by Atomic Force Microscopy Adhesion Measurement. *Pharm Res* 23, 401–407. doi:10.1007/s11095-005-9144-1
- Zhao, S.X., 2009. Experimental and numerical investigations on skim milk powder stickiness and deposition mechanisms (M.Phil.). University of Waikato, Hamilton, New Zealand.
- Zillwood, B., 2010. Particulate Emission Report Skim Milk Products - Drier 5 (Confidential). Hamilton, New Zealand.

- Zuo, J.Y., 2004. The stickiness curve of dairy powders (M.Tech. thesis). Massey University, Palmerston North, New Zealand.
- Zuo, J.Y., Paterson, A.H.J., Bronlund, J.E., Chatterjee, R., 2007. Using a particle-gun to measure initiation of stickiness of dairy powders. *International Dairy Journal* 17, 268–273. doi:10.1016/j.idairyj.2006.02.010



# Appendix A

## Lists of figures and tables

---

### List of figures

Figure 1-1: Process heat use for manufacturing derived from coal, natural gas and wood in 2012 (“New Zealand Energy Use: Industrial and trade sector 2012,” 2013). .....	1
Figure 1-2: The conversion of liquid milk into powdered milk using spray drying.	2
Figure 1-3: Comparison of food processing capital to energy costs in New Zealand showing a linear extrapolation (Statistics NZ, 2013). ....	3
Figure 1-4: Intensification of milk powder stickiness as exhaust heat is recovered. .....	5
Figure 2-1: Key areas relating to maximising heat recovery in milk powder processing. ....	9
Figure 2-2: Milk powder plant schematic. ....	10
Figure 2-3: Common falling film evaporator integration methods in the dairy industry. ....	14
Figure 2-4: Heat integration of evaporator systems with the background process heating and cooling requirements. ....	15
Figure 2-5: Options of spray dryer exhaust heat recovery. ....	18
Figure 2-6: Indirect HRL integration system with storage. ....	22
Figure 2-7: Relationship between the composite curve, shifted composite curve and grand composite curve. ....	26
Figure 2-8: Indirect heat integration using multiple Heat Storage Units (HSU) (Krummenacher and Favrat, 2001). ....	30
Figure 2-9: Example of a network superstructure for stream $i$ (Escobar and Trierweiler, 2013). ....	32
Figure 2-10: Liquid couple loop heat exchanger system. ....	36
Figure 2-11: Relationship between $T_g$ and $X_{eq}$ . ....	39

Figure 2-12: Sorption isotherm for skim milk powder. ....	39
Figure 2-13: Effect of $T - T_g$ on percent deposition for whole milk powder (compared the amount of powder tested) obtained using the particle gun test with a reported air velocity of 20 m/s. Data taken from Paterson et al. (2007a).....	41
Figure 2-14: Effect of velocity on $(T - T_g)_{crit}$ of SMP using the particle gun technique. Median particle size for Zhao (2009) was 61 $\mu\text{m}$ and Murti (2006) did not report a particle size.....	44
Figure 2-15: SEM photos of milk powder particles dried using varying inlet air temperatures into a lab scale spray dryer (Nijdam and Langrish, 2005).....	45
Figure 2-16: Relationship between particle stickiness and a particle surface area factor, $d_{(0.5)}^2$ for SMP, results from particle gun test (Zhao, 2009). ....	45
Figure 2-17: Initiation of stickiness curve for whole milk powder measured using the particle gun test (Zuo, 2004). ....	48
Figure 2-18: Determination of $(T - T_g)_{crit}^*$ using a clear ring diameter. Test conditions: $d_{(0.5)}$ 61 $\mu\text{m}$ , normal impingement and jet velocity 15.0 $\text{ms}^{-1}$ , data from Zhao (2009).....	51
Figure 3-1: Milk powder plant schematic including current HEN. ....	60
Figure 3-2: Composite curve for entire site including the evaporators including the MVR and TVR units. Soft temperatures: exhaust air $T_t$ is 55 $^{\circ}\text{C}$ and COW $T_t$ is 13 $^{\circ}\text{C}$ . Pinch temperature at 10.5 $^{\circ}\text{C}$ . ....	65
Figure 3-3: Grand composite curve for evaporators and background process. Soft temperatures: exhaust air $T_t$ is 55 $^{\circ}\text{C}$ and COW $T_t$ is 13 $^{\circ}\text{C}$ . Pinch temperature at 10.5 $^{\circ}\text{C}$ .....	66
Figure 3-4: The effect of the soft target discharge temperatures on heat recovery and utility targets. Graph a – exhaust air $T_t$ is 75 $^{\circ}\text{C}$ and b – COW $T_t$ is 13 $^{\circ}\text{C}$ . ....	67
Figure 3-5: The effect of the soft return temperature on heat recovery and utility targets for the condenser loop (a) and the exhaust loop (b). Soft temperatures: exhaust air $T_t$ is 55 $^{\circ}\text{C}$ and COW $T_t$ is 13 $^{\circ}\text{C}$ . ....	68
Figure 3-6: Total site profiles. Soft temperatures: exhaust air $T_t$ is 55 $^{\circ}\text{C}$ , COW $T_t$ is 13 $^{\circ}\text{C}$ , and condenser loop return $T_t$ is 18.5 $^{\circ}\text{C}$ .....	69
Figure 3-7: Heat exchanger network grid and flow diagrams for the milk powder plant with direct condenser integration. ....	72

Figure 3-8: Heat exchanger network grid and flow diagrams for the milk powder plant with indirect condenser integration. ....	73
Figure 3-9: Heat exchanger network grid and flow diagrams for the milk powder plant with indirect condenser integration after network relaxation. ....	74
Figure 3-10: Heat sink options for indirect exhaust air heat recovery. ....	75
Figure 3-11: Schemes for evaporator zone integration including CIP water. ....	75
Figure 4-1: Impact of increasing the area of recovery exchanger 1 by $dA$ . ....	81
Figure 4-2: Analysis of heat duty flow-on through HENs. ....	85
Figure 4-3: Heat duty flow-on pathways. ....	89
Figure 4-4: Non-self-interacting open heat loops (a) and self-interacting closed heat loops (b). ....	91
Figure 4-5: Heat duty flow-on in three general self-interacting closed heat loops. ....	92
Figure 4-6: The impact of target temperature constraints on HE sizing. ....	95
Figure 4-7: Impact of increasing area of RE 1 and 3 on the duty of RE <sub>2</sub> that is constrained by a target temperature. ....	96
Figure 4-8: Flow sheet of Pinch Design Method and Cost Derivative Method. ....	99
Figure 4-9: Optimising the milk split fraction to milk/condenser vapour match. ....	100
Figure 4-10: Heat exchanger network design solutions of the PDM and CDM for MER A. Duties based on a milk powder plant producing 23 t <sub>p</sub> /h. ....	101
Figure 4-11: Heat exchanger network design solutions of the PDM and CDM for MER B. Duties based on a milk powder plant producing 23 t <sub>p</sub> /h. ....	102
Figure 4-12: The impact of the utility-capital ratio on the total area and heat recovery of the CDM solution for MER A and B. ....	104
Figure 4-13: Degree of heat integration versus total HE area for CDM solutions and PDM networks from Chapter 3. ....	104
Figure 4-14: Heat exchanger network for a distillation process using the PDM with $\Delta T_{min} = 12.5$ °C and the CDM. Duties are in kW. ....	105
Figure 5-1: Heat recovery loop network including the milk powder plant spray dryer. ....	111

Figure 5-2: Example raw and ordered heat capacity flow rate of a stream. Data taken from M. R. W. Walmsley et al. (2013b).	114
Figure 5-3: Inter-plant composite curve for indirect heat recovery using a HRL with CTS. Steam data given in M. R. W. Walmsley et al. (2013b).	115
Figure 5-4: Procedure for targeting and designing a HRL with VTS.	116
Figure 5-5: Composite Curves for the integration of solar heating with HRLs for processes with cold storage pinch (a) and hot storage pinch (b).	123
Figure 5-6: Condenser duty for a 72 hour period (a) and as ordered values for the entire two months (b).	125
Figure 5-7: Site hot water supply temperature and heat capacity flow rate for a 72 hour period (a) and as ordered values for the entire two months (b).	126
Figure 5-8: Solar irradiance recorded by closest weather station to the dairy factory (NIWA, 2013).	127
Figure 5-9: Time average composite curves of available streams for the HRL. Solar heating is not included.	127
Figure 5-10: Heat recovery targeting for CTS based on a $\Delta T_{min}$ of 5 °C. Cheese A and B removed from analysis.	128
Figure 5-11: Effect of cold storage temperature selection on total area and loop flow rate for a CTS HRL based on a $\Delta T_{min}$ of 5 °C.	129
Figure 5-12: Heat recovery targeting for VTS based on a $\Delta T_{min}$ of 5 °C.	130
Figure 5-13: Effect of cold storage temperature selection on total area and loop flow rate for a VTS HRL based on a $\Delta T_{min}$ of 5 °C.	130
Figure 5-14: Heat recovery versus minimum approach temperature.	131
Figure 5-15: Heat recovery versus total area including the dryer exhaust exchanger.	132
Figure 5-16: Heat recovery versus total area excluding the dryer exhaust exchanger.	133
Figure 5-17: Heat recovery versus heat capacity flow rate of the loop.	134
Figure 5-18: Maximum and practical average heat recovery and solar heating targets for a CTS HRL based on a $\Delta T_{min}$ of 5 °C.	135
Figure 5-19: Maximum and practical average heat recovery and solar heating targets for a VTS HRL based on a $\Delta T_{min}$ of 5 °C.	135

Figure 5-20: Thermal storage dynamics for CTS design using 500 m <sup>3</sup> hot and cold storage tanks.....	139
Figure 5-21: Thermal storage dynamics for CTS with solar heating design using 500 m <sup>3</sup> hot and cold storage tanks. ....	139
Figure 5-22: Thermal storage dynamics for VTS design using 500 m <sup>3</sup> hot and cold storage tanks.....	140
Figure 5-23: Thermal storage dynamics for VTS with solar heating design using 500 m <sup>3</sup> hot and cold storage tanks. ....	140
Figure 5-24: Effect of thermal storage volume on HRL performance. ....	142
Figure 5-25: Effect of average thermal storage capacity on HRL performance as a percentage of the HRL performance with infinite storage.....	142
Figure 5-26: Actual duty versus heat capacity flow rate of Whey B for CTS design. ....	144
Figure 5-27: Temperature effectiveness versus heat capacity flow rate of Whey B for CTS design.....	144
Figure 5-28: Temperature effectiveness versus inlet temperature of SHW for CTS design. ....	146
Figure 5-29: Outlet temperature versus inlet temperature of SHW for CTS design. ....	146
Figure 6-1: Schematic of the particle gun test apparatus.....	154
Figure 6-2: Normalised velocity profile 10 mm (a) and 20 mm (b) away from and parallel to the plate obtained using PIV.....	157
Figure 6-3: Normalised velocity magnitude contours of a normal impingement jet obtained using PIV. ....	158
Figure 6-4: Correlation between PIV and 15 mm diameter anemometer velocities of a 11 mm air jet.....	158
Figure 6-5: Effect of $T - T_g$ on the deposition % at the centre of the plate. Test conditions: $d_{(0.5)}$ 267 $\mu\text{m}$ , average jet velocity 15.0 m/s and normal impingement. ....	159
Figure 6-6: Effect of $T - T_g$ on the clear ring diameter. Test conditions: $d_{(0.5)}$ 61 $\mu\text{m}$ , normal impingement and jet velocity 15.0 ms <sup>-1</sup> , data from Zhao (2009).....	160

Figure 6-7: Influence of plate temperature on $(T - T_g)_{crit}^*$ . Test conditions: $d_{(0.5)}$ 267 $\mu\text{m}$ and normal impingement.....	161
Figure 6-8: Effect of particle size on $(T - T_g)_{crit}^*$ in a normal impingement jet. Trends for 5.4 and 25.0 m/s are estimates. ....	162
Figure 6-9: Effect of normal particle impact velocity on $(T - T_g)_{crit}^*$ with normal impingement, i.e. an impact angle of zero degrees.....	163
Figure 6-10: Effect of impact angle on $(T - T_g)_{crit}^*$ . Particle size $d_{(0.5)}$ 100 $\mu\text{m}$ . ..	164
Figure 6-11: Combined effect of particle size, impact angle and velocity on deposition. The work of Zhao is corrected (*) for plate temperature effects. ....	165
Figure 7-1: Deposition test rig schematic.....	168
Figure 7-2: Wall shear stress for round (a), elliptical (b) and turned squared (c) tubes using CFD. Refer to Walmsley et al. (2012b) for CFD model parameters. ....	170
Figure 7-3: Photograph of fin bank.....	171
Figure 7-4: The effect of increasing stickiness on the frontal deposition for round tube. From top, $T - T_g^*$ conditions are 43.3, 47.6 and 52.6 $^{\circ}\text{C}$ . Photographs were taken at the end of the test.....	173
Figure 7-5: The effect of increasing stickiness on the frontal deposition for elliptical tubes. From top, $T - T_g^*$ conditions are 50.0, 54.8 and 62.5 $^{\circ}\text{C}$ . Photographs were taken at the end of the test.....	174
Figure 7-6: The effect of increasing stickiness on the frontal deposition for turned square tube. $T - T_g^*$ conditions are 56.7 $^{\circ}\text{C}$ (left) and 61.2 $^{\circ}\text{C}$ . Photographs were taken at the end of the test.....	175
Figure 7-7: Deposition morphology on round and elliptical tubes. $T - T_g^*$ conditions are 52.6 $^{\circ}\text{C}$ (left) and 54.8 $^{\circ}\text{C}$ . Photographs were taken at the end of the test.....	175
Figure 7-8: Critical local wall shear stress plotted against $T - T_g$ for round, elliptical, and turned square tubes. ....	176
Figure 7-9: Schematic showing how the impact angle is defined and how it changes for: a) elliptical tubes; b) round tubes; c) turned square tubes.....	177
Figure 7-10: Estimated critical impact angle for the round, elliptical and turned square tubes. Models assume a particle size of 104 $\mu\text{m}$ . ....	178

Figure 7-11: Predicted frontal face deposition coverage versus $T - T_g^*$ using the deposition model based on an air velocity, i.e. particle impact velocity, of 4.5 m/s. .....	180
Figure 7-12: Predicted frontal area deposition coverage versus $T - T_g^*$ using the deposition model based on an air velocity, i.e. particle impact velocity, of 4.5 m/s. .....	180
Figure 7-13: Pressure drop over time across a single round tube for three levels of stickiness showing a first order exponential approximation with a time constant of 420 s. ....	181
Figure 7-14: Final pressure drop versus $T - T_g^*$ for the round and elliptical tubes. .....	182
Figure 7-15: Pressure drop across the fin bank for different open area fractions. .....	183
Figure 7-16: Pressure drop across the fin bank over time. Air temperatures as labelled with air moisture content constant at 60 g/kg. ....	185
Figure 7-17: Photographs of frontal fouling for various air temperatures and a constant air moisture content of 60 g/kg. Photos were taken at the end of each test. ....	185
Figure 7-18: The relationship of fin bank pressure drop and particle stickiness, $T - T_g^*$ . ....	187
Figure 7-19: The impact of particle stickiness, $T - T_g$ , on the equilibrium velocity through the open area of the fin bank. ....	187
Figure 7-20: Psychrometric plot of the effect of exhaust heat recovery. ....	188
Figure 8-1: The exhaust heat exchanger design challenge. ....	192
Figure 8-2: Screenshot of heat exchanger user defined parameters in spreadsheet tool. ....	193
Figure 8-3: Screenshot of fouling and cleaning user defined parameters from spreadsheet tool. ....	196
Figure 8-4: Heat exchanger fouling model flow diagram. ....	198
Figure 8-5: Particle size distribution of baghouse and bulk product SMP. ....	199
Figure 8-6: Screenshot of utility, capital and miscellaneous user defined parameters. ....	202

Figure 8-7: Screenshot of cost/benefit analysis results. ....	203
Figure 8-8: Interface for setting up a user defined macro for testing a range of inputs.....	203
Figure 8-9: Estimated heat recovery and pressure drop for a period of four weeks. Exhaust heat exchanger with 14 tube rows of either finned round tube (CF-9.05-3/4J (C)), bare round tube (CB-1.5:1.25 (CFD)) and elliptical tube (EB-1.5:1.25 (CFD)). Inlet heat exchanger with 12 tube rows of finned round tube (CF-9.05-3/4J (C)). Both heat exchangers have a face velocity of 4 m/s. ....	205
Figure 8-10: Number of exhaust tube rows versus NPV and IRR at 4 m/s air velocity for finned round tube (CF-9.05-3/4J (C)), bare round tube (CB-1.5:1.25 (CFD)) and elliptical tube (EB-1.5:1.25 (CFD)). ....	206
Figure 8-11: Exhaust outlet temperature versus NPV and IRR at 4 m/s air velocity for finned round tube (CF-9.05-3/4J (C)), bare round tube (CB-1.5:1.25 (CFD)) and elliptical tube (EB-1.5:1.25 (CFD)). Inlet air temperature to exhaust heat exchanger is 75 °C. ....	207
Figure 8-12: Heat exchanger face velocity versus the peak NPV and IRR values for a bare round tube exhaust heat exchanger and finned tube inlet heat exchanger. ....	208
Figure C-1: Heat duty flow-on in heat exchanger networks – example.....	248
Figure C-2: Heat duty flow-on in heat exchanger networks – example.....	250
Figure C-3: Heat duty flow-on in interacting closed loops.....	254
Figure C-4: Example of heat duty flow-on in interacting closed loops. ....	260
Figure C-5: Impact of increasing area of RE 1 and 3 on the duty of RE <sub>2</sub> that is constrained by a target temperature. ....	261

## List of tables

Table 2-1: Specific energy consumption for industrial milk powder production in various countries. Sources: <sup>a</sup> Xu and Flapper (2011), <sup>b</sup> Lovell-Smith and Baldwin (1988), <sup>c</sup> Robertson and Baldwin (1993). .....	12
Table 2-2: Summary of hot utility savings for the several heat recovery schemes (Atkins et al., 2011). .....	19
Table 2-3: Comparison of definitions for effectiveness and NTU in the $\epsilon$ -NTU and P-NTU methods. ....	34
Table 2-4: Summary of sorption isotherm constants. ....	41
Table 3-1: Process stream data extracted for the industrial milk powder plant. Soft temperatures indicated using *. .....	61
Table 3-2: Initial $\Delta T_{cont}$ assignment. ....	62
Table 3-3: Overall heat transfer coefficients (Kakaç and Liu, 2002), $\epsilon$ -NTU correlations (Kays and London, 1998; Navarro and Cabezas-Gómez, 2005) and cost functions (Bouman et al., 2005) for various types of heat exchangers. Refer to Appendix B for $\epsilon$ -NTU correlations. ....	63
Table 3-4: Soft temperature limits. ....	63
Table 3-5: Modified process stream data. Soft data indicated using *. ....	70
Table 3-6: Inter- and intra-zonal heat recovery targets. ....	71
Table 3-7: Comparison of proposed MER networks to current industry practice networks based on a dryer producing 23.5 t <sub>p</sub> /h. ....	76
Table 4-1: Sign of heat duty flow-on factor. Positive is increased heat recovery, negative is increased utility use. ....	89
Table 4-2: General formulas for heat duty flow-on factors in interacting closed heat loops where $G_L$ is the function describing the closed loop and $G_{OL}$ is the function describing the open loop. Refer to Appendix C for examples. ....	92
Table 4-3: Expression for terminal recovery exchangers for two cases presented in Figure 4-7. ....	97
Table 4-4: A detailed comparison of PDM and CDM solutions for MER A. ....	102
Table 4-5: A detailed comparison of PDM and CDM solutions for MER B. ....	103

Table 4-6: Process and utility stream data for a simple distillation process from Gundersen (2000).....	105
Table 4-7: A detailed comparison of PDM ( $\Delta T_{\min} = 12.5$ °C) and CDM solutions for the distillation process. ....	106
Table 4-8: Comparison of heat integration solutions for the distillation process. Non-Linear Programming (NLP), Superstructure, Hyperstructure and Synheat solutions are taken from Escobar & Trierweiler (2013).....	107
Table 5-1: Extracted stream data including the spray dryer exhaust and solar heating.....	124
Table 5-2: HRL design specifications. ....	137
Table 5-3: Average hot and cold storage temperatures and the associated impact on thermal storage density and capacity. ....	138
Table 5-4: Comparison of combined heat recovery and solar heating targets to actual modelled performance highlighting the root causes of the difference. ..	141
Table 5-5: Contributions to hot utility reduction assuming 500 m <sup>3</sup> of storage. .	147
Table 6-1: SMP particle size distribution parameters used in deposition tests..	156
Table 6-2: Mechanical properties and constants of stainless steel and amorphous lactose (Murti, 2006; Perkins et al., 2007; Zhang et al., 2006). ....	165
Table 6-3: Constants for SMP deposition model.....	166
Table 8-1: Heat exchanger geometry information. Key for heat exchanger surface codes: C – circular (round); E – elliptical; B – bare; F – finned; KL – Kays and London (1998); W – Walmsley et al. (2012b); numbers and other letters refer to the specific surface arrangement. ....	195

# Appendix B

## Common $\varepsilon$ -NTU relationships and their derivatives

This appendix presents common  $\varepsilon$ -NTU relationships from Shah and Sekulić (2003) and their first derivatives. Table B-1 contains seven common  $\varepsilon$ -NTU relationships with effectiveness as the subject and, where possible, Table B-2 presents the relationships with NTU as the subject. Table B-3 contains the derivatives of  $\varepsilon$ -NTU relationships, i.e.  $d\varepsilon/dNTU$ , as functions of  $\varepsilon$  and  $C^*$ , where  $C^*$  is constant, which is the case for direct heat recovery exchangers. Table B-4 provides derivatives of P-NTU relationships as functions of  $P_p$  and  $R_p$ , where  $P_p$  and  $R_p$  are both affected by an incremental change in  $NTU_p$ , which is the case for utility exchangers.

**Table B-1: Heat exchanger effectiveness relationships.**

Flow Arrangement	$\varepsilon = f(NTU, C^*)$ , $[0 \leq C^* < 1]$	$\varepsilon = f(NTU)$ , $[C^* = 1]$
Counter Flow	$\varepsilon = \frac{1 - \exp(-NTU(1 - C^*))}{1 - C^* \exp(-NTU(1 - C^*))}$	$\varepsilon = \frac{NTU}{1 + NTU}$
Parallel Flow	$\varepsilon = \frac{1 - \exp(-NTU(1 + C^*))}{1 + C^*}$	$\varepsilon = \frac{1}{2}(1 - \exp(-NTU))$
Cross-flow Both Fluids Unmixed	$\varepsilon = 1 - \exp(-NTU) - \exp(-(1 + C^*)NTU) \sum_{i=1}^{\infty} (C^*)^i L_n$ where $L_n = \frac{1}{(i+1)!} \sum_{j=1}^i \binom{i-j+1}{j} \frac{NTU^{i+j}}{j!}$	$\varepsilon = 1 - \exp(-NTU) - \exp(-2NTU) \sum_{i=1}^{\infty} L_n$
Cross-flow $C_{\min}$ Mixed, $C_{\max}$ Unmixed	$\varepsilon = 1 - \exp\left[-\frac{1}{C^*}(1 - \exp(-NTU \cdot C^*))\right]$	$\varepsilon = 1 - \exp[-(1 - \exp(-NTU))]$
Cross-flow $C_{\min}$ Unmixed, $C_{\max}$ Mixed	$\varepsilon = \frac{1}{C^*} [1 - \exp(-C^*(1 - \exp(-NTU)))]$	$\varepsilon = 1 - \exp[-(1 - \exp(-NTU))]$
1-2 TEMA E Shell and Tube	$\varepsilon = \frac{2}{(1 + C^*) + (1 + C^{*2})^{1/4} \coth\left(\frac{NTU \cdot (1 + C^{*2})^{1/2}}{2}\right)}$	$\varepsilon = \frac{2}{2 + 2^{1/4} \coth\left(\frac{NTU}{\sqrt{2}}\right)}$
Condensing and Evaporating Fluids	$\varepsilon = 1 - \exp(-NTU)$	N/A

**Table B-2: Heat exchanger NTU relationships.**

Flow Arrangement	$NTU = f(\varepsilon, C^*), [0 \leq C^* < 1]$	$NTU = f(\varepsilon), [C^* = 1]$
Counter Flow	$NTU = \frac{1}{1-C^*} \ln \left  \frac{1-\varepsilon C^*}{1-\varepsilon} \right $	$NTU = \frac{\varepsilon}{1-\varepsilon}$
Parallel Flow	$NTU = -\frac{\ln 1-\varepsilon(1+C^*) }{1+C^*}$	$NTU = -\frac{1}{2} \ln 1-2\varepsilon $
Cross-flow Both Fluids Unmixed	Numerical solution	Numerical solution <sup>1</sup>
Cross-flow $C_{\min}$ Mixed, $C_{\max}$ Unmixed	$NTU = -\frac{1}{C^*} \ln 1+C^* \ln 1-\varepsilon  $	$NTU = -\ln 1+\ln 1-\varepsilon  $
Cross-flow $C_{\min}$ Unmixed, $C_{\max}$ Mixed	$NTU = -\ln \left  1 + \frac{1}{C^*} \ln 1-\varepsilon C^*  \right $	$NTU = -\ln 1+\ln 1-\varepsilon  $
1-2 TEMA E Shell and Tube	$NTU = \frac{1}{(1+C^{*2})^{1/2}} \ln \left  \frac{2-\varepsilon D_1}{2-\varepsilon D_2} \right $ , where $D_1 = 1+C^*-(1+C^{*2})^{1/4}$ , $D_2 = 1+C^*+(1+C^{*2})^{1/4}$	$NTU = \frac{1}{2^{1/2}} \ln \left  \frac{2-\varepsilon(2-2^{1/4})}{2-\varepsilon(2+2^{1/4})} \right $
Condensing and Evaporating Fluids	$NTU = -\ln 1-\varepsilon $	N/A

**Table B-3: Derivatives of  $\varepsilon$ -NTU relationships for constant  $C^*$  (heat recovery exchanger).**

Flow Arrangement	$\frac{d\varepsilon}{dNTU} = f(\varepsilon, C^*), [0 \leq C^* < 1]$	$\frac{d\varepsilon}{dNTU} = f(\varepsilon), [C^* = 1]$
Counter Flow	$\frac{d\varepsilon}{dNTU} = (1-\varepsilon)(1-\varepsilon C^*)$	$\frac{d\varepsilon}{dNTU} = (1-\varepsilon)^2$
Parallel Flow	$\frac{d\varepsilon}{dNTU} = 1-\varepsilon(1+C^*)$	$\frac{d\varepsilon}{dNTU} = 1-2\varepsilon$
Cross-flow Both Fluids Unmixed	$\frac{d\varepsilon}{dNTU} = \exp(-NTU) + (1+C^*) \exp(-(1+C^*)NTU) \sum_{n=1}^{\infty} (C^{*n} L'_n)$ where $L'_n = \frac{1}{(i+1)!} \sum_{j=1}^i \left( (i-j+1) \frac{NTU^{i+j}}{j!} - (i+j) NTU^{i-1} \right)$	$\frac{d\varepsilon}{dNTU} = \exp(-NTU) + 2 \exp(-2NTU) \sum_{n=1}^{\infty} (L'_n)$
Cross-flow $C_{\min}$ Mixed, $C_{\max}$ Unmixed	$\frac{d\varepsilon}{dNTU} = (1-\varepsilon)(1+C^* \ln 1-\varepsilon )$	$\frac{d\varepsilon}{dNTU} = (1-\varepsilon)(1+\ln 1-\varepsilon )$
Cross-flow $C_{\min}$ Unmixed, $C_{\max}$ Mixed	$\frac{d\varepsilon}{dNTU} = (1-\varepsilon C^*) \left( 1 + \frac{1}{C^*} \ln 1-\varepsilon C^*  \right)$	$\frac{d\varepsilon}{dNTU} = (1-\varepsilon)(1+\ln 1-\varepsilon )$
1-2 TEMA E Shell and Tube	$\frac{d\varepsilon}{dNTU} = (1+C^{*2})^{1/2} \left( \frac{D_2}{2-\varepsilon D_2} - \frac{D_1}{2-\varepsilon D_1} \right)^{-1}$ , where $D_1 = 1+C^*-(1+C^{*2})^{1/4}$ , $D_2 = 1+C^*+(1+C^{*2})^{1/4}$	$\frac{d\varepsilon}{dNTU} = 2^{1/2} \left( \frac{2+2^{1/4}}{2-\varepsilon(2+2^{1/4})} - \frac{2-2^{1/4}}{2-\varepsilon(2-2^{1/4})} \right)^{-1}$
Condensing and Evaporating Fluids	$\frac{d\varepsilon}{dNTU} = 1-\varepsilon$	N/A

**Table B-4: Derivatives of P-NTU relationships for variable  $C_{ut}$  (utility exchanger).**

Flow Arrangement	$\frac{dP_p}{dNTU_p} = f(P_p, R_p), [R_p \neq 1]$ where $P_p = \frac{\Delta T_p}{\Delta T_{max}}, R_p = \frac{C_p}{C_{ut}}$	$\frac{dP_p}{dNTU_p} = f(P_p), [R_p = 1]$
Counter Flow	$\frac{dP_p}{dNTU_p} = \frac{P_p(1-R_p)(1-P_p)}{\frac{P_p}{1-P_p R_p} - \frac{R_p}{1-R_p} \ln \left  \frac{1-P_p R_p}{1-P_p} \right }$	$\frac{dP_p}{dNTU_p} = (1-P_p)^2$
Parallel Flow	$\frac{dP_p}{dNTU_p} = \frac{P_p(1+R_p)(1-P_p)}{P_p - \frac{R_p}{1+R_p} \ln  1-P_p(1+R_p) }$	$\frac{dP_p}{dNTU_p} = 1-2P_p$
Cross-flow Both Fluids Unmixed	Numerical solution	Numerical solution
Cross-flow $C_{min}$ Mixed, $C_{max}$ Unmixed	$\frac{dP_p}{dNTU_p} = \frac{P_p(1-P_p)}{\frac{P_p + \ln  1-P_p }{1+R_p \ln  1-P_p } - \frac{1}{R_p} \ln  1+R_p \ln  1-P_p  }$	$\frac{dP_p}{dNTU_p} = (1-P_p)(1 + \ln  1-P_p )$
Cross-flow $C_{min}$ Unmixed, $C_{max}$ Mixed	$\frac{dP_p}{dNTU_p} = \frac{-\left(1 + \frac{1}{R_p} \ln  1-P_p R_p \right)(1-P_p)(1-P_p R_p)}{P_p + \frac{1-P_p R_p}{P_p R_p} \ln  1-P_p R_p }$	$\frac{dP_p}{dNTU_p} = (1-P_p)(1 + \ln  1-P_p )$
1-2 TEMA E Shell and Tube	$\frac{dP_p}{dNTU_p} = \frac{-(1+R_p^2)^{1/4}}{D_1 - R_p \frac{dD_1}{dR_p} - \frac{D_2 - R_p \frac{dD_2}{dR_p} - R_p^2 \ln \left  \frac{2-P_p D_1}{2-P_p D_2} \right }{(2-P_p D_1) + (2-P_p D_2) - \frac{R_p^2 \ln \left  \frac{2-P_p D_1}{2-P_p D_2} \right }{P_p(1+R_p^2)(1-P_p)}}$ where $D_1 = 1+R_p - (1+R_p^2)^{1/4}, D_2 = 1+R_p + (1+R_p^2)^{1/4},$ $\frac{dD_1}{dR_p} = 1 - \frac{1}{4} R_p (1+R_p^2)^{-3/4}, \frac{dD_2}{dR_p} = 1 + \frac{1}{4} R_p (1+R_p^2)^{-3/4}$	$\frac{dP_p}{dNTU_p} = 2^{1/2} \left( \frac{2+2^{1/4}}{2-P_p(2+2^{1/4})} - \frac{2-2^{1/4}}{2-P_p(2-2^{1/4})} \right)^{-1}$
Condensing and Evaporating Fluids	$\frac{dP_p}{dNTU_p} = 1-P_p$	N/A



# Appendix C

## Cost Derivative Method: Derivations, proofs and examples

---

In this appendix three derivations of various parts of the Cost Derivate Method are presented. Derivations and examples presented are (in order):

- (1)  $dQ/dA$  for direct heat recovery exchangers
- (2)  $d\varepsilon/dNTU$  for counterflow direct heat recovery exchangers
- (3)  $dQ/dA$  for utility exchangers
- (4)  $dP/dNTU$  for counterflow utility exchangers
- (5) Examples of forming network specific heat duty flow-on factors
- (6) Relationship between individual heat duty flow-on factors with common flow-on pathways
- (7) Relationship between overall heat duty flow-on factors
- (8) Heat duty flow-on factor for closed loops

Derivatives of other common heat exchanger arrangements have been found (derivations not presented) and are summarised in the Tables of Appendix B. The final section of this Appendix provides three examples illustrating how equations for the heat duty flow-on factor may be quickly formulated for any HE.

### Derivation of $dQ/dA$ for direct heat recovery exchangers

An expression for  $dQ/dA$  for direct heat recovery exchangers is obtained using the definitions of  $Q$  in terms of  $\varepsilon$  and  $A$  in terms of  $NTU$ ,

$$\frac{dQ}{dA} = \frac{d(\varepsilon C_{\min} \Delta T_{\max})}{d\left(\frac{C_{\min} NTU}{U}\right)}, \quad \text{where } \Delta T_{\max} = T_x^{in} - T_y^{in} \quad (C-1)$$

Assuming  $U$ ,  $\Delta T_{\max}$ , and  $C_{\min}$  are constant, the above equations simplifies to

$$\frac{dQ}{dA} = U \Delta T_{\max} \frac{d\varepsilon}{dNTU} \quad (C-2)$$

## Derivation of $d\varepsilon/dNTU$ for counterflow direct heat recovery exchangers

For counter flow exchangers, the  $\varepsilon$ -NTU relationship with  $NTU$  as the subject is

$$NTU = \frac{1}{1-C^*} \ln \left| \frac{1-\varepsilon C^*}{1-\varepsilon} \right|, \quad \text{where } C^* = \frac{C_{\min}}{C_{\max}} \quad (\text{C-3})$$

Taking the derivative with respect to  $NTU$  and applying the chain and quotient rules gives

$$dNTU = \frac{1}{(1-C^*)(1-\varepsilon C^*)} \frac{-C^*(1-\varepsilon)d\varepsilon + (1-\varepsilon C^*)d\varepsilon}{(1-\varepsilon)^2} \quad (\text{C-4})$$

Simplifying and making  $d\varepsilon/dNTU$  the subject obtains

$$\frac{d\varepsilon}{dNTU} = (1-\varepsilon)(1-\varepsilon C^*), \quad [0 \leq C^* \leq 1] \quad (\text{C-5})$$

## Derivation of $dQ/dA$ for utility exchangers

When a heat duty flow-on effect influences the inlet temperature of a process stream ( $dT_{p1}$ ) to a UE, the required utility flow rate ( $C_u$ ) is adjusted to meet the new duty. At the same time the area of the exchanger is adjusted to maintain the same inlet to outlet temperature difference of the utility stream, while achieving the target temperature of the process stream. To find an expression for  $dQ/dA$  of UEs, it is best to base  $\varepsilon$ ,  $NTU$  and  $C^*$  on one of the streams (the process stream in this case) instead of the stream with  $C_{\min}$ . This is commonly called the P-NTU method. By applying the definition of  $Q$  from the temperature  $\varepsilon$ -NTU method, we obtain

$$\left( \frac{dQ}{dA} \right)_{ut} = \frac{d(P_p C_p \Delta T_{\max})}{dA}, \quad \text{where } P_p = \frac{\Delta T_p}{\Delta T_{\max}}, \quad R_p = \frac{C_p}{C_{ut}} \quad (\text{C-6})$$

By applying the product rule and recognising that  $d(\Delta T_{\max}) = dT_{p1}$  and  $C_p$  is a constant, we now obtain

$$\left(\frac{dQ}{dA}\right)_{ut} = P_p C_p \frac{dT_p^{in}}{dA} + C_p \Delta T_{\max} \frac{dP_p}{dA} \quad (\text{C-7})$$

Substituting  $dQ$  for  $C_p dT_{p1}$  and rearranging to make  $dQ/dA$  the subject gives

$$\left(\frac{dQ}{dA}\right)_{ut} = \frac{C_p \Delta T_{\max}}{1 - P_p} \frac{dP_p}{dA} \quad (\text{C-8})$$

Substituting the definition of  $NTU$  for  $A$  and simplifying gives

$$\left(\frac{dQ}{dA}\right)_{ut} = \frac{U \Delta T_{\max}}{1 - P_p} \frac{dP_p}{dNTU_p} \quad (\text{C-9})$$

### Derivation of $dP_p/dNTU_p$ for counterflow utility exchangers

To find an expression for  $dP_p/dNTU_p$  of UEs, it is best to base  $\varepsilon$ ,  $NTU$  and  $C^*$  on one of the streams (the process stream in this case) instead of the stream with  $C_{\min}$ . As a result the counterflow heat exchanger relationship for  $NTU_p$  as a function of  $P_p$  and  $R_p$  is

$$NTU_p = \frac{1}{1 - R_p} \ln \left| \frac{1 - P_p R_p}{1 - P_p} \right|, \quad [0 \leq R_p \neq 1] \quad (\text{C-10})$$

Rearranging terms gives

$$R_p NTU_p - NTU_p = \ln \left| \frac{1 - P_p}{1 - P_p R_p} \right| \quad (\text{C-11})$$

Taking the derivative of  $P_p$  and  $R_p$  with respect to  $NTU_p$  and simplifying obtains

$$NTU_p dP_p - (1 - R_p) dNTU_p = \frac{P_p dR_p + R_p dP_p}{1 - P_p R_p} - \frac{dP_p}{1 - P_p} \quad (\text{C-12})$$

Rearranging terms gives

$$\left( NTU_p - \frac{P_p}{1 - P_p R_p} \right) \frac{dR_p}{dNTU_p} + \left( \frac{1}{1 - P_p} - \frac{R_p}{1 - P_p R_p} \right) \frac{dP_p}{dNTU_p} = (1 - R_p) \quad (\text{C-13})$$

An expression for  $dP_p/dR_p$  is needed to make  $dP_p/dNTU_p$  the subject in the above equation. The heat balance for the UE is

$$Q = P_p C_p \Delta T_{\max} = C_u \Delta T_u \quad (\text{C-14})$$

Taking the derivative leads to

$$P_p C_p dT_{p1} + C_p \Delta T_{\max} dP_p = \Delta T_u dC_u \quad (\text{C-15})$$

Furthermore taking the derivative of the definition for effectiveness gives

$$P_p = \frac{\Delta T_p}{\Delta T_{\max}} \rightarrow dT_{p1} = \frac{\Delta T_{\max}}{1 - \varepsilon_p} dP_p \quad (\text{C-16})$$

which may be substituted into the previous equation and rearranged to obtain

$$\frac{dP_p}{dC_u} = \frac{\Delta T_u (1 - P_p)}{C_p \Delta T_{\max}} \quad (\text{C-17})$$

where  $dC_u$  is related to  $dR_p$  by

$$R_p = \frac{C_p}{C_u} \rightarrow dR_p = -\frac{C_p}{C_u^2} dC_u \quad (\text{C-18})$$

which may be substituted into the previous equation and rearranged to obtain

$$\frac{dP_p}{dR_p} = -\frac{P_p (1 - P_p)}{R_p} \quad (\text{C-19})$$

Having found  $dP_p/dR_p$ , an expression for  $dP_p/dNTU_p$  may now be found. Substituting the above equation into Eq. C-13 and simplifying obtains

$$\left( \left( \frac{1}{1 - P_p} - \frac{R_p}{1 - P_p R_p} \right) - \left( NTU_p - \frac{P_p}{1 - P_p R_p} \right) \frac{R_p}{P_p (1 - P_p)} \right) \frac{dP_p}{dNTU_p} = (1 - R_p) \quad (\text{C-20})$$

which, after substituting in the definition for  $NTU_p$ , rearranges to

$$\frac{dP_p}{dNTU_p} = \frac{P_p(1-P_p)(1-R_p)}{\frac{P_p}{1-P_p R_p} - \frac{R_p}{1-R_p} \ln \left| \frac{1-P_p R_p}{1-P_p} \right|}, \quad [R_p \neq 1] \quad (\text{C-21})$$

For the special case when  $R_p = 0$ , e.g. steam utility, the above equation simplifies to

$$\frac{dP_p}{dNTU_p} = 1 - P_p, \quad [R_p = 0] \quad (\text{C-22})$$

When  $R_p = 1$ , the relationship between  $NTU_p$  and  $P_p$  is

$$NTU_p = \frac{P_p}{1 - P_p} \quad (\text{C-23})$$

which implies

$$\frac{dP_p}{dNTU_p} = (1 - P_p)^2, \quad [R_p = 1] \quad (\text{C-24})$$

## Examples of forming network specific heat duty flow-on factors

The steps for constructing equations for  $\theta$  are:

1. Identify flow-on pathways between selected  $RE_n$  (origin) and  $UE_{ut}$  (termination)
2. For one pathway, write the energy balance for  $UE_{ut}$  using Eq. 29
3. Move toward the RE using flow-on pathway by substituting in Eq. 24 or 26 for  $dT$
4. Once the RE is reached, apply Eq. 20 for  $RE_n$ .
5. Rearrange to form an equation for  $\theta$  as defined in Eq. 6 for the flow-on path.
6. If applicable, repeat steps 2 – 5 for other flow-on pathways
7. Sum equations for the different pathways to find  $\theta$ .

The HEN in Figure C-1 is used to demonstrate how equations for heat duty flow-on factors may be formulated.

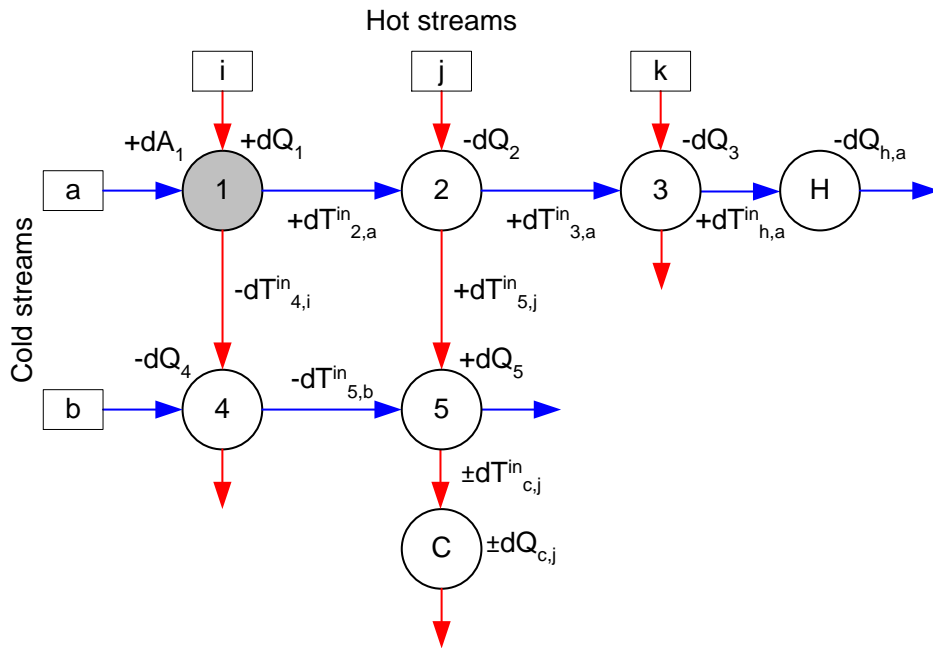


Figure C-1: Heat duty flow-on in heat exchanger networks – example.

**Example 1:** Find an equation for  $\theta_1^{h,a}$ , i.e. the heat duty flow-on factor from RE<sub>1</sub> to UE<sub>h,a</sub>.

Step 1: One pathway from RE<sub>1</sub> to UE<sub>a</sub>; 1,2,3,H<sub>a</sub>.

$$\text{Step 2: } dQ_{h,a} = -C_a dT_{h,a}^{in}$$

$$\text{Step 3: } dQ_{h,a} = -C_a dT_{3,a}^{in} (1 - P_{2,a})$$

$$dQ_{h,a} = -C_a dT_{2,a}^{in} (1 - P_{2,a}) (1 - P_{3,a})$$

$$\text{Step 4: } dQ_{h,a} = -C_a \frac{dQ_1}{C_a} (1 - P_{2,a}) (1 - P_{3,a})$$

$$\text{Step 5: } \theta_1^{h,a} = (1 - P_{2,a}) (1 - P_{3,a})$$

**Example 2:** Find an equation for  $\theta_1^{u,b}$ , i.e. the heat duty flow-on factor from RE<sub>1</sub> to UE<sub>c,b</sub>.

Step 1: Two pathways from RE<sub>1</sub> to UE<sub>b</sub>; 1,2,4,C and 1,3,4,C.

*Analysis of pathway 1,2,5,C.*

$$\text{Step 2: } dQ_{c,j}(1,2,5,C) = C_j dT_{c,j}^{in}$$

$$\text{Step 3: } dQ_{c,j}(1,2,5,C) = C_j dT_{5,j}^{in} (1 - P_{5,j})$$

$$dQ_{c,j}(1,2,5,C) = C_j dT_{2,a}^{in} P_{2,j} (1 - P_{5,j})$$

$$\text{Step 4: } dQ_{c,j}(1,2,5,C) = C_j \frac{dQ_1}{C_a} P_{2,j} (1 - P_{5,j})$$

$$\text{Step 5: } \theta_1^{c,j}(1,2,5,C) = -\frac{C_j}{C_a} P_{2,j} (1 - P_{5,j})$$

*Analysis of pathway 1,4,5,C.*

$$\text{Step 6: } dQ_{c,j}(1,4,5,C) = C_j dT_{c,j}^{in}$$

$$dQ_{c,j}(1,4,5,C) = C_j dT_{5,b}^{in} P_{5,j}$$

$$dQ_{c,j}(1,4,5,C) = C_j dT_{4,i}^{in} P_{4,j} P_{5,j}$$

$$dQ_{c,j}(1,4,5,C) = C_j \frac{-dQ_1}{C_i} P_{4,j} P_{5,j}$$

$$\theta_1^{c,j}(1,4,5,C) = \frac{C_j}{C_i} P_{4,j} P_{5,j}$$

$$\text{Step 7: } \theta_1^{c,j} = \theta_1^{c,j}(1,2,5,C) + \theta_1^{c,j}(1,4,5,C) = \frac{C_j}{C_i} P_{4,j} P_{5,j} - \frac{C_j}{C_a} P_{2,j} (1 - P_{5,j})$$

The above results for this example suggests that heat duty flow-on through pathway 1,2,5,C causes an increase in utility use for  $UE_{c,j}$ , whereas the heat duty flow-on through pathway 1,4,5,C causes a reduction in utility use. In effect, the two pathways partially cancel each other out for this case.

## Relationship between heat duty flow-on factors with common flow-on pathways

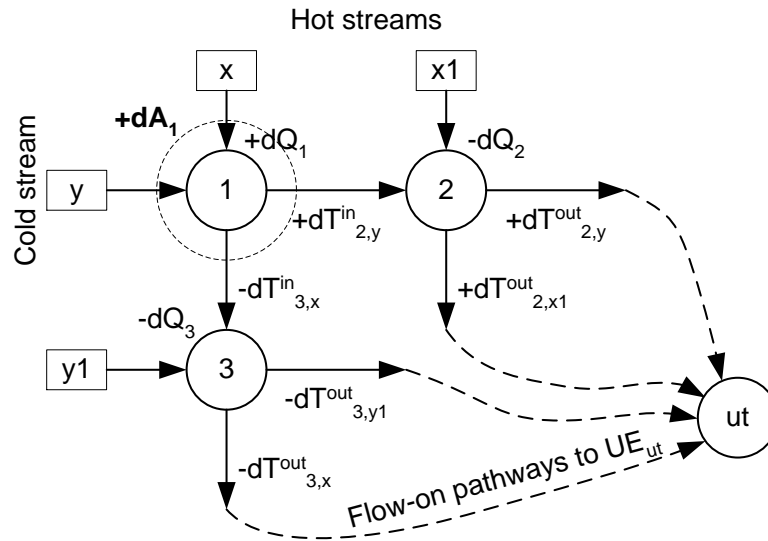


Figure C-2: Heat duty flow-on in heat exchanger networks – example.

Consider the network in Figure C-2 where  $dA$  is added to RE<sub>1</sub> resulting in a heat duty flow-on effect through the network to UE<sub>ut</sub>. For stream  $y$  exiting RE<sub>1</sub>, the differential energy balance is

$$dQ_1 = C_y dT_{2,y}^{in} \quad (C-25)$$

The change in duty of  $dQ_1$  is now related to the outlet temperature of stream  $y$  from RE<sub>2</sub>

$$dQ_1 = \frac{C_y dT_{2,y}^{out}}{1 - P_{2,y}} \quad (C-26)$$

The heat duty flow-on factor for RE<sub>2</sub> is

$$\theta_{2(y)}^{ut} = \frac{-dQ_{ut}}{dQ_2} \rightarrow dT_{2,y}^{out(*)} = \frac{-dQ_{ut}}{C_y \theta_{2(y)}^{ut}} \quad (C-27)$$

When  $dA$  is added to RE<sub>1</sub>, the outlet temperature of cold stream  $y$  will increase, which will also increase the outlet temperature of stream  $y$  exiting RE<sub>2</sub>. Likewise, if  $dA$  were to be added to RE<sub>2</sub> then the change in outlet temperature of stream  $y$  is positive. As a result we set equal these two outlet temperature to be equal

$$dT_{2,y}^{out} = dT_{2,y}^{out(*)} \quad (C-28)$$

The “\*” indicates the hypothetical situation of adding  $dA$  to  $RE_2$  so that its flow-on factor may be related to the  $RE_1$ . Substituting this result into Eq. C-26 gives

$$dQ_1 = -\frac{C_y}{1-P_{2,y}} \frac{dQ_{ut}}{C_y \theta_{2(y)}^{ut}} \quad (C-29)$$

which simplifies to

$$\theta_{1(y-y)}^{ut} = \theta_{2(y)}^{ut} (1 - P_{2,y}) \quad (C-30)$$

Now we focus on the heat duty flow-on down stream  $x1$  from stream  $y$ . Using the same energy balance as before, we find

$$dQ_1 = \frac{C_y dT_{2,x1}^{out}}{P_{2,x1}} \quad (C-31)$$

The heat duty flow-on factor for  $RE_2$  in terms of the outlet temperature of stream  $x1$  is

$$\theta_{2(x1)}^{ut} = \frac{-dQ_{ut}}{dQ_2} \rightarrow dT_{2,x1}^{out(*)} = \frac{-dQ_{ut}}{C_{x1} \theta_{2(x1)}^{ut}} \quad (C-32)$$

When  $dA$  is added to  $RE_1$ , the outlet temperature of cold stream  $y$  will increase, which will reduce the duty of  $RE_2$  and cause the outlet temperature of hot stream  $x1$  to also increase. In contrast, if  $dA$  were to be added to  $RE_2$  then the change in outlet temperature of stream  $x1$  is negative. As before, we set equal these two outlet temperature to be equal expect the relationship is negative,

$$dT_{2,x1}^{out} = -dT_{2,x1}^{out(*)} \quad (C-33)$$

Substituting back into Eq. C-31 gives

$$dQ_1 = \frac{C_y}{P_{2,x1}} \frac{dQ_{ut}}{C_{x1} \theta_{2(x1)}^{ut}} \quad (C-34)$$

which simplifies to

$$\theta_{1(y-x)}^{ut} = -\theta_{2(x)}^{ut} P_{2,y}, \quad \text{where } P_{2,y} = \frac{C_{x1}}{C_y} P_{2,x1} \quad (\text{C-35})$$

The heat duty flow-on factor along stream y for RE<sub>1</sub> is

$$\theta_{1(y)}^{ut} = \theta_{1(y-y)}^{ut} + \theta_{1(y-x)}^{ut} = \theta_{2(y)}^{ut} (1 - P_{2,y}) - \theta_{2(x)}^{ut} P_{2,y} \quad (\text{C-36})$$

A similar analysis of the possible flow-on pathways along stream x from RE<sub>1</sub> gives an equation with the same form as above.

$$\theta_{1(x)}^{ut} = \theta_{1(x-x)}^{ut} + \theta_{1(x-y)}^{ut} = \theta_{3(x)}^{ut} (1 - P_{3,x}) - \theta_{3(y)}^{ut} P_{3,x} \quad (\text{C-37})$$

### Relationship between overall heat duty flow-on factors

The overall heat duty flow-on factor is

$$\theta_1 = \sum \theta_1^{h(i)} = \sum \theta_1^{c(i)} \quad (\text{C-38})$$

Using the analysis the last section and without specifying whether the flow-on is to coolers or heaters, we may write

$$\theta_1 = \sum \theta_{1(x)}^{ut(i)} + \sum \theta_{1(y)}^{ut(i)} \quad (\text{C-39})$$

which is expanded to obtain

$$\theta_1 = \sum \theta_{1(x-x)}^{ut(i)} + \sum \theta_{1(x-y)}^{ut(i)} + \sum \theta_{1(y-y)}^{ut(i)} + \sum \theta_{1(y-x)}^{ut(i)} \quad (\text{C-40})$$

where *i* refers to each hot (or cold) utility exchanger. Substituting the previous analysis gives

$$\theta_1 = \sum (\theta_{3(x)}^{ut(i)} (1 - P_{3,x})) - \sum (\theta_{3(y)}^{ut(i)} P_{3,x}) + \sum (\theta_{2(y)}^{ut(i)} (1 - P_{2,y})) - \sum (\theta_{2(x)}^{ut(i)} P_{2,y}) \quad (\text{C-41})$$

Respective temperature effectiveness, *P*, values are the same for all flow-on pathways, which implies

$$\theta_1 = (1 - P_{3,x}) \sum (\theta_{3(x)}^{ut(i)}) - P_{3,x} \sum (\theta_{3(y)}^{ut(i)}) + (1 - P_{2,y}) \sum (\theta_{2(y)}^{ut(i)}) - P_{2,y} \sum (\theta_{2(x)}^{ut(i)}) \quad (\text{C-42})$$

Which is rearranged to obtain

$$\theta_1 = \sum(\theta_{3(x)}^{ut(i)}) + \sum(\theta_{2(y)}^{ut(i)}) - P_{2,y}(\sum(\theta_{2(y)}^{ut(i)}) + \sum(\theta_{2(x1)}^{ut(i)})) \quad (C-43)$$

$$\dots - P_{3,x}(\sum(\theta_{3(x)}^{ut(i)}) + \sum(\theta_{3(y1)}^{ut(i)}))$$

Consider if there was a hot utility on stream y immediately after RE<sub>2</sub>, then the heat duty flow-on factor from RE<sub>2</sub> to the heater is unity. Similarly if there were multiple flow-on pathways along stream y from RE<sub>2</sub>, we find that the sum of these flow-on factors must also be unity.

$$\theta_{2(y)}^{h,y} = 1 \Rightarrow \sum(\theta_{2(y)}^{ut(i)}) = 1 \quad (C-44)$$

In the case of stream x from RE<sub>3</sub>, there cannot be a heater immediately after RE<sub>3</sub> on stream x since it is a hot stream and the utility is always cold utility.

$$\theta_{3(x)}^{h,x} = 0 \Rightarrow \sum(\theta_{3(x)}^{ut(i)}) = 0 \quad (C-45)$$

Reversing the situation to look at the flow-on to coolers gives the opposite result. This analysis therefore implies

$$\sum(\theta_{3(x)}^{ut(i)}) + \sum(\theta_{2(y)}^{ut(i)}) = 1 \quad (C-46)$$

regardless of whether the flow-on is to heaters or coolers. The overall heat duty flow-on factors for RE<sub>2</sub> and RE<sub>3</sub> are defined as

$$\theta_2 = \sum(\theta_{2(y)}^{ut(i)}) + \sum(\theta_{2(x1)}^{ut(i)}) \quad (C-47)$$

$$\theta_3 = \sum(\theta_{3(x)}^{ut(i)}) + \sum(\theta_{3(y1)}^{ut(i)}) \quad (C-48)$$

Substituting the above results into Eq. C-43 gives

$$\theta_1 = 1 - P_{2,y}\theta_2 - P_{3,x}\theta_3 \quad (C-49)$$

The above equation may be modified to take into account stream splits, which gives

$$\theta_1 = 1 - \sum_{i_0=1}^i (\beta_{y(i)} P_{2,y(i)} \theta_{2(i)}) - \sum_{j_0=1}^j (\beta_{x(j)} P_{3,x(j)} \theta_{3(j)}) \quad (C-50)$$

## Heat duty flow-on factors for closed loops

In this section, the derivation of general formulas for describing the heat duty flow-effect in interacting closed heat loops is presented. Four groups of general cases have been constructed (Figure C-3) to base the analysis on. In all cases,  $dA$  is added to  $RE_1$ , which is the match between stream  $s$  and  $t$ . Stream are labelled so that the heat duty flow-on effect primarily flows along stream  $s$  to  $UE_{ut}$ . Square boxes in Figure C-3 are used to represent the function  $G$  that describes the heat duty flow-on effect through an unspecified number and arrangement of REs. Circles represent heat exchangers.

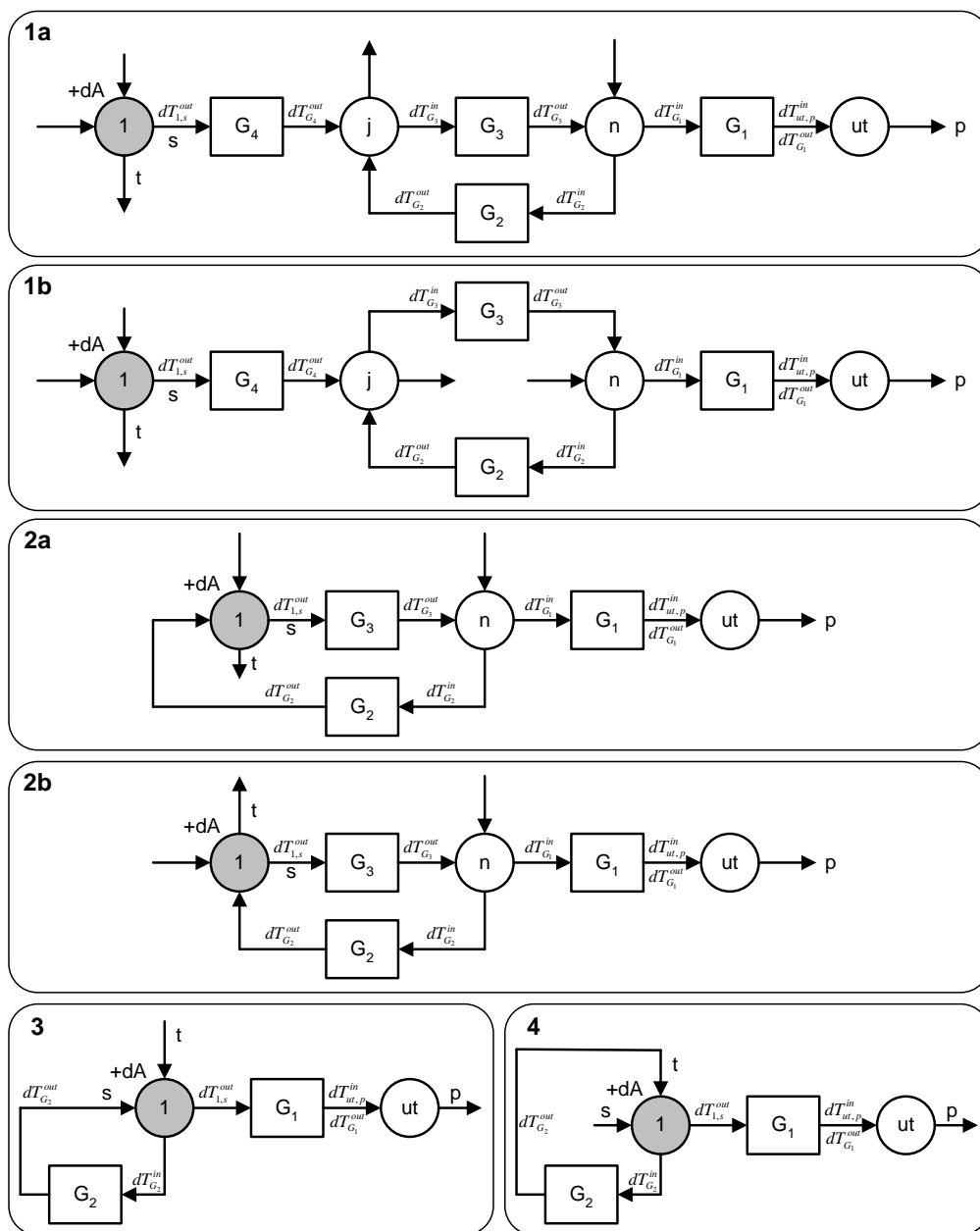


Figure C-3: Heat duty flow-on in interacting closed loops.

### Case 1: RE<sub>1</sub> positioned outside a closed heat loop

For cases 1a and b, the RE initiating the heat duty flow-on effect is outside the closed heat loop. The change in duty of UE<sub>ut</sub> may be related to the inlet  $dT_{G3}$  by moving upstream through the network starting at UE<sub>ut</sub>.

$$dQ_{ut} = C_{ut,p} dT_{ut,p}^{in} \quad (C-51)$$

$$dQ_{ut} = C_{ut,p} G_3 (1 - P_{n,i}) G_1 dT_{G_3}^{in} \quad (C-52)$$

The inlet  $dT_{G3}$  is affected by the outlet  $dT$ 's of  $G_4$  and  $G_2$  that enter RE<sub>j</sub>,

$$dT_{G_3}^{in} = (1 - P_{j,i}) dT_{G_4}^{out} + dT_{G_2}^{out} P_{j,i} \quad (C-53)$$

The inlet  $dT_{G3}$  is related to outlet  $dT_{G4}$  by the closed heat loop.

$$dT_{G_2}^{out} = \frac{G_L}{P_{j,i}} dT_{G_3}^{in}, \quad \text{where } G_L = P_{j,i} G_2 P_{n,i} G_3 \quad (C-54)$$

Substituting into the previous equation gives

$$dT_{G_3}^{in} = (1 - P_{j,i}) dT_{G_4}^{out} + G_L dT_{G_3}^{in} \quad (C-55)$$

which rearranges to

$$dT_{G_3}^{in} = \frac{1 - P_{j,i}}{1 - G_L} dT_{G_4}^{out} \quad (C-56)$$

Substituting Eq. C-56 into Eq. C-52 and simplifying gives the following the equations.

$$dQ_{ut} = C_{ut,p} \frac{(1 - P_{j,i}) G_3 (1 - P_{n,i}) G_1}{1 - G_L} dT_{G_4}^{out} \quad (C-57)$$

$$dQ_{ut} = C_{ut,p} \frac{(1 - P_{j,i}) G_3 (1 - P_{n,i}) G_1}{1 - G_L} dT_{G_4}^{out} \quad (C-58)$$

$$-dQ_{ut} = \pm C_{ut,p} \frac{G_4 (1 - G_{j,i}) G_3 (1 - G_{n,i}) G_1}{1 - G_L} \frac{dQ_1}{C_{1,s}} \quad (C-59)$$

From which the heat duty flow-on factor is found,

$$\theta_1^{ut} = \pm \frac{C_{ut,p}}{C_{1,s}} \frac{G_{OL}}{1-G_L}, \quad \text{where } G_{OL} = G_4(1-G_{j,i})G_3(1-G_{n(i)})G_1 \quad (\text{C-60})$$

Applying the same procedure as Case 1a, the general formula is obtained for case 1b. As a result, the derivation is abbreviated to show only the most important steps, commentary is omitted and only the final equation is assigned a reference number.

$$dQ_{ut} = C_{ut,p} G_3 P_{n,i} G_1 dT_{G_3}^{in}$$

$$dT_{G_3}^{in} = dT_{G_4}^{out} P_{j,i} + (1-P_{j,i}) \frac{G_L}{1-P_{j,i}} dT_{G_3}^{in}, \quad \text{where } G_L = (1-P_{j,i})G_2(1-P_{n,i})G_3$$

$$dT_{G_3}^{in} = \frac{P_{j,i}}{1-G_L} dT_{G_4}^{out}$$

$$dQ_{ut} = C_{ut,p} \frac{G_4 P_{j,i} G_3 P_{n,i} G_1}{1-G_L} dT_{1,s}^{out}$$

$$\theta_1^{ut} = \pm \frac{C_{ut,p}}{C_{1,s}} \frac{G_{OL}}{1-G_L}, \quad \text{where } G_{OL} = G_4 P_{j,i} G_3 P_{n,i} G_1 \quad (\text{C-61})$$

The general formula obtained in cases 1a and b is the same.

### Case 2: RE<sub>1</sub> positioned inside a closed heat loop

The second group of cases in Figure C-3 looks at how a change in area of a RE inside a closed heat loop affects the load of UE<sub>ut</sub>. The procedure for finding the general formula for case 2 is the same as case 1. The derivation is abbreviated once again.

$$dQ_{ut} = C_{ut,p} G_3 (1-P_{n,i}) G_1 dT_{1,s}^{out}$$

$$dT_{1,s}^{out} = \frac{dQ_1^{eff}}{C_{1,s}} + dT_{G_2}^{out} (1-P_{1,s}), \quad \text{where } dQ_1^{eff} = C_{1,\min} \Delta T_{\max,1} d\varepsilon_1$$

$$dT_{G_2}^{out} = \frac{G_L}{(1-P_{1,s})} dT_{1,s}^{out}, \quad \text{where } G_L = (1-P_{1,s})G_2 P_{n,i} G_3$$

$$dT_{1,s}^{out} = \frac{dQ_1^{eff}}{C_{1,s}} + G_L dT_{1,s}^{out} \Rightarrow dT_{1,s}^{out} = \frac{dQ_1^{eff}}{C_{1,s}} \frac{1}{1-G_L}$$

$$\theta_1^{ut} = \pm \frac{C_{ut,p}}{C_{1,s}} \frac{G_{OL}}{1-G_L}, \quad \text{where } G_{OL} = G_3(1-P_{n,i})G_1 \quad (\text{C-62})$$

Repeating the same procedure for case 2b obtains the following formulae.

$$dQ_{ut} = C_{ut,p} G_3(1-P_{n,i})G_1 dT_{1,s}^{out}$$

$$dT_{1,s}^{out} = \frac{dQ_1^{eff}}{C_{1,s}} + dT_{G_2}^{out} P_{1,s}, \quad \text{where } dQ_1^{eff} = C_{1,\min} \Delta T_{\max,1} d\varepsilon_1$$

$$dT_{G_2}^{out} = \frac{G_L}{P_{1,s}} dT_{1,s}^{out}, \quad \text{where } G_L = P_{1,s} G_2 P_{n,i} G_3$$

$$dT_{1,s}^{out} = \frac{dQ_1^{eff}}{C_{1,s}} + G_L dT_{1,s}^{out} \Rightarrow dT_{1,s}^{out} = \frac{dQ_1^{eff}}{C_{1,s}} \frac{1}{1-G_L}$$

$$\theta_1^{ut} = \pm \frac{C_{ut,p}}{C_{1,s}} \frac{G_{OL}}{1-G_L}, \quad \text{where } G_{OL} = G_3(1-P_{n,i})G_1 \quad (\text{C-63})$$

The general formula for cases 1a and b and 2a and b is the same:

$$\theta_1^{ut} = \pm \frac{C_{ut,p}}{C_{1,s}} \frac{G_{OL}}{1-G_L} \quad (\text{C-64})$$

where  $G_{OL}$  is the function that describes the heat duty flow-on effect as if there were no closed heat loop and  $G_L$  describes the flow-on effect within the loop.

### Case 3: RE<sub>1</sub> positioned on the “corner” of a closed heat loop

The final set of cases is where RE<sub>1</sub> is on the “edge” of the closed heat loop as shown in Figure C-3. The change in duty of UE<sub>ut</sub> may be related to the outlet  $dT_{1,s}$  of RE<sub>1</sub> by moving upstream through the network starting at UE<sub>ut</sub>.

$$dQ_{ut} = C_{ut,p} G_1 dT_{1,s}^{out} \quad (\text{C-65})$$

The outlet  $dT$  of RE<sub>1</sub> is affected by the change in area ( $dA$ ) and the outlet  $dT$  of  $G_2$  such that,

$$dT_{1,s}^{out} = dT_{G_2}^{out} (1 - P_{1,s}) - \frac{dQ_1^{eff}}{C_{1,s}}, \quad \text{where } dQ_1^{eff} = C_{1,\min} \Delta T_{\max,1} d\varepsilon_1 \quad (\text{C-66})$$

The outlet  $dT_{G_2}$  may be related to the outlet  $dT_{1,s}$  by the closed heat loop,

$$dT_{G_2}^{out} = G_2 dT_{G_2}^{in}, \quad \text{where } dT_{G_2}^{in} = \frac{dQ_1^{eff}}{C_{1,t}} + P_{1,t} dT_{G_2}^{out} \quad (\text{C-67})$$

$$dT_{G_2}^{out} = G_2 \frac{dQ_1^{eff}}{C_{1,t}} \frac{1}{1 - G_L}, \quad \text{where } G_L = G_2 P_{1,t} \quad (\text{C-68})$$

Substituting Eq. C-68 into Eq. C-66, which result is then substituted into Eq. C-65, obtains

$$dQ_{ut} = C_{ut,p} G_1 \left( G_2 \frac{1}{C_{1,t}} \frac{1}{1 - G_L} (1 - P_{1,s}) - \frac{1}{C_{1,s}} \right) dQ_1^{eff} \quad (\text{C-69})$$

which is rearranged to find the heat duty flow-on factor

$$\theta_1^{ut} = C_{ut,p} G_1 \left( \frac{1}{C_{1,s}} - G_2 \frac{1}{C_{1,t}} \frac{1}{1 - G_L} (1 - P_{1,s}) \right) \quad (\text{C-70})$$

and simplified to obtain a general formula

$$\theta_1^{ut} = \pm \frac{C_{ut,p}}{C_{1,s}} G_1 \left( \frac{P_{1,s} - G_L}{P_{1,s} (1 - G_L)} \right) \quad (\text{C-71})$$

#### Case 4: RE<sub>1</sub> positioned on the “edge” of a closed heat loop

The procedure for case 4 is the same as case 3. Like previous cases the derivation is abbreviated.

$$dQ_{ut} = C_{ut,p} G_1 dT_{1,s}^{out}$$

$$dT_{1,s}^{out} = dT_{G_2}^{out} P_{1,s} - \frac{dQ_1^{eff}}{C_{1,s}}, \quad \text{where } dQ_1^{eff} = C_{1,\min} \Delta T_{\max,1} d\varepsilon_1$$

$$dT_{G_2}^{out} = G_2 dT_{G_2}^{in}, \quad \text{where } dT_{G_2}^{in} = \frac{dQ_1^{eff}}{C_{1,t}} + (1 - P_{1,t}) dT_{G_2}^{out}$$

$$dT_{G_2}^{out} = G_2 \frac{dQ_1^{eff}}{C_{1,t}} \frac{1}{1 - G_L}, \quad \text{where } G_L = G_2(1 - P_{1,t})$$

$$dQ_{ut} = -C_{ut,p} G_1 \left( \frac{1}{C_{1,s}} - G_2 \frac{1}{C_{1,t}} \frac{1}{1 - G_L} P_{1,s} \right) dQ_1^{eff}$$

$$\theta_1^{ut} = \pm \frac{C_{ut,p}}{C_{1,s}} G_1 \left( 1 - \frac{G_2 P_{1,t}}{1 - G_L} \right)$$

$$\theta_1^{ut} = \pm \frac{C_{ut,p}}{C_{1,s}} G_1 \left( \frac{(1 - P_{1,t}) - G_L}{(1 - P_{1,t})(1 - G_L)} \right) \quad (C-72)$$

The analysis of four general cases has resulted in the identification of three general formulas for describing the heat duty flow-on effect through and in interacting closed heat loops.

### Application to a simple HEN with an interacting closed heat loop

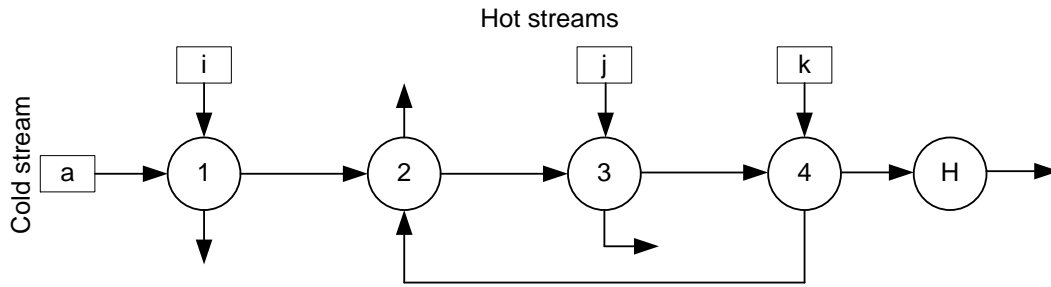


Figure C-4: Example of heat duty flow-on in interacting closed loops.

Location where $dA$ is added	Formula
1	$\theta_1^{h,a} = \frac{(1 - P_{2,a})(1 - P_{3,a})(1 - P_{4,a})}{1 - P_{4,k}P_{2,a}(1 - P_{3,a})}$
2	$\theta_2^{h,a} = \frac{(1 - P_{3,a})(1 - P_{4,a})}{1 - P_{4,k}P_{2,a}(1 - P_{3,a})}$
3	$\theta_3^{h,a} = \frac{(1 - P_{4,a})}{1 - P_{4,k}P_{2,a}(1 - P_{3,a})}$
4	$\theta_4^{h,a} = \frac{P_{4,a} - P_{4,k}P_{2,a}(1 - P_{3,a})}{P_{4,a}(1 - P_{4,k}P_{2,a}(1 - P_{3,a}))}$

## Analysis of a terminal recovery exchanger

In this section, two general cases of a terminal recovery exchanger (TE) are analysed. Figure C-5 presents the two cases using a generic HEN where  $dA$  is added to REs 1 and 3. Initial sizing of the REs suggest the target temperature on stream Y can be achieved by heat recovery.

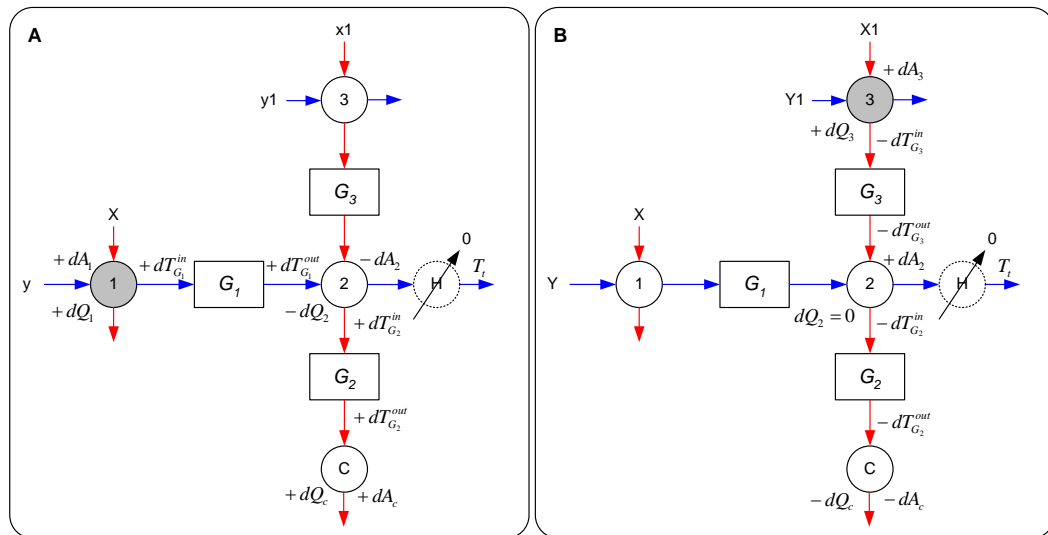


Figure C-5: Impact of increasing area of RE 1 and 3 on the duty of RE2 that is constrained by a target temperature.

### Case A

By adding  $dA$  to RE<sub>1</sub>, the duty on RE<sub>2</sub> is reduced requiring less area and resulting in a capital cost savings. This cost savings needs to be added to the other capital cost savings from reducing the area of a utility exchanger. The differential capital savings of a TE, i.e.  $dCC_{TE}/dA_1$ , caused by adding  $dA_1$  is

$$\frac{dCC_2}{dA_1} = -\frac{dQ_1}{dA_1} \frac{(bnA^{n-1})_2 \theta_1^2}{(dQ_2/dA_2)_{TE}} \quad (C-73)$$

Eq. C-73 is the same as presented in Eq. 4-11 (Chapter 4) for UEs. Adding  $dA$  to RE<sub>1</sub> increases its duty by  $dQ_1$ , which flows-on through  $G_1$  to TE<sub>2</sub> such that the heat duty flow-on factor from RE<sub>1</sub> to TE<sub>2</sub> is

$$\theta_1^2 = \frac{-dQ_2}{dQ_1} = G_1 \quad (C-74)$$

The expression for  $(dQ_2/dA_2)_{TE}$  is based on  $TE_2$  being regarded as a UE whereas the slope of the effectiveness-NTU relationship is derived based on  $TE_2$  being viewed as a RE because the flow rates through the exchanger are constant.

$$\left(\frac{dQ_2}{dA_2}\right)_{TE} = \frac{U\Delta T_{\max}}{1-P_{2,y}} \frac{dP_y}{dNTU_y}, \quad \text{where } \frac{dP_y}{dNTU_y} = (1-P_y)(1-P_y R_y) \quad (C-75)$$

In Eq. C-75 the slope of the effectiveness-NTU relationship is presented for a counterflow heat exchanger.

The utility savings from adding  $dA$  to  $RE_1$  is reduced since the target temperature on stream  $y$  is already achieved and the  $dQ$  of  $UE_{h,y}$  is zero. However there is a flow-on effect to other UEs such as the cold utility on stream  $x1$ . To find an expression for this new heat duty flow-on factor, the relationship between the inlet and outlet temperatures of  $TE_2$  are

$$dT_{2,x1}^{out} = \frac{C_y}{C_{x1}} dT_{2,y}^{in} \quad (C-76)$$

The new heat duty flow-on factor from  $RE_1$  to the cooler on stream  $x1$  is

$$\theta_1^{c,x1} = -\frac{C_{x1}}{C_y} G_1 \frac{C_y}{C_{x1}} G_2 = -G_1 G_2 \quad (C-77)$$

The incremental utility savings is then calculated using Eq. 4-7 from Chapter 4 based on reformulated heat duty flow-on factors.

### Case B

Focus is now turned to analysing case B in Figure C-5 where  $dA$  is added to  $RE_3$ . Since the change in duty of  $TE_2$  is nil, the previous chain rule expansion for the differential capital savings of a  $TE_2$  (Eq. 4-10, Chapter 4) is modified.

$$\frac{dCC_2}{dA_3} = \frac{dCC_2}{dA_2} \cdot \frac{dA_2}{dQ_{2,x1}^{in}} \cdot \frac{dQ_{2,x1}^{in}}{dQ_3} \cdot \frac{dQ_3}{dA_3}, \quad \text{where } dQ_{2,x1}^{in} = C_{x1} dT_{2,x1}^{in} \quad (C-78)$$

Substituting known terms into Eq. C-78 gives

$$\frac{dCC_2}{dA_3} = -\frac{dQ_3}{dA_3} \frac{(bnA^{n-1})_2 \theta_3^2}{(dQ_{2,x1}^{in}/dA_2)_{RU}}, \quad \text{where } \theta_3^2 = -\frac{dQ_{2,x1}^{in}}{dQ_3} \quad (\text{C-79})$$

The heat duty flow-on factor from RE<sub>3</sub> to TE<sub>2</sub> is

$$\theta_3^2 = \frac{-dQ_{2,x1}^{in}}{dQ_3} = G_3 \quad (\text{C-80})$$

An expression for the derivative of the duty-area relationship is found by taking the derivative of duty with respect to area for TE<sub>2</sub> for case B is

$$\left(\frac{dQ}{dA}\right)_2 = \frac{d(P_{x1} C_{x1} \Delta T_{\max})}{dA_2} = 0 \quad (\text{C-81})$$

which expression expands to

$$C_{x1} \Delta T_{\max} \frac{dP_{x1}}{dA_2} - P_{x1} C_{x1} \frac{dT_{2,x1}^{in}}{dA_2} = 0, \quad \text{where } d(\Delta T_{\max}) = -dT_{2,x1}^{in} \quad (\text{C-82})$$

Using *NTU* to define *A* and rearranging gives

$$\frac{dQ_{2,x1}^{in}}{dA_2} = \frac{U \Delta T_{\max}}{P_{x1}} \frac{dP_{x1}}{dNTU_{x1}} \quad (\text{C-83})$$

Case B also has a utility savings reduction due to no utility savings contribution from UE<sub>h,y</sub>. Since *dQ*<sub>2</sub> is zero, this implies

$$dT_{2,x1}^{out} = dT_{2,x1}^{in} \quad (\text{C-84})$$

The new heat duty flow-on factor to the cold utility on stream x1 is

$$\theta_1^{c,x1} = G_3 G_2 \quad (\text{C-85})$$

With the reconstructed heat duty flow-on factors, the sum of the utility savings may be calculated for case B.



# Appendix D

## Exhaust-inlet liquid coupled loop heat exchanger system

---

### Intermediate loop temperatures for liquid-coupled loop heat exchanger systems with optimum loop flow rate

The loop temperatures may be calculated using the  $\varepsilon$ -NTU method assuming a fixed loop flow rate,  $C_l$ . For energy recovery continuity, it is known,

$$Q_r = -Q_c = Q_h = Q_l \quad (D-1)$$

The first part of this derivation focused on finding the cold loop temperature,  $T_{lc}$ . Substituting the definition of  $Q_c$  from the  $\varepsilon$ -NTU method gives

$$Q_r = -\varepsilon_c C_{c,\min} (T_{cl} - T_{lh}) \quad (D-2)$$

The intermediate loop temperatures are related by

$$T_{lh} = T_{lc} + \frac{Q_r}{C_l} \quad (D-3)$$

Substituting into the previous equation and simplifying gives

$$Q_r = \varepsilon_c C_{c,\min} \left( \left( T_{lc} + \frac{Q_r}{C_l} \right) - T_{cl} \right) \quad (D-4)$$

Rearranging for  $Q_r$  gives

$$Q_r = \frac{\varepsilon_c C_{c,\min}}{1 - \frac{\varepsilon_c C_{c,\min}}{C_l}} (T_{lc} - T_{cl}) \quad (D-5)$$

Substituting the definition of  $Q_h$  for  $Q_r$  obtains

$$\varepsilon_h C_{h,\min} (T_{h1} - T_{lc}) = \frac{\varepsilon_c C_{c,\min}}{1 - \frac{\varepsilon_c C_{c,\min}}{C_l}} (T_{lc} - T_{c1}) \quad (D-6)$$

Rearranging for  $T_{lc}$  and simplifying gives

$$T_{lc} = \frac{\varepsilon_h C_{h,\min} \left(1 - \frac{\varepsilon_c C_{c,\min}}{C_l}\right) T_{h1} + \varepsilon_c C_{c,\min} T_{c1}}{\varepsilon_h C_{h,\min} \left(1 - \frac{\varepsilon_c C_{c,\min}}{C_l}\right) + \varepsilon_c C_{c,\min}} \quad (D-7)$$

Assuming the loop heat capacity flow rate is defined, all variables in the above equation are known and the cold loop temperature is defined. Similar fashion a formula for the hot loop temperature may be found

$$T_{lh} = \frac{\varepsilon_h C_{h,\min} T_{h1} + \varepsilon_c C_{c,\min} \left(1 - \frac{\varepsilon_h C_{h,\min}}{C_l}\right) T_{c1}}{\varepsilon_h C_{h,\min} \left(1 - \frac{\varepsilon_c C_{c,\min}}{C_l}\right) + \varepsilon_c C_{c,\min}} \quad (D-8)$$

Using the formulas for the hot and cold loop temperatures, a formula for the difference in temperature across the loop may be determined.

$$T_{lh} - T_{lc} = \frac{T_{h1} - T_{c1}}{\frac{C_l}{\varepsilon_c C_{c,\min}} + \frac{C_l}{\varepsilon_h C_{h,\min}} - 1} \quad (D-9)$$